INFORMATION TO USERS

This manuscript has been reproduced from the microfilm master. UMI films the text directly from the original or copy submitted. Thus, some thesis and dissertation copies are in typewriter face, while others may be from any type of computer printer.

The quality of this reproduction is dependent upon the quality of the copy submitted. Broken or indistinct print, colored or poor quality illustrations and photographs, print bleedthrough, substandard margins, and improper alignment can adversely affect reproduction.

In the unlikely event that the author did not send UMI a complete manuscript and there are missing pages, these will be noted. Also, if unauthorized copyright material had to be removed, a note will indicate the deletion.

Oversize materials (e.g., maps, drawings, charts) are reproduced by sectioning the original, beginning at the upper left-hand corner and continuing from left to right in equal sections with small overlaps.

Photographs included in the original manuscript have been reproduced xerographically in this copy. Higher quality 6" x 9" black and white photographic prints are available for any photographs or illustrations appearing in this copy for an additional charge. Contact UMI directly to order.

ProQuest Information and Learning
300 North Zeeb Road, Ann Arbor, MI 48106-1346 USA
800-521-0600

Interlaminar Stresses and Fracture Behavior in Thickness-Tapered Composite Laminates

Kan He

A Thesis

in

The Department

of

Mechanical Engineering

Submitted in Partial Fulfillment of the Requirements

for the Degree of Doctor of Philosophy at

Concordia University

Montreal, Quebec, CANADA

March 2002

ABSTRACT

Interlaminar Stresses and Fracture Behavior in Thickness-Tapered Composite Laminates

Kan He, Ph.D.

Concordia University, 2002

Design and manufacture of a variable thickness composite laminate such as a helicopter yoke involves tapering the laminate by dropping individual plies at discrete internal locations, in order to tailor the stiffness of the laminate. The ply drop in the laminate creates large interlaminar stresses and initiates delamination. Therefore, there is a necessity to investigate the fundamental failure mechanisms and controlling parameters that account for the delamination mode of failure in tapered laminates. In this thesis, a numerical and experimental study on interlaminar stresses and delamination in tapered laminates is presented, including a critical and comprehensive review on earlier works on this type of structure. Numerical analyses performed involved development of partial hybrid stress finite elements needed to enhance computational efficiency, and development of a physical concept-based modified shear-lag model that is based on the essential assumptions that both plies and resin layers are treated as carriers of tensile stress and also to act as stress-transfer media. Experimental analysis was attempted to assess the accuracy of the numerical predictions. For this purpose, tapered NCT-301

Graphite/Epoxy specimens were manufactured using a ply in-fill technique for the cured consolidation and tested under quasi-static uniaxial tension. To perform strength and delamination analyses of the tapered laminate, the laminate was modeled as a generalized plane deformation problem, where all the variables involved in the model are independent of the coordinate system. Also quasi-three dimensional partial hybrid finite elements were used to quantify the analysis. In addition to the plies, the inter-ply resin at the critical ply interface was also modeled in order to have direct and realistic interlaminar responses. Stress-based criteria that have proved to be effective in determination of critical location and load of delamination onset were utilized in this study to predict the delamination strength of the laminate. A good correlation between the predictions and experimental results were observed. Evaluation of strain energy release rates of delaminations occurring at the critical interfaces of the tapered laminate was carried out by using the *J*-integral approach. This was possible because of the path-independence of the *J*-integral that results in avoiding the need for analyzing the singular stress field near the delamination tip and reducing the computing effort required. Effects of various design parameters on the structural performance of the tapered laminate were studied so as to gain an insight into design considerations for tapered composite structures.

ACKNOWLEDGEMENTS

I would like to thank my co-supervisors, Professors Suong V. Hoa and Rajamohan Ganesan, for providing me with the tools to conduct this work, through the lectures on composite materials and structures and the consent to access the lab facilities, for their financial supports through research funds, and for their consistent encouragement and patience throughout the course of this research.

I would like to acknowledge Concordia University's School of Graduate Studies for the presentations of Concordia University Graduate International Student Fee Remission Awards in the earlier course studies and research.

I would also like to thank professors E I. Plotkin, L. Lessard, K. Ha, V. Latinovic and M. Pugh for their willingness to serve as member of the doctoral examination committee.

I am indebted to Dr. Ming Xie and Mr. Paul Ouellette for their assistance in setting up the instrumentation for the experimental tests.

Finally, to my parents, wife and daughter, I thank you for your patience throughout this endeavor. The inspiration and morale support you bring to me makes accomplishments like this possible.

TABLE OF CONTENTS

LIST OF FGIURES

LIST OF TABLES

Chapter 1

LITERATURE REVIEW AND OBJECTIVE

The application of advanced composites in aerospace structures has increased significantly in the past three decades. The advantages of composite materials lie in their high specific stiffness and strength, low weight, and elastic tailoring design capability. These allow the development of lighter, more efficient aircraft structures and machine components.

When composite materials are used in aerospace structural components and machine elements, it is usually desirable to tailor the material to match the localized strength and stiffness requirements in order to minimize the weight. For a fibrous composite laminate composed of unidirectional layers, this is often realized by changing the number of plies. This abrupt change in thickness, which is referred to as a ply-drop-off, introduces a stress concentration that promotes premature delamination failure of a laminate. It is this interlaminar stress concentration that is the subject of the present research.

1.1 Literature Review

This section presents a review of the recent advances in the study of tapered laminated composite structures. Following the regular laminated composite plates and beams, tapered composites formed by terminating or dropping off some plies in some primary structures have received much attention from researchers since the midst 80's. Their elastic tailoring properties and potential for creating more significant weight savings than commonly used laminated components allow an increasing use of the tapered composites in commercial and military aircraft applications.

A typical example is the helicopter yoke that is shown in Fig.1-1, where a progressive variation in the thickness of the yoke is required to provide high stiffness at the hub and relative flexibility at the mid-length of the yoke to accommodate flapping. The first commercial composite rotor-blade yoke assembly made from fiberglass was fabricated at Bell Helicopter Textron in 1995. Constructed completely from S-2 Glass, the dual yoke assemblies on the Bell 430 helicopter endure several times the number of flight hours than traditional titanium or steel yokes, and provide improved safety, as well. Much more tolerance to damage than conventional materials, and the elimination of corrosion is also displayed by these composite components. Other applications include composite aircraft wing skins, helicopter flexbeams, flywheels, etc.

A significant amount of research work has been done on the delamination analysis of tapered composites. A review of these developments is given in the following. The review is restricted to the studies published in the English language, mostly during the past two decades.

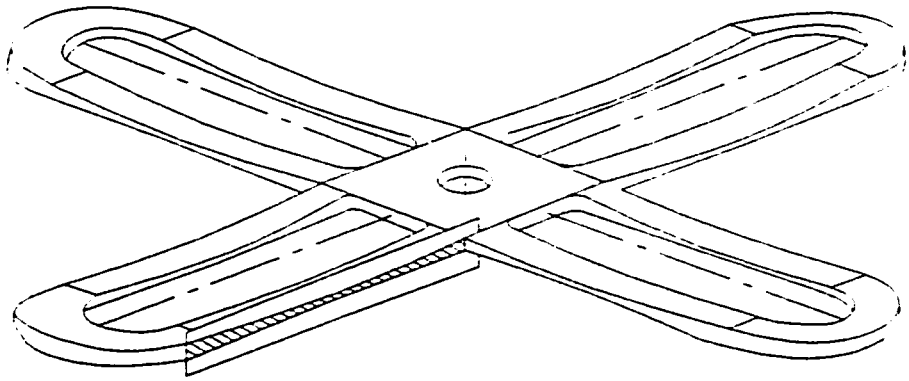

Figure 1-1 Helicopter yoke

1.1.1 Overall review

Tapered composite structures formed by terminating some of the plies create geometry and material discontinuities that act as sources for delamination initiation and propagation. From earlier research works concerning this type of structures, two major categories of work on tapered composites can be identified. The first is to understand failure mechanisms induced by drop-off plies in tapered construction. This work encompasses the determination of the state of interlaminar stresses in the vicinity of ply-drop-offs, the calculation of strain energy release rate associated with delamination within the tapered region, and the direct modeling of delamination progress using finite elements. The initiation and propagation of delaminations could thus be predicted. A large number of investigators have been engaged in conducting research on this respect. The list includes the works of Kemp and Johnson, [1] Curry et al., [2] Hoa et al., [3] Fish and Lee, [4] Salpekar et al.,[5] Murri et al.,[6, 8, 16] Armanios and Parnas,[7] Vizzini and Lee,[9] Wisnom et al.,[10-12] Harrison and Johnson,[13] Vizzini,[14, 32] Rhim and Vizzini,[17] Adams et

al.,[47] Wu and Webber,[19] Wu,[20] Miravete,[21] Thomsen et al,[41-43] Mortensen and Thomsen,[18] Mukherjee and Varughese,[22] Poon et al.,[35] Hofman and Ochoa,[31] Ochoa and Chan,[45] Davila and Johnson[49] and Trethewey et al.[46] The second category has been to seek more rational or optimal designs of damage resistant tapered composite structures by investigating the parameters that have substantial influences on the structural integrity. The works relating to parametric studies on tapered composites were conducted by Daoust and Hoa, [23] Llanos and Vizzini,[24] Thomas and Webber, [25] Cui et al.,[26] Vizzini, [27] Botting et al.,[28] Manne and Tsai,[29] Cairns et al.,[30] Fish and Vizzini[39-40], Pogue and Vizzini[44] and those who created ESDU Data Item 91003.[48]

This review concentrates on the works mentioned above, specifically 1) stress analysis, 2) delamination analysis, and 3) parametric study.

There are several basic types of tapers that are often used and analyzed, and they can be identified as shown in Fig. 1-2.

External-ply-drop-off tapers, defined as those in which the dropped plies are on a surface of the laminate, were examined by Wu and Webber[19], Wu, [20] Thomsen, [41-42], and by Miravete.[21] Wu and Webber applied a quasi-three-dimensional iso-parametric finite element for the linear elastic static analysis of a tapered laminated plate of infinite width subjected to a uniform in-plane load. Numerical results were given for a single step plate with various arrangements for the ply fibre directions. Very high peak stresses were predicted in the corner region of the step, but these were reduced when a resin fillet was included in the theoretical model for the step region. Following this analysis was a continuation work by Wu[2], in which the non-linear material behavior was considered to account for the redistribution of stresses in the resin that would occur in the presence of

the peak stresses. Compared with the linear results, the non-linear ones show that the peak stresses are reduced by about half as a result of non-linear deformation of the resin and the non-linear model gave more realistic prediction of interlaminar stress distributions and failure mode at the ply-drop-offs. Thomsen et al [41-42] used a simple mechanical model to investigate the local bending effects of ply-drop-offs in CFRP/honeycomb sandwich panels. The interaction between the core material and the face laminates was modeled using a two-parameter elastic foundation model. It was concluded from the examples given that the elastic response is strongly influenced by the presence of a supporting core material and that out-of-plane stiffness of the honeycomb core, the bending stiffness of base-line face laminate and the bending stiffness of the dropped sub-laminates provide significant bending effects induced by ply-drop-offs. Experimental investigation based on using electronic speckles pattern interferometers (ESPI) was conducted to validate the simple model and it was shown that the theoretically predicted and measured out-of-plane deflection profiles correlated well with respect to the local bending response induced by the ply-drop-offs. The model was extended to delamination failure analysis[43] and stress analysis for internal drop-off tapered laminates.[18] Miravete presented a study of mechanical behavior of variable thickness composite beams subjected to transverse load. A theoretical model based on a plane strain finite element theory was carried out to analyze the stress distribution near the areas of change of thickness, which is strongly dependent on thickness ratio. For low values of the angle of variation of thickness, the strength is outstanding and the variable thickness effect does not alter the mechanical behavior of the plate. For large angle of taper, the strength is lower because of variable thickness effect and failure occurs at the

location where thickness varies. The delamination mechanism is due to high interlaminar shear stress generated by the variable thickness effect.

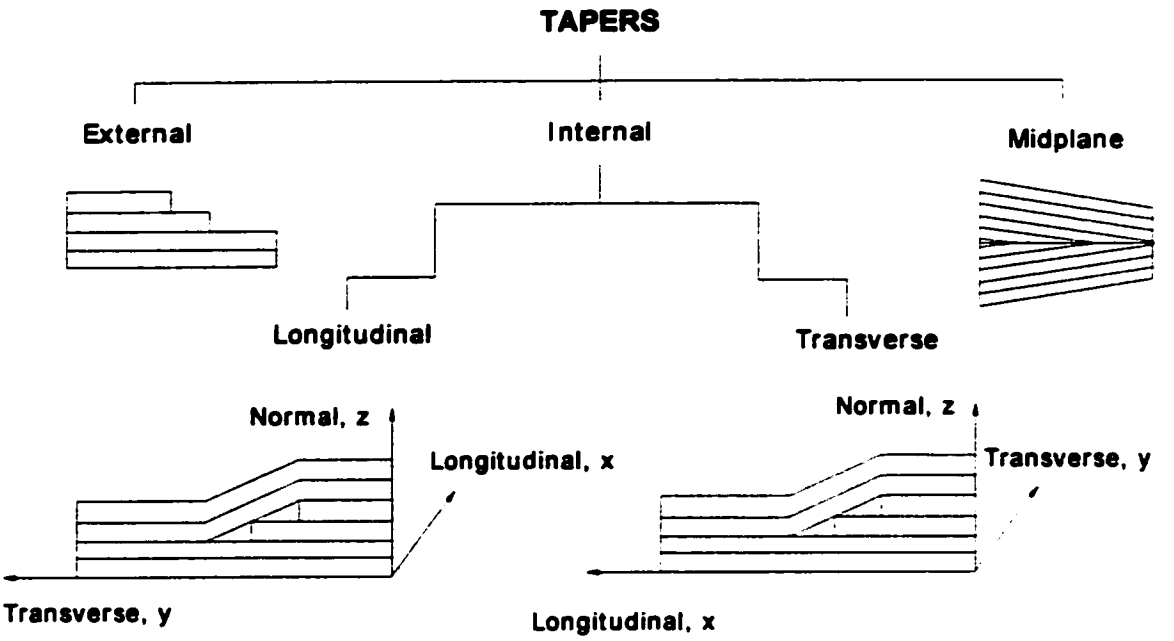

Figure 1-2 Basic types of tapers with dropped plies

Midplane-ply-drop-off tapers, defined as those in which the plies are terminated at the midplane, were examined by Hofman and Ochoa[31] with a shear deformable composite element. The shear deformable element was modified to accommodate variable element thickness with midplane layer drop-off. With the example problem it is shown that the tapered element formulation in the QHD40 element, which was developed by Ochoa for analysis and design of complex shape composite components, adequately models tapered and layered plates. The finite element modeling, however, was simplified

by neglecting the presence of small resin pockets caused by forming the terminated layers.

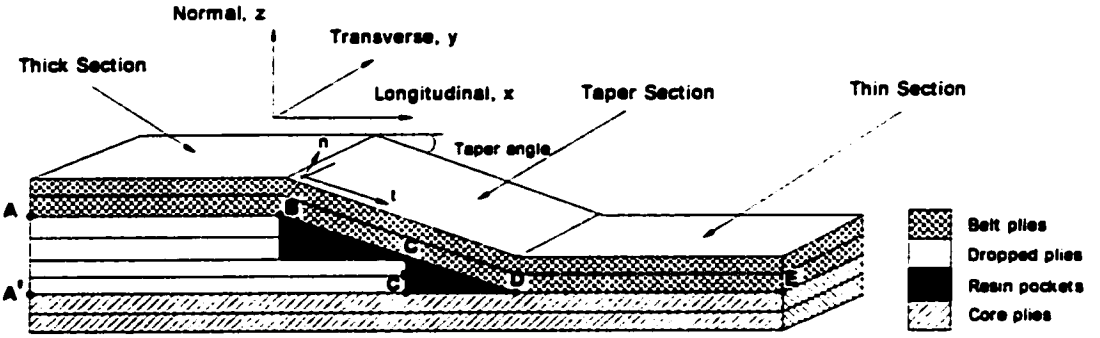

Figure 1-3 Schematic of taper with internal dropped plies

Two types of *internal-ply-drop-off-tapers* can be identified in terms of loading direction.

Longitudinal-ply-drop-off tapers are defined as those in which the internal discontinuities of the laminate are parallel to the applied load. In general, this type of taper was used to change the stress state in the free edge in order to suppress the delamination due to free edge effects. Vizzini[32] used quasi-three-dimensional finite element approach for strength prediction. In his analytical work, which correlated well with experimental evidence, Vizzini found that modeling a discontinuity with an associated resin pocket provides direct evaluation of the stresses in the region where failure occurs. Pogue and Vizzini[44] extended the structural tailoring techniques to the

suppression of the delamination at stress free edge by dropping plies just around the edge of the laminates. This is one of four-edge alteration techniques applied to prevent the delamination induced by the stress free edge of composite laminates. The introduction of the taper around the edge can change the state of stress at the free edge while introducing an internal discontinuity. It may help to decrease the interlaminar stresses, which arise as a result of the stress-free edge; however, the newly introduced internal edge may be prone to internal damage that is difficult to detect nondestructively. The fact that benefits and detriments of tapering exist simultaneously shows that much care must be taken in choosing an appropriate tailoring technique. Ochoa and Chan[45] also examined the longitudinal taper under tensile, bending and torsion loads using finite elements in analyzing laminates with 90 deg plies dropped symmetrically just inside the free edge. They found that under tensile loading interlaminar stresses at the free edge were reduced significantly, while under bending and torsion loading only a small amount of increase of interlaminar stress values was found.

Transverse-ply-drop-off tapers, defined as those in which the dropped plies are terminated from the interior of the laminate and the variation of the thickness goes along the primary loading direction, are concentrated in the remainder of this review because of their prevalent application in engineering. Most of the previous works in regard to delamination analysis of transverse-ply-drop-off tapers were towards ideally two-, quasi-three- or full three- dimensional representation of the geometry of the taper. In general, they may consist of 0, 90, ±45, ±15 deg plies or a certain combination of them with a tapering angle of less than 15 deg, usually with 5.71 deg for a 10-to-1 taper ratio. Most papers deal with symmetric laminates, while a few papers investigated asymmetric

laminates that are typically used in applications where a flat surface is important such as wing skins. Both numerically intensive finite element models and simplified analyses have been attempted. Experimentally, tapered specimens have been manufactured from graphite-epoxy and glass-epoxy composites and tested under quasi-static loading conditions and fatigue. The schematic of tapers with internally dropped plies is shown in Fig. 1-3.

1.1.2 Interlaminar stresses

The kernel part of investigation on delamination analysis of tapered laminates lies in how to accurately describe the interlaminar stress state in the critical region of components. Finite element method is the most prevalent and powerful tool in dealing with geometrically complex problems such as tapered composites as applied by a large number of authors. However, some authors either aimed at developing a simple physical model to demonstrate stress transfer mechanisms at the drop-off location or intended to develop a complex model as to find out the true stress distribution at the critical region. All of these methods are named here as non-FEM approaches.

Non-FEM approaches

A simple model for interlaminar stresses at the interface between the continuous plies and drop-off plies was developed by Armanios and Parnas.[7] on the basis of equilibrium conditions on the continuous sublaminate (belt) and with local stiffness variations at the ply-drop locations. In this model, the resin pockets were assumed as primarily shear stress carriers and ply-drop locations as extensional and concentrated

shear springs. The estimation of the interlaminar stresses was determined by application of a minimum complementary energy principle. Although the interlaminar shear stress from their model was in qualitative agreement with a finite element solution, it failed to capture the tensile nature of the interlaminar normal stress at the ply-drops.

Vizzini[14] employed the so-called shear-lag model to analyze interlaminar stresses in the region around drop-offs. In his model, resin layers were assumed to act as media carrying shear stresses only, while fiber layers as media carrying tension stresses. The stress state at the ply-drop region was modeled as a three-zone problem, in each of which force equilibrium was implemented. The resulting governing differential equations, subjected to satisfaction of constraints on displacement at the boundary by finite element results from the global analysis, the inter-zone constraints on displacements and forces, and constraints due to degenerate cases involving zero thickness, were solved with assumed polynomials for the displacements in the fiber layers. In comparison with the finite element results, he found that the shear-lag model could capture a majority of the load transfer mechanisms about internally dropped plies under tension stresses.

A simple mechanical model, which was originally developed by Thomsen et al [41-43] to investigate bending effects of the sandwich laminate with external drop-offs, was extended to obtain the stress distribution in laminates/sandwich laminates with internal ply-drop-offs. The structural modeling for the sub-laminates was based on Kirchoff assumptions, and the classical laminated plate theory (CLT) was used to describe the constitutive behavior of the sub-laminates. The resin layers were modeled as continuously distributed linear tension/compression and shear springs. In the case where the drop occurs in the face laminate of a sandwich panel, the interaction between the

laminates and the core material is modeled using a two-parameter elastic foundation model, which accounts for the shear interaction between the laminate and the core. One of them is used to determine the compressive /tensile strain in the core material, and the other to determine the shear strain in the core material. The system equations subject to the prescribed boundary conditions were solved through the multi-segment method of integration. It was shown that the interlaminar stresses calculated by the proposed simplified approach correlated very well with the finite element analysis. Meanwhile, the adaptability and limitation of the model were also presented through the discussion on structural parameters of sandwich laminates such as elastic wavelength, thickness of resin layers, cell-size of the honeycomb, etc.

Based on the Hellinger-Reissner variational functional, Harrison and Johnson[13] developed a stress-based method of approximation for the prediction of interlaminar stresses in the vicinity around ply-drops. The approach chosen was to follow Pagano's laminate structural theory, which modeled the laminate by a series of layers with the stress field assumed within each layer. The stresses were assumed to be explicit functions of the thickness coordinate with stress variables as coefficients. These stress variables were functions of the longitudinal coordinate only. Substituting the assumed stress field into the Hellinger-Reissner variational principle and invoking the stationary condition with respect to all admissible stresses and displacements led to a system of differential-algebraic equations (DAEs) that could be solved by finite difference method. The solution for interlaminar stresses in the modeled tapered laminates that were assumed to be under generalized plane deformation was found to be in good agreement with finite element solution.

In general, simplified mechanical models as shown in the mentioned works for the interlaminar stress analysis of tapered laminates provides more physical insight than that provided by FEM, and reasonable results with comparison to that calculated with FEM are reachable based on physically appropriate assumptions.

Displacement based finite element approaches

As for other composite structures, the majority of approaches to predict interlaminar stress and delamination in tapered composites are based on Finite Element methods. Displacement based finite elements and assumed stress hybrid elements are most commonly applied in these areas and deserve more discussion in this review.

In displacement based finite element models, also called "compatible models" by Pian and Tong,[33] the displacements are assumed and are required to be continuous over the whole domain. They are the most commonly used finite element models because of their inherent ease of formulation for most applications and efficiency of computation. Their ease of formulation is due to the relatively loose restriction of continuity on the assumed displacement field, which on the other hand, leads to a loss of accuracy in predicting stresses due to the fact that equilibrium of the stresses within the elements is satisfied only in an integral sense.

The Full three-dimensional displacement based finite element approach was employed in some of the studies, including the works by Adams, et al., [47] Hoa, et al.,[3] Daoust and Hoa.[23] In Ref. 47, nonlinear material response and thermal residual stresses of porous laminates with ply-drop-offs were investigated. Free-edge effects, however, were not included due to the generalized plane strain assumption imposed. Finite

element meshing adopted in this model was very coarse in that at the ply-drop region no longitudinal mesh refinement was made. In Ref. 3, the three-dimensional mesh at the ply-drop region was refined by a sub-modeling technique. This approach involved successive reduction and refinement of the mesh in the region of interest while retaining the results of the previous iteration as boundary conditions for the refined mesh. The purpose of this method was to have a refined mesh in the region of large stress gradients while keeping the number of degrees of freedom of the solution required for each pass of the finite element solver within the capability of the computer that was available. In Ref. 23, an extension of this work, three-dimensional finite elements were employed again with development of a more efficient computer program for parameter analysis.

Some of the studies employed *Quasi-3D (Q3D) displacement based finite element* approaches by reducing the domain into two-dimensional boundary problem based on the assumptions of either generalized plane deformation, or generalized plane strain. In both the theories all the cross sections would remain plane, and the stresses, geometric and material properties, and strains would be independent of the coordinate normal to the plane of analysis. The difference between these two theories lies in the fact that the former allows bending about the coordinates comprised of the analyzed plane and twisting about the remaining coordinate, of which the variables are independent. This theory is applicable to nonsymmetric laminates under extension loading conditions prescribed so as to accommodate deflections and rotations caused by the eccentricity of the load path. The latter is ideal for the analysis of long symmetric structures under tensile loading condition. Typical applications of Q3D approaches based on the above theories for transverse-ply-drop-off tapers include the work of Kemp and Johnson[1] and

Curry et al.[2] In each of these models, the displacements normal to the plane of the model were still included and therefore these models have five or six nonzero components of strain. In Ref. 1, four elements through the thickness in the plies in the vicinity of the drop-off were set up to perform the analysis as required to reasonably satisfy the continuity of intralaminar stresses and strains. The analyzed results show that the interlaminar stresses reach the maximum at the ply-drop location. Curry et al.[2] conducted global/local approach to tapered composite analysis. The global analysis was performed using the general-purpose computer program STAGS, while the local analysis for determining the three-dimensional state of stress in the vicinity of the dropped plies was based on the generalized plane deformation. Their study shows that interlaminar normal stress in the interface or resin layer reaches a maximum at the end of the dropped plies, and at the same location where the interlaminar shear stress is close to its maximum value. Variughese and Mukherjee[15] also made global-local approach for the analysis of tapered composites. Considering that the drop-off needs not pass through a nodal line in global analysis, they developed drop-off elements that can be independent of the location of the drop-offs. The elements were used in global analysis to reduce the size of global structural matrix and showed more flexibility in meshing division. An accurate stress distribution around the ply-drop-offs was determined by local analysis with refined finite elements over the critical region and the input from the global analysis as the boundary conditions. Good correlation was found by comparing the results obtained using this approach with published results obtained based on three-dimensional modeling.

Some of the authors, however, were more interested in performing *plane stress and plane strain finite element analysis* by reasonably reducing the domain of the

problem into two dimensions in order to avoid the computationally intensive nature of three-dimensional finite element model. Salpekar, et al.[5] and Murri, et.al.[6, 8, 16] are among those authors who performed interlaminar analysis and furthermore determined strain energy release rate associated with the delamination growth.

Assumed stress hybrid finite element approaches

The majority of finite elements used for stress analysis of tapered composites are based on displacement formulation, particularly those employed in commercial software packages. This is due to the simple approach to the element formulation provided by the displacement model. However, there are some disadvantages inherent in the displacement approach in analysis of laminated composites, which have limited its application in accurately describing the response of the critical area in tapered laminated composites. The main disadvantages of displacement elements include the fact that they can not satisfy continuity conditions on displacements and transverse stresses at interlaminar surfaces due to the discontinuity in material properties, and the fact that the convergence of displacement element model for problems with large gradients of stresses, as in the case of the drop-off location in tapered composites, is very slow. Moreover, the modeling leads to excessive requirement of computer resources for finer element meshing that is needed to determine more accurate structural and local responses of the composite. In general, analysis of tapered composites based on displacement approaches can only provide qualitative and trend information on responses of the structure under certain loading.

On the other hand, *assumed stress hybrid elements*, motivated by an attempt to overcome the shortcomings of displacement elements, was developed in 1964 by Pian[34] and have since been extensively applied in the analysis of regular laminated composites. As in the equilibrium model, this hybrid element model uses assumed equilibrating stress fields within the elements which enhances stress accuracy and also uses assumed boundary displacements in terms of nodal values such that they satisfy inter-element continuity.

Fish and Lee[4] first introduced hybrid elements in the analysis of tapered composites. In their work, *3D assumed hybrid elements* were used to develop a methodology for the prediction of delamination onset in tapered composite laminates containing multiple ply-drop steps. The model contained 433 eight-node brick elements and six-node pentahedral elements for a total 2,916 global degrees of freedom. The eight-node hexahedral elements were based on an assumed stress hybrid formulation and could provide more accurate stresses than linear displacement element. The six-node pentahedral elements were based on the assumed displacement formulation. The influences of the sublaminates above and below the plydrop steps were investigated. Both experimental testing and finite element modeling of the tapered region were conducted. The failure of the tapered laminates is due to the interlaminar shear stress and occurs at the last ply-drop step.

This approach has been systematically employed by the research group at University of Maryland. In addition to the above, the topics that they studied with this method also include delamination failure mechanism analysis,[9] delamination prevention techniques,[24] effects of realistic taper geometries on the stress state at critical regions[27],

shear-lag analysis about an internally-dropped ply,[14] delamination of ply-drop configurations and tailoring concepts.[28, 39-40] Vizzini[32] and Fish and Lee[4] also used *Q3D assumed stress hybrid* method to perform strength analysis of laminated composites with internal discontinuities parallel to the applied load, and to examine the free edge effects in a dropped ply specimen, respectively.

Another elaborate model that consists of shell elements, solid elements and transition elements was developed by Davila and Johnson[49] to capture post buckling response in the internally dropped laminates. The shell elements employed to model the majority of the laminate is a 9-node assumed natural strain (ANS) element with 5 degrees of freedom per node. The solid element used to model the ply-drop-off region is a 20-node serendipity brick element with 3 displacement degrees of freedom per node. A transition element that has 15-node element with 51 degrees of freedom per node and permits the connection of shell and solid element was constructed by degenerating the 20-node solid element. The influences of the geometric nonlinearity on the stress concentration and the delamination initiation were examined through the analysis by this advanced element.

1.1.3 Delamination analysis

Delamination analysis of tapered composites involves determination of interlaminar stresses using finite element methods as described in the first part of this review, prediction of delamination onset location, and simulation of delamination crack propagation.

In order to predict delamination onset and growth and hence the performance of the various laminates studied, some kind of failure analysis was applied. Two general approaches exist for this purpose. They are the *strength-of-materials approach* (stress-strength approach) and the *strain-energy-release-rate approach* (Fracture Mechanics approach). In the strength-of-materials approach, the local stress or strain state is compared to the material strength allowables. In the strain-energy-release-rate approach, which is based on fracture mechanics, the laminate is assumed to fail when the available strain energy of a delamination crack in a ply interface exceeds the critical strain energy release rate for the material.

Strength-of-materials approach

In application of this approach to perform delamination analysis, usually more than one failure criterion was used to predict the weakest location over the whole structure. Frequently, different criteria were used for prediction of in-plane and out-of-plane failure of the plies as well as for out-of-plane failure between plies.

Kemp and Johnson[1] used the maximum stress criterion to predict the failure in the rich resin surrounding the dropped plies, while applying the Tsai-Wu criterion for intralaminar failure prediction. With these criteria in consideration, they found that majority of the first failure events in either tension or compression are resin failures in a few cases for which failure occurred at the ply-drop.

Both interlaminar and intralaminar failure criteria were used by Curry et al.[2] for their analysis. The interlaminar criterion they used, which is based on matrix failure

mode developed by Hashin, was evaluated at all interfaces between plies with different fiber orientations in the local model, while the intralaminar criterion was a modification of Tsai-Wu, in which only the strength parameters that correspond to the failure mode were included. The failure analysis with the above criteria and finite analysis results indicated that the first major failure event for the laminate studied was a delamination at the interface between the dropped ply and continuous ply that appeared to initiate at the end of the dropped ply. These failure analyses, however, underestimated the experimental failure load by more than 30%.

Fish and Lee[4] used modified Tsai-Wu criterion to predict the out-of-plane failure of the composite laminates in their study. They introduced the average stress concept for the situations where the stress state is dominated by a single stress and applied it to the out-of-plane stress distributions obtained from the numerical analysis, thus the maximum stress failure was considered. They found that the maximum stress criterion, using an interlaminar stress averaging distance of one ply thickness, provided consistent and accurate delamination onset predictions for the laminates investigated, which was also supported by the experimental observations.

On the basis of the assumption that the primary failure in the tapered composites is to be delamination and to occur in the interply resin layer, Vizzini [27, 32] employed the von Mises stress criterion, an isotropic failure criterion, to be a measure of the overall stress state for a given configuration. In Ref. 27, the maximum von Mises stress in the realistic laminate with an ill-formed pocket modeled as to be four sided rather than triangular as is usually assumed, or with unsymmetric ply-drops, occurred around the last ply-drop-offs. He found that the results agreed well with his finite element analysis, and

further the von Mises stress for the laminate with a fracture void increased by more than 50%, which indicated that the presence of a void greatly affected the stress state around the ply-drop and that the interlaminar stress criterion that excludes voids will overpredict the onset of damage. In Ref. 32, von Mises criterion was used to determine the strength of the resin pocket at the discontinuity. Falling within the scatter of the experimental data for delamination initiation, this resin pocket model predicted very well the initiation of damage for the laminates dominated by the internal edge failure.

Harrison and Johnson[13] used the delamination fraction concept, which was proposed by Brewer and Lagace, as a measure to investigate the effect of eccentricity and stiffness discontinuity on the tendency of laminates with dropped plies to delaminate. In combination with their mixed variational approach, they found that the highest delamination fraction value contributed by both the interlaminar normal and shear stresses at ply-drop region and show that it is the stiffness discontinuity rather than eccentricity of the laminate that has a larger influence on the interlaminar stresses and eventual delamination.

Thomsen and Mortensen[18] applied a point stress criterion for prediction of delamination failure in composite laminates with external ply-drop-offs. The stress at a certain characteristic length away from the drop step was evaluated with a simplified analytical model. Delamination failure is considered to occur if the calculated stress exceeds the strength of the interply resin layers. An empirical formula for the characteristic length calculation and the respective characteristic length stress criterion were suggested. It was concluded that the proposed approach works well due to the good match between experimental and analytical results.

It is seen that in strength-of-materials approach for delamination analysis two kinds of criteria, i.e. point stress approach, as used in Ref. 43, and stress averaging approach, can be identified in terms of the techniques used to obtain principal stresses, both of which was introduced due to the singular nature of interlaminar stress distribution at ply-drop-off positions, where the interlaminar stress peaks occur and by far exceed the interface material allowables at the load levels where delamination failure can be detected experimentally. Thus, it is impossible to provide physically meaningful prediction of delamination initiation in laminated tapered composites by direct application of the calculated peak stresses together with some point stress criteria. To overcome the difficulties induced by the inherent singularity some other techniques like 'stress averaging' or 'effective/characteristic length' were applied and approved to be effective in dealing with delamination initiation analysis of tapered laminates.

Strain-energy-release-rate approach

Strain energy release rate is a concept from fracture mechanics. It may be interpreted as the amount of work required to close a delamination by an incremental length. Much of the work has been done to calculate the modes of strain energy release rate using finite element method for delamination in tapered composites.

In Reference[48] the general design guidelines and analysis capability for the prediction of delamination of tapered composites are presented. Two cases are studied, i.e. zero transverse strain for a wide plate or zero transverse loads for a longitudinal strip. It is indicated that a value for the critical strain energy release rate associated with delamination between layers is required for delamination initiation and growth analysis,

and notes are included on how that may be measured experimentally. Guidance is given on good design practice in tapering a laminate to reduce the likelihood of delamination. Results from the analysis are compared with limited experimental data from the literature, and agreement is seen to be reasonable.

Salpekar, et al.[5] conducted delamination analysis of tapered composites with this approach. The virtual crack closure technique (VCCT), combined with a 2D finite element model, was used in their analysis to obtain the strain-energy-release rate components, in mode I (G_I), and in mode II (G_{II}), based on the local forces at and ahead of the delamination tip and the relative displacements behind the delamination tip. Two models were shown in this work, one for the interlaminar stress distribution along the interface BCDE (Fig. 1-3) and the other for the strain-energy-release-rate variation for various size delaminations assumed along the interface BCDE. With the first model, they found that the interlaminar normal stress shows peaks near the ply-drop-offs and the largest one occurred at the transition point D. The sudden changes in the stress distributions at drop-off location indicated that stress singularities are more likely present. In the second model, the strain energy release rate was calculated for a delamination assumed to initiate at the juncture of the intersection of the taper and the thin laminate, point D. The delamination along the thin section of the laminate consisted of predominately of mode I component, while the delamination along thick section initially consisted of mode I component and was replaced by the mode II component afterwards. This linear fracture mechanics approach presented a new vision to predict failure of tapered composites, but it lacked an experimental investigation to validate the conclusions drawn.

Trethewey et al. [46] also employed linear elastic fracture mechanics to determine the mode I and II components of strain energy release rate. Their analytical model was based on shear deformation plate theory with a through-width delamination embedded at the interface between continuous and discontinuous sublaminates. The influence of geometry and material properties on the structural performance of the tapered laminate was determined with the parametric study. It was shown that among the geometric parameters, the number of discontinuous layers at a single axial position had the strongest influence, while the crack size of the delamination had a less pronounced effect.

Murri, et al.[6] later extended their analysis to fatigue delamination onset prediction in unidirectional tapered laminates, using nearly the same techniques as in Ref. 5 except for the experiments included to verify the analysis results. It was shown in the experiments that for some of the laminates studied initial stable delamination that often started with a resin crack at the drop-off and final unstable delaminations that initiated at the junction of the thin and thick sections of the laminate were observed. Finite element calculations for the strain energy release rate associated with the initial resin delamination showed good agreement with this phenomenon.

Ref. 8 by Murri et al. was a follow up of the analysis in Ref. 5, in which delamination of tapered multi-angle laminates under tension fatigue loading was examined numerically and experimentally. In addition to the delamination existing at the interface between the belt and core as in Ref. 5 and 6 the matrix ply cracking resulted from the presence of ±45° plies in the laminate of analysis was also modeled by an observed failure mode. Only one type of the laminates examined tended to fail as modeled using the finite element analysis since the delaminations in other types of

laminates were dominated by matrix ply cracks and were always at locations other than interface BCDE.

In Ref. 16, Murri, et. al. examined the effect of combined tension-bending loading on glass-epoxy laminates with a nonlinear taper and internal ply-drops. The delamination growth originating from the initial tension crack at the drop-off was simulated in the 2D finite element model by releasing pairs of multi-point constraints at the critical interfaces, and the strain energy release rates were thus calculated using VCCT for a delamination starting at the ply-drop-off location and growing toward the thick or thin section. They found that the initial delamination grows first toward the thick section where the delamination is predominately G_{II}, (shear mode) and grows all the way, as the fatigue loading was continued, to the junction of the tapered and thick section where the delamination is predominately G_I (opening mode). The results obtained from their model also indicated that the mode ratios are very sensitive to the discrete angle changes in the model.

Wisnom, el al.[10] presented the results of the tests carried out on the rapidly tapered specimens with dropped ±45° and 0° plies in order to determine static and fatigue strengths. The failure modes for the three types of specimens studied are either fiber breaks initiated near the first dropped ply or delamination occurring at the dropped 0° plies which is more susceptible to delamination than ±45° plies. Wisnom et al. continued this analysis in the paper[12] by comparison of tapered laminate delamination with delamination in internal cut plies under fatigue loading. They found that the delamination in the cut ply specimens propagated in both directions from the cut, whereas for the dropped ply specimens it propagated only to the thick end with slower delamination rate

than cut ply specimens due to the effect of through-thickness compressive stresses in the region where delamination initiated. Normalization of strain energy release rates calculated from a simple equation was made by dividing the cyclic strain-energy-release-rate range ΔG by the fracture energy G_c deduced from a static tension delamination test, and obtained the similarity between the delaminations in the specimens under fatigue and static loadings.

In Ref. 11 by Wisnom et al., three asymmetrical composites with 0/±45° layups loaded in tension were chosen to carry out an experimental investigation on the effects of the tapered geometry and the stiffness of the discontinuous plies for asymmetrically tapered sections based on the conclusion that the strain energy release rate associated with the discontinuous plies was the critical factor controlling delamination into the thick section, with the effect of the tapered geometry being of secondary importance. In comparison with the previous results for the thick section delamination failure mechanisms in the symmetric tapers studied in Ref. 12, they concluded that the asymmetry does not appear to have a significant effect on thick section delamination. Existence of thin section delamination induced by specimens tapered geometry, which is less severe than thick section delamination, however, showed a different delamination behavior from the previously tested symmetric specimens and therefore further investigation was encouraged to explain it. The taper angle and the degree of consolidation in the region around the dropped plies are likely the reasons suggested by the authors for the question. A summary of the results for transverse-ply-drop tapers is listed in Table 1-1. It was indicated in this table that the specimens often used for analysis and testing were made from Glass/Epoxy or Graphite/Epoxy, and were

configured in multidirectional and symmetric form. The majority of the work was done based on an experimental program wherein the test coupons were subjected to static and /or fatigue loading. Various finite element modeling and non-finite element approaches were used in the analysis of tapered laminates. Strength-of-materials criteria and fracture criteria were almost equally applied by the authors. The maximum interlaminar shear stress was found by most works to appear at the ply-drop step, while the maximum interlaminar normal stress was found to appear at the ply-drop step by about half of the authors, and at the taper root by the other half of the authors. The final delamination will grow into the thick and thin sections simultaneously, but the location of delamination initiation was found to appear at the ply-drop step in some works, and at the taper root in others.

There are many factors contributing to the stress state, but among them most important one is the configuration of a laminate. So for different configurations of a laminated composite, it is impossible to make a categorical statement as to the location where stress peaks appear. However, the contradiction in this regard with an identical configuration under same loading conditions and same constraints can only be attributed to the methodology used in modeling the taper. It seems that the model employed by Vizzini, Lee, etc., where 3-dimensional assumed hybrid element was implemented with inclusion of interply resin layers approximates the true stress state better than others. Zero thickness resin layer causes singularity at ply-drop region, and variation of interply layer

Table 1-1 Summary of data and results for monolithic laminated composites with internal transverse-ply-drop-off tapers

Reference No.		1	2	3	4	5	6	7	8	9	10	11	12	13	14	15	16	17	18
Materials	Glass / Epoxy			•	•	•	•	•	•	•	•		•		•		•	•	
	Graphite / Epoxy	•	•	•			•		•				•			•			
	Carbon / Epoxy										•	•							
	Al / Epoxy																		•
Configuration	Symmetric	•		•	•	•	•	•	•	•	•		•		•		•	•	
	Nonsymmetric	•	•									•		•	•	•		•	•
	Unidirectional			•					•				•		•			•	•
	Multidirectional	•	•		•	•	•	•		•	•	•		•		•	•	•	
Loading	Static	•	•	•	•	•		•		•	•	•	•	•	•	•		•	•
	Fatigue						•		•		•	•	•				•		
Experiment			•	•	•		•		•	•	•	•	•				•		
Numerical Modeling	3D-d			•															
	Q3D-d	•	•																
	2D-d					•	•		•							•	•	•	
	3D-h				•					•									
	Q3D-h				•														
	Other							•			•	•	•	•	•				•
Failure Criterion	SM	•	•	•	•					•				•					•
	SERR					•	•	•	•		•	•	•				•		
Maximum Interlaminar Stress	σ_n or σ_{zz} at C		•		•					•				•	•	•		•	
	D	•		•		•	•	•	•										•
	σ_t or σ_{xz} at C	•	•	•	•	•	•	•	•	•				•	•	•		•	
	D																		•
Delamination Initiation and Growth	Initiating at C				•					•	•	•	•				•		
	D		•	•		•	•	•	•										
	Growing into																		
	Thin section		•	•	•	•	•	•	•	•		•					•		
	Thick section		•	•	•	•	•	•	•	•	•	•	•				•		
Reference No.		1	2	3	4	5	6	7	8	9	10	11	12	13	14	15	16	17	18

Notations:

3D-d – Three-dimensional displacement based finite element;

Q3D-d – Quasi-three-dimensional displacement based finite element;

2D-d – Two-dimensional displacement based finite element;

3D-h – Three-dimensional assumed stress hybrid finite element;

Q3D-h – Quasi-three-dimensional assumed stress hybrid finite element;

SM – Strength-of- Materials approach;

SERR – Strain-Energy-Release Rate approach;

C – Point of the intersection between the inner drop ply and the belt plies (ply-drop-off step);

D – Point of the juncture between core plies and belt plies (taper root).

thickness can alter stress state at ply-drop region. So a model without relatively accurate thin interply resin layers is inadequate if refined results are desired.

1.1.4 Parametric study and design considerations

In order to design damage resistant tapered structures, many parameters such as taper geometry, locations of ply-drops, and configurations of ply-drops through-the-thickness that would affect delamination at dropped plies, have been studied.[23-28, 39-40]. Moreover, optimization design considerations for the external tapered composite structures have been investigated.[29-30]

Daoust and Hoa[23] developed an extensive finite element program for the study of tapered laminates. The parameters that influence the strength of the laminate were also examined through evaluating the efficiency of the tapered laminates. The efficiency is defined as a ratio of the maximum applied load with the drop-off to the one without drop-off, and it can be calculated using finite element method. The analysis results show that internal drop-offs are roughly two times stronger than external ones; that the layer drop-off does not affect torsion resistance; that extending the length of the drop-off hole while keeping the same drop-off height reduces interlaminar stress levels.

Llanos and Vizzini [24] evaluated two commonly used tailoring techniques in free-edge delamination prevention in flat laminates, i.e. addition of softer inner layer (structural adhesive) and ply angle alteration, for the prevention of delamination in tapered structures. Another technique applied and approved to be efficient by the comparison of the analysis results and experimental observations was to add resin layers in their model. It was demonstrated that the addition of adhesive film reduced the

interlaminar stresses in some of the components analyzed, but provided no significant change in the others. Both alterations of the small internal edge of the last ply-drop and the complete ply-drop can be introduced to produce a substantial reduction in the magnitudes and gradients of the interlaminar stresses at the last ply-drop region.

Thomas and Webber[25] used linear elastic fracture mechanics combined with simple strength of material theory to predict the tensile delamination load of tapered laminated plate subject to a certain geometric variation. It was shown that the delamination load is very sensitive to the thickness of the dropped sublaminate and that varying the lay-up angle of a dropped sublaminate from 0 to ± 90 deg with respect to the direction of loading could increase the delamination load as the angle tended toward ± 90 deg.

Cui et al.[26] investigated the effect of the distance between neighboring drop steps in a staircase arrangement, with the objective of finding out the point at which the interaction between neighbouring steps becomes significant. The critical stepping distance calculated with a simple formula was used to assess the extent to which the step spacing affects on the delamination stress. The step spacing could have a significant effect on delamination, particularly within small range of step spacing. Based on their newly developed variable fracture energy concept they also concluded that the fracture energy is not a material constant.

Vizzini[27] studied the effects of realistic taper geometries on the stress state at and near the ply-drops using finite element analysis. Ill-formed pockets, unsymmetric ply-drops, and fracture resin pockets (voids) were considered in his model. It was concluded that all realistic geometries tend to increase the interlaminar stress state and the effect that

these geometries have on the damage onset point and the failure mode is of importance. Therefore, any quantitative results from analysis models that do not take into account realistic geometries may be questionable and even misleading.

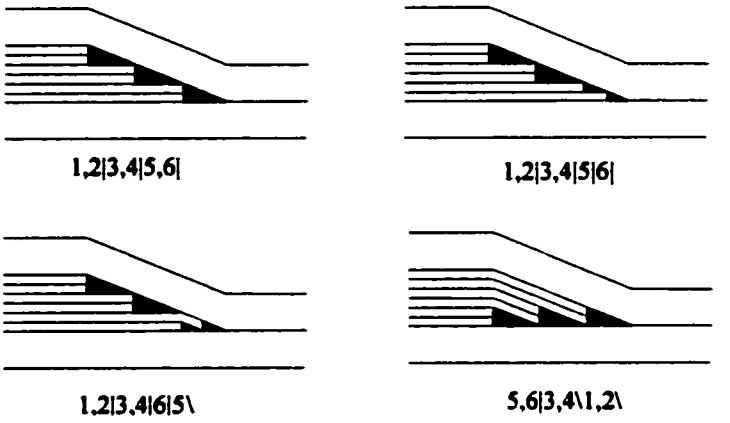

Figure 1-4 Schematic drawings of alternate ply-drop sequences in Ref. 28

Botting et al.[28] examined through finite element analysis the stress state in tapered laminates with different ply-drop configurations with the inclusion of stress free edge effect. One standard staircase ply-drop configuration and the three alternate ply-drop configurations as shown in Fig.1-4 were investigated. In all cases studied, the results from finite element analysis showed that altering the ply-drop configuration could decrease the stress state at the ply-drop. This conclusion was experimentally validated by the improvement in the damage onset stress of the laminate investigated. Fish and Vizzini[39-40] continued this work by analyzing unidirectional glass/epoxy tapered laminates with four different ply-drop configurations and failure modes as shown in Fig.1-5 a) and b), respectively. Two of them were chosen for further study under cyclic

loads. Their analysis indicated that tapered laminates could be tailored for stiffness and strength by altering the internal ply-drop configuration. The overlapped-dispersed configuration could achieve stable delamination initiation and growth and provide the best overall structural performance with intermediate delamination strength, the highest bending stiffness retention, and good damage tolerance characteristics.

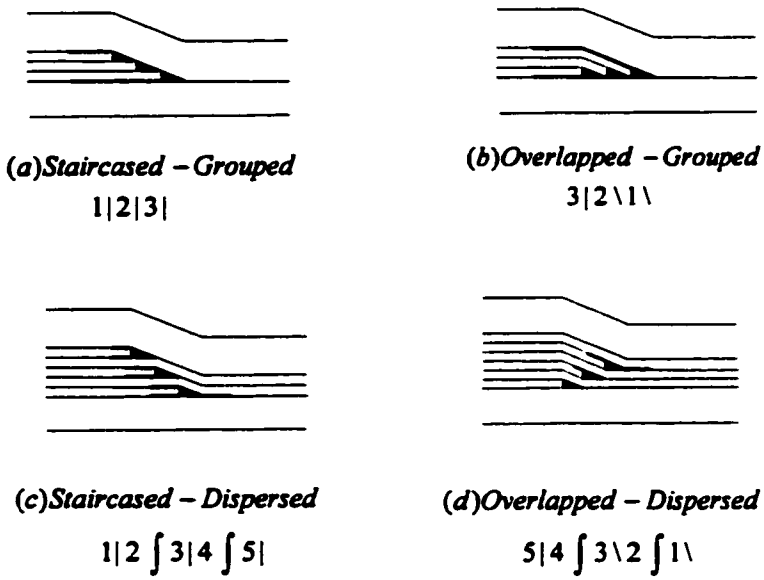

Figure 1-5 Schematic drawings of alternate ply-drop configurations and failure model in Ref. 39-40

Notation for drop-off sequence and configuration in Fig. 1-5: "|", "\" and " ∫" stand for a ply or sublaminate that is dropped, folded & dropped, and continuous, respectively. Plies or sublaminates are counted from the top to the bottom of the laminate, excluding the belt and core plies. The drop-off sequence starts from the left side of each notation.

Manne and Tsai[29] investigated how sublaminates made of multiple plies at various orientations, combining one or more materials are repeated or dropped in different zones of the structure, yielding the external ply-drop taper while ensuring physical continuity of the fibers in all composite layers. The orientation and thickness of each ply group in this reference sublaminate as well as its number of repetitions in the zones across the structures were optimized with the objective of minimum weight, subject to the constraints of strength, stiffness and manufacturing complexity. This new design methodology was due to an attempt of combining the considerations of low weight and easy manufacturing requirements. The introduction of a reference sublaminate, called base sublaminate or design unit could achieve the double objectives. The sublaminate repeated or dropped a given number of times forms a laminate. The optimum uniform thickness design and the best quasi-isotropic design are respectively 16% and 110% heavier than the optimum plydrops one.

Reference work[30] by Cairns et al. was to explore various factors such as thickness, ply stacking sequences, and ply-drop geometries and manufacturing considerations for design of composite blades with ply-drops. Fatigue loading was also considered with respect to delamination initiation and growth. Delamination prevention techniques such as the inclusion of random mat fabric between the ply-drop and the continuous layer, "feathering" (alternating tows are pulled out to provide a less defined delamination site), "Z-spiking" (removing the scrim from the fabric and driving the fiber tows into the lower layers), and addition of an adhesive region were used to enhance the structural integrity. Two epoxy adhesives were applied to repair the delamination in an exterior ply-drop sample. The general conclusions drawn from their work about the delamination and

preventing delamination can therefore be summarized as in the following. An optimum configuration of dropping plies is to have an internal ply-drop, with a combination of either "Z-spiking", an adhesive, or "feathering" used in the construction.

1.1.5 Concluding remarks

To accurately describe the delamination mechanisms in tapered laminate composites and to correlate them well with experiments have been challenging tasks for researchers for more than a decade. The difficulties in modeling tapered composite structures for stress analysis, and delamination initiation and growth lies in their geometric and material discontinuities as well as free-edge effect. All of these would give rise to complicated stress distribution around ply-drop-off region, typically interlaminar stresses that would cause delamination failure of the whole structure.

Both FEM and non-FEM approaches were implemented to determine the interlaminar stress profile around ply-drop-offs, initial delamination onset location along with a strength-of-materials based criterion, and to stimulate delamination mechanisms by releasing failed elements. They were also used to calculate the strain energy release rates associated with delamination within tapered laminates for the fracture modes I (opening) and II (shearing). Hybrid elements were overwhelmingly applied in 3D problems with the consideration of including free-edge effects, while easily formulated displacement elements were preferred by most of authors for solving 2D problem.

Several distinguishable methodologies for analysis of delamination initiation and propagation can be identified according to finite element modeling, failure criteria chosen, and special techniques applied.

Vizzini, Lee, etc. used 3D or Q3D assumed stress hybrid elements to accurately determine interlaminar stresses together with the application of stress averaging concept and applied strength-of-materials criterion to do failure analysis. Stress-free-edge effect was included using a coarse mesh in some of their analyses. Resin layers were introduced in their models so as to reflect the accurate stress state at and near the drop steps in tapered laminates. It was found in their analysis that in most of the laminates studied both maximum interlaminar stresses (normal and shear) and delamination initiation located at the ply-drop step (point C in Fig. 1-3), where stress singularity was likely generated. A delamination initiation location is significantly affected by local taper angles, the amount of offset of the ply-drops and presence of fracture pockets in realistic tapers.[27] They concluded that delamination growth simulated by the progressive damage finite element model could agree with experimental observation and hence correctly predict stable and unstable growth only with assumed initial damage.[9] With respect to parametric study, structural tailoring techniques such as edge alterations, changing ply-drop configurations and addition of film adhesive between the critical interfaces were investigated to find out the effects of these changes on the structural integrity.

Murri, O'Brien, Salpekar, etc. used 2D displacement based finite element and strain-energy-release rate approach to analyze tapered laminates loaded in tension and/or fatigue. In their studies, the maximum interlaminar normal stress was found to be located at the taper root (point D in Fig. 1-3), with the maximum shear stresses at the drop-off

step (point C). The location where a delamination initiated was either assumed [5-6, 8] to be at the taper root or directly borrowed [16] from the experimental observation. Delamination growth could be further simulated by the finite element model. However, the efficiency and accuracy of the simulation wholly depends on the delamination initiation site chosen.

Wisnom, et. al. conducted their experimental and analytical works through behavior comparisons between tapered laminates with drop-off plies and laminates with cut plies / untapered laminates with the same discontinuous plies, and between tapered laminates with drop-off plies and the same geometrical laminates with low stiffness fill-in discontinuous plies. On this basis, they concluded that for both symmetrically and unsymmetrically tapered laminates the strain energy release rate associated with discontinuous plies was the critical parameter controlling delamination into the thick section, while the taper geometry effect was the primary factor for delamination into the thin section. Confirmed by finite element analysis, a simple calculation model for strain-energy-release rate was applied in their analysis of delamination initiation.

Another research area of interest, which is pursued by O. T. Thomsen, et al, is on the study of interlaminar response in sandwich panels with internal or external tapered face sheets. They resort to a simplified model, instead of a FEM model, as a tool to perform the analysis. Experimental investigations were conducted to validate analytical results.

All other works mainly focused on stress analysis around critical regions of the tapered laminate.

It can be seen in this review that the finite element method is an almost indispensable tool in the analysis of tapered composites, either for determining

interlaminar stresses and strain energy release rate or for verifying simple formulations. Both hybrid and displacement elements were widely employed, with the former providing more accurate stresses than the latter. Researchers implemented finite element analysis of taper composites by directly applying elements developed for the analysis of continuous media to the laminated tapers, without taking into account the multilayer nature of the laminated structures. In addition, neither of these two types of elements could completely satisfy displacement and traction continuities simultaneously along bi-material interfaces in tapered composite structures. Moreover, the overwhelming dependence of finite elements on modeling the tapers would require huge computational resources for accurate analysis. Because finite element modeling is carried out subject to personal experience and the methodology chosen, variation of results would be expected, even for the same problem. Non-FEM approaches that are formed based on physical concepts, and can provide equivalent accuracy as FEM approach deserve special attention. Fracture mechanics and damage mechanics may provide a potential and effective way in delamination analysis of laminated tapers according to their structural characteristics.

Experiments are essential for tapered laminate analysis. Correct prediction of delamination initiation and propagation by finite element modeling and strain energy release approach depends on the initial crack site observed in experiments. An initial crack site assumed without theoretical justifications may lead to wrong conclusions about delamination failure mechanisms unless an experimental program is conducted to validate them.

In contrast with the strain energy release rate approach, the strength-of-materials approach is more efficient in seeking for the point of delamination initiation as was done in some of the works. However, the strength-of-materials approach, which is based on mechanics of materials, cannot characterize delamination propagation as efficiently as strain energy release rate approach due to the fact that the delamination propagation undergoes progressive growth phenomenon. Therefore, both these approaches have their own merits and limitations in failure prediction.

In addition to strain energy release rate, the crucial parameters that have significant effects on delamination in tapered laminates also include the geometry of the taper, especially the angle of the taper. Therefore, ideally modeled tapered sections without consideration of variations formed due to manufacturing tolerance are inadequate if quantitative analysis is desired.

Increasing the structural integrity of the tapered section can be realized by application of a few rules that have been drawn from the parametric studies. For example, the addition of film adhesive around the dropped plies to strengthen the region about the drop can modify the load transfer, thus decrease the interlaminar stress state. This method is successful in certain configurations. Reconfiguration of the ply-drop may also increase the structural integrity and alter the failure mechanism. The taper with dropped plies interleaved with continuous plies displays better behavior than the other taper with grouped dropped plies. A minor alternation or modification to the constitution and geometry of the taper may lead to completely different mechanical behavior for the structure studied.

Based on the reviewed works, the following aspects with regard to analysis and design of internally tapered laminated composite structures need to be investigated further from either a point of view of filling up void areas of interest or improving methodologies available:

1. Further investigations on improvement of finite element modeling incorporating interlaminar characteristics of laminated composites is required so as to increase computational efficiency shown in displacement-based FEM or assumed stress FEM. Development of new finite elements is required in this regard.

2. Investigation into the influences of some structural parameters such as resin toughness on interlaminar fracture toughness of tapered laminates is needed in order to gain insight into employing toughened composites laminated tapers in engineering applications.

3. Reactions of multiple delaminations in the tapered laminates have not been touched so far. Failure mechanisms induced at geometric and material discontinuities can be thoroughly understood only after gaining this insight.

4. Optimization of tapered laminated composite structures such as helicopter yoke arms and rotor blades should be targeted. This work will involve devising a method of defining variations of structural properties as functions of the construction and materials of optimized laminates. The optimization techniques should also incorporate manufacturing constraints.

5. It is worth noting that earlier researchers have not conducted materially non-linear analysis of internally tapered laminates. However, realistic response in internal

tapered laminates significantly depends on constitutive laws that describe material properties. Both composite lamina and resins that constitute a laminated structure exhibit non-linear stress-strain relationship, especially for shear stress-strain relations of lamina and for all properties in resins. Material nonlinear properties must be incorporated in quantitative analysis of tapered laminates.

1.2 Objective of the Thesis Work

The objective of the thesis is to develop and apply highly efficient partial hybrid finite element and physical concept based shear-lag models to examine interlaminar stress distributions in the vicinity of ply terminations, and to investigate damage failure mechanisms using linear fracture mechanics methods. *J*-integrals together with other conventional approaches were used to determine the strain energy release rate of delamination in the tapered laminate, aiming at developing a methodology that can accurately reflect the true influences of geometry and material discontinuity of the laminate with taper on the strength of the laminate. Therefore, the distributions of the interlaminar stresses and delamination mechanisms obtained would be applied with confidence in design and manufacture of the tapered laminated structure.

Many salient points are demonstrated in this work. Specifically, they include 1) formulation and application of partial hybrid finite element models - more efficient than conventional displacement based and hybrid stress elements, 2) formulation and application of a modified shear-lag model - physical concept based, simple, but with strong capability for analysis of laminates, 3) evaluation of energy release rate of

delamination in the tapered laminate using path-independent J-integral approach, 4) investigation of influence of various factors such as resin thickness on composite fracture toughness so as to gain insight into employing interleaving composites as good candidates for design of the tapered laminated structure, and 5) use of experimental results to assess the accuracy of numerical predictions.

Chapter 2

PARTIAL HYBRID STRESS FINITE ELEMENT MODELS

2.1 Introduction

It has been shown in the literature review presented in Chapter 1 of the thesis that the majority of finite elements used for analysis of tapered laminated composites are based on displacement formulations. This is because of ease of the element development with the relatively loose restriction of continuity on the assumed displacement field. However, there are some inherent limitations in this approach, particularly in analysis of composites. The main disadvantages of displacement elements include a loss of accuracy in prediction of stress state and the slow convergence in problems having steep gradients of stresses, as in ply drop-off locations in tapered composites. Moreover, the modelling leads to excessive requirement of computer resources to determine more accurate responses of the composite. In general, analysis of tapered composites based on displacement approaches can only provide qualitative trend information on responses of the structure under certain loading.

On the other hand, assumed stress hybrid elements, motivated by an attempt to overcome the disadvantages of displacement elements, was developed in 1964 by Pian and have since been extensively applied in the analysis of regular laminated composites. As in the equilibrium model, this hybrid element model uses assumed equilibrating stress

fields within the elements which enhances stress accuracy and also uses assumed boundary displacements in terms of nodal values such that they satisfy inter-element continuity.

The conventional hybrid stress finite element, however, induces two difficulties in its formulation and implementation. Firstly it involves large computational effort to construct a stiffness matrix of an elements that is dependent of the number of stress parameters assumed. All six-stress components are assumed in the conventional hybrid stress element and therefore the computing resources required are sometimes prohibitive. Another limitation of the hybrid element formulation is the difficulty in searching the stress shape function that is both absent from zero-energy kinematic modes and satisfaction of equilibrium conditions.

On the other hand, in the partial hybrid stress finite element, only three interlaminar stress components and in-plane strains identified as globally continuous variables constitute the control variable field in Helligner-Reissner variational principle. As a result, only three interlaminar stress components that dominate interlaminar failure at the critical interfaces, rather than all six stress components as in the conventional hybrid finite element, are assumed through this scheme and computational efforts for inverting $[H]$ and calculating $[K_h]$ are therefore significantly reduced in comparison with conventional hybrid elements. It is this inherent advantage that inspired the author to develop and apply the partial hybrid finite element, which is seeking a balance and efficiency among the conventional displacement- and stress-based elements, to model and analyze laminated composites.

In this Chapter, 5 partial hybrid stress elements, i.e. 3-D 6 and 15 node triangular prism elements, 3-D 6 node wedge element, quasi 3-D 6 node triangular and 8 node quadrilateral elements, have been formulated and applied to analysis of composite laminated plates. In the formulation procedure, a focus was given on properly establishing stress functions in terms of avoiding zero energy deformation mode caused either by the rigid body modes or unsuitable assumed stress fields. The motivation for formulating those elements is based on the following considerations:

(a). The triangular element, mingled with the rectangular element, can be used to model a complex structure. Addressed, as examples in the thesis, are the laminated composite plates, either with a taper or with a central hole;

(b). Finding interlaminar stress function by the method introduced is easier in comparison to the one employed for the full hybrid element method, which is because of huge effort needed in the full hybrid element formulation for seeking the stress function that satisfies equilibrium conditions for all the stress variables;

(c). The number of stress parameters is fewer than that in the counterpart element;

(d). Fulfillment in compensating the shortage of partial hybrid element realm with the current ones.

2.2 Interlaminar Continuity Conditions

In the analysis of laminated composite structures, the laminae are assumed to be bonded perfectly and the individual laminae are treated as homogeneous orthotropic material. Therefore, the lamination and anisotropy constitute the distinct behavior of the laminated composite structures. They lead to the conjunction conditions at interfaces

between adjacent layers in laminated composite structures. The conjunction conditions refer to the continuity conditions of partial stresses and strains at interfaces.

In order to satisfy conjunction conditions, the identification of globally continuous variables and locally continuous variables is required. In laminated composites, all components of displacement, strain, and stress are continuous within each layer due to the fact that the individual laminae are treated as homogeneous orthotropic material. At the layer interface with perfect bonding, the displacements are also continuous due to the compatibility condition, leading to the in-plane strain continuity across the thickness. Meanwhile, the reaction forces give rise to transverse stresses (interlaminar stresses) and they are also continuous across the thickness because of the equilibrium condition. It is thus seen that the following continuity conditions hold between the stress and strain fields of adjacent layers at their interface (see Figure 2-1):

$$\begin{Bmatrix} \varepsilon_x \\ \varepsilon_y \\ \gamma_{xy} \end{Bmatrix}^{(k)} = \begin{Bmatrix} \varepsilon_x \\ \varepsilon_y \\ \gamma_{xy} \end{Bmatrix}^{(k+1)} \quad ; \quad \begin{Bmatrix} \tau_{xz} \\ \tau_{yz} \\ \sigma_z \end{Bmatrix}^{(k)} = \begin{Bmatrix} \tau_{xz} \\ \tau_{yz} \\ \sigma_z \end{Bmatrix}^{(k+1)} \tag{2-1}$$

while in general

$$\begin{Bmatrix} \sigma_x \\ \sigma_y \\ \tau_{xy} \end{Bmatrix}^{(k)} \neq \begin{Bmatrix} \sigma_x \\ \sigma_y \\ \tau_{xy} \end{Bmatrix}^{(k+1)} \quad ; \quad \begin{Bmatrix} \gamma_{xz} \\ \gamma_{yz} \\ \varepsilon_z \end{Bmatrix}^{(k)} \neq \begin{Bmatrix} \gamma_{xz} \\ \gamma_{yz} \\ \varepsilon_z \end{Bmatrix}^{(k+1)} \tag{2-2}$$

This means that, along the thickness direction of composites, the in-plane strains and transverse stresses are globally continuous variables, while the transverse strains and in-plane stresses are usually not continuous at the interfaces although they must be continuous within each layer. The latter are called locally continuous variables. Thus, the

globally continuous variables are those that are continuous not only within the plane of the lamina but also across the interface from one layer to the next. This is the result of consideration for compatibility and equilibrium. The locally continuous variables are those that are continuous only within the plane of the lamina but not necessarily continuous across the interfaces.

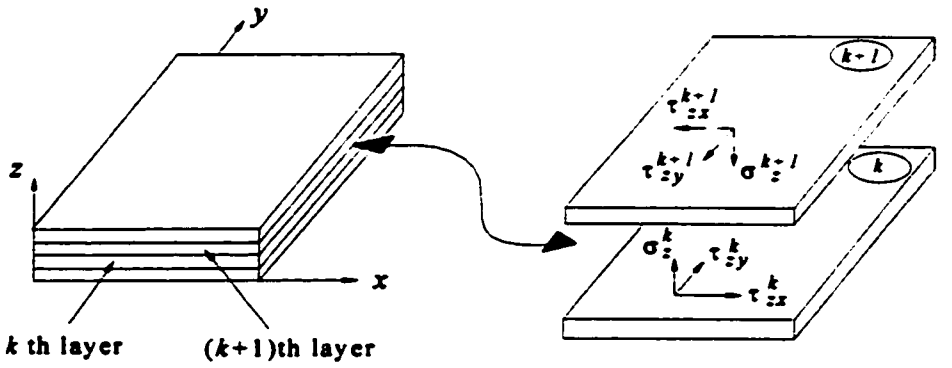

Figure 2-1 Interface traction continuity conditions in laminated composites

By classifying the variables into globally- and locally- continuous variables, both the stress components and strain components can be partitioned into two groups:

$$\sigma_l = \begin{Bmatrix} \sigma_x \\ \sigma_y \\ \tau_{xy} \end{Bmatrix} ; \quad \sigma_g = \begin{Bmatrix} \sigma_z \\ \tau_{zy} \\ \tau_{zx} \end{Bmatrix} ; \quad \varepsilon_g = \begin{Bmatrix} \varepsilon_x \\ \varepsilon_y \\ \gamma_{xy} \end{Bmatrix} ; \quad \varepsilon_l = \begin{Bmatrix} \varepsilon_z \\ \gamma_{zy} \\ \gamma_{zx} \end{Bmatrix} \tag{2-3}$$

where subscripts g and l denote global (interlaminar) and local variables, respectively. Coupling the globally and locally continuous variables results in the new variable vectors, which can be substituted into the modified Hellinger-Reissner variational

principle to form the element. The formulation of this type of elements is described in detail in Ref. 36.

2.3 The 3-D 6-Node Triangular Prism Partial Hybrid Element

2.3.1 Shape functions

In order to define the basic characteristics of the three-dimensional triangular-prism element, such as the shape functions, geometry and displacement field of the element, the standard idea of iso-parametric elements is applied and the reference element is shown in Figure 2-2.

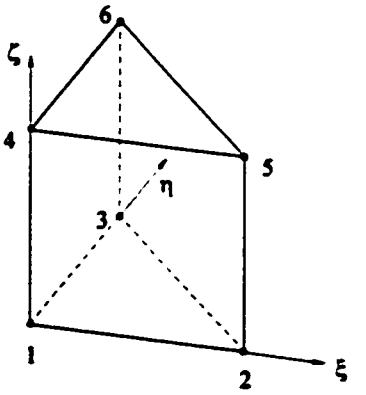

Figure 2-2 6-node master triangular-prism finite element

The proper shape functions are defined as tensor products of two-dimensional shape functions corresponding to the triangular base of the element defined within ξ, η –plane and one-dimensional shape functions corresponding to the direction ζ. More precisely, if ψ_1, ψ_2 and ψ_3 denote vertex node shape function for a two-dimensional triangular master element and φ_1 and φ_2 are shape functions corresponding to vertex nodes of one-

dimensional master element, then the three-dimensional shape functions can be defined as

$$\begin{aligned} N_1 &= \psi_1 \varphi_1 \\ N_2 &= \psi_2 \varphi_1 \\ N_3 &= \psi_3 \varphi_1 \\ N_4 &= \psi_1 \varphi_2 \\ N_5 &= \psi_2 \varphi_2 \\ N_6 &= \psi_3 \varphi_2 \end{aligned} \tag{2-4}$$

or in matrix form

$$N = \begin{bmatrix} \psi_1 & 0 \\ \psi_2 & 0 \\ \psi_3 & 0 \\ 0 & \psi_1 \\ 0 & \psi_2 \\ 0 & \psi_3 \end{bmatrix} \begin{Bmatrix} \varphi_1 \\ \varphi_2 \end{Bmatrix} \tag{2-5}$$

where

$$\psi_1 = 1 - \xi - \eta, \quad \psi_2 = \xi \quad \text{and} \quad \psi_3 = \eta \tag{2-6}$$

The form of the one-dimensional shape functions appearing in Eq. (2-5) and corresponding to two vertex nodes are defined as follows

$$\begin{aligned} \varphi_1 &= 1 - \zeta \\ \varphi_2 &= \zeta \end{aligned} \tag{2-7}$$

The final form of the shape functions is

$$\left.\begin{aligned} N_1 &= 1-\xi-\eta-\zeta+\xi\zeta+\eta\zeta \\ N_2 &= \xi-\xi\zeta \\ N_3 &= \eta-\eta\zeta \\ N_4 &= \zeta-\xi\zeta-\eta\zeta \\ N_5 &= \xi\zeta \\ N_6 &= \eta\zeta \end{aligned}\right\} \tag{2-8}$$

2.3.2 Geometry of element

For a 3-D 6-node prism isoparametric element, mapping from the global coordinate system (x, y, z) to the parametric coordinate system (ξ η, ζ) is carried out by

$$x=\sum_{i=1}^{6} N_i x_i \qquad y=\sum_{i=1}^{6} N_i y_i \qquad z=\sum_{i=1}^{6} N_i z_i \tag{2-9}$$

where (x_i, y_i, z_i)are the global coordinates of the i-th node (i = 1, 2, ...,6), and N_i are the shape functions expressed as in Eq. (2-8).

2.3.3 Displacement field

As an isoparametric element allows the same geometry and displacement interpolation function, a displacement field, within the element, can be assumed as

$$u=\sum_{i=1}^{6} N_i u_i \qquad v=\sum_{i=1}^{6} N_i v_i \qquad w=\sum_{i=1}^{6} N_i w_i \tag{2-10}$$

where (u_i, v_i, w_i) are the i-th nodal displacements in the global coordinate system (i = 1, 2, ...6), and N_i are the same shape functions as in Eq. (2-8). The displacement field can also be written in a matrix form as

$$\boldsymbol{u} = [N]\boldsymbol{d} = [N_1 I \quad N_2 I \cdots N_6 I]\begin{Bmatrix} \boldsymbol{d}_1 \\ \boldsymbol{d}_2 \\ \vdots \\ \boldsymbol{d}_6 \end{Bmatrix} \tag{2-11}$$

2.3.4 Partial strain fields

Partial strain fields are obtained with the assumed displacement filed as follows

$$\boldsymbol{\varepsilon}_g = [\varepsilon_x, \varepsilon_y, \gamma_{xy}]^T = \mathbf{D}_g \boldsymbol{u} = \begin{Bmatrix} \dfrac{\partial u}{\partial x} \\ \dfrac{\partial v}{\partial y} \\ \dfrac{\partial u}{\partial y} + \dfrac{\partial v}{\partial x} \end{Bmatrix} = [\mathbf{B}_g]\boldsymbol{d} \tag{2-12}$$

in which,

$$[B_g] = [B_{g1} \; B_{g2} \cdots B_{g6}] \tag{2-13}$$

where,

$$[B_{gi}] = \begin{bmatrix} N_{i,x} & 0 & 0 \\ 0 & N_{i,y} & 0 \\ N_{i,y} & N_{i,x} & 0 \end{bmatrix} \tag{2-14}$$

Similarly, the other half of strain field that corresponds to the transverse strain-displacement relation that has to be satisfied a posteriori can be obtained as in the following,

$$\boldsymbol{\varepsilon}_l = [\varepsilon_z, \gamma_{yz}, \gamma_{xz}]^T = \mathbf{D}_l \boldsymbol{u} = \begin{Bmatrix} \dfrac{\partial w}{\partial z} \\ \dfrac{\partial v}{\partial z} + \dfrac{\partial w}{\partial y} \\ \dfrac{\partial w}{\partial x} + \dfrac{\partial u}{\partial z} \end{Bmatrix} = [\mathbf{B}_l]\boldsymbol{d} \tag{2-15}$$

in which,

$$[B_l] = [B_{l1}\ B_{l2} \cdots B_{l6}] \tag{2-16}$$

where

$$[B_{li}] = \begin{bmatrix} 0 & 0 & N_{i,z} \\ 0 & N_{i,z} & N_{i,y} \\ N_{i,z} & 0 & N_{i,x} \end{bmatrix} \tag{2-17}$$

Mapping the derivatives from global coordinate system to local coordinate system as required by performing the evaluation of iso-parametric element matrices is realized by

$$\begin{pmatrix} N_{i,\xi} \\ N_{i,\eta} \\ N_{i,\zeta} \end{pmatrix} = \begin{bmatrix} x_{,\xi} & y_{,\xi} & z_{,\xi} \\ x_{,\eta} & y_{,\eta} & z_{,\eta} \\ x_{,\zeta} & y_{,\zeta} & z_{,\zeta} \end{bmatrix} \begin{pmatrix} N_{i,x} \\ N_{i,y} \\ N_{i,z} \end{pmatrix} = [J] \begin{pmatrix} N_{i,x} \\ N_{i,y} \\ N_{i,z} \end{pmatrix} \tag{2-18}$$

where

$$x_{,\xi} = \sum_{i=1}^{6} N_{i,\xi}\, x_i \quad \cdots \quad z_{,\zeta} = \sum_{i=1}^{6} N_{i,\zeta}\, z_i \tag{2-19}$$

The Jacobian matrix $[J]$ can also be written as

$$[J] = \begin{bmatrix} \dfrac{\partial N_1}{\partial \xi} & \dfrac{\partial N_2}{\partial \xi} & \cdots & \dfrac{\partial N_6}{\partial \xi} \\ \dfrac{\partial N_1}{\partial \eta} & \dfrac{\partial N_2}{\partial \eta} & \cdots & \dfrac{\partial N_6}{\partial \eta} \\ \dfrac{\partial N_1}{\partial \zeta} & \dfrac{\partial N_2}{\partial \zeta} & \cdots & \dfrac{\partial N_6}{\partial \zeta} \end{bmatrix} \begin{bmatrix} x_1 & y_1 & z_1 \\ x_2 & y_2 & z_2 \\ \vdots & \vdots & \vdots \\ x_6 & y_6 & z_6 \end{bmatrix} \tag{2-20}$$

Thus, given the global coordinates (x_i, y_i, z_i) of element nodes and shape functions N_i used for geometry, the Jacobian matrix can be evaluated using Eq. (2-20). Another form for Eq. (2-17) can be written as

$$\begin{pmatrix} N_{i,x} \\ N_{i,y} \\ N_{i,z} \end{pmatrix} = [J]^{-1} \begin{pmatrix} N_{i,\xi} \\ N_{i,\eta} \\ N_{i,\zeta} \end{pmatrix} \tag{2-21}$$

in which

$$\begin{bmatrix} N_{1,\xi} \\ N_{2,\xi} \\ N_{3,\xi} \\ N_{4,\xi} \\ N_{5,\xi} \\ N_{6,\xi} \end{bmatrix} = \begin{Bmatrix} -1+\zeta \\ 1-\zeta \\ 0 \\ -\zeta \\ \zeta \\ 0 \end{Bmatrix} \quad \begin{bmatrix} N_{1,\eta} \\ N_{2,\eta} \\ N_{3,\eta} \\ N_{4,\eta} \\ N_{5,\eta} \\ N_{6,\eta} \end{bmatrix} = \begin{Bmatrix} -1+\zeta \\ 0 \\ 1-\zeta \\ -\zeta \\ 0 \\ \zeta \end{Bmatrix} \quad \begin{bmatrix} N_{1,\zeta} \\ N_{2,\zeta} \\ N_{3,\zeta} \\ N_{4,\zeta} \\ N_{5,\zeta} \\ N_{6,\zeta} \end{bmatrix} = \begin{Bmatrix} -1+\xi+\eta \\ -\xi \\ -\eta \\ 1-\xi-\eta \\ \xi \\ \eta \end{Bmatrix} \tag{2-22}$$

2.3.5 Gauss Integration

The numerical integration takes advantage of the so-called symmetrical Gauss quadrature rule for a triangle [52], applied to longitudinal normalized coordinates ξ and η of the master triangle and standard Gauss integration rule applied to the third, transverse normalized coordinate ζ of the one-dimensional master element, which when mixed together form a three-dimensional, symmetrical-standard-product Gauss integration scheme. Thus, each integrand $f(\xi, \eta, \zeta)$ of the stiffness matrix can be integrated according to the rule

$$\int_0^1 \int_0^1 \int_0^{1-\eta} f(\xi,\eta,\zeta)\, d\xi\, d\eta\, d\zeta$$

$$= \frac{1}{2} \sum_{l=1}^{M_G} \sum_{k=1}^{N_G} w_l w_k f(\xi_k, \eta_k, \zeta_l) \tag{2-23}$$

where N_G, w_k, ξ_k, η_k and M_G, w_l, ζ_l are the number of Gauss points, Gauss point weights and coordinates, for the triangle and the third direction, respectively.

2.3.6 Interlaminar stress interpolation functions

Within the element, a partial stress field is assumed independently as

$$\sigma_g = \begin{Bmatrix} \sigma_z \\ \tau_{yz} \\ \tau_{xz} \end{Bmatrix} = [P_g]\beta = [\sigma_{g1}, \sigma_{g2}, \cdots \sigma_{gm}] \begin{Bmatrix} \beta_1 \\ \beta_2 \\ \cdots \\ \beta_m \end{Bmatrix} \tag{2-24}$$

There are several methods available for obtaining stress modes for hybrid element. By satisfying equilibrium conditions, one β-stress term per one α-mode scheme [50] is applied here to derive the initial interlaminar stress modes. This method can be used to suppress the kinematic deformation and to limit the number of stress modes as minimum as possible. The number of α-modes (deformation modes, M) is dependent of the difference (M = n - r = 12) between the number of total d.o.f.s (n = 3×6) of the element and the number of the rigid body motions (r = 6) of the element. The assumed deformation may be expressed as

$$\begin{aligned} u &= a_1 + a_2\xi + a_3\eta + a_4\zeta + a_5\xi\zeta + a_6\eta\zeta \\ v &= b_1 + b_2\,\xi + b_3\eta + b_4\zeta + b_5\xi\zeta + b_6\eta\zeta \\ w &= c_1 + c_2\xi + c_3\eta + c_4\zeta + c_5\xi\zeta + c_6\eta\zeta \end{aligned} \tag{2-25}$$

and corresponding strains are

$$
\begin{aligned}
\varepsilon_\xi &= \frac{\partial u}{\partial \xi} = a_2 + a_5\zeta = \alpha_1' + \alpha_2'\zeta \\
\varepsilon_\eta &= \frac{\partial v}{\partial \eta} = b_3 + b_6\zeta = \alpha_3' + \alpha_4'\zeta \\
\varepsilon_\zeta &= \frac{\partial w}{\partial \zeta} = c_4 + c_5\xi + c_6\eta = \alpha_5' + \alpha_6'\xi + \alpha_7'\eta \\
\gamma_{\eta\zeta} &= \frac{\partial w}{\partial \eta} + \frac{\partial v}{\partial \zeta} = \underline{(c_3 + b_4)} + b_5\xi + b_6\eta + c_6\zeta = \alpha_8' + \alpha_9'\xi + \alpha_{10}'\eta + \alpha_{11}'\zeta \\
\gamma_{\xi\zeta} &= \frac{\partial w}{\partial \xi} + \frac{\partial u}{\partial \zeta} = \underline{(c_2 + a_4)} + a_5\xi + \underline{(c_5 + c_6)}\zeta = \alpha_{12}' + \alpha_{13}'\xi + \alpha_{14}'\zeta \\
\gamma_{\xi\eta} &= \frac{\partial v}{\partial \xi} + \frac{\partial u}{\partial \eta} = \underline{(a_3 + b_2)} + \underline{(b_5 + a_6)}\zeta = \alpha_{15}' + \alpha_{16}'\zeta
\end{aligned}
\tag{2-25a}
$$

So corresponding stress components are of form:

$$
\begin{aligned}
\sigma_\xi &= \beta_1' + \beta_2'\zeta \\
\sigma_\eta &= \beta_3' + \beta_4'\zeta \\
\sigma_\zeta &= \beta_5' + \beta_6'\xi + \beta_7'\eta \\
\tau_{\eta\zeta} &= \beta_8' + \beta_9'\xi + \beta_{10}'\eta + \beta_{11}'\zeta \\
\tau_{\xi\zeta} &= \beta_{12}' + \beta_{13}'\xi + \beta_{14}'\zeta \\
\tau_{\xi\eta} &= \beta_{15}' + \beta_{16}'\zeta
\end{aligned}
\tag{2-25b}
$$

The equilibrium conditions

$$
\begin{aligned}
\frac{\partial \sigma_\xi}{\partial \xi} + \frac{\partial \tau_{\xi\eta}}{\partial \eta} + \frac{\partial \tau_{\xi\zeta}}{\partial \zeta} &= 0 \\
\frac{\partial \tau_{\eta\xi}}{\partial \xi} + \frac{\partial \sigma_\eta}{\partial \eta} + \frac{\partial \tau_{\eta\zeta}}{\partial \zeta} &= 0 \\
\frac{\partial \tau_{\zeta\xi}}{\partial \xi} + \frac{\partial \tau_{\zeta\eta}}{\partial \eta} + \frac{\partial \sigma_\zeta}{\partial \zeta} &= 0
\end{aligned}
\tag{2-25c}
$$

leads to

$$\begin{aligned} \beta_{14}' &= 0 \\ \beta_{11}' &= 0 \\ \beta_{13}' + \beta_{10}' &= 0 \end{aligned} \tag{2-25d}$$

The interlaminar stress matrix achieved through this scheme is thus expressed as

$$[P_\varepsilon] = \begin{bmatrix} 1 & 0 & 0 & \xi & 0 & 0 & \eta \\ 0 & 1 & 0 & 0 & \xi & -\eta & 0 \\ 0 & 0 & 1 & 0 & 0 & \xi & 0 \end{bmatrix} \tag{2-26}$$

It is seen that seven stress modes are available in the above stress matrix. However, the minimum number of stress modes required for the correct stiffness rank for the element studied is $m_{min} = n(3\times 6) - r(6) - n_d(6) = 6$. Therefore, the initial stress matrix needs to be further refined to suppress one unnecessary mode. Eigenvalue analysis incorporated with the classification technique[51] has been applied for this purpose to obtain the representative modes corresponding to m_{min} natural deformation modes. The representative stress matrix which assures absence of rank deficiency of the stiffness matrix of the element with the elimination of the zero-energy inducing mode $\{\eta,0,0\}^T$ is thus obtained and of the form

$$[P_\varepsilon^*] = \begin{bmatrix} 1 & 0 & 0 & \xi & 0 & 0 \\ 0 & 1 & 0 & 0 & \xi & -\eta \\ 0 & 0 & 1 & 0 & 0 & \xi \end{bmatrix} \tag{2-27}$$

The number of stress parameters for the stress shape function above is two less than that required in the 8-node solid partial hybrid element [50]. To let the stiffness matrix of the hybrid element have sufficient rank and be free of kinematic deformation modes, the following procedure can be employed to determine the stress matrix as in the above. The numbers shown below are calculated and extracted from the currently developed new element.

1. An initial stress matrix $[P_g]_{3\times7}$ is developed from one β-stress term per one α-mode scheme;
2. Determination of the rank ($r_d = 6$) of the semi-stiffness matrix formulated from the globally continuous strains;
3. The minimum number ($m_{\min}$) of stress modes responding to the natural deformation of the element is determined using the condition

$$m_{\min} = n(3\times6) - r(6) - n_d(6) = 6$$

where n is the number of freedoms of the element, r the number of rigid motions of the element, and n_d the rank of the displacement based element stiffness matrix;

4. Through eigenvalue tests the initial stress matrix $[P_g]_{3\times7}$ with a number of stress modes larger than minimum required number ($m_{\min} = 6$) is refined to be $[P_g^*]$ which is verified for its rank deficiency absence for the element (see Table 2-1).

Table 2-1 Results of eigenvalue examination of the partial hybrid stress element

0.000000	0.000000	0.000000	0.000000	0.000000	0.000000
0.329786	1.161439	1.534557	2.953247	2.988672	3.624301
4.642650	11.215609	12.597004	12.634584	23.687095	72.023983

Parameters used are the same as in the example given in the following.

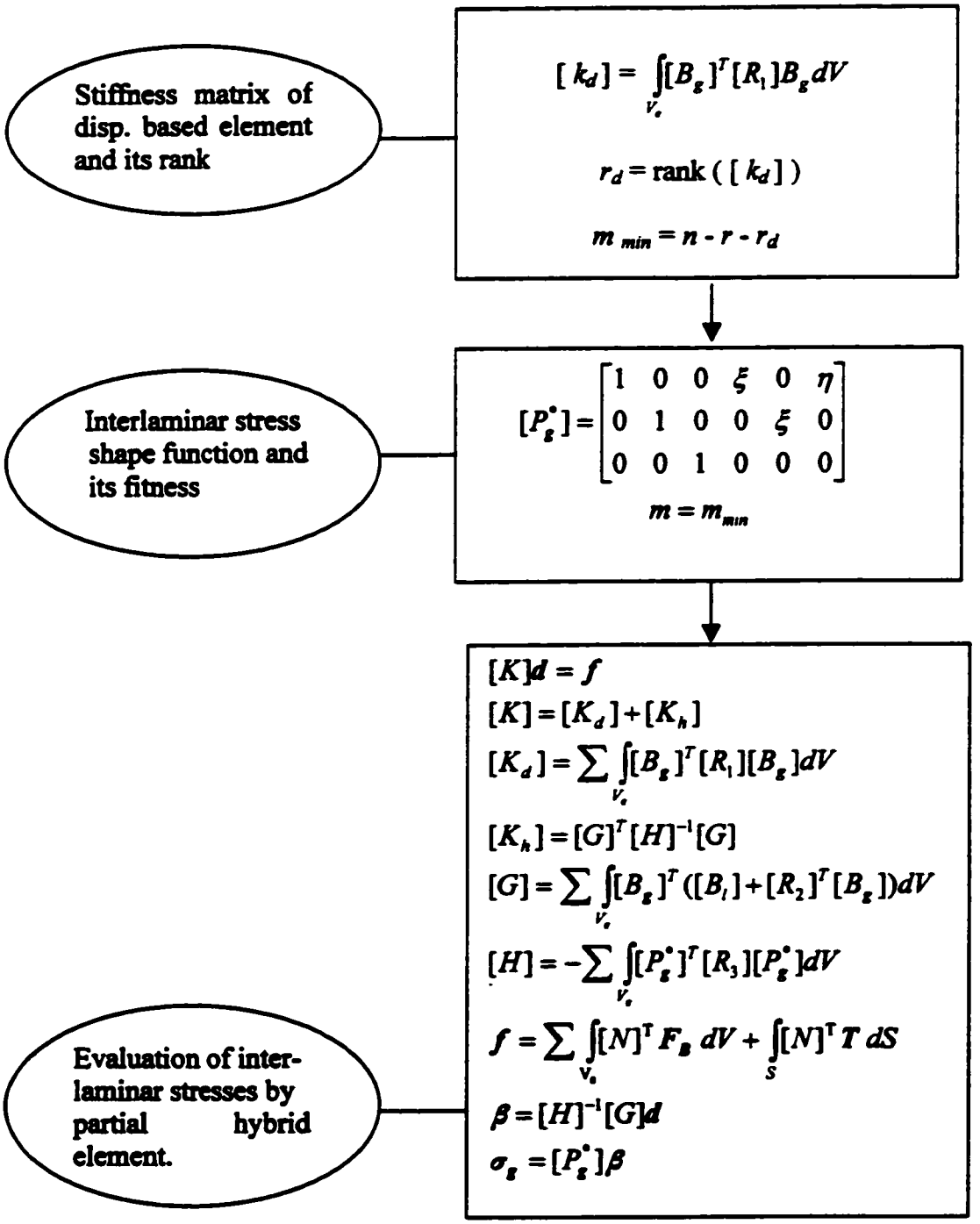

Figure 2-3 A flowchart for computing interlaminar stress components

2.3.7 Numerical example

The newly developed element was first employed to predict the interlaminar stress distribution in a $[90/0]_s$ composite laminate with a central circular hole subjected to a uniaxial tension in the longitudinal direction.

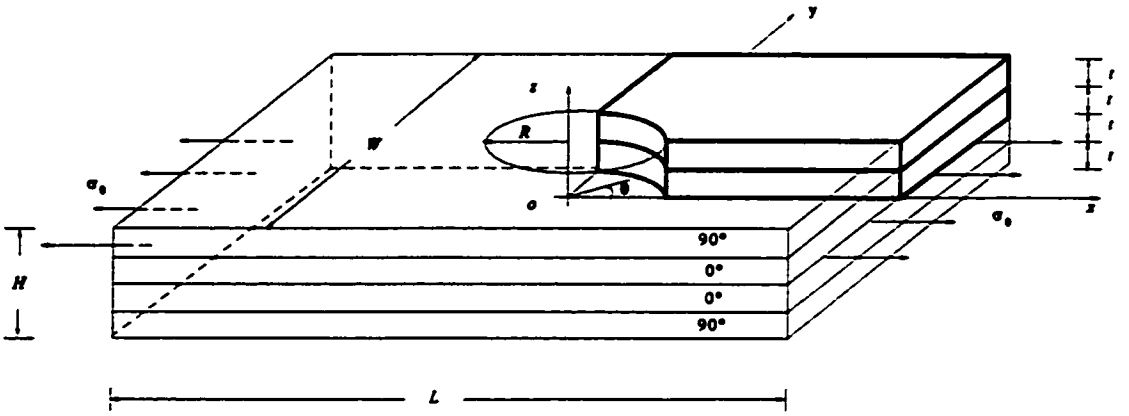

Figure 2-4 A $[90/0]_s$ laminate with a circular hole under uniaxial tension

Geometric and material properties for the structure analyzed as shown in Figure 2-4 are listed in Tables 2-2 and 2-3. Each ply is treated as a homogeneous elastic and orthotropic material as in the case of Raju and Crews[53]. Due to the conditions given in the problem, only one-eighth of the laminate needs to be modeled. Two models are considered in this investigation. In model A, each of the plies was represented by one triangular prism element in the normal direction, while in model B, two elements were used. A mesh refinement around the hole is required to account for the interlaminar stress concentration expected in this region. The finite element meshes in the x-y plane are

shown in Figure 2-5. The minimum length of the element adopted is equal to one half of the ply thickness. The FE model A consists of 292 elements and 642 degrees of freedom, and model B 584 elements and 1128 degrees of freedom. The imposed boundary conditions are $u\ (0, y, z) = v\ (x, 0, z) = w\ (x, y, 0) = 0$. Figure 2-6 and 2-7 show respectively normalized interlaminar normal stress σ_z / σ_0 vs θ and normalized interlaminar shear stress $\sigma_{z\theta} / \sigma_0$ vs θ for models A and B.

Table 2-2 Dimensions of the $[90/0]_s$ Laminate (mm)

Length	Width	Height	Hole Radius	Ply Thickness
L = 60	W = 30	H = 0.5	R = 2.5	t = 0.125

Table 2-3 Material Properties of the 0° Lamina in the $[90/0]_s$ Laminate

Extensional Modulus (GPa)	Poisson's Ratio	Shear Modulus (GPa)
E1 = 138	$\nu_{12} = 0.21$	$G_{12} = 5.86$
E2 = 14.5	$\nu_{13} = 0.21$	$G_{13} = 5.86$
E3 = 14.5	$\nu_{23} = 0.21$	$G_{23} = 5.86$

Subscripts 1, 2 and 3 denote the fiber, transverse and thickness directions, respectively.

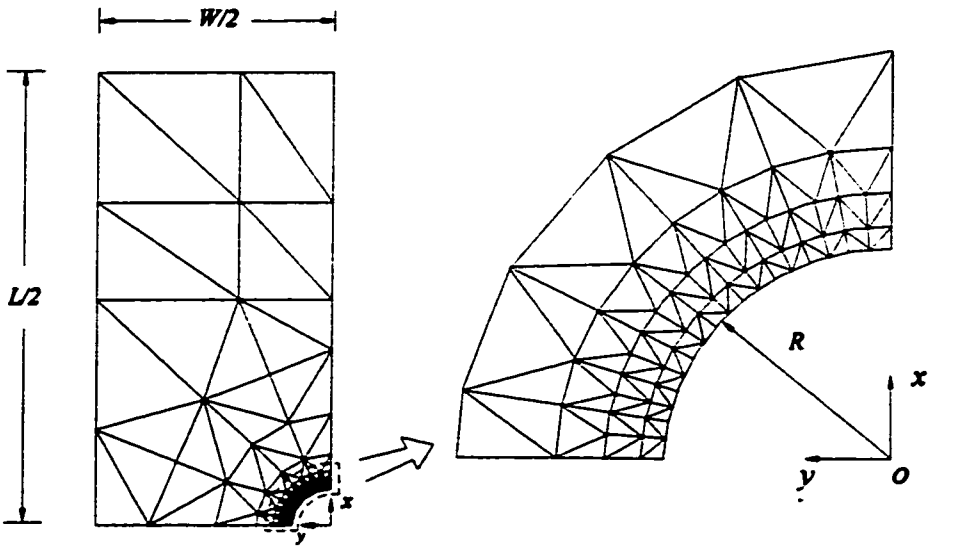

Figure 2-5 In-plane finite element meshes

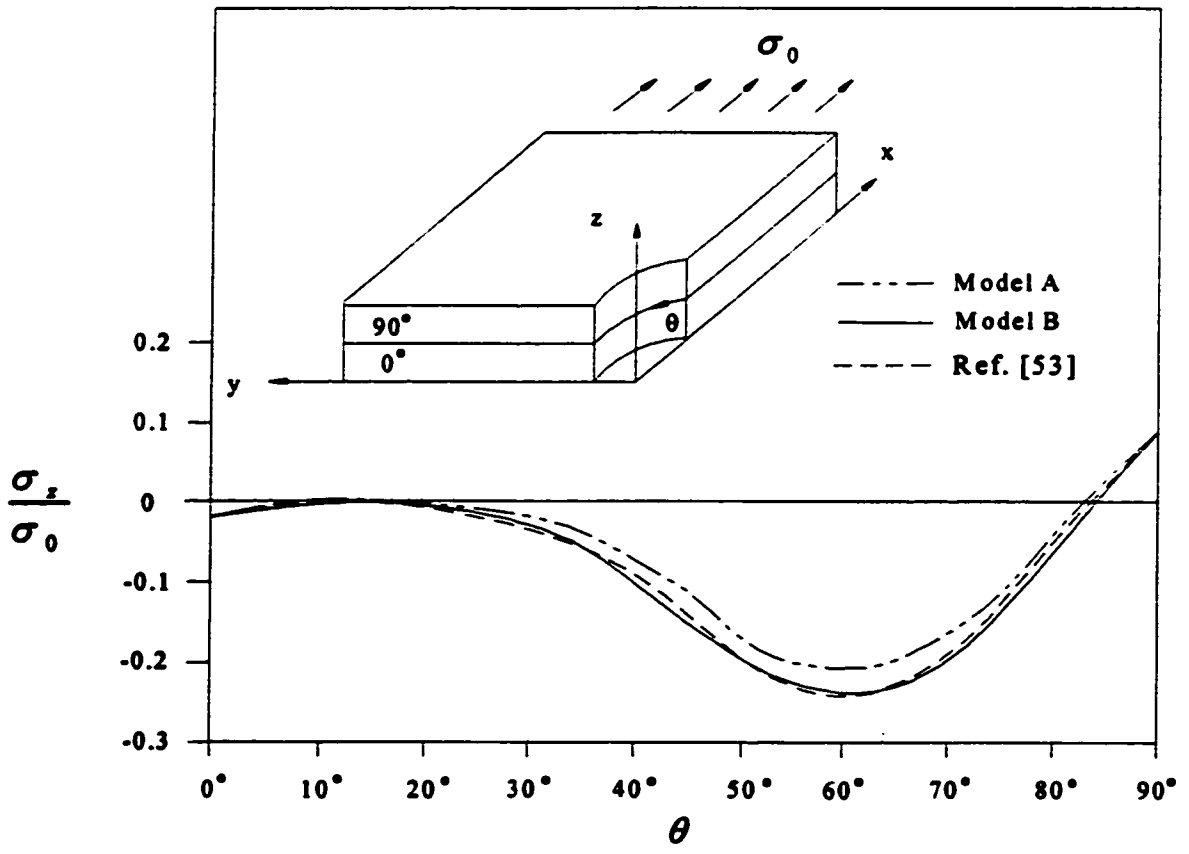

Figure 2-6 Normalized interlaminar normal stress along θ at the 90° / 0° interface

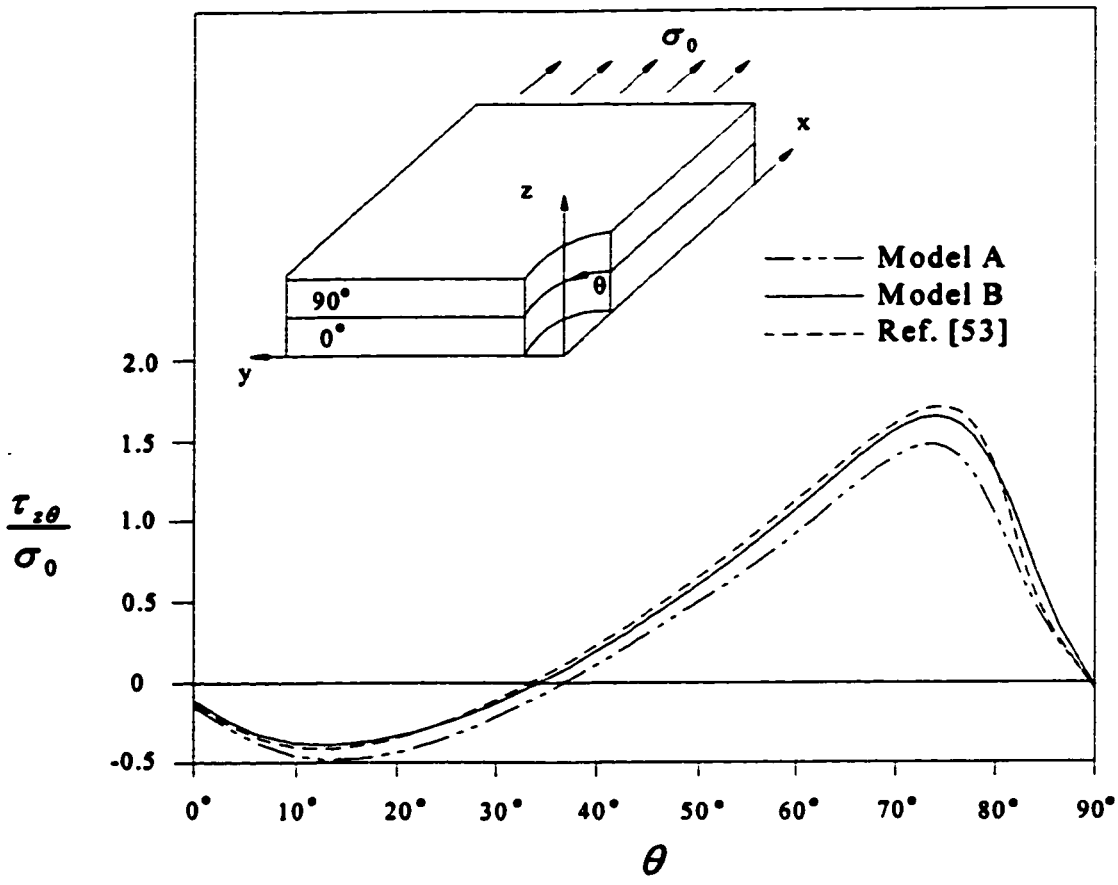

Figure 2-7 Normalized interlaminar shear stress along θ at the 90° / 0° interface

In Figure 2-6 the distribution of normalized interlaminar normal stress around the hole at the 90 / 0 interface is illustrated for model A and model B, with comparison to the results obtained by Raju & Crews based on three-dimensional displacement based finite element method. In their model, 20-node isoparametric brick elements consisting of a about 19,000 degrees of freedom that is approximately 15 times as many as in model B were used. Good agreement between the results is obtained from the present element and those predicted by Raju & Crews. The same tendency for the stress distribution of $\tau_{z\theta}$ can

also be observed in Figure 2-7. The shear stress component τ_{zr} is very small compared to the other interlaminar components and can be neglected.

2.3.8 Summary

A three-dimensional triangular prism partial hybrid element has been developed based on the identification of interlaminar stress components and in-plane strains as constituting the control variable field in Helligner-Reissner variational principle. The initially assumed interlaminar stress field was established first by invoking its consistence with strain that is compatible with the assumed displacement. The optimal interlaminar stress matrix, which possesses the minimum number of stress parameters required for suppression of zero-energy deformation modes has been found by refining the initial stress field. It has also been validated through demonstrating the absence of rank deficiency for the element stiffness matrix based on the eigenvalue analysis. The number of stress parameters for the present element considered is 75 percent of that for 8-node solid counterpart element. A numerical example for the determination of interlaminar stress distribution in the $[90/0]_s$ laminate with a central hole was used to illustrate the computational accuracy of the new element. It is concluded that accurate solutions to the interlaminar stress distribution in the laminated composites can be predicted by the proposed element.

2.4 3-D 15-Node Triangular Prism Partial Hybrid Element

In the 3-D 6-node element formulated, the stress function contains only constant and linear terms, which could not allow exact satisfaction on the continuity conditions at the interface on the element-wise basis. However, the 15-node element is a high-order element that can be manipulated to meet the above continuity conditions. This element is competitive both with the full hybrid element, where all six stress components are independently assumed, and another type of partial hybrid element, where only two interlaminar shear stresses are assumed, in terms of computing efficiency with less stress parameters than and similar accuracy.

2.4.1 Shape functions

In order to define the basic characteristics of the three-dimensional triangular-prism element, such as shape functions, geometry and displacement field of the element the standard idea of isoparametric elements is applied and the reference element is shown in Figure 2-8. The basis of 15-node prism element is

$$P_d = \{1,\ \xi,\ \eta,\ \zeta,\ \xi\zeta,\ \eta\zeta,\ \xi^2\zeta,\ \xi\eta\zeta,\ \eta^2\zeta,\ \zeta^2,\ \xi\zeta^2,\ \eta\zeta^2,\ \xi^2\zeta^2,\ \xi\eta\zeta^2,\ \eta^2\zeta^2\}$$

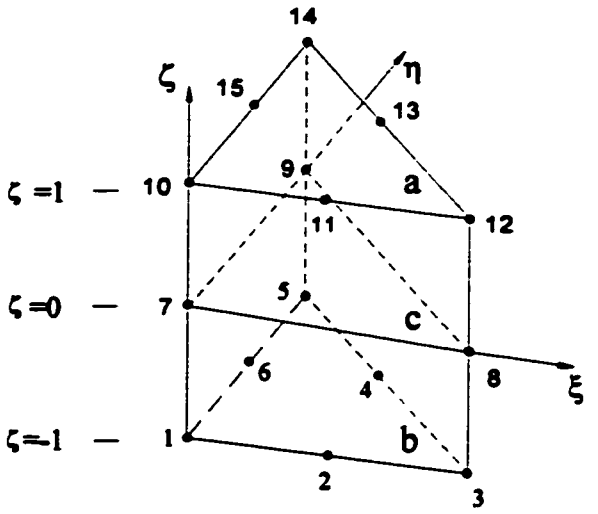

Figure 2-8 The 15-node triangular-prism finite element

In the figure, 'a' and 'b' denote the top and bottom surfaces of the element. Shape functions for each node are listed in the following forms:

Nodes 1 ~ 6:

$$\{N\}=\begin{Bmatrix}-\lambda(1-2\lambda)\\4\xi\lambda\\-\xi(1-2\xi)\\4\xi\eta\\-\eta(1-2\eta)\\4\eta\lambda\end{Bmatrix}\left\{-\frac{1}{2}\zeta(1-\zeta)\right\} \qquad \{\partial N/\partial\xi\}=\begin{Bmatrix}1-4\lambda\\4(\lambda-\xi)\\-1+4\xi\\4\eta\\0\\-4\eta\end{Bmatrix}\left\{-\frac{1}{2}\zeta(1-\zeta)\right\} \tag{2-28}$$

$$\{\partial N/\partial\eta\}=\begin{Bmatrix}1-4\lambda\\-4\xi\\0\\4\xi\\-1+4\eta\\4(\lambda-\eta)\eta\end{Bmatrix}\left\{-\frac{1}{2}\zeta(1-\zeta)\right\} \qquad \{\partial N/\partial\zeta\}=\begin{Bmatrix}-\lambda(1-2\lambda)\\4\xi\lambda\\-\xi(1-2\xi)\\4\xi\eta\\-\eta(1-2\eta)\\4\eta\lambda\end{Bmatrix}\left\{-\frac{1}{2}(1-2\zeta)\right\}$$

Nodes 10 ~ 15:

$$\{N\}=\begin{Bmatrix}-\lambda(1-2\lambda)\\4\xi\lambda\\-\xi(1-2\xi)\\4\xi\eta\\-\eta(1-2\eta)\\4\eta\lambda\end{Bmatrix}\left\{\frac{1}{2}\zeta(1+\zeta)\right\} \qquad \{\partial N/\partial\xi\}=\begin{Bmatrix}1-4\lambda\\4(\lambda-\xi)\\-1+4\xi\\4\eta\\0\\-4\eta\end{Bmatrix}\left\{\frac{1}{2}\zeta(1+\zeta)\right\} \tag{2-29}$$

$$\{\partial N/\partial\eta\}=\begin{Bmatrix}1-4\lambda\\-4\xi\\0\\4\xi\\-1+4\eta\\4(\lambda-\eta)\eta\end{Bmatrix}\left\{\frac{1}{2}\zeta(1+\zeta)\right\} \qquad \{\partial N/\partial\zeta\}=\begin{Bmatrix}-\lambda(1-2\lambda)\\4\xi\lambda\\-\xi(1-2\xi)\\4\xi\eta\\-\eta(1-2\eta)\\4\eta\lambda\end{Bmatrix}\left\{\frac{1}{2}(1+2\zeta)\right\}$$

Nodes 7 ~9:

$$\{N\}=\begin{Bmatrix}\lambda(1-\zeta^2)\\ \xi(1-\zeta^2)\\ \eta(1-\zeta^2)\end{Bmatrix} \qquad \{\partial N/\partial\xi\}=\begin{Bmatrix}-(1-\zeta^2)\\ 1-\zeta^2\\ 0\end{Bmatrix}$$

$$\{\partial N/\partial\eta\}=\begin{Bmatrix}-(1-\zeta^2)\\ 0\\ 1-\zeta^2\end{Bmatrix} \qquad \{\partial N/\partial\zeta\}=\begin{Bmatrix}-2\zeta\lambda\\ -2\xi\zeta\\ -2\eta\zeta\end{Bmatrix} \tag{2-30}$$

where $\lambda = 1-\xi-\eta$

2.4.2 Geometry of element

For a 3-D 15-node prism isoparametric element, mapping from the global coordinate system (x, y, z) to the parametric coordinate system (ξ η, ζ) is carried out by

$$x=\sum_{i=1}^{15}N_i x_i \qquad y=\sum_{i=1}^{15}N_i y_i \qquad z=\sum_{i=1}^{15}N_i z_i \tag{2-31}$$

where (x_i, y_i, z_i) are the global coordinates of the i-th node (i = 1, 2, ...,15), and N_i are the shape functions expressed in Eqs. (2-28) ~ (2-30).

2.4.3 Displacement field

As an isoparametric element allows the same geometry and displacement interpolation function, a displacement field, within the element, can be assumed as

$$u = \sum_{i=1}^{15} N_i u_i \qquad v = \sum_{i=1}^{15} N_i v_i \qquad w = \sum_{i=1}^{15} N_i w_i \tag{2-32}$$

where (u_i, v_i, w_i) are the i-th nodal displacements in the global coordinate system (i = 1, 2, ...15), and N_i are the same shape functions as in Eq. (2-28) ~ Eq. (2-30). The displacement field can also be written in a matrix form, as

$$u = [N]d = [N_1 I \quad N_2 I \cdots N_{15} I] \begin{Bmatrix} d_1 \\ d_2 \\ \vdots \\ d_{15} \end{Bmatrix} \tag{2-33}$$

2.4.4 Partial strain fields

Partial strain fields are obtained with the assumed displacement filed as follows,

$$e_g = [\varepsilon_x, \varepsilon_y, \gamma_{xy}]^T = \mathbf{D}_g u = \begin{Bmatrix} \dfrac{\partial u}{\partial x} \\ \dfrac{\partial v}{\partial y} \\ \dfrac{\partial u}{\partial y} + \dfrac{\partial v}{\partial x} \end{Bmatrix} = [\mathrm{B}_g]d \tag{2-34}$$

in which,

$$[B_g] = [B_{g1} \; B_{g2} \cdots B_{g15}] \tag{2-35}$$

where,

$$[B_{gi}]=\begin{bmatrix} N_{i,x} & 0 & 0 \\ 0 & N_{i,y} & 0 \\ N_{i,y} & N_{i,x} & 0 \end{bmatrix} \tag{2-36}$$

Similarly, the other half of strain field that corresponds to the transverse strain-displacement relation that has to be satisfied a posteriori can be obtained in the following,

$$\boldsymbol{\varepsilon}_t=[\varepsilon_z,\gamma_{yz},\gamma_{xz}]^T=\mathbf{D}_t\boldsymbol{u}=\begin{Bmatrix} \dfrac{\partial w}{\partial z} \\ \dfrac{\partial v}{\partial z}+\dfrac{\partial w}{\partial y} \\ \dfrac{\partial w}{\partial x}+\dfrac{\partial u}{\partial z} \end{Bmatrix}=[\mathrm{B}_t]\boldsymbol{d} \tag{2-37}$$

in which,

$$[B_t]=[B_{t1}\ B_{t2}\cdots B_{t15}] \tag{2-38}$$

where

$$[B_{ti}]=\begin{bmatrix} 0 & 0 & N_{i,z} \\ 0 & N_{i,z} & N_{i,y} \\ N_{i,z} & 0 & N_{i,x} \end{bmatrix} \tag{2-39}$$

Mapping the derivatives from global coordinate system to local coordinate system as required by performing the evaluation of isoparametric element matrices is realized by

$$\begin{pmatrix} N_{i,\xi} \\ N_{i,\eta} \\ N_{i,\zeta} \end{pmatrix} = \begin{bmatrix} x_{,\xi} & y_{,\xi} & z_{,\xi} \\ x_{,\eta} & y_{,\eta} & z_{,\eta} \\ x_{,\zeta} & y_{,\zeta} & z_{,\zeta} \end{bmatrix} \begin{pmatrix} N_{i,x} \\ N_{i,y} \\ N_{i,z} \end{pmatrix} = [J] \begin{pmatrix} N_{i,x} \\ N_{i,y} \\ N_{i,z} \end{pmatrix} \tag{2-40}$$

where

$$x_{,\xi} = \sum_{i=1}^{15} N_{i,\xi}\, x_i \quad \cdots \quad z_{,\zeta} = \sum_{i=1}^{15} N_{i,\zeta}\, z_i \tag{2-41}$$

[J] can also be written as

$$[J] = \begin{bmatrix} \dfrac{\partial N_1}{\partial \xi} & \dfrac{\partial N_2}{\partial \xi} & \cdots & \dfrac{\partial N_{15}}{\partial \xi} \\ \dfrac{\partial N_1}{\partial \eta} & \dfrac{\partial N_2}{\partial \eta} & \cdots & \dfrac{\partial N_{15}}{\partial \eta} \\ \dfrac{\partial N_1}{\partial \zeta} & \dfrac{\partial N_2}{\partial \zeta} & \cdots & \dfrac{\partial N_{15}}{\partial \zeta} \end{bmatrix} \begin{bmatrix} x_1 & y_1 & z_1 \\ x_2 & y_2 & z_2 \\ \vdots & \vdots & \vdots \\ x_{15} & y_{15} & z_{15} \end{bmatrix} \tag{2-42}$$

Thus, given the global coordinates (x_i, y_i, z_i) of element nodes and shape functions N_i used for geometry, the Jacobian matrix can be evaluated using Eq. (2-40). Another form for Eq. (2-40) can be written as

$$\begin{pmatrix} N_{i,x} \\ N_{i,y} \\ N_{i,z} \end{pmatrix} = [J]^{-1} \begin{pmatrix} N_{i,\xi} \\ N_{i,\eta} \\ N_{i,\zeta} \end{pmatrix} \tag{2-43}$$

2.4.5 Gauss integration

The method of numerical integration takes advantage of the so-called symmetrical Gauss quadrature rule for a triangle[52], applied to longitudinal normalized coordinates ξ and η of the master triangle and standard Gauss integration rule applied to the third, transverse normalized coordinate ζ of the one-dimensional master element, which when mixed together form a three-dimensional, symmetrical-standard-product Gauss integration scheme. Thus, each integrand $f(\xi, \eta, \zeta)$ of the stiffness matrix can be integrated according to the rule

$$\int_0^1 \int_0^1 \int_0^{1-\eta} f(\xi, \eta, \zeta)\, d\xi\, d\eta\, d\zeta = \frac{1}{2} \sum_{l=1}^{M_G} \sum_{k=1}^{N_G} w_l w_k f(\xi_k, \eta_k, \zeta_l) \tag{2-44}$$

where N_G, w_k, ξ_k, η_k and M_G, w_l, ζ_l are the number of Gauss points, Gauss point weight and coordinate, for the triangle and the third direction, respectively.

2.4.6 Interlaminar stress interpolation functions

Within the element, a partial stress field is assumed independently as

$$\sigma_g = \begin{Bmatrix} \sigma_z \\ \tau_{yz} \\ \tau_{xz} \end{Bmatrix} = [P_g]\beta = [\sigma_{g1}, \sigma_{g2}, \cdots \sigma_{gm}] \begin{Bmatrix} \beta_1 \\ \beta_2 \\ \cdots \\ \beta_m \end{Bmatrix} \tag{2-45}$$

The initial stress shape functions are determined based on the one β-stress term per one deformation α-mode scheme as applied in the development of 6-nodal triangular prism element shown in Section 2-3 to suppress the zero-deformation mode in Ref. 50. The general procedures are first to establish the strain fields from the displacement basis for the 15-node prism element and then to copy the format of interlaminar strains as interlaminar stress interpolated function. The basis for 15-node prism element is

$$P_d = \{1,\ \xi,\ \eta, \zeta,\ \xi\zeta, \eta\zeta, \xi^2\zeta, \xi\eta\zeta, \eta^2\zeta, \zeta^2, \xi\zeta^2, \eta\zeta^2, \xi^2\zeta^2, \xi\eta\zeta^2,\ \eta^2\zeta^2\} \tag{2-46}$$

and the displacement field is thus in form of

$$\begin{aligned} u &= a_1 + a_2\xi + a_3\eta + a_4\zeta + a_5\xi\zeta + a_6\eta\zeta + a_7\xi^2\zeta + a_8\xi\eta\zeta + a_9\eta^2\zeta + a_{10}\zeta^2 \\ &\quad + a_{11}\xi\zeta^2 + a_{12}\eta\zeta^2 + a_{13}\xi^2\zeta^2 + a_{14}\xi\eta\zeta^2 + a_{15}\eta^2\zeta^2 \\ v &= b_1 + b_2\xi + b_3\eta + b_4\zeta + b_5\xi\zeta + b_6\eta\zeta + b_7\xi^2\zeta + b_8\xi\eta\zeta + b_9\eta^2\zeta + b_{10}\zeta^2 \\ &\quad + b_{11}\xi\zeta^2 + b_{12}\eta\zeta^2 + b_{13}\xi^2\zeta^2 + b_{14}\xi\eta\zeta^2 + b_{15}\eta^2\zeta^2 \\ w &= c_1 + c_2\xi + c_3\eta + c_4\zeta + c_5\xi\zeta + c_6\eta\zeta + c_7\xi^2\zeta + c_8\xi\eta\zeta + c_9\eta^2\zeta + c_{10}\zeta^2 \\ &\quad + c_{11}\xi\zeta^2 + c_{12}\eta\zeta^2 + c_{13}\xi^2\zeta^2 + c_{14}\xi\eta\zeta^2 + c_{15}\eta^2\zeta^2 \end{aligned} \tag{2-47}$$

The corresponding interlaminar strain components are

$$\varepsilon_\zeta = \frac{\partial w}{\partial \zeta}$$
$$\gamma_{\eta\zeta} = \frac{\partial w}{\partial \eta} + \frac{\partial v}{\partial \zeta} \tag{2-48}$$
$$\gamma_{\xi\zeta} = \frac{\partial w}{\partial \xi} + \frac{\partial u}{\partial \zeta}$$

$$\varepsilon_\zeta = (c_4 + c_5\xi + c_6\eta + c_7\eta^2 + c_8\xi\eta + c_9\eta^2) + \zeta(2c_{10} + 2c_{11}\xi + 2c_{12}\eta + 2c_{13}\eta^2 + 2c_{14}\xi\eta + c_{15}\eta^2)$$

$$\gamma_{\xi\zeta} = \underline{(a_4 + c_2)} + a_5\xi + a_6\eta + a_7\eta^2 + a_8\xi\eta + a_9\eta^2 + \zeta[\underline{(2a_{10} + c_5)} + \underline{2(a_{11} + c_7)}\xi + \underline{(2a_{12} + c_8)}\eta + 2a_{13}\xi^2 + 2a_{14}\xi\eta + 2a_{15}\eta^2] + \zeta^2(c_{11} + 2c_{13}\xi + c_{14}\eta) \tag{2-49}$$

$$\gamma_{\eta\zeta} = \underline{(b_4 + c_3)} + b_5\xi + b_6\eta + b_7\eta^2 + b_8\xi\eta + b_9\eta^2 + \zeta[\underline{(2b_{10} + c_6)} + \underline{(2b_{11} + c_8)}\xi + \underline{2(b_{12} + c_9)}\eta + 2b_{13}\xi^2 + 2b_{14}\xi\eta + 2b_{15}\eta^2] + \zeta^2(c_{12} + c_{14}\xi + 2c_{15}\eta)$$

To facilitate the writing of the equation, the following form is used

$$\varepsilon_\zeta = [(\alpha_1 + \alpha_2\xi + \alpha_3\eta + \alpha_4\xi\eta + \alpha_5\xi^2 + \alpha_6\eta^2) + \zeta(\alpha_7 + \alpha_8\xi + \alpha_9\eta + \alpha_{10}\xi\eta + \alpha_{11}\xi^2 + \alpha_{12}\eta^2)]$$

$$\gamma_{\eta\zeta} = [(\alpha_{13} + \alpha_{14}\xi + \alpha_{15}\eta + \alpha_{16}\xi\eta + \alpha_{17}\xi^2 + \alpha_{18}\eta^2) + \zeta(\alpha_{19} + \alpha_{20}\xi + \alpha_{21}\eta + \alpha_{22}\xi\eta + \varepsilon_{23}\xi^2 + \alpha_{24}\eta^2) + \zeta^2(\alpha_{25} + \alpha_{26}\xi + \alpha_{27}\eta)] \tag{2-50}$$

$$\gamma_{\xi\zeta} = [(\alpha_{28} + \alpha_{29}\xi + \alpha_{30}\eta + \varepsilon_{31}\xi\eta + \alpha_{32}\xi^2 + \alpha_{33}\eta^2) + \zeta(\alpha_{34} + \alpha_{35}\xi + \alpha_{36}\eta + \alpha_{37}\xi\eta + \alpha_{38}\xi^2 + \alpha_{39}\eta^2) + \zeta^2(\alpha_{40} + \alpha_{41}\xi + \alpha_{42}\eta]$$

There are total 36 independent parameters α_i involved in Eq. (2-49). Comparison of above two equations gives the following parameter relationships:

$$\begin{aligned} \alpha_{25} &= \alpha_9 = \alpha_{41} \\ \alpha_{26} &= \alpha_{42} = \frac{1}{2}\alpha_{10} \\ \alpha_{27} &= \alpha_{12} \\ \alpha_{40} &= \frac{1}{2}\alpha_8 \end{aligned} \tag{2-51}$$

The stress shape function can be thus formulated based on the one β-stress term per one deformation α-mode scheme, and can be written below for *i*-th layer element as shown in Fig. 2-9

$$\begin{aligned} \sigma_\zeta^i &= \left[(\beta_1 + \beta_2\xi + \beta_3\eta + \beta_4\xi\eta + \beta_5\xi^2 + \beta_6\eta^2)\right. \\ &\left. + \zeta(\beta_7 + \beta_8\xi + \beta_9\eta + \beta_{10}\xi\eta + \beta_{11}\xi^2 + \beta_{12}\eta^2)\right]^i \\ \tau_{\eta\zeta}^i &= \left[(\beta_{13} + \beta_{14}\xi + \beta_{15}\eta + \beta_{16}\xi\eta + \beta_{17}\xi^2 + \beta_{18}\eta^2)\right. \\ &\left. + \zeta(\beta_{19} + \beta_{20}\xi + \beta_{21}\eta + \beta_{22}\xi\eta + \beta_{23}\xi^2 + \beta_{24}\eta^2) + \zeta^2(\beta_{25} + \beta_{26}\xi + \beta_{27}\eta)\right]^i \\ \tau_{\xi\zeta}^i &= \left[(\beta_{28} + \beta_{29}\xi + \beta_{30}\eta + \beta_{31}\xi\eta + \beta_{32}\xi^2 + \beta_{33}\eta^2)\right. \\ &\left. + \zeta(\beta_{34} + \beta_{35}\xi + \beta_{36}\eta + \beta_{37}\xi\eta + \beta_{38}\xi^2 + \beta_{39}\eta^2) + \zeta^2(\beta_{40} + \beta_{41}\xi + \beta_{42}\eta\right]^i \end{aligned} \tag{2-52}$$

Since the interlaminar stress field is assumed for each layer, the term ζ is defined to vary from –1 to +1 in each layer. Similarly, of the total 42 stress parameters in the above field, 6 are not independent and the correlations:

$$\begin{aligned} \beta_{25} &= \beta_9 = \beta_{41} \\ \beta_{26} &= \beta_{42} = \frac{1}{2}\beta_{10} \\ \beta_{27} &= \beta_{12} \\ \beta_{40} &= \frac{1}{2}\beta_8 \end{aligned} \tag{2-53}$$

By imposing the following traction continuity conditions, the final interlaminar stress field of each layer can be constructed.

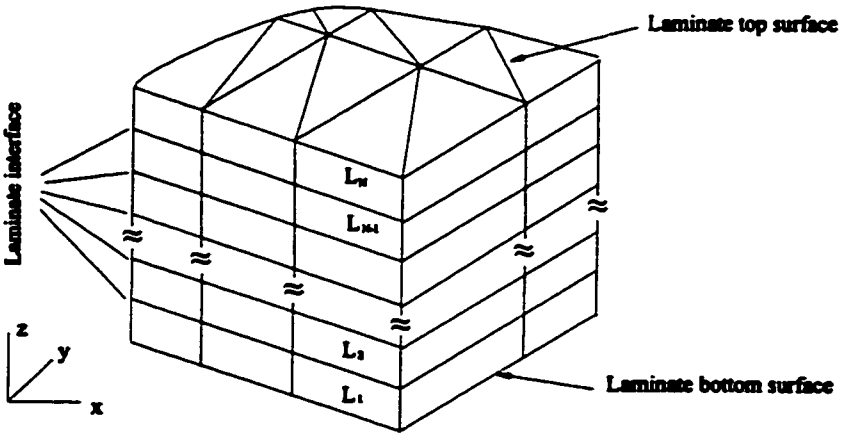

Figure 2-9 Illustration of element geometry of the laminate

Traction-free boundary conditions on the top and bottom surfaces of the laminate:

$$\tau_{\xi\zeta} = \tau_{\eta\zeta} = 0\Big|_{top\ of\ the\ laminate}$$
$$\sigma_\zeta = \tau_{\xi\zeta} = \tau_{\eta\zeta} = 0\Big|_{bottom\ of\ the\ laminate} \tag{2-54}$$

Interlaminar interface traction continuity conditions:

$$(\sigma_z, \tau_{xz}, \tau_{yz})\Big|_{top\ of\ the\ ith\ layer} \equiv (\sigma_z, \tau_{xz}, \tau_{yz})\Big|_{bottom\ of\ the\ (i+1)th\ layer} \tag{2-55}$$

At the upper surface of the i - th layer element ($\zeta = 1$), the interlaminar stresses are

$$\begin{aligned}
\sigma_\zeta^i &= [(\beta_1 + \beta_7) + (\beta_2 + \beta_8)\xi + (\beta_3 + \beta_9)\eta \\
&\quad + (\beta_4 + \beta_{10})\xi\eta + (\beta_5 + \beta_{11})\xi^2 + (\beta_6 + \beta_{12})\eta^2)]^i \\
\tau_{\eta\zeta}^i &= [(\beta_{13} + \beta_{19} + \beta_{25}) + (\beta_{14} + \beta_{20} + \beta_{26})\xi + (\beta_{15} + \beta_{21} + \beta_{27})\eta \\
&\quad + (\beta_{16} + \beta_{22})\xi\eta + (\beta_{17} + \beta_{23})\xi^2 + (\beta_{18} + \beta_{24})\eta^2]^i \\
\tau_{\xi\zeta}^i &= [(\beta_{28} + \beta_{34} + \beta_{40}) + (\beta_{29} + \beta_{35} + \beta_{41})\xi + (\beta_{30} + \beta_{36} + \beta_{42})\eta \\
&\quad + (\beta_{31} + \beta_{37})\xi\eta + (\beta_{32} + \beta_{38})\xi^2 + (\beta_{33} + \beta_{39})\eta^2]^i
\end{aligned} \tag{2-56}$$

At the lower surface of the i-th layer element ($\zeta = -1$), the interlaminar stresses are

$$\sigma_\zeta^l = [(\beta_1 - \beta_7) + (\beta_2 - \beta_8)\xi + (\beta_3 - \beta_9)\eta$$

$$+ (\beta_4 - \beta_{10})\xi\eta + (\beta_5 - \beta_{11})\xi^2 + (\beta_6 - \beta_{12})\eta^2)]^l$$

$$\tau_{\eta\zeta}^l = [(\beta_{13} - \beta_{19} + \beta_{25}) + (\beta_{14} - \beta_{20} + \beta_{26})\xi + (\beta_{15} - \beta_{21} + \beta_{27})\eta$$

$$+ (\beta_{16} - \beta_{22})\xi\eta + (\beta_{17} - \beta_{23})\xi^2 + (\beta_{18} - \beta_{24})\eta^2]^l \quad (2\text{-}57)$$

$$\tau_{\xi\zeta}^l = [(\beta_{28} - \beta_{34} + \beta_{40}) + (\beta_{29} - \beta_{35} + \beta_{41})\xi + (\beta_{30} - \beta_{36} + \beta_{42})\eta$$

$$+ (\beta_{31} - \beta_{37})\xi\eta + (\beta_{32} - \beta_{38})\xi^2 + (\beta_{33} - \beta_{39})\eta^2]^l$$

The traction free conditions on the top surface of the laminate are satisfied by setting

$$\beta_k^N + \beta_{k+6}^N = 0, \quad k = 1\sim6,\ 16\sim18 \ \textit{and}\ 31\sim33$$

$$\beta_k^N + \beta_{k+6}^N + \beta_{k+12}^N = 0, \quad k = 13\sim15 \ \textit{and}\ 28\sim30 \quad (2\text{-}58)$$

on the bottom surface of the laminate by

$$\beta_k^1 - \beta_{k+6}^1 = 0, \quad k = 1\sim6,\ 16\sim18 \ \textit{and}\ 31\sim33$$

$$\beta_k^1 - \beta_{k+6}^1 + \beta_{k+12}^1 = 0, \quad k = 13\sim15 \ \textit{and}\ 28\sim30 \quad (2\text{-}59)$$

Similarly, the interlaminar interface traction continuity conditions are satisfied by demanding that

$$\beta_k^{i+1} - \beta_{k+6}^{i+1} = \beta_k^i + \beta_{k+6}^i, \quad k = 1\sim6,\ 16\sim18 \ \textit{and}\ 31\sim33$$

$$\beta_k^{i+1} - \beta_{k+6}^{i+1} + \beta_{k+12}^{i+1} = \beta_k^i + \beta_{k+6}^i + \beta_{k+12}^i, \quad k = 13\sim15 \ \textit{and}\ 28\sim30 \tag{2-60}$$

The final stress shape functions that satisfy traction continuity conditions can thus be defined completely in terms of stress parameters.

Consider a laminate composed of N layers of lamina (layer 1 is designated as bottom layer and layer N top layer). So there are (N - 1) interlaminar interfaces and the number of the total constraints induced by Eqs. (2-54) and Eq. (2-55) is [18 × (N – 1)+(12+18)] and the average number of stress parameters per layer is therefore {36 × N – [18 × (N–1)+(12+18)] } / N = 18 – 12 / N. From a computational point of view, the new element developed is very economical not only in comparison with the full hybrid stress element developed by Spilker[54] (52 – 12 / N), but also competitive to another partial hybrid element developed by yong[89] (18 – 12 / N), wherein only two transverse stresses τ_{yz} and τ_{xz} are independently assumed.

Interlaminar stress functions for a single, double and triple layered laminates under transverse loading are listed according to the above formulation.

Single layer laminate:

$$\sigma_z = (1+\zeta)(\beta_1 + \beta_2\xi + \beta_3\eta + \beta_4\xi\eta + \beta_5\xi^2 + \beta_6\zeta^2)$$

$$\tau_{yz} = (1-\zeta^2)(\beta_{13} + \beta_{14}\xi + \beta_{15}\eta) \tag{2-61}$$

$$\tau_{xz} = (1-\zeta^2)(\beta_{28} + \beta_{29}\xi + \beta_{30}\eta)$$

Double layer laminate:

Layer #1

$$\sigma_x^{(1)} = \left[(1+\zeta)(\beta_1 + \xi\beta_2 + \eta\beta_3 + \xi\eta\beta_4 + \xi^2\beta_5 + \eta^2\beta_6\right]^{(1)}$$

$$\tau_{yz}^{(1)} = \left[(1+\zeta)(\beta_{13} + \xi\beta_{14} + \eta\beta_{15} + \xi\eta\beta_{16} + \xi^2\beta_{17} + \eta^2\beta_{18}\right]^{(1)}$$

$$+\zeta(1+\zeta)(\beta_3 + .5\xi\beta_4 + \eta\beta_6)^{(1)} \qquad (2\text{-}62)$$

$$\tau_{xz}^{(1)} = \left[(1+\zeta)(\beta_{28} + \xi\beta_{29} + \eta\beta_{30} + \xi\eta\beta_{31} + \xi^2\beta_{32} + \eta^2\beta_{33}\right]^{(1)}$$

$$+\zeta(1+\zeta)(.5\beta_2 + \xi\beta_3 + .5\eta\beta_4)^{(1)}$$

Layer #2

$$\sigma_x^{(2)} = \left[(1+\zeta)(\beta_1 + \xi\beta_2 + \eta\beta_3 + \xi\eta\beta_4 + \xi^2\beta_5 + \eta^2\beta_6\right]^{(2)}$$

$$-2\zeta\left[(\beta_1 + \xi\beta_2 + \eta\beta_3 + \xi\eta\beta_4 + \xi^2\beta_5 + \eta^2\beta_6\right]^{(1)}$$

$$\tau_{yz}^{(2)} = (1-\zeta)[\beta_{13} + \beta_{14}\xi + \beta_{15}\xi\eta + \beta_{16}\xi + \beta_{17}\xi^2 + \beta_{18}\eta^2)]^{(1)}$$

$$+(1-\zeta)(3+2\zeta)(\beta_3 + .5\xi\beta_4 + \eta\beta_6)^{(1)}$$

$$-(1-\zeta^2)(\beta_3 + .5\xi\beta_4 + \eta\beta_6)^{(2)}$$

$$\tau_{xz}^{(2)} = (1-\zeta)[\beta_{28} + \beta_{29}\xi + \beta_{30}\xi\eta + \beta_{31}\xi + \beta_{32}\xi^2 + \beta_{33}\eta^2)]^{(1)}$$

$$+(1-\zeta)(3+2\zeta)(.5\beta_2 + \xi\beta_3 + .5\eta\beta_4)^{(1)}$$

$$-(1-\zeta^2)(.5\beta_2 + \xi\beta_3 + .5\eta\beta_4)^{(2)} \qquad (2\text{-}63)$$

Triple layer laminate:

Layer #1

$$\sigma_z^{(1)} = \left[(1+\zeta)(\beta_1 + \xi\beta_2 + \eta\beta_3 + \xi\eta\beta_4 + \xi^2\beta_5 + \eta^2\beta_6\right]^{(1)}$$

$$\tau_{yz}^{(1)} = \left[(1+\zeta)(\beta_{13} + \xi\beta_{14} + \eta\beta_{15} + \xi\eta\beta_{16} + \xi^2\beta_{17} + \eta^2\beta_{18}\right]^{(1)}$$

$$+\zeta(1+\zeta)(\beta_3 + .5\xi\beta_4 + \eta\beta_6)^{(1)} \qquad (2\text{-}64)$$

$$\tau_{xz}^{(1)} = \left[(1+\zeta)(\beta_{28} + \xi\beta_{29} + \eta\beta_{30} + \xi\eta\beta_{31} + \xi^2\beta_{32} + \eta^2\beta_{33}\right]^{(1)}$$

$$+\zeta(1+\zeta)(.5\beta_2 + \xi\beta_3 + .5\eta\beta_4)^{(1)}$$

Layer #2

$$\sigma_z^{(2)} = \left[(1-\zeta)(\beta_1 + \xi\beta_2 + \eta\beta_3 + \xi\eta\beta_4 + \xi^2\beta_5 + \eta^2\beta_6\right]^{(1)}$$

$$+\left[.5(1+\zeta)(\beta_1 + \xi\beta_2 + \eta\beta_3 + \xi\eta\beta_4 + \xi^2\beta_5 + \eta^2\beta_6\right]^{(3)}$$

$$-\left[.5(1+\zeta)(\beta_7 + \xi\beta_8 + \eta\beta_9 + \xi\eta\beta_{10} + \xi^2\beta_{11} + \eta^2\beta_{12}\right]^{(3)}$$

$$\tau_{yz}^{(2)} = \left[(1-\zeta)(\beta_{13} + \xi\beta_{14} + \eta\beta_{15} + \xi\eta\beta_{16} + \xi^2\beta_{17} + \eta^2\beta_{18}\right]^{(1)}$$

$$+\left[(1+\zeta)(\beta_{13} + \xi\beta_{14} + \eta\beta_{15} + \xi\eta\beta_{16} + \xi^2\beta_{17} + \eta^2\beta_{18}\right]^{(3)}$$

$$+(1-\zeta)(2+\zeta)\left[\beta_3 + .5\xi\beta_4 + \eta\beta_6\right]^{(1)} \qquad (2\text{-}65)$$

$$-(1-\zeta^2)\left[.5\beta_3 + .25\xi\beta_4 + \eta\beta_6\right]^{(3)}$$

$$+(1+\zeta)(3-\zeta)\left[.5\beta_9 + .25\xi\beta_{10} + .5\eta\beta_{12}\right]^{(3)}$$

$$\tau_{xz}^{(2)} = \left[(1-\zeta)(\beta_{28} + \xi\beta_{29} + \eta\beta_{30} + \xi\eta\beta_{31} + \xi^2\beta_{32} + \eta^2\beta_{33}\right]^{(1)}$$

$$+\left[(1+\zeta)(\beta_{28} + \xi\beta_{29} + \eta\beta_{30} + \xi\eta\beta_{31} + \xi^2\beta_{32} + \eta^2\beta_{33}\right]^{(3)}$$

$$+(1-\zeta)(2+\zeta)[.5\beta_2 + \xi\beta_3 + .5\eta\beta_4]^{(1)} + (1-\zeta^2)[.25\beta_2 + .5\xi\beta_3 - .25\eta\beta_4]^{(3)}$$

$$+(1+\zeta)(3-\zeta)[.25\beta_8 + .5\xi\beta_9 + .25\eta\beta_{10}]^{(3)}$$

Layer #3

$$\sigma_z^{(3)} = \left[(\beta_1 + \xi\beta_2 + \eta\beta_3 + \xi\eta\beta_4 + \xi^2\beta_5 + \eta^2\beta_6\right]^{(3)}$$

$$+\left[\zeta(\beta_7 + \xi\beta_8 + \eta\beta_9 + \xi\eta\beta_{10} + \xi^2\beta_{11} + \eta^2\beta_{12}\right]^{(3)}$$

$$\tau_{yz}^{(3)} = \left[(1-\zeta)(\beta_{13} + \xi\beta_{14} + \eta\beta_{15} + \xi\eta\beta_{16} + \xi^2\beta_{17} + \eta^2\beta_{18}\right]^{(3)} \qquad (2\text{-}66)$$

$$+\zeta(-1+\zeta)(\beta_9 + .5\xi\beta_{10} + \eta\beta_{12})^{(3)}$$

$$\tau_{xz}^{(3)} = \left[(1-\zeta)(\beta_{28} + \xi\beta_{29} + \eta\beta_{30} + \xi\eta\beta_{31} + \xi^2\beta_{32} + \eta^2\beta_{33}\right]^{(1)}$$

$$+\zeta(-1+\zeta)(.5\beta_8 + \xi\beta_9 + .5\eta\beta_{10})^{(3)}$$

The superscripts in the above equations denote the layer number that the stress parameters are related to.

2.4.7 Numerical results and discussion

In order to validate the present finite element formulation, a number of typical laminated plate problems are analyzed and the results are compared with analytical solutions as well as finite element solutions available in the published literature. Two categories of laminated plate problems considered in the examples are:

CASE I: Simply supported laminate under cylindrical bending and subjected to sinusoidal loading

$$q(x,y) = q_0 \sin(\pi x / a) \tag{2-67}$$

CASE II: Simply supported laminate with the shape of a square plate (a×a) under bi-directional sinusoidal loading

$$q(x,y) = q_0 \sin(\pi x / a)\sin(\pi y / a) \tag{2-68}$$

The material constants used in the simulations are listed in Table 2-4.

Table 2-4 Material properties used in the examples

E_1	E_2	G_{12}	G_{23}	ν_{12}	ν_{23}
174.6 GPa	7 GPa	3.5 GPa	1.4 GPa	0.25	0.25

1, 2 and 3 refer to the material principal axes

These are the same as those used in the literature[89, 56]. In addition, the numerical results are normalized for the consistency in comparison with other works. Hereafter, the

displacement or stress components with overbars denote the corresponding normalized quantities as shown in the following:

$$\bar{u} = \frac{E_2 u}{q_0 h S^3} \qquad \bar{w} = \frac{100 E_2 w}{q_0 h S^4} \tag{2-69}$$

$$\left(\bar{\sigma}_x, \bar{\sigma}_y, \bar{\tau}_{xy}\right) = \frac{1}{q_0 h S^4}\left(\sigma_x, \sigma_y, \tau_{xy}\right) \tag{2-70}$$

$$\left(\bar{\tau}_{xz}, \bar{\tau}_{yz}, \bar{\sigma}_z\right) = \frac{1}{q_0 S^2}\left(\tau_{xz}, \tau_{yz}, \sigma_z\right) \tag{2-71}$$

$$S = a/h \qquad \bar{z} = z/h \tag{2-72}$$

For all the examples employed to demonstrate the efficiency and accuracy of the element, the loading is assumed to be applied on the top surface of the laminate. Owing to symmetry, only a quarter of the plate is used in the analysis.

CASE I: CYLINDRICAL BENDING PROBLEM

Example 1:

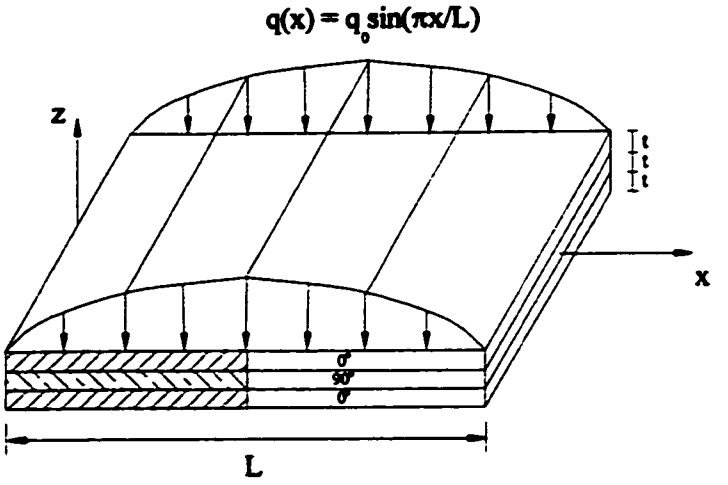

Figure 2-10 Illustration of cylindrical bending problem for a three layered laminate

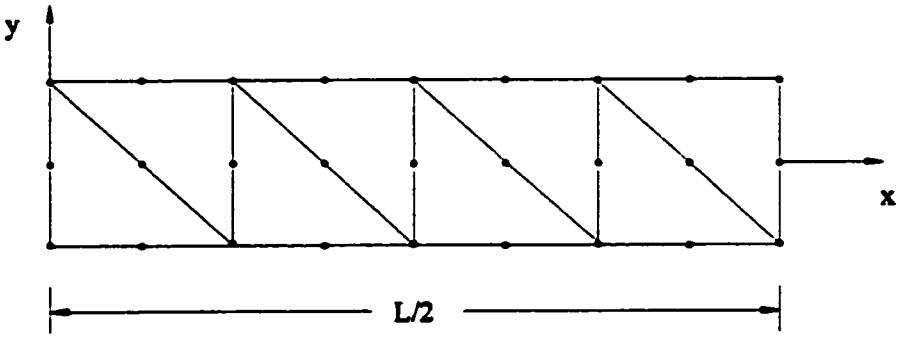

Figure 2-11 In-plane finite element mesh

The laminated plate considered in this example is a three-layered symmetric cross-ply square laminate (0°/90°/0°) subjected to bending loads (see Figure 2-10). The laminate is simply supported at edges $x = 0$ and $x = L$ with a plate span-to-thickness ratio of S = L/T = 4, "L" being the side length of the plate and "T" its overall thickness. Figure 2-11 shows the in-plane finite element mesh for the model. The boundary conditions are

$$\sigma_z(x,T/2)=q(x)$$

$$\sigma_z(x,-T/2)=\tau_{xz}(x,T/2)=0 \qquad (2\text{-}73)$$

$$\sigma_x(0,z)=\sigma_x(L,z)=0$$

$$w(0,z)=w(L,z)=0$$

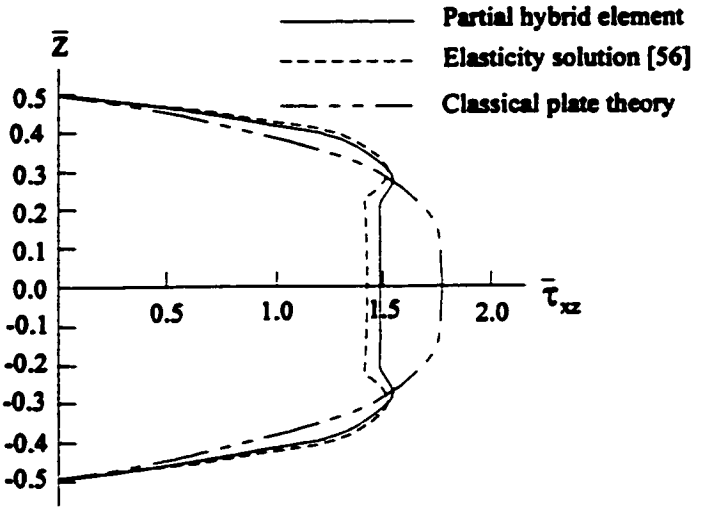

Figure 2-12 Variation of normalized transverse shear stress ($\bar{\tau}_{xz}$) through the thickness at $x = 0$, $y = a/2$ due to a sinusoidal load applied on a thick square plate ($L/T = 4$) with three laminae (0°/90°/0°)

Figure 2-12 presents the result for a plate (span-to-thickness ratio S = 4) with configuration [0°/90°/0°] under cylindrical bending. The orientation of the fibers in the top and bottom laminae is parallel to the length of the plate and in the middle layer it is

transverse to the length. The normalized interlaminar shear stress value plotted in Figure (2-12) shows excellent agreement with the solution of Pagano [56].

Example 2:

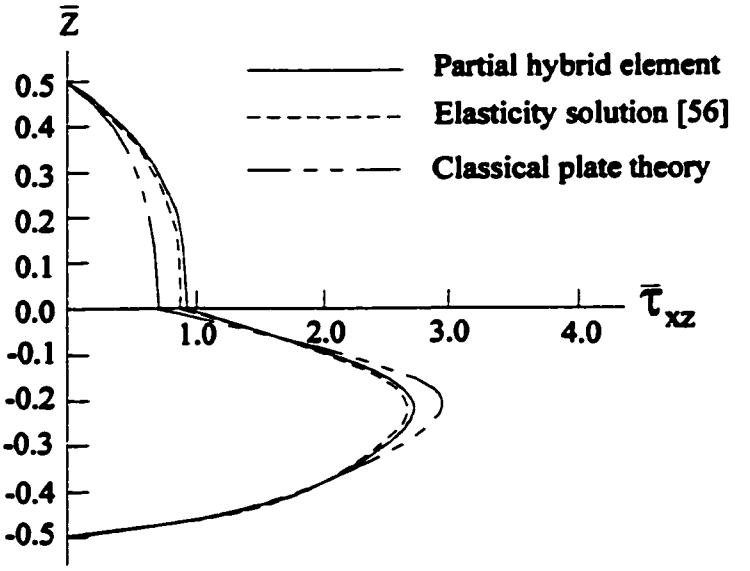

Figure 2-13 Variation of normalized transverse shear ($\bar{\tau}_{xz}$) through thickness at $x = 0$ due to the cylindrical bending of a plate with two laminae (0°/90°) and L/T = 4.0

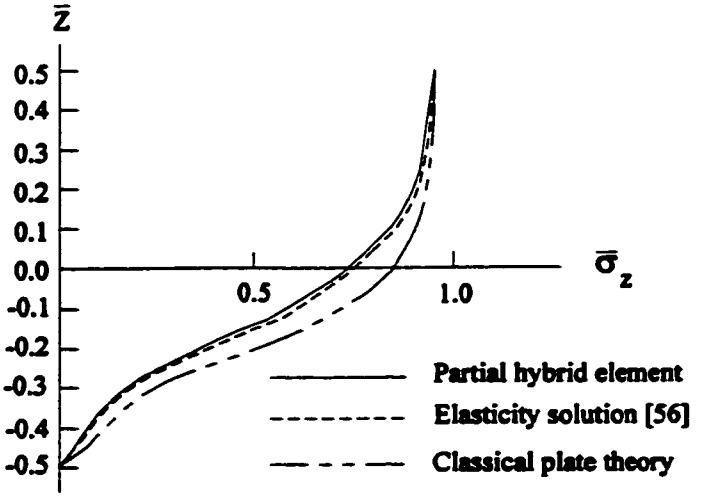

Figure 2-14 Variation of normalized transverse normal stress ($\bar{\sigma}_z$) through the thickness at $x = 0$ due to the cylindrical bending of a plate, with two laminae (0°/90°) and L/T = 4

In this example, plates with two cross-ply laminae (0°/90°) of equal thickness and made of transversely isotropic materials are considered. The orientation of the fibre in the bottom layer is parallel to the length of the strip (say x-direction) and in the top layer the orientation is transverse to the length. For a laminated plate (S = 4) variation of the normalized interlaminar normal stress $\bar{\sigma}_z$ at x =L/2 across the thickness and that of the interlaminar shear stress $(\bar{\tau}_{xz})$ at x = 0 are shown in Figures 2-13 and 2-14. The close agreement of the stress values obtained based on the present method and Pagano's elasticity solution is quite obvious from these plots. It is also apparent that even for the thick plate considered, the discrepancy in the stress values based on the Classical Plate Theory (CPT) is not as large as in the case of normalized displacement *w*.

CASE II: SIMPLY SUPPORTED SQUARE LAMINATE UNDER BIDIRECTIONAL SINUSOIDAL LOADING

Example 3:

Table 2-5 Normalized center deflection of two-layer angle-ply ($-\theta/+\theta$) simply supported square plate under sinusoidal loading

θ	Normalized center deflection		
	3D Elasticity	First order plate theory	Partial hybrid element
15°	1.7059	1.7638	1.6998
30°	1.7297	1.7724	1.7284
45°	1.6887	1.7403	1.6903

Table 2-5 contains the maximum values of transverse deflection of the midplane for square plates for different lamination scheme. The angle θ indicated in the table is

measured from the positive x-axis. The results obtained with partial hybrid element are compared with the values obtained from the first-order shear deformation theory[89] and exact analytical results given by Pagano[56].

Example 4:

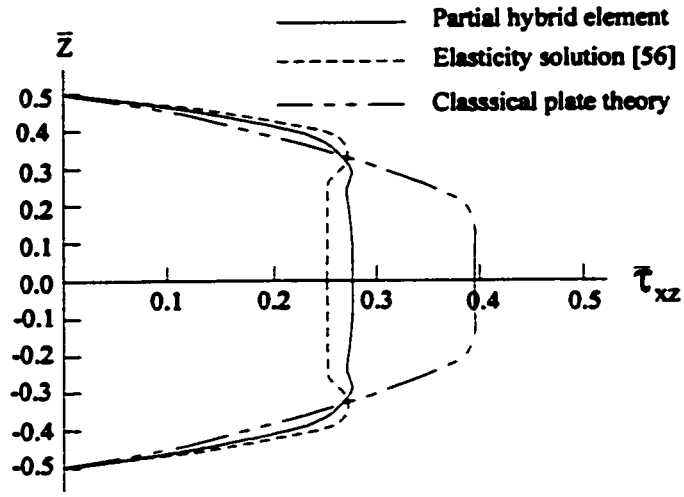

Figure 2-15 Variation of normalized transverse shear stress ($\bar{\tau}_{xz}$) through the thickness at $x = 0, y = a/2$ due to a sinusoidal load applied on a thick square plate ($L/T = 4$) with three laminae (0°/90°/0°)

In this example, a laminated cross-ply square plate (0/90/0) is considered and the results based on the present element formulation are compared with the theoretical results of Pagano[56] based on the theory of elasticity and with those obtained from classical plate theory. The plate is simply supported at its four edges and due to symmetry only one quarter of the plate is considered which is modelled with just one finite element. In Figure 2-15, the transverse shear stresses exhibit close agreement with Pagano's solution.

2.4.8 Summary

A three-dimensional 15-node triangular prism partial hybrid element has been developed based on the identification of interlaminar stress components and in-plane strains as constituting the control variable field in Helligner-Reissner variational principle. The interlaminar stress interpolation function was first constructed based on the one β-stress term per one deformation α-mode scheme, which is appropriate to suppress the zero-deformation mode as used in Ref. 50. Furthermore, with interlaminar traction continuity conditions at interface and free traction conditions at the top and bottom surfaces of the laminate the interlaminar stress function is defined completely in terms of stress parameters. From a computational point of view, the new element with the number of stress parameters per layer ($18 - 12 / N$) is very economical not only in comparison with the full hybrid stress element developed by Spilker[54] (number of stress parameters = $52–12/N$), but also competitive to another partial hybrid element by Yong[89] (number of stress parameters = $18–12/N$), where only two transverse stresses τ_{yz} and τ_{xz} are independently assumed. The efficiency and accuracy of the newly developed element have also been validated through some typical examples of analysis of composite plates under cylindrical bending and bi-directional sinusoidal loading conditions. The feasibility of the element is proved by the examples, in the determination of interlaminar stress components and deflection. It is concluded that accurate solutions to the interlaminar stress distribution in the laminated composites can be predicted by the proposed element.

2.5 Three- and Quasi-Dimensional Partial Hybrid Finite Element Analysis of Tapered Laminated Composites

2.5.1 3-D 6-node wedge partial hybrid element

This element, incorporated with the 8-node solid element by Hoa and Feng[36], was intended for analysis of tapered laminated composites, which is a core job of the thesis. In modeling the tapered laminate, the wedge element is required for meshing the taper root region as shown in Figure 2-20. So there is a necessity for formulating this element.

Shape functions

In order to define basic characteristics of the three-dimensional triangular-prism element, such as shape functions, geometry and displacement field of the element the standard idea of isoparametric elements is applied. This means that the construction of the FE Interpolants describing geometry or displacements takes place on the so-called master element shown in Figure 2-16. The master (reference) element is a simple triangular prism defined with the so-called normalized coordinates ξ η and ζ as shown in the Figure.

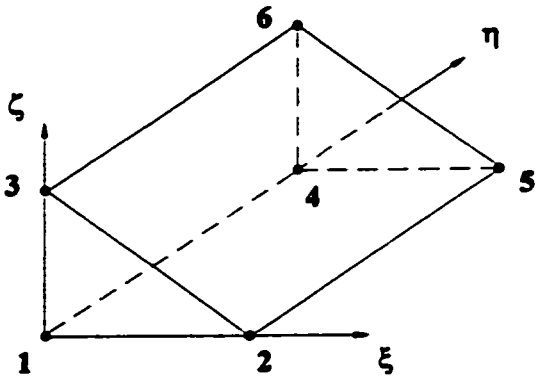

Figure 2-16 3-D 6-node wedge element

The proper shape functions are defined as tensor products of two-dimensional shape functions corresponding with the triangular base of the element defined within ξ, ζ –plane and one-dimensional shape functions corresponding with the direction η. More precisely, if ψ_1, ψ_2 and ψ_3 denote vertex node shape function for a two-dimensional triangular master element and φ_1 and φ_2 are the shape functions corresponding to vertex nodes of one-dimensional master element, then the three-dimensional shape functions can be defined as

$$\left.\begin{aligned} N_1 &= \psi_1\varphi_1 \\ N_2 &= \psi_2\varphi_1 \\ N_3 &= \psi_3\varphi_1 \\ N_4 &= \psi_1\varphi_2 \\ N_5 &= \psi_2\varphi_2 \\ N_6 &= \psi_3\varphi_2 \end{aligned}\right\} \qquad (2\text{-}74)$$

or in matrix form

$$N = \begin{bmatrix} \psi_1 & 0 \\ \psi_2 & 0 \\ \psi_3 & 0 \\ 0 & \psi_1 \\ 0 & \psi_2 \\ 0 & \psi_3 \end{bmatrix} \begin{Bmatrix} \varphi_1 \\ \varphi_2 \end{Bmatrix} \tag{2-75}$$

where

$$\psi_i = \lambda_i, \quad i = 1,2,3 \tag{2-76}$$

Note that we use so called affined (or area) coordinates λ_1 , λ_2 and λ_3 in Eq. (2-76), which can be expressed through normalized coordinates ξ , ζ with simple formulas

$$\lambda_1 = 1 - \xi - \zeta, \quad \lambda_2 = \xi \quad \text{and} \quad \lambda_3 = \zeta \tag{2-77}$$

The form of the one-dimensional shape functions appearing in Eq. (2-74) and corresponding with two vertex nodes are defined as follows

$$\begin{aligned} \varphi_1 &= 1 - \eta \\ \varphi_2 &= \eta \end{aligned} \tag{2-78}$$

The final form of the shape functions is

$$\left.\begin{aligned} N_1 &= 1 - \xi - \eta - \zeta + \xi\eta + \eta\zeta \\ N_2 &= \xi - \xi\eta \\ N_3 &= \zeta - \eta\zeta \\ N_4 &= \eta - \xi\eta - \eta\zeta \\ N_5 &= \xi\eta \\ N_6 &= \eta\zeta \end{aligned}\right\} \tag{2-79}$$

Geometry of element

For a 3-D 6-node wedge isoparametric element, the mapping from the global coordinate system (x, y, z) to the parametric coordinate system (ξ η, ζ) is carried out by

$$x = \sum_{i=1}^{6} N_i x_i \qquad y = \sum_{i=1}^{6} N_i y_i \qquad z = \sum_{i=1}^{6} N_i z_i \tag{2-80}$$

where (x_i, y_i, z_i) are the global coordinates of the i-th node (i = 1, 2, ...,6), and N_i are the shape functions expressed as Eq. (2-74)

Displacement field

As an isoparametric element allows the same geometry and displacement interpolation function, a displacement field, within the element, can be assumed as

$$u = \sum_{i=1}^{6} N_i u_i \qquad v = \sum_{i=1}^{6} N_i v_i \qquad w = \sum_{i=1}^{6} N_i w_i \tag{2-81}$$

where (u_i, v_i, w_i) are the i-th nodal displacements in the global coordinate system (i = 1, 2, ...6), and N_i are the same shape function as in Eq. (2-74). The displacement field can also be written in a matrix form,

$$\boldsymbol{u} = [N]\boldsymbol{d} = [N_1 I \quad N_2 I \cdots N_6 I]\begin{Bmatrix} \boldsymbol{d}_1 \\ \boldsymbol{d}_2 \\ \vdots \\ \boldsymbol{d}_6 \end{Bmatrix} \tag{2-82}$$

Partial strain fields

Partial strain fields are obtained with the assumed displacement filed as follows,

$$\boldsymbol{\varepsilon}_g = [\varepsilon_x, \varepsilon_y, \gamma_{xy}]^T = \mathbf{D}_g \boldsymbol{u} = \begin{Bmatrix} \dfrac{\partial u}{\partial x} \\ \dfrac{\partial v}{\partial y} \\ \dfrac{\partial u}{\partial y} + \dfrac{\partial v}{\partial x} \end{Bmatrix} = [\mathrm{B}_g]\boldsymbol{d} \tag{2-83}$$

in which,

$$[B_g] = [B_{g1}\ B_{g2} \cdots B_{g6}] \tag{2-84}$$

where,

$$[B_{gi}] = \begin{bmatrix} N_{i,x} & 0 & 0 \\ 0 & N_{i,y} & 0 \\ N_{i,y} & N_{i,x} & 0 \end{bmatrix} \tag{2-85}$$

Similarly, the other half of strain field that corresponds to the transverse strain-displacement relation and has to be satisfied a posteriori can be obtained in the following,

$$\boldsymbol{\varepsilon}_t = [\varepsilon_z, \gamma_{yz}, \gamma_{xz}]^T = \mathbf{D}_t \boldsymbol{u} = \begin{Bmatrix} \dfrac{\partial w}{\partial z} \\ \dfrac{\partial v}{\partial z} + \dfrac{\partial w}{\partial y} \\ \dfrac{\partial w}{\partial x} + \dfrac{\partial u}{\partial z} \end{Bmatrix} = [\mathrm{B}_t]\boldsymbol{d} \tag{2-86}$$

in which,

$$[B_t] = [B_{t1}\ B_{t2} \cdots B_{t6}] \tag{2-87}$$

where

$$[B_{ti}] = \begin{bmatrix} 0 & 0 & N_{i,z} \\ 0 & N_{i,z} & N_{i,y} \\ N_{i,z} & 0 & N_{i,x} \end{bmatrix} \tag{2-88}$$

Mapping the derivatives from global coordinate system to local coordinate system as required by performing the evaluation of isoparametric element matrices is realized by

$$\begin{pmatrix} N_{i,\xi} \\ N_{i,\eta} \\ N_{i,\zeta} \end{pmatrix} = \begin{bmatrix} x_{,\xi} & y_{,\xi} & z_{,\xi} \\ x_{,\eta} & y_{,\eta} & z_{,\eta} \\ x_{,\zeta} & y_{,\zeta} & z_{,\zeta} \end{bmatrix} \begin{pmatrix} N_{i,x} \\ N_{i,y} \\ N_{i,z} \end{pmatrix} = [J] \begin{pmatrix} N_{i,x} \\ N_{i,y} \\ N_{i,z} \end{pmatrix} \tag{2-89}$$

where

$$x_{,\xi} = \sum_{i=1}^{6} N_{i,\xi}\, x_i \quad \cdots \quad z_{,\zeta} = \sum_{i=1}^{6} N_{i,\zeta}\, z_i \tag{2-90}$$

Another form for Eq. (2-15) can be written as

$$\begin{pmatrix} N_{i,x} \\ N_{i,y} \\ N_{i,z} \end{pmatrix} = [J]^{-1} \begin{pmatrix} N_{i,\xi} \\ N_{i,\eta} \\ N_{i,\zeta} \end{pmatrix} \tag{2-91}$$

in which

$$\left.\begin{array}{lll} N_{1,\xi} = -(1-\eta) & N_{1,\eta} = -(1-\xi-\zeta) & N_{1,\zeta} = -(1-\eta) \\ N_{2,\xi} = (1-\eta) & N_{2,\eta} = -\xi & N_{2,\zeta} = 0 \\ N_{3,\xi} = 0 & N_{3,\eta} = -\zeta & N_{3,\zeta} = 1-\eta \\ N_{4,\xi} = -\eta & N_{4,\eta} = 1-\xi-\zeta & N_{4,\zeta} = -\eta \\ N_{5,\xi} = \eta & N_{5,\eta} = \xi & N_{5,\zeta} = 0 \\ N_{6,\xi} = 0 & N_{6,\eta} = \zeta & N_{6,\zeta} = \eta \end{array}\right\} \tag{2-92}$$

Partial stress field using iso-function method

Within the element, a partial stress field is assumed independently as

$$\sigma_g = \begin{Bmatrix} \sigma_z \\ \tau_{yz} \\ \tau_{zx} \end{Bmatrix} = [P_g]\beta = [\sigma_{g1}, \sigma_{g2}, \cdots \sigma_{gm}] \begin{Bmatrix} \beta_1 \\ \beta_2 \\ \cdots \\ \beta_m \end{Bmatrix} \tag{2-93}$$

A partial stress matrix using iso-function method can be directly derived from the displacement field as follows

$$\left.\begin{aligned} u &= a_0 + a_1\xi + a_2\eta + a_3\zeta + a_4\xi\eta + a_5\eta\zeta \\ v &= b_0 + b_1\xi + b_2\eta + b_3\zeta + b_4\xi\eta + b_5\eta\zeta \\ w &= c_0 + c_1\xi + c_2\eta + c_3\zeta + c_4\xi\eta + c_5\eta\zeta \end{aligned}\right\} \tag{2-94}$$

or in matrix form

$$\boldsymbol{u} = \boldsymbol{\Phi a} \tag{2-95}$$

where,

$$\boldsymbol{\Phi} = \begin{bmatrix} 1 & 0 & 0 & \xi & 0 & 0 & \eta & 0 & 0 & \zeta & 0 & 0 & \xi\eta & 0 & 0 & \eta\zeta & 0 & 0 \\ 0 & 1 & 0 & 0 & \xi & 0 & 0 & \eta & 0 & 0 & \zeta & 0 & 0 & \xi\eta & 0 & 0 & \eta\zeta & 0 \\ 0 & 0 & 1 & 0 & 0 & \xi & 0 & 0 & \eta & 0 & 0 & \zeta & 0 & 0 & \xi\eta & 0 & 0 & \eta\zeta \end{bmatrix} \tag{2-96}$$

$$\boldsymbol{a} = \{a_0 \quad b_0 \quad c_0 \quad a_1 \quad b_1 \quad c_1 \cdots a_5 \quad b_5 \quad c_5\}^T \tag{2-97}$$

The strains derived from the assumed displacement field are

$$\left.\begin{aligned} \varepsilon_\xi &= \frac{\partial u}{\partial \xi} = a_1 + a_4\eta \\ \varepsilon_\eta &= \frac{\partial v}{\partial \eta} = b_2 + b_4\xi + b_5\zeta \\ \varepsilon_\zeta &= \frac{\partial w}{\partial \zeta} = c_3 + c_5\eta \\ \gamma_{\eta\zeta} &= \frac{\partial w}{\partial \eta} + \frac{\partial v}{\partial \zeta} = (c_2 + b_3) + c_4\xi + b_5\eta + c_5\zeta \\ \gamma_{\xi\zeta} &= \frac{\partial w}{\partial \xi} + \frac{\partial u}{\partial \zeta} = (c_1 + a_3) + (a_5 + c_4)\eta \\ \gamma_{\xi\eta} &= \frac{\partial v}{\partial \xi} + \frac{\partial u}{\partial \eta} = (b_1 + a_2) + a_4\xi + b_4\eta + a_5\zeta \end{aligned}\right\} \tag{2-98}$$

The stress field is related to the assumed displacement with the following

$$\boldsymbol{\sigma} = \boldsymbol{C\,\varepsilon} \tag{2-99}$$

where,

$$\begin{aligned}\sigma &= \{\sigma_\xi,\ \sigma_\eta,\ \sigma_\zeta,\ \tau_{\eta\zeta},\ \tau_{\xi\zeta},\ \tau_{\xi\eta}\}^T \\ \varepsilon &= \{\varepsilon_\xi,\ \varepsilon_\eta,\ \varepsilon_\zeta,\ \gamma_{\eta\zeta},\ \gamma_{\xi\zeta},\ \gamma_{\xi\eta}\}\end{aligned} \tag{2-100}$$

For specially (on-axis) orthotropic material

$$C = \begin{bmatrix} C_{11} & C_{12} & C_{13} & 0 & 0 & 0 \\ C_{21} & C_{22} & C_{23} & 0 & 0 & 0 \\ C_{31} & C_{32} & C_{33} & 0 & 0 & 0 \\ 0 & 0 & 0 & C_{44} & 0 & 0 \\ 0 & 0 & 0 & 0 & C_{55} & 0 \\ 0 & 0 & 0 & 0 & 0 & C_{66} \end{bmatrix} \tag{2-101}$$

Thus

$$\left.\begin{aligned}\sigma_\zeta &= C_{31}\varepsilon_\xi + C_{32}\varepsilon_\eta + C_{33}\varepsilon_\zeta \\ \tau_{\eta\zeta} &= C_{44}\gamma_{\eta\zeta} \\ \tau_{\xi\zeta} &= C_{55}\gamma_{\xi\zeta}\end{aligned}\right\} \tag{2-102}$$

or in matrix form

$$\sigma_s = \Theta\alpha \tag{2-103}$$

where,

$$\sigma_s = [\sigma_\zeta,\ \tau_{\eta\zeta},\ \tau_{\xi\zeta}]^T \tag{2-104}$$

$$\left.\begin{aligned}\sigma_\zeta &= a_1 + a_4\xi + a_7\eta + a_9\zeta \\ \tau_{\eta\zeta} &= a_2 + a_5\xi + a_8\eta + a_{10}\zeta \\ \tau_{\xi\zeta} &= a_3 + a_6\eta\end{aligned}\right\} \tag{2-105}$$

$$\Theta = \begin{bmatrix} 1 & 0 & 0 & \xi & 0 & 0 & \eta & 0 & \zeta & 0 \\ 0 & 1 & 0 & 0 & \xi & 0 & 0 & \eta & 0 & \zeta \\ 0 & 0 & 1 & 0 & 0 & \xi & 0 & 0 & 0 & 0 \end{bmatrix} \tag{2-106}$$

$$\alpha = \{a_1\ \ a_2\ \ a_3\ \ a_4\ \ a_5\ \ a_6\ \ a_7\ \ a_8\ \ a_9\ \ a_{10}\}^T \tag{2-107}$$

$$\left.\begin{aligned}
a_1 &= C_{31}a_1 + C_{32}b_2 + C_{33}c_3 \\
a_2 &= C_{44}(c_2 + b_3) \\
a_3 &= C_{55}(c_1 + a_3) \\
a_4 &= C_{32}b_4 \\
a_5 &= C_{44}c_4 \\
a_6 &= C_{55}(a_5 + c_4) \\
a_7 &= C_{33}c_5 + C_{31}a_4 \\
a_8 &= C_{44}b_5 \\
a_9 &= C_{32}b_5 \\
a_{10} &= C_{55}c_5
\end{aligned}\right\} \tag{2-108}$$

The resulting partial stress field is therefore, according to the iso-function method, in the form of

$$\sigma_g = P\beta \tag{2-109}$$

where the partial stress field function

$$P = \Theta = \begin{bmatrix} 1 & 0 & 0 & \xi & 0 & 0 & \eta & 0 & \zeta & 0 \\ 0 & 1 & 0 & 0 & \xi & 0 & 0 & \eta & 0 & \zeta \\ 0 & 0 & 1 & 0 & 0 & \xi & 0 & 0 & 0 & 0 \end{bmatrix} \tag{2-110}$$

Modeling of a tapered laminated composite plate

A three-dimensional finite element model for stress analysis is used to calculate the stress state in the ply drop region of the unidirectional tapered laminate made of glass fiber-epoxy. Three factors determined the specimen chosen to be investigated. The first is that some of aircraft components such as helicopter rotor blades are often made predominantly from unidirectional composites since the loading is mainly in the spanwise direction. The second is that a free edge effect is not present in unidirectional composites and an investigation of fundamental mechanisms solely controlling delamination in

tapered section is possible. The third one is that glass fibre-epoxy is a good material with which to study delamination because it is possible to detect the initiation and propagation of delamination visually. The interply resin region surrounding the ply drops is modeled as well as the laminate and is shown by the shaded area as in Figure 2-17. The dimensions of the model, in terms of the ply thickness t_{ply}, and the resin layer thickness 0.1 t_{ply} and the global coordinate system are also shown in Figure 2-19. The resin layer thickness between plies is assumed to be ten per cent of the ply thickness. Eight-node solid elements[36] and six-node wedge element developed are involved in the partial hybrid finite modeling as shown in the former sections.

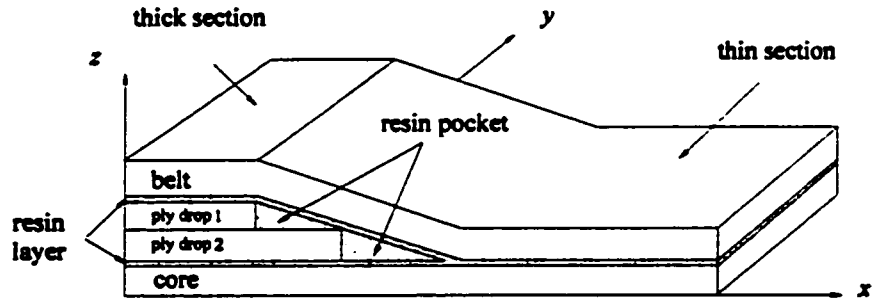

Figure 2-17 Schematic of tapered specimen

Each of the plies and the resin layer between the plies is modeled through the thickness by one element. However, the resin rich region ahead of the ply drop steps is modeled by as many as four elements through the thickness. Each element spans the half-width of the laminate and the mesh becomes very fine along the length of the laminate in the vicinity of the last ply drop step, where the maximum interlaminar stresses are located. The finite element mesh surrounding the last ply drop step is shown in Figures (2-19) and (2-20). The local coordinate systems for the

sublaminates above and below the ply drops, and the coordinate, X', representing the distance along the laminate length from the last ply-drop step, are also shown in the figure.

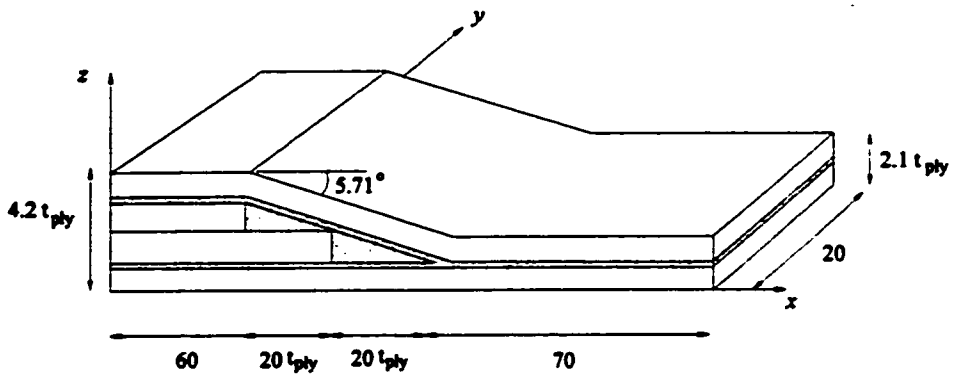

Figure 2-18 Dimension of the finite element model (not to scale)

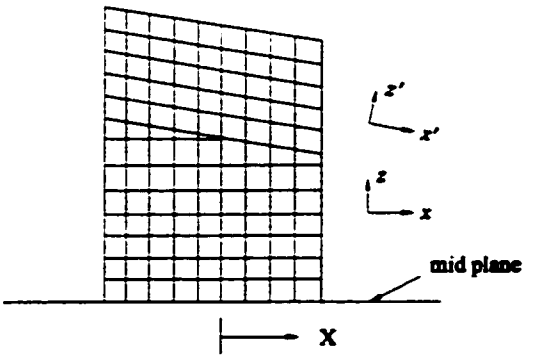

Figure 2-19 Fine mesh surrounding last ply-drop step

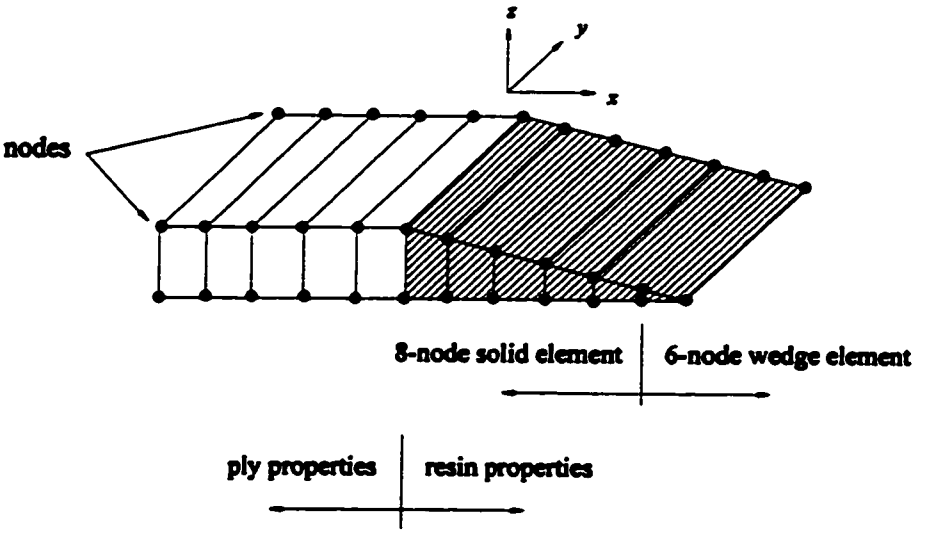

Figure 2-20 Schematic drawing of dropped ply

2.5.2 Quasi-three-dimensional partial hybrid stress finite element

In order to reduce computing efforts involved in the stress and delamination analysis of tapered laminated composites, quasi three-dimensional elements were formulated below based on the generalized plane deformation theory. Most of the researchers on tapered composites would like to convert a 3-dimentional problem into a 2-dimentional one so as to decrease the computing load, which induces a loss of accuracy. The quasi-three dimensional element, however, stands in between 2D and 3D elements, and is characterized in seeking a balance between computation efforts needed and targeted result accuracy. There is a good potential for the elements to be widely employed in engineering applications. This is also the reason that the elements, after gaining the confidence of its application to stress analysis, were further implemented to conduct fracture analysis of tapered laminates.

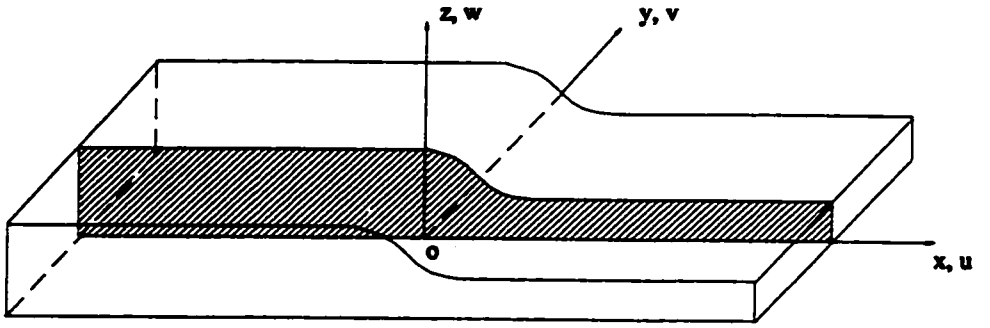

Figure 2-21 Generalized plane deformation of plate

In the so-called generalized plane deformation theory of Lekhnitskii[37], all the cross-sections would remain plane, and the stresses, geometric and material properties, and strains would be independent of the co-ordinate normal to the plane of analysis, i.e. y-axis as shown in Figure 2-21. The elasticity fundamentals and formulation of the finite elements are briefed as follows.

Elasticity fundamentals

Displacement assumptions

$$\begin{aligned} u &= u(x,z) \\ v &= v(x,z) \\ w &= w(x,z) \end{aligned} \tag{2-111}$$

and the corresponding strain field

$$
\begin{aligned}
\varepsilon_x &= u_{,x} \\
\varepsilon_y &= 0 \\
\varepsilon_z &= w_{,z} \\
\gamma_{yz} &= v_{,z} \\
\gamma_{xz} &= w_{,x} + u_{,z} \\
\gamma_{xy} &= v_{,x}
\end{aligned}
\tag{2-157}
$$

Equilibrium conditions

$$
\begin{aligned}
\frac{\partial \sigma_x}{\partial x} + \frac{\partial \tau_{xz}}{\partial z} &= 0 \\
\frac{\partial \tau_{yx}}{\partial x} + \frac{\partial \tau_{yz}}{\partial z} &= 0 \\
\frac{\partial \tau_{xz}}{\partial x} + \frac{\partial \sigma_z}{\partial z} &= 0
\end{aligned}
\tag{2-113}
$$

Constitution relations

$$
\{\sigma\} = [C]\{\varepsilon\} \tag{2-114}
$$

Two transformations need to be considered (layer angle relative to loading direction and taper angle) (See Appendix A.1).

6-Node triangular element

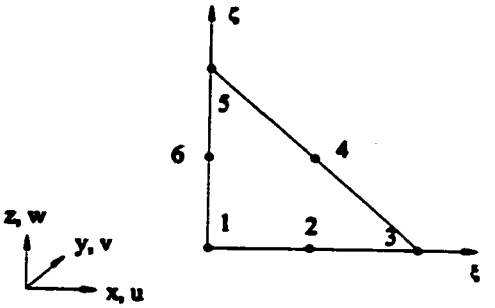

Figure 2-22 6-node triangular element

Displacement basis for the element is

$$\langle P_d \rangle = \{1 \quad \xi \quad \zeta \quad \xi^2 \quad \xi\zeta \quad \zeta^2\} \tag{2-115}$$

Nodes 1~6:

$$\{N\} = \begin{Bmatrix} -\lambda(1-2\lambda) \\ 4\xi\lambda \\ -\xi(1-2\xi) \\ 4\xi\zeta \\ -\zeta(1-2\zeta) \\ 4\zeta\lambda \end{Bmatrix}, \quad \{\partial N/\partial\xi\} = \begin{Bmatrix} 1-4\lambda \\ 4(\lambda-\xi) \\ -1+4\xi \\ 4\zeta \\ 0 \\ -4\zeta \end{Bmatrix}, \quad \{\partial N/\partial\zeta\} = \begin{Bmatrix} 1-4\lambda \\ -4\xi \\ 0 \\ 4\xi \\ -1+4\zeta \\ 4(\lambda-\zeta) \end{Bmatrix} \tag{2-116}$$

where $\lambda = 1-\xi-\zeta$

and the interlaminar stress function based on the one β-stress term per one deformation α-mode scheme, incorporated with force equilibrium, is formulated in the following:

Displacement field is

$$
\begin{aligned}
u &= a_1 + a_2\xi + a_3\zeta + a_4\xi^2 + a_5\xi\zeta + a_6\zeta^2 \\
v &= b_1 + b_2\xi + b_3\zeta + b_4\xi^2 + b_5\xi\zeta + b_6\zeta^2 \\
w &= c_1 + c_2\xi + c_3\zeta + c_4\xi^2 + c_5\xi\zeta + c_6\zeta^2
\end{aligned}
\tag{2-117}
$$

Strain field:

$$
\begin{aligned}
\varepsilon_\xi &= \frac{\partial u}{\partial \xi} = a_2 + 2a_4\xi + a_5\zeta \\
\varepsilon_\eta &= \frac{\partial v}{\partial \eta} = 0 \\
\varepsilon_z &= \frac{\partial w}{\partial \zeta} = c_3 + c_5\xi + 2c_6\zeta \\
\gamma_{\eta\zeta} &= \frac{\partial v}{\partial \zeta} + \frac{\partial w}{\eta} = b_3 + b_5\xi + 2b_6\zeta \\
\gamma_{\xi\zeta} &= \frac{\partial u}{\partial \zeta} + \frac{\partial w}{\xi} = \underline{(a_3 + c_2)} + \underline{(a_5 + 2c_4)}\xi + \underline{(2a_6 + c_5)}\zeta \\
\gamma_{\xi\eta} &= \frac{\partial u}{\partial \zeta} + \frac{\partial v}{\xi} = b_2 + 2b_4\xi + b_5\zeta ..
\end{aligned}
\tag{2-118}
$$

or of form

$$
\begin{aligned}
\varepsilon_\xi &= \alpha_1 + \alpha_2\xi + \alpha_3\zeta \\
\varepsilon_\eta &= 0 \\
\varepsilon_z &= \alpha_4 + \alpha_5\xi + \alpha_6\zeta \\
\gamma_{\eta\zeta} &= \alpha_7 + \alpha_8\xi + \alpha_9\zeta \\
\gamma_{\xi\zeta} &= \alpha_{10} + \alpha_{11}\xi + \alpha_{12}\zeta \\
\gamma_{\xi\eta} &= \alpha_{13} + \alpha_{14}\xi + \alpha_{15}\zeta
\end{aligned}
\tag{2-119}
$$

Interlaminar stress function is thus written as

$$
\begin{aligned}
\sigma_\zeta &= \beta_1 + \beta_2\xi + \beta_3\zeta \\
\tau_{\eta\zeta} &= \beta_4 + \beta_5\xi + \alpha_6\zeta \\
\tau_{\xi\zeta} &= \beta_7 + \beta_8\xi + \beta_8\zeta
\end{aligned}
\tag{2-120}
$$

From the equilibrium condition, we have

$$
\frac{\partial \tau_{\xi\zeta}}{\partial \xi} + \frac{\partial \sigma_\zeta}{\partial \zeta} = \beta_8 + \beta_3 = 0 \tag{2-121}
$$

so the final form the stress function is

$$\begin{aligned}\sigma_\zeta &= \beta_1 + \beta_2\xi + \beta_3\zeta \\ \tau_{\eta\zeta} &= \beta_4 + \beta_5\xi + \beta_6\zeta \\ \tau_{\xi\zeta} &= \beta_7 - \beta_5\xi + \beta_8\zeta\end{aligned} \tag{2-122}$$

or in a matrix form

$$\begin{Bmatrix}\sigma_\zeta \\ \tau_{\eta\zeta} \\ \tau_{\xi\zeta}\end{Bmatrix} = \begin{bmatrix}1 & \xi & \zeta & 0 & 0 & 0 & 0 & 0 \\ 0 & 0 & 0 & 1 & \xi & \zeta & 0 & 0 \\ 0 & 0 & -\xi & 0 & 0 & 0 & 1 & \zeta\end{bmatrix}\begin{Bmatrix}\beta_1 \\ \beta_2 \\ \vdots \\ \beta_8\end{Bmatrix} \tag{2-123}$$

8-Node quadrilateral element

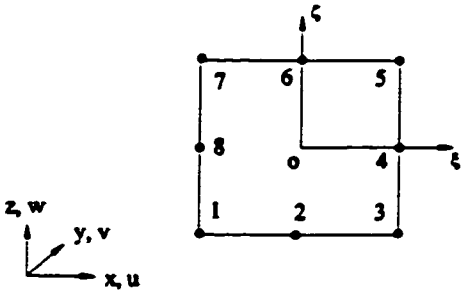

Figure 2-23 8-node quadratic element

Displacement basis

$$\langle P_d \rangle = \{1 \quad \xi \quad \zeta \quad \xi^2 \quad \xi\zeta \quad \zeta^2 \quad \xi^2\zeta \quad \xi\zeta^2\} \tag{2-124}$$

Nodes 1~8

$$\{N\}=\begin{Bmatrix}-(1-\xi)(1-\zeta)(1+\xi+\zeta)/4\\(1-\xi^2)(1-\zeta)/2\\-(1+\xi)(1-\zeta)(1-\xi+\zeta)/4\\(1+\xi)(1-\zeta^2)/2\\-(1+\xi)(1+\zeta)(1-\xi-\zeta)/4\\(1-\xi^2)(1+\zeta)/2\\-(1-\xi)(1+\zeta)(1+\xi-\zeta)/4\\(1-\xi)(1-\zeta^2)/2\end{Bmatrix}$$

$$\{\partial N/\partial\xi\}=\begin{Bmatrix}(1-\zeta)(2\xi+\zeta)/4\\-(1-\zeta)\xi\\(1-\zeta)(2\xi-\zeta)/4\\(1-\zeta^2)/2\\(1+\zeta)(2\xi+\zeta)/4\\-(1+\zeta)\xi\\(1+\zeta)(2\xi-\zeta)/4\\-(1-\zeta^2)/2\end{Bmatrix}$$

$$\{\partial N/\partial\zeta\}=\begin{Bmatrix}(1-\xi)(\xi+2\zeta)/4\\-(1-\xi^2)/2\\-(1+\xi)(\xi-2\zeta)/4\\-(1+\xi)\zeta\\(1+\xi)(\xi+2\zeta)/4\\(1-\xi^2)/2\\-(1-\xi)(\xi-2\zeta)/4\\-(1-\xi)\zeta\end{Bmatrix} \qquad (2\text{-}125)$$

and the interlaminar stress shape functions are given by the similar way as above for 6-node 3-D quasi element:

$$\begin{aligned}\sigma_\zeta &= \beta_1+\beta_2\xi+\beta_3\zeta-2\beta_4\xi\zeta+\beta_5\xi^2+\beta_6\zeta^2\\ \tau_{\eta\zeta} &= \beta_7+\beta_8\xi+\beta_9\zeta+\beta_{10}\xi\zeta+\beta_{11}\xi^2+\beta_{12}\zeta^2\\ \tau_{\xi\zeta} &= \beta_{13}-\beta_9\xi+\beta_{14}\zeta-2\beta_6\xi\zeta+\beta_4\xi^2\end{aligned} \qquad (2\text{-}126)$$

or in a matrix form

$$\begin{Bmatrix} \sigma_\zeta \\ \tau_{\eta\zeta} \\ \tau_{\xi\zeta} \end{Bmatrix} = \begin{bmatrix} 1 & \xi & \zeta & -2\xi\zeta & \xi^2 & \zeta^2 & 0 & 0 & 0 & 0 & 0 & 0 & 0 & 0 \\ 0 & 0 & 0 & 0 & 0 & 0 & 1 & \xi & \zeta & \xi\zeta & \xi^2 & \zeta^2 & 0 & 0 \\ 0 & 0 & 0 & \xi^2 & 0 & -2\xi\zeta & 0 & 0 & -\xi & 0 & 0 & 0 & 1 & 0 \end{bmatrix} \begin{Bmatrix} \beta_1 \\ \beta_2 \\ \vdots \\ \beta_{14} \end{Bmatrix} \tag{2-127}$$

2.5.3 Validation of the models through example

The example exercised to validate the models developed is similar to the one given in Ref. 14. It was also used in Chapter 5 for the modified shear-lag analysis. All plies in the model as shown in Figure 2-24 are 0° unidirectional glass/epoxy with material properties given in Table 2-1, which, for convenience of comparison and evaluation, are quoted from Ref.14. Also, thin (0.1-t_{ply} thick) resin layers are included in the model to allow for the direct calculation of interlaminar stresses. In this problem, an eight-ply laminate is tapered to four plies in a symmetric fashion. The laminate is 50.8 mm (2 in) long in the thick section, 50.8 mm (2 in) long in the thin section, 25.4 mm (1in) wide and has a taper ratio of 10:1 (Ply drop-off step space s is 10 times ply thickness). Uniaxial tension is applied by fixing the thicker end of the laminate and applying an axial displacement of 0.0254 mm (0.001in) at the other end.

Table 2-1 Material Properties

Glass/Epoxy Unidirectional Tape			Resin
Extensional Moduli, msi			Young's Modulus, msi
$E_L = 6.4$	$E_T = 1.8$	$E_N = 1.8$	$E = 0.57$ msi
Shear Moduli, msi			Shear Moduli, msi
$G_{LT} = 0.65$	$G_{TN} = 0.65$	$G_{NL} = 0.60$	$G = 0.21$
Poisson's Ratios			Poisson's Ratio
$\nu_{LT} = 0.29$	$\nu_{LN} = 0.29$	$\nu_{TN} = 0.50$	$\nu = 0.37$
			Tensile Strength
			$\sigma_0 = 9$ ksi

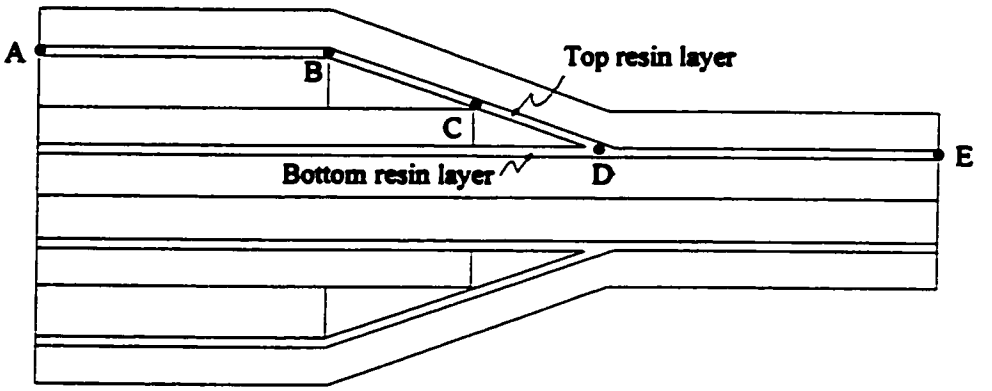

Figure 2-24 Schematic drawing of tapered laminate

Meshing of quasi three-dimensional elements is shown in Figure (2-25). Figures (2-26) and (2-27) illustrate interlaminar stress peak values about the foremost ply drop (Point C in Figure 2-24), where a critical load transfer occurs and further induces delamination failure at the interfaces between dropped plies and continuous plies. Predictions by the both models agree well with the referred finite element solution[14], showing in quality the trend of stress distribution. At the drop-off location, both interlaminar shear and normal stresses appear to be at peak values. For interlaminar normal stress, whether at the top resin layer or at the bottom resin layer, a similar trend of change is observed: the stress around the drop-off changes to compression just at the left side of the ply-drop end from tension at the right side of the ply-drop end. The interlaminar stress gradient over this critical region is high and a singularity may exist. It is also suggested that the interlaminar normal stress, although peaking at the drop off location, plays a role not so strong as to initiate a fracture at this critical region. On the other hand, interlaminar shear stress not only has its peak value at the drop-off, but also shows the change of sign in both top and lower resin layers. Therefore, in the drop-off location, the interlaminar shear stress seems to contribute more to the first damage failure event than interlaminar normal stress.

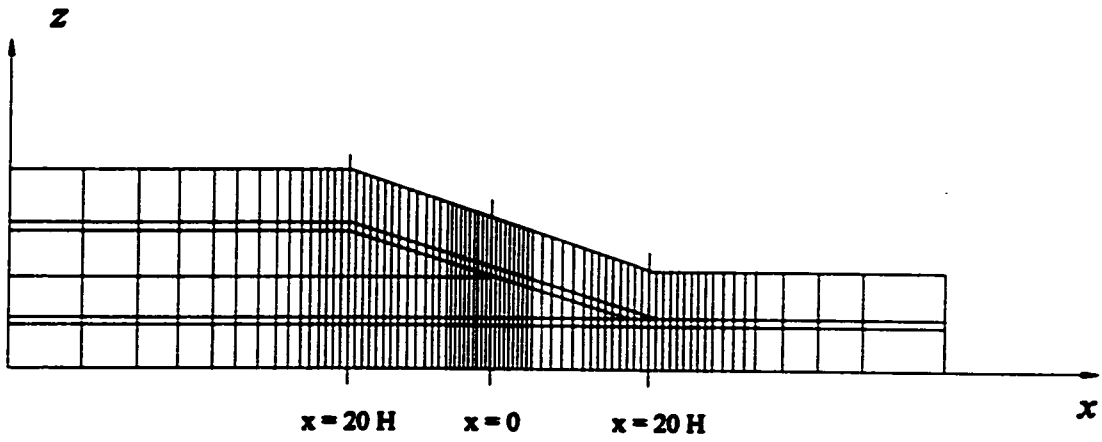

Figure 2-25 Finite element mesh for quasi three dimensional elements

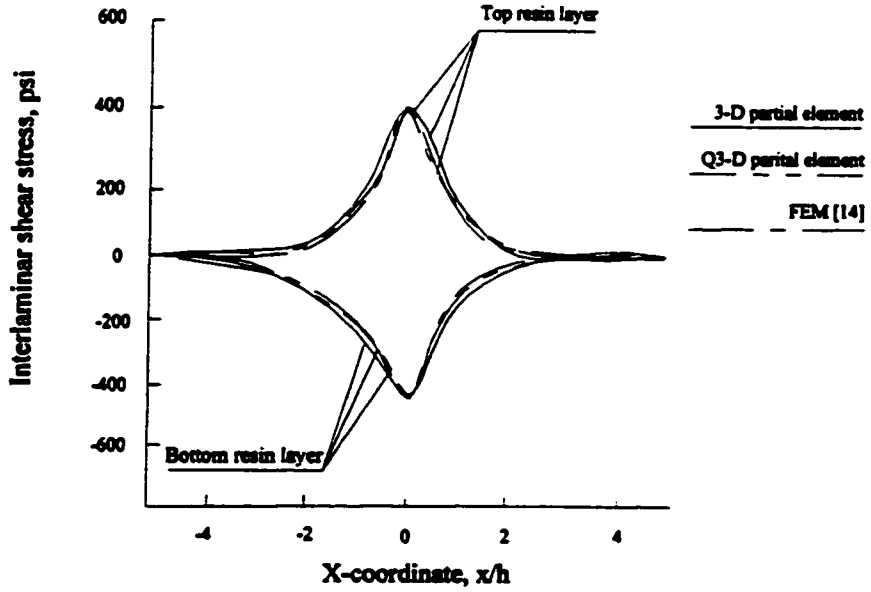

Figure 2-26 Comparison of interlaminar shear stress distributions

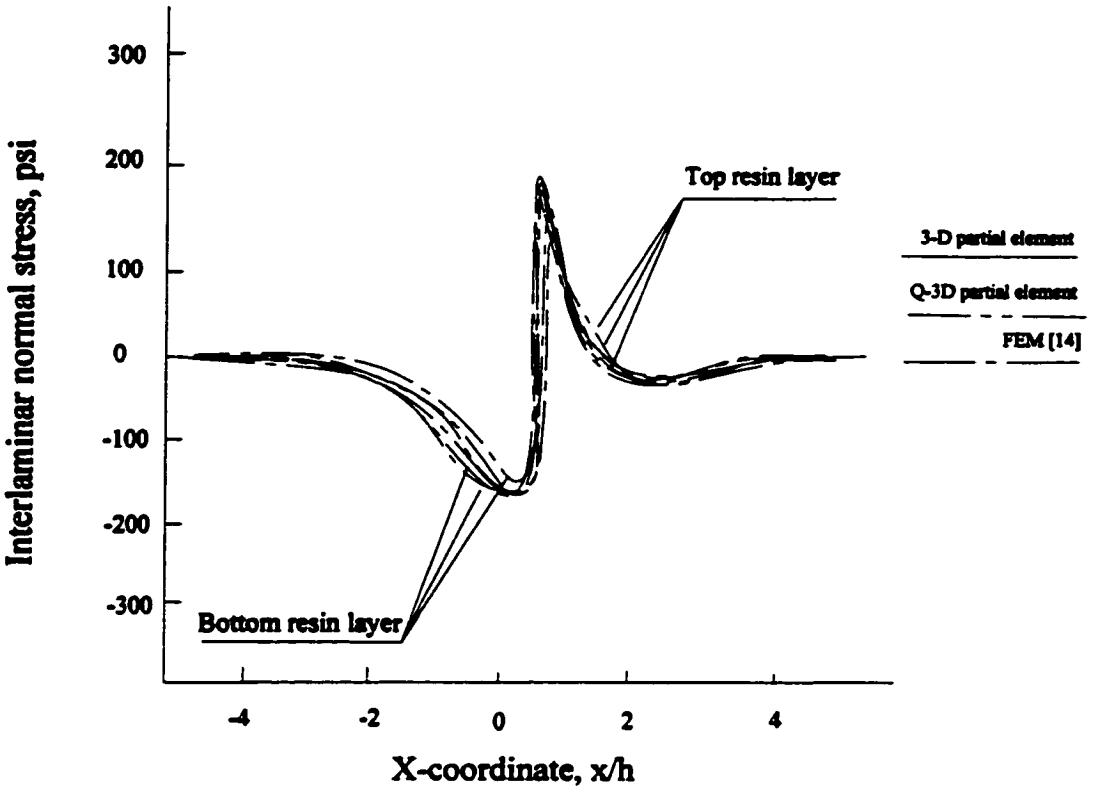

Figure 2-27 Comparison of interlaminar normal stress distributions

Chapter 3

EXPERIMENTAL PROGRAM

3.1 Description

The tapered specimens to be studied in the experimental program are composed of three sublaminates as indicated in Figure 3-1: one internally dropped sublaminate, and two outer continuous sublaminates (also called belt sublaminates) that cover the dropped sublaminate. All of the laminates investigated are symmetric and unidirectional. The laminates were tapered from 12 plies to 6 plies through a taper angle of approximately ten degrees. The dropped sublaminate contains six plies and terminates at the mid-plane of the laminates. The hatched triangular section in Figure 3-1 represents a resin rich region ahead of the ply-drop step that results from the curing process. The basis for selecting this type of structure for experimental study and numerical analysis is to avoid complications involved in complex laminates with multiple dropped plies and free-edge stresses which will present more difficulties in gaining insight into the failure mechanisms and controlling parameters.

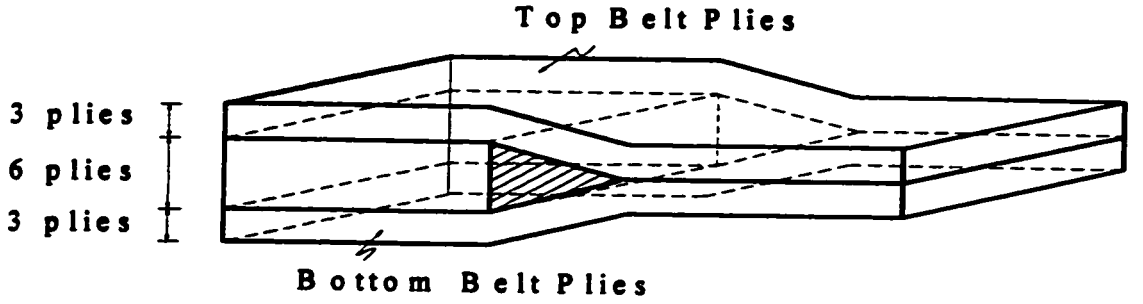

Figure 3-1 View of the tapered laminate

3.2 Manufacturing of Specimens

The material that was used to fabricate the specimens is NCT 301 unidirectional prepreg tape manufactured by Newport Adhesives and Composites, Inc. It consists of the continuous unidirectional graphite fibers embedded in the epoxy resin, and it is intended for structural applications over a temperature range of –65° F to 250° F. The material is supplied in rolls and kept in the refrigerator. The unidirectional prepreg tape was first cut with standard knives with replaceable blades into the appropriate lengths for hand lay-up. The laminate panels were made using a ply in-fill technique as shown in Figure 3-2 whereby an equivalent tapered section is built up on the other side of the release cloth. Formation of the laminate panel with this technique is described as follows:

1. Lay up 4 basic blocks, each of which constitutes three unidirectional prepreg plies, so as to build the laminate;
2. Use 2 of the 4 blocks to construct the top and bottom belts;
3. Cut each of the remaining 2 blocks into 3 pieces; 2 of them were included in the lay-up of the laminate and the third was placed on the outside of the release cloth,

allowing good consolidation to be obtained when the panel was cured in the autoclave.

4. Cut the panel, after curing, into the specimens with the dimensions shown in Figure 3-5 for test.

Generally a triangular resin-rich pocket could be seen at the tip of the dropped plies. The taper angle could be estimated from photographs of the cross sections by measuring the height and length of the triangular resin pockets. This technique allows panels to be made between flat plates, producing good consolidation without the need for special tooling. All of the full-length plies for the laminates have in-plane dimensions of

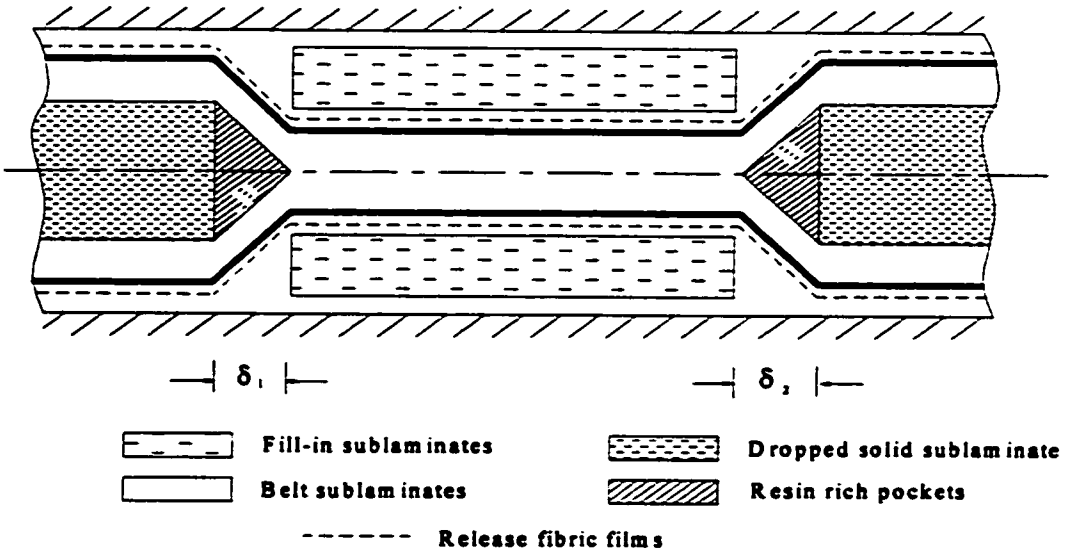

Figure 3-2 Ply in-fill technique for manufacturing of the tapered laminate

approximately 240 mm in length and 30 mm in width. The internally dropped plies that make up the ply-drop step were also 30 mm in width and 120 mm in length.

A thick aluminum plate was used to support laminates during curing. Release agent was applied over the cure area of the plate for subsequent tool release. Preparation of the assembly began by placing resin-damming material around the perimeter of the cured area on the cured plate. Next, the composite part was placed on the plate covered with a sheet of release film to isolate the excess resin from the aluminum plate. A sheet of porous Teflon fabric was added to allow the resin to flow away from the laminate to the bleeder material. Two sheets of paper bleeder were then placed on the assembly to absorb the majority of the excess resin from the laminates. A large section

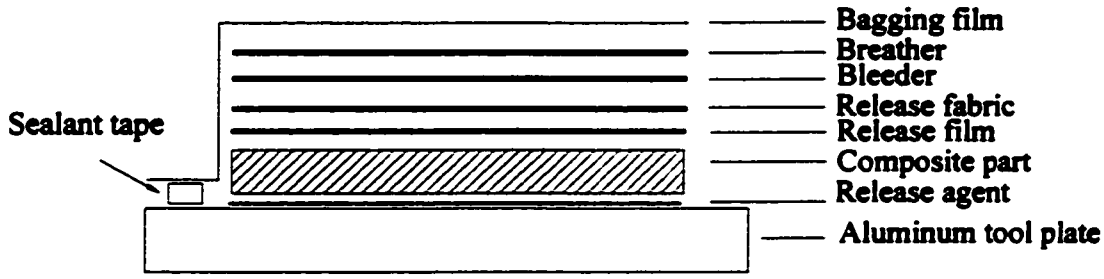

Figure 3-3 Lay-up of cure materials for tapered laminates

of synthetic fiber breather material was placed over the assembly and down to the surface of the vacuum plate to allow gases to vent away from the assembly. Vacuum bag sealant was then placed on the vacuum plate around the perimeter of the assembly. Finally, a large section of bagging film, with a quick disconnect vacuum valve attached, was placed over the assembly and pressed onto the sealant. An electrically heated autoclave was used to cure the laminates. The laminates were cured according to the manufacturer's specifications. A full vacuum of 28 in.Hg was drawn over the assembly and the bag was inspected for leaks. The entire assembly was then placed in the autoclave and the door is

closed and secured. The lay-up of the assembly and the curing cycle are shown in Figure 3-3 and Figure 3-4, respectively.

The laminate and cure materials were removed from the aluminum plates and the laminate was post-cured for ten hours. After the post-cure, the excess resin from the laminate was trimmed off with a circular sander using medium grit sandpaper. The final step in the specimen fabrication process was the bonding of glass-epoxy tabs to the ends of the laminates to prevent grip damage during the tension tests. A band saw was used to cut a 2.5 mm-thick sheet of glass polyester into tab sections measuring approximately 25 mm in length 30 mm in width.

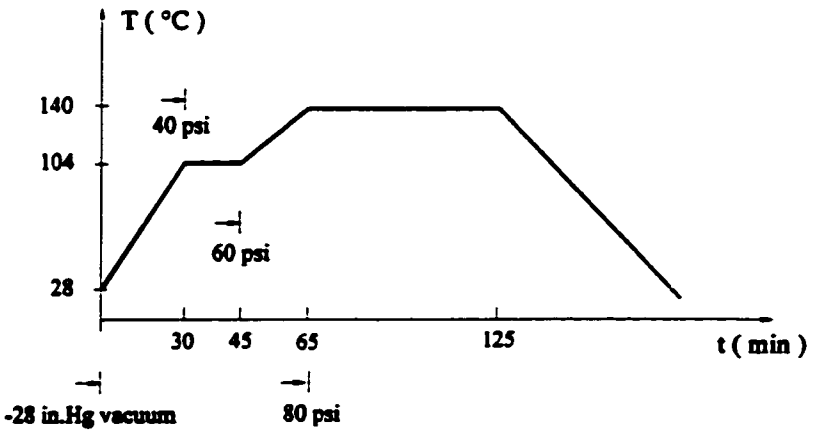

Figure 3-4 Curing cycle

One end of the tabs was then beveled across the width to an angle of approximately thirty degrees, using sand paper. The tabs were bonded to the ends of laminates, with the

beveled section placed toward the laminate center, using adhesives. The bonding tabs are shown in Figure 3-5.

3.3 Experimental Investigation

Prior to conducting the tests, strain gages were bonded to the specimens. For each of the tapered specimens, 2 gages were placed longitudinally at the center on one surface in order to be able to monitor the axial strain. Pairs of gages were located on both sides of the drop-off, 10 mm from the end of the discontinuous plies (see Figure 3-5).

Gages of type CEA-06-125UW-350, manufactured by Micro-Measurements of Measurements Group, Inc., were used and attached onto the specimens with M-Bond 200 adhesive as prescribed by Instructions Bulletin B-127-6. Briefly, the procedure involves the following steps: degreasing the gaged area with Freon TF, marking the gage alignment lines with a pencil, applying M-Prep Conditioner and M-Prep Neutralizer 5, placing cellophane tape over the gage, positioning the assembly within the layout lines, applying M-Bond 200 catalyst, applying the adhesive, applying thumb pressure to press the adhesive, and peeling the tape away from the specimen and gage. Lead-in wires were then soldered onto the gages.

The tension tests were conducted with a digital control MTS Servo Hydraulic Testing Machine. The machine uses self-aligning wedge grips to hold the specimen during testing. Output from the load cell of the testing machine and crosshead displacement was continuously monitored with MTS 431 X – Y Recorder. A long distance Questar QM1 (Maksutov-Cassegrain Catadioptric) telescope manufactured by Questar Corporation was used to observe and record damage development during the test.

The blackened specimen edges were inspected with the camera. Any damage to the specimen edges was easily recognized as light areas on the dark surface. The strain gages on the test specimens were always placed on the side opposite the lamps, to minimize thermal effects on the gages. The position of the light was also needed to be properly adjusted to give maximum shade contrast between the rich pocket and its adjacent areas so as to clearly see cracking progress. The experiment was required stopped in order to observe the whole specimen when a noise was heard, which means cracking occurred in some place of the laminate. Afterwards the experiment was continued until the specimen failed.

Figure 3-5 shows the specimen arrangement and nominal dimensions. The material properties are listed in Table 4-1. The tensile tests were conducted at a crosshead rate of 0.5mm/min. Damage was monitored and recorded with the camera and lamp set-up as each test progressed. Strains, load and crosshead displacement were logged into a computer.

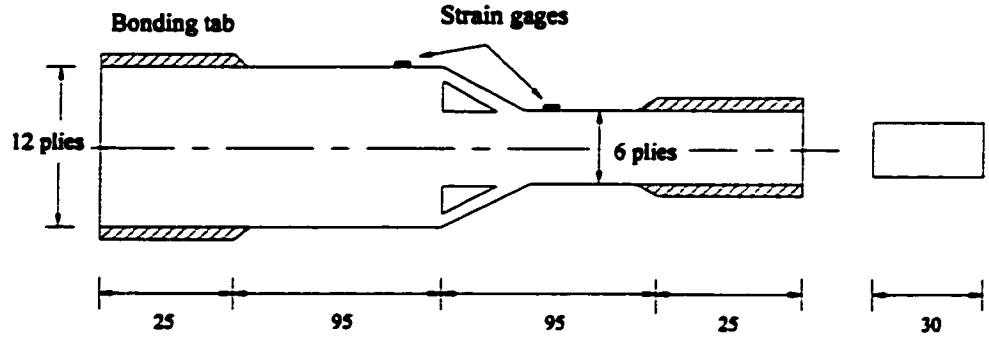

Figure 3-5 Specimen dimensions (not to scale)

3.4 Experimental Results and Observations

A typical load versus strain curve from one of the tensile tests is shown in Figure 3-6. The marks along the curve indicate points at which delamination onset (DOT), global delamination propagation (GDP), and ultimate failure (ULT) occurred during the test.

Delamination onset in the specimens is easily observed which is in general accompanied by a cracking sound, an appearance of crack in the specimens, and a load drop. Delamination in the majority of the laminate specimens initiated in the region above and below the drop step.

Global delamination propagation was easily detected by a drop in load, as well as by both visual and audible indications.

Failure of the adhesive, used in bonding the end tabs to the specimens, occurred during the tests for the ultimate strength of the laminate specimens. The true ultimate failure values for some specimens were not attainable.

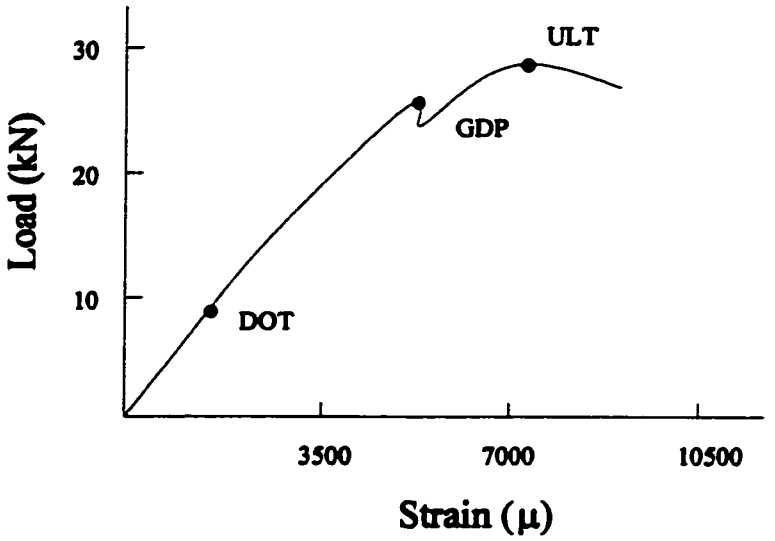

Figure 3-6 A typical load-strain curve

The loads and axial stresses for the damage events are presented in Table 3-1 and 3-2, respectively. The damage event stresses are determined by dividing the relevant load by the measured cross-sectional area of the thin section of the specimen.

Table 3-1 Damage Event Loads for Tapered Laminates

Specimen #	DOT (N)	GDP (N)	ULT (N)
1	8140	29998	>32000
2	9123	28985	>33000
3	8746	24009	34023
4	6739	26349	>34000
5	8970	27510	33457
6	9430	29458	33968
7	8350	30355	>32000
8	7780	27651	>31000
9	9321	31006	33031
10	7689	28561	>31000
11	7856	29890	>31000
12	8543	31002	32096
Mean	**8391**	**28731**	N.A.
C.V. (%)	3.9	7.9	

Table 3-2 Delamination Stresses in Tapered Laminates

Specimen #	DOT (MPa)	GDP (MPa)
1	362	1334
2	405	1288
3	433	1166
4	300	1123
5	399	1222
6	419	1308
7	371	1350
8	346	1228
9	414	1378
10	342	1270
11	349	1307
12	380	1380
Mean	**373**	**1271**
C.V. (%)	**3.9**	**7.9**

Figures 3-7 ~ 3-9 illustrate a typical delamination progression in the laminate under tension test, from an intact state to eventual delamination failure. To get close examination of the delamination progress, a telescope instrument together with a monitor is used. Because the resin pocket critical for delamination initiation is very small it usually will take a long time to pinpoint that area. Properly positioning the light is helpful in determining the location of the resin pocket. The above figures were therefore gathered by photographing the screen of the monitor screen at an instant that a sudden change such as noise and/or crack occurrence takes place and the load is immediately paused for the further observation of the laminate.

A dark and triangular resin pocket can be seen clearly in Figure 3-7. The formation of the resin pocket is due to lay-up operation and curing process. Figure 3-8 shows a typical cracking configuration about the resin pocket. The resin pocket is the delamination source that presents significant influence on fracture toughness of the laminate. Figures 3-9(a) through Figure 3-9(i) illustrate progressive delamination demonstrated in a typical tapered laminate during the test, from an intact state to a delamination propagation. The transverse cracking shown in Figure 3-9(b) for the sample first appears at a low load, starting from the corner point of dropped plies. It is indicated by a darken shade line at the left side of resin rich area. As the load increases, the darken shade line is shaping into an oval, showing a delamination between the belt plies and dropped layers occurs, which in general companies with a big noise. A sudden appreciable load drop of about 100 N that is in response to the global delamination propagation (see Figure 3-9(i)) can be observed both in the strain gages attached onto the specimens and the instrument for measure. The eventual fracture of the specimen occurs either at the tab of the thickness end by sliding or fiber fractured.

Delamination onset load that is difficult to be captured by the appearance of crack is obtained in accordance of the first big sound induced in the test, and the value for this typical specimen (#5) is 8970 N. The ultimate load occurs due to the fracture failure at the tab of the thicker end of the laminate and its value is 33457 N.

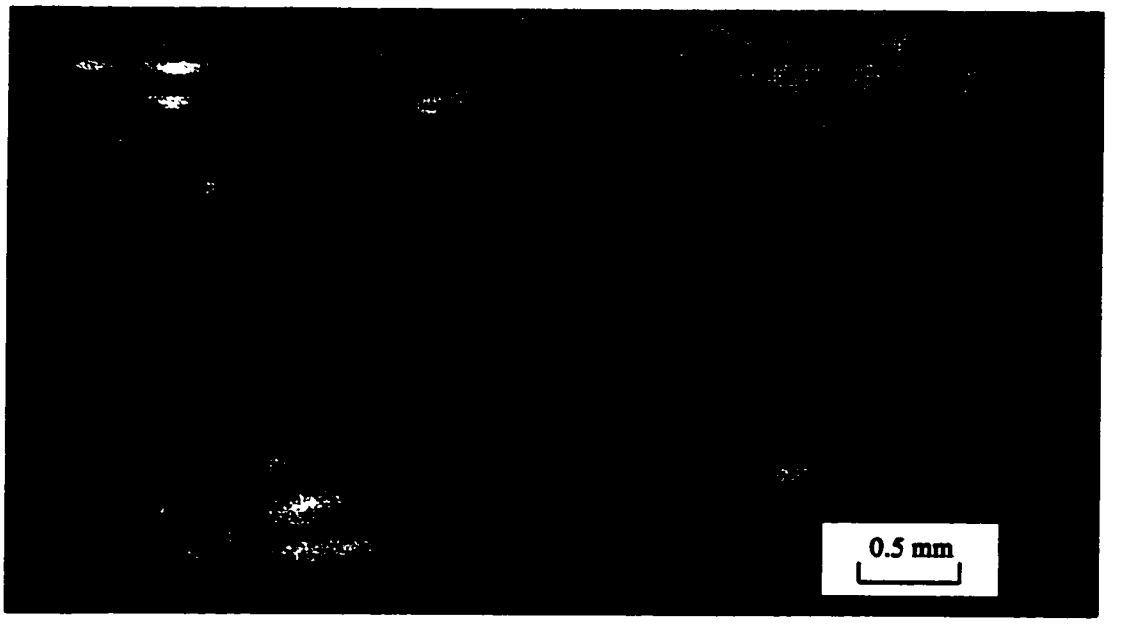

Figure 3-7 A typical resin-rich pocket before damage

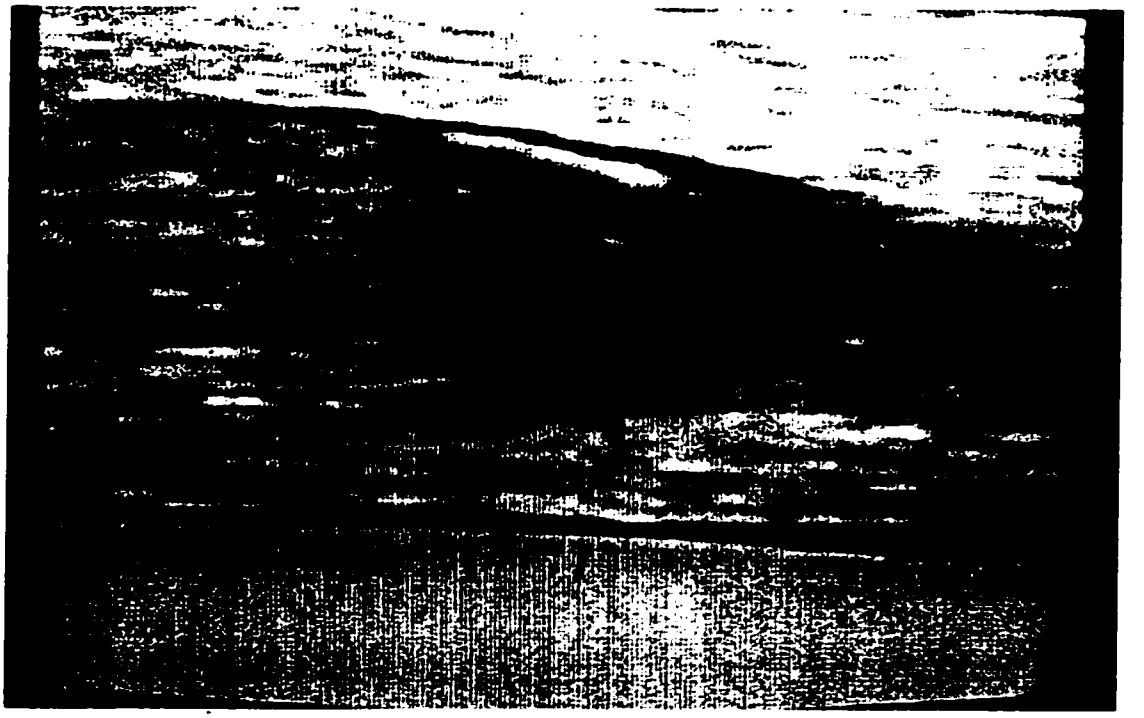

Figure 3-8 A typical crack configuration

Figure 3-9(a) Intact specimen (P = 0 N)

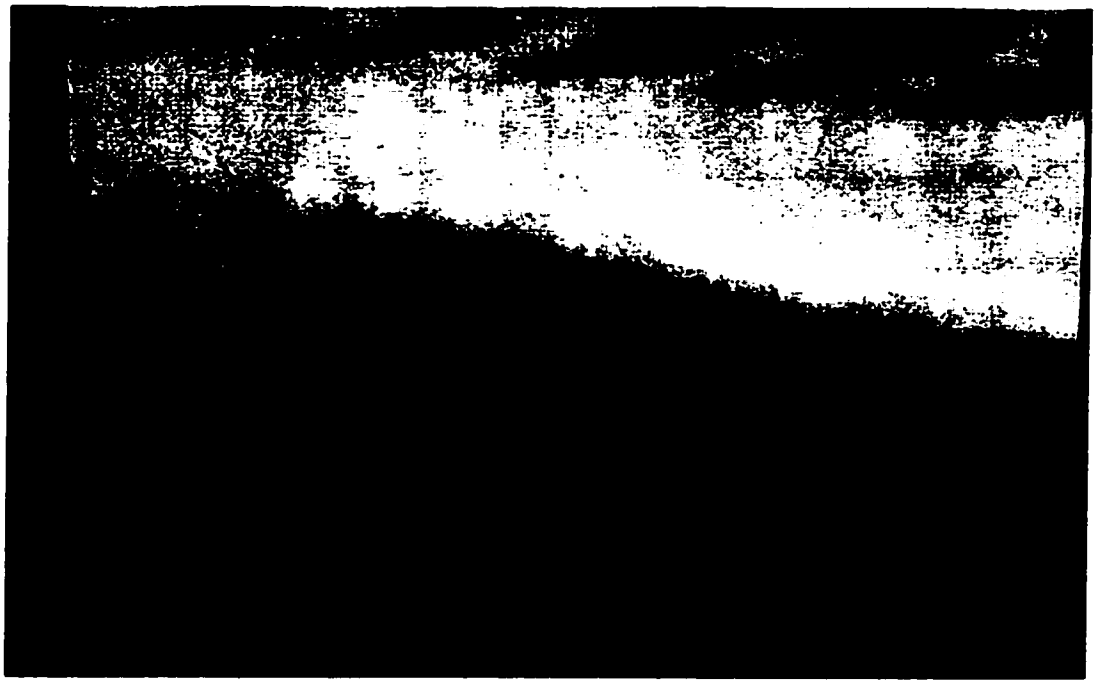

Figure 3-9 (b) Progressive delamination (P = 14630 N)

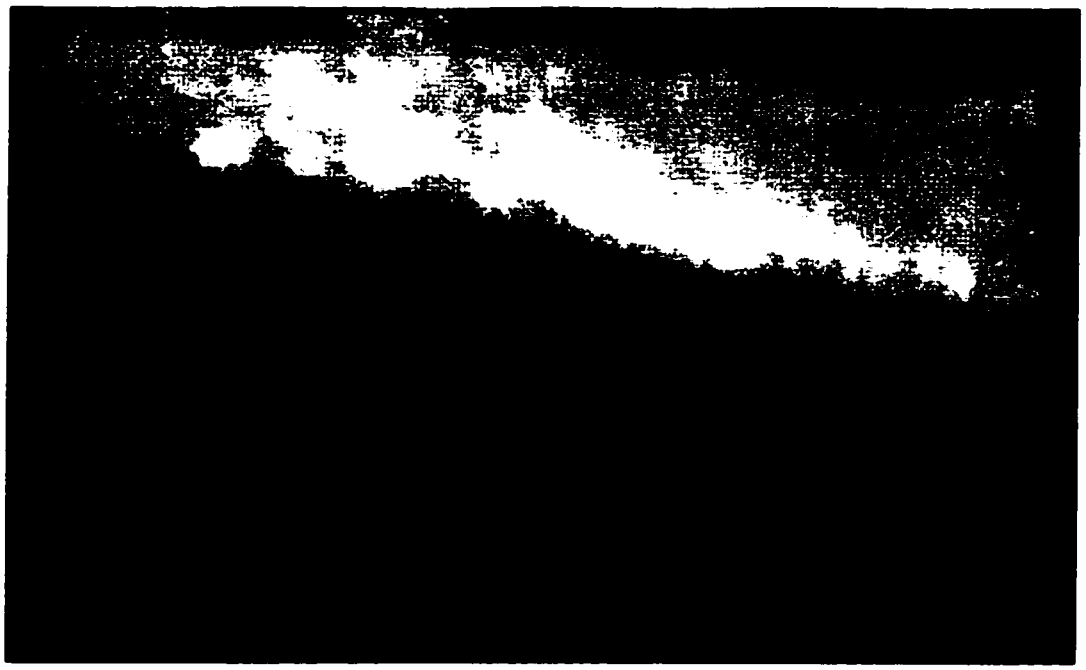

Figure 3-9 (c) Progressive delamination (P = 20670N)

Figure 3-9 (d) Progressive delamination (P = 26100N)

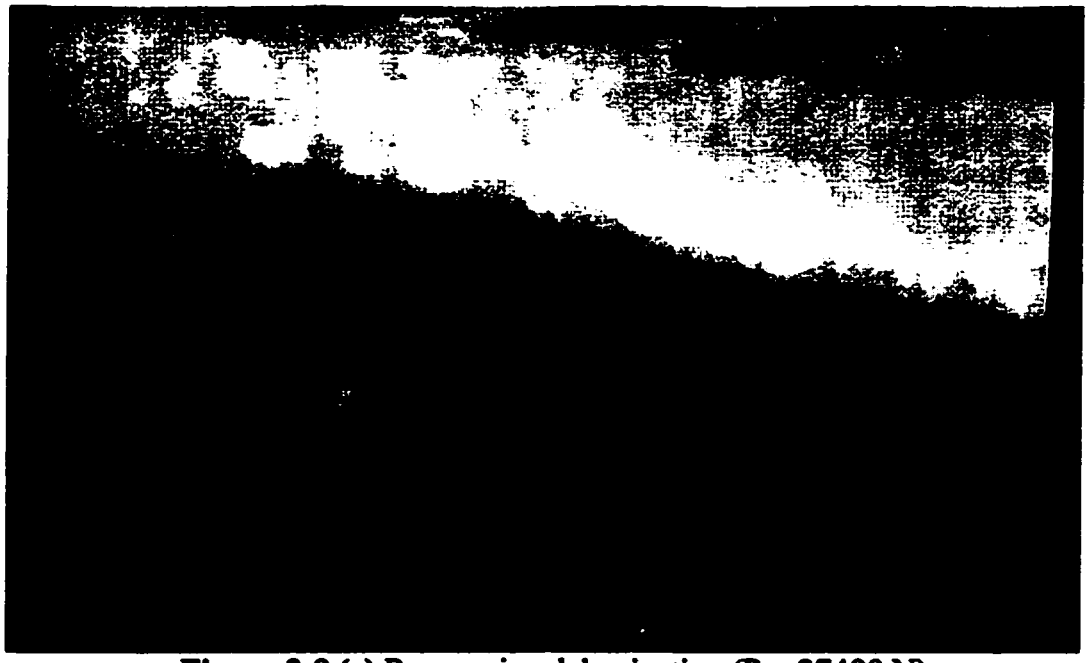

Figure 3-9 (e) Progressive delamination (P = 27400 N)

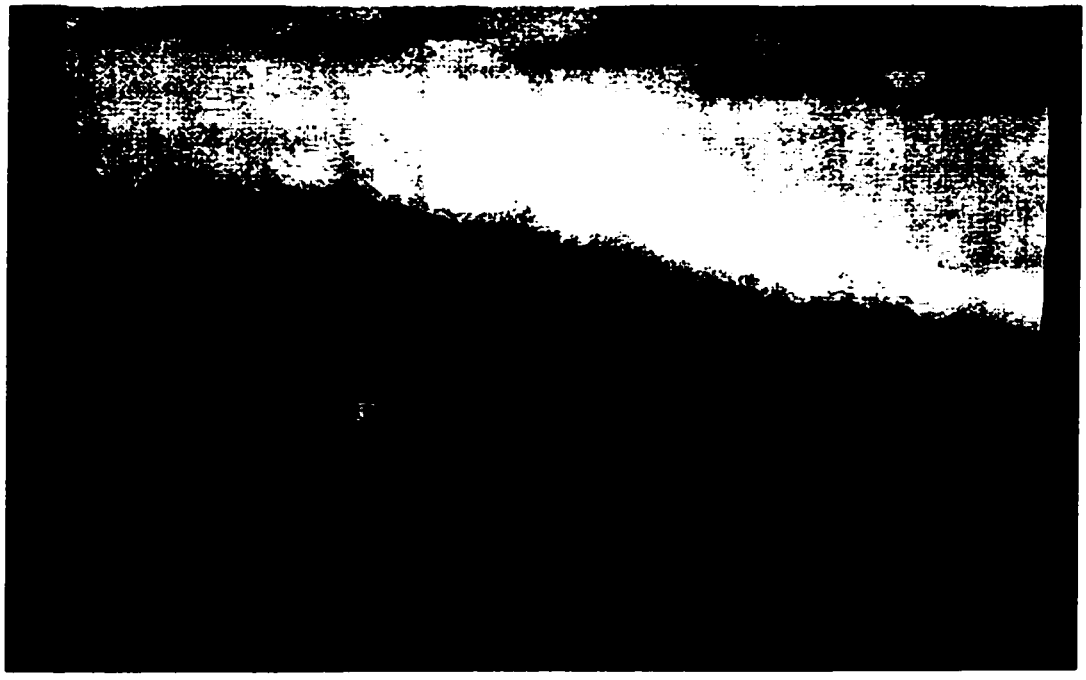

Figure 3-9 (f) Progressive delamination (P = 28190 N)

Figure 3-9 (g) Progressive delamination (P = 29600 N)

Figure 3-9 (h) Progressive delamination (P = 30850 N)

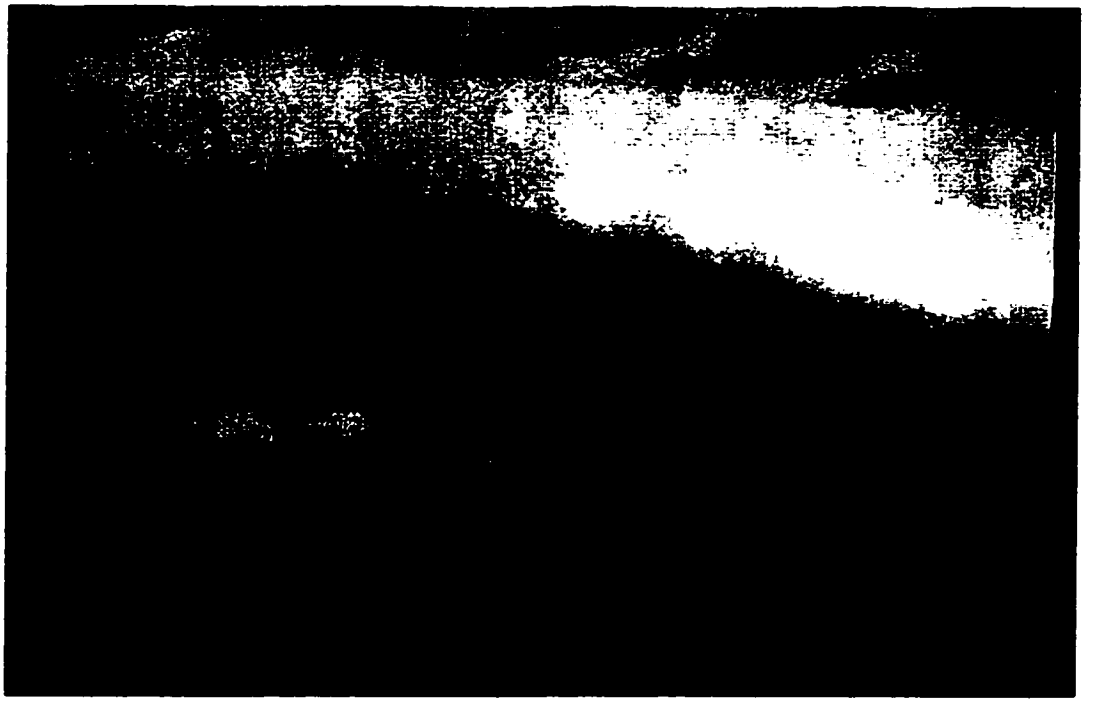

Figure 3-9 (i) Progressive delamination (P = 31340 N)

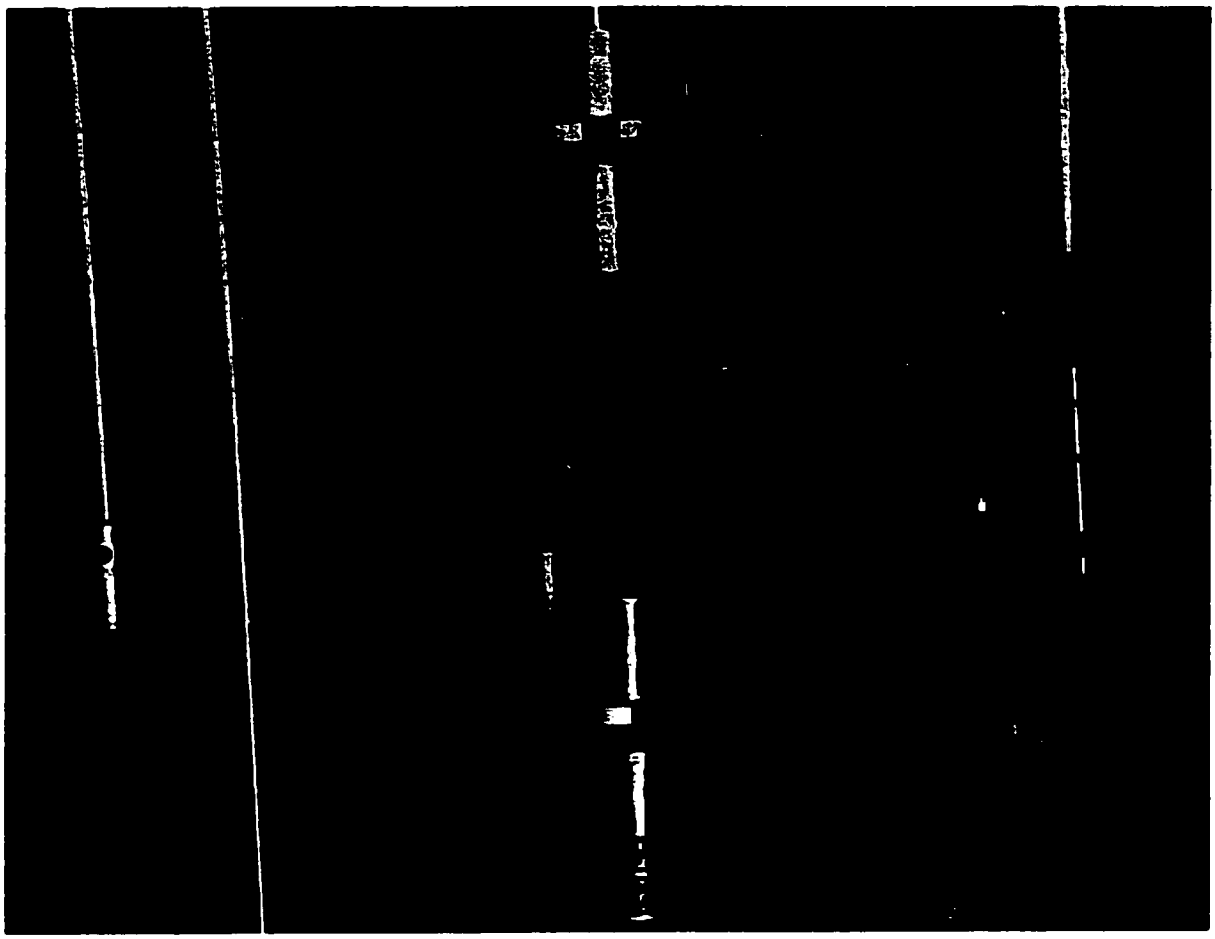

Figure 3-10 Testing of the specimens using MTS machine

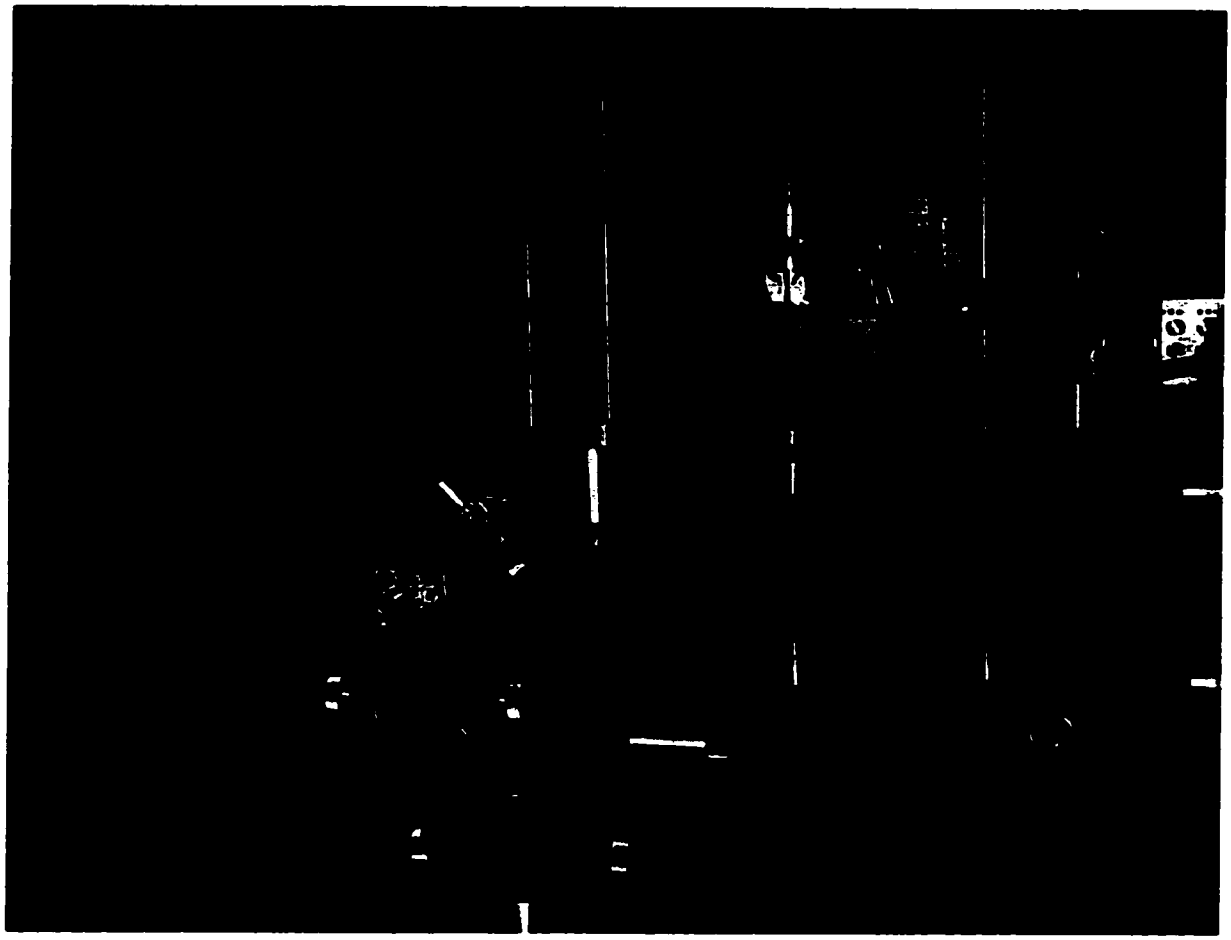

Figure 3-11 Visualizing the cracked state of specimen using the telescope apparatus

Figure 3-12 Monitoring of the crack propagation through telescope

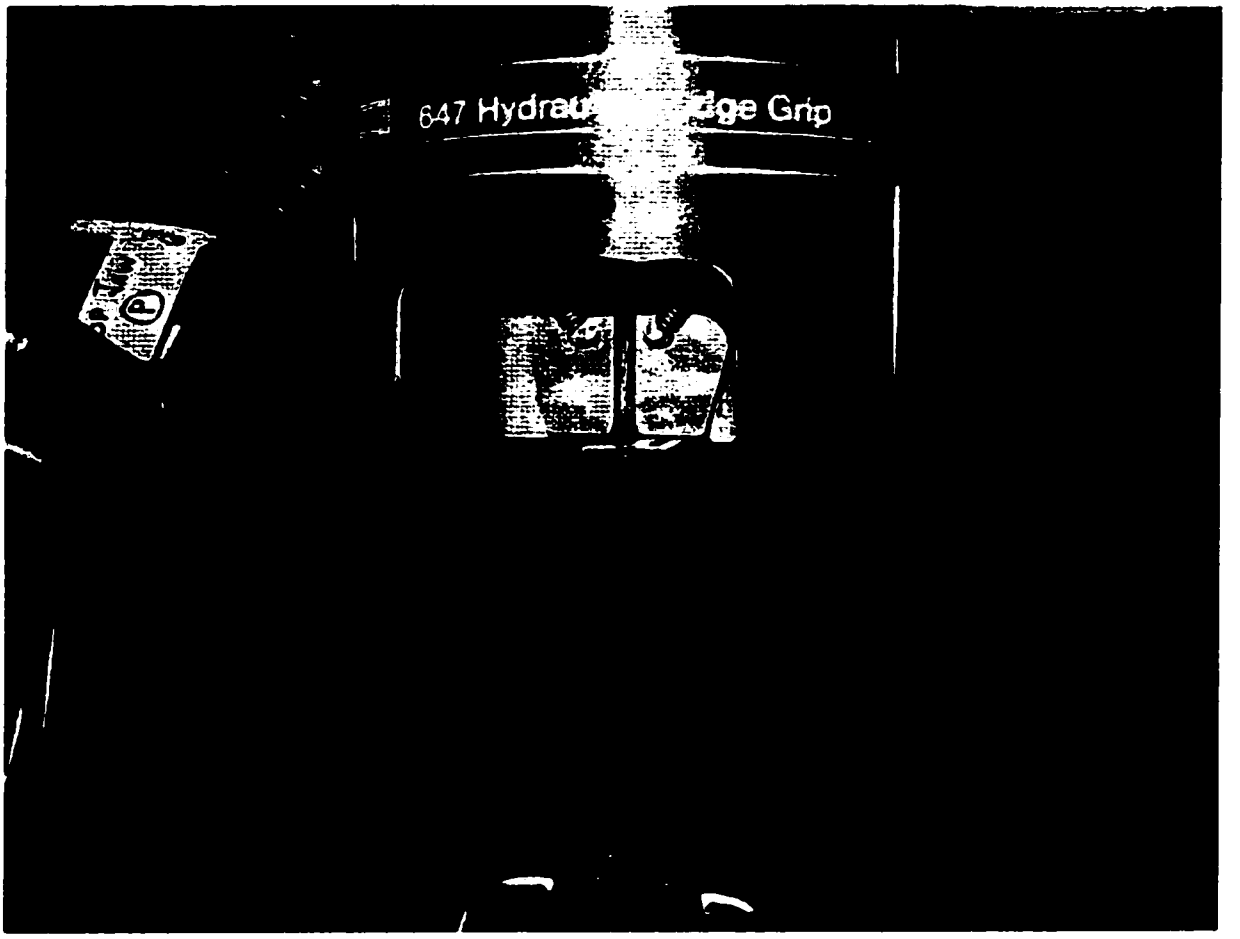

Figure 3-13 Delaminated failed specimen

Chapter 4

INTERLAMINAR DELAMINATION ANALYSIS

4.1 Introduction

Delamination of a laminated composite may be considered as interlaminar failure phenomena manifesting the out-of-plane separation of two adjacent plies within the laminate. If a composite laminate is examined through its thickness in a microscopic way, as illustrated in Figure 4-1, it is observed that the laminate constitutes two phases: the plies themselves and resin rich region, which are all macroscopically homogeneous. So delamination may be described as the out-of-plane failure of the interply resin layer within a laminate.

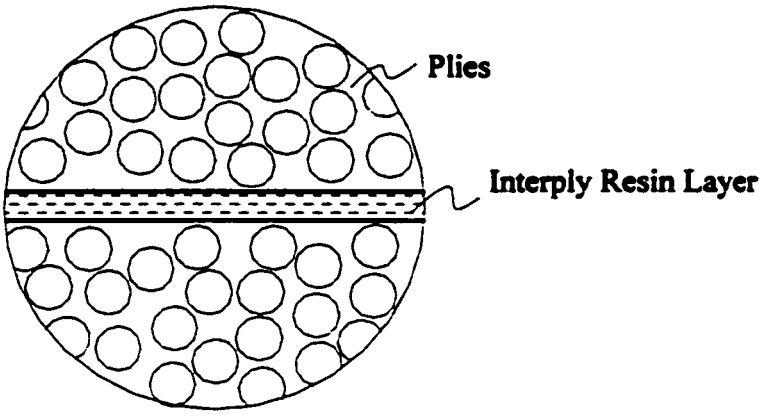

Figure 4-1 Interply resin layer

Delamination analysis of the tapered laminated composite usually involves two types of idealizations. An idealization of a composite laminate that is free from any defects within the structure is a classical and convenient approach in engineering practice and academic research, aiming at ascertaining a critical stress state and seeking a way to improve the structural performance. The methods often used in earlier works with this respect are described in detail in the review part of the thesis. The other more advanced approach, popularly adopted for characterizing fracture behavior in the tapered laminated composites, is fracture mechanics based methodology, in which it is assumed that a structure always possesses to some degree a defect, either resulting from manufacture, or from service. Fracture Mechanics is thus a key tool in dealing with this type of problem. Along this approach, one would not be much concerned with when and how an initial defect has been formed in the structures. It is the life span and period of service time a laminate containing defects can sustain that is of interest to researchers and engineers. This is in fact a damage tolerance concept that will be detailed later in this chapter.

It has been seen from the review that the so-called stress-based approach and the fracture mechanics approach were both extensively, but independently, employed in the early research on failure and delamination analysis of tapered composites. The stress-based approach proves to be advantageous in seeking the failure initiation (damage onset) location, while the fracture mechanics approach demonstrates well in being able to characterize the initiation and propagation of delamination. These two distinct methodologies respectively represent a way in resolving the problems like those mentioned before, but they were never concurrently applied to a particular tapered

laminated composite structure. Therefore it is a good idea that a combination of these two approaches at different phases of the overall structural analysis would be made. Computational efficiency and accuracy may result.

4.2 Delamination Onset

4.2.1 Finite element analysis

The laminate plate that is to be modeled and analyzed is the same as the one studied in the experimental program as described in Chapter 3. The basis for selecting this type of structure for experimental study and numerical analysis is to avoid complications such as complex laminates with multiple dropped plies and free-edge stresses which will present more difficulties in gaining insight into the failure mechanisms and controlling parameters.

The axis system used in the finite element model is depicted in Figure 4-3. The laminate was modeled with the quasi-three-dimensional 8-node quadrilateral and 6-node triangular partial hybrid elements presented in Chapter 2 to predict a stress state and the consequent strength of the laminate studied. Due to symmetry, only one quarter of the laminate is modeled. Fine meshes of 20 elements and 10 elements with a size of 0.5H (ply thickness H = 0.125mm) are used to model the ply drop region and taper root region in the longitudinal direction respectively.

A thin resin region is included in the model representing the interface between the ply drop and the top and bottom plies adjacent to them. The resin layer of about 1/10 the

thickness of a lamina always exists between layers. However the resin layer is added into the model here because of its importance in the fracture behavior of the sample. Also the thickness of this resin layer is modified later on to examine its effect. This resin layer therefore may not come from the normal lay up process but additional resin thickness can be added.

Each of the plies, 12 in the thick section and 6 in the thin section, and the resin layer are modeled with row of elements in the longitudinal direction and one element for each resin layer and ply in thickness direction. A section of the model at the ply drop is shown in Figure 4-3. The resin is assumed to be isotropic and the plies to be orthotropic. The material properties of NCT 301 used are listed in Table 4-1, which was provided by manufacturer Newport Adhesives and Composites, Inc. The total number of degrees of freedom in the model is 654.

To determine the stress state in the tapered specimen, the thick end of the specimen is held fixed in the longitudinal direction and a uniform uniaxial displacement is applied on the thin end. The corresponding reaction forces at the thin end can be used to determine the equivalent force or stress level on the specimen. The interlaminar stresses can be determined directly from the stress state in the interply resin layers.

4.2.2 Strength predictions

Stress-based criteria proved to be effective in the prediction of the onset of damage and consequent strength of the laminate. Many possible failure surfaces in stress space are available for the prediction of the delamination strength of composite laminate

structures. The simplest approximation of the failure surface is a maximum stress criterion, with which, failure is assumed to occur when any one of stress components exceeds its ultimate value. Due to its simplicity of concept and ease of use, the criterion appears quite attractive. The approximation may be acceptable for stress states which are dominated by only one stress. However, the exclusion of the remaining stresses may lead to unacceptable results in states of combined stress where the interaction of stress components is important.

Because the primary failure is assumed to be dominant in delamination and to occur in the interply resin layer, an isotropic failure criterion such as von Mises can be employed to predict the onset load. All six-stress components are used to determine the equivalent von Mises stress given by

$$\sigma_e = \sqrt{\sigma_x^2 + \sigma_y^2 + \sigma_z^2 - \sigma_y\sigma_z - \sigma_z\sigma_x - \sigma_x\sigma_y + 3(\tau_{yz}^2 + \tau_{zx}^2 + \tau_{xy}^2)} \qquad (4\text{-}1)$$

In this maximum distortion energy theory, failure by yielding occurs when, at any point in the body, the distortion energy per unit volume in a state of combined stresses becomes equal to that associated with yielding in a simple tension test. Note that unlike most delamination criteria, the von Mises stress considers equally both tensile and compressive values of the interlaminar normal stress. Moreover, in-plane stresses are included as well. Thus, the von Mises stress is a measure of the overall stress state for a given configuration. An increase in the von Mises stress would indicate a decrease in the damage onset load.

Taking into account the fact that delamination is an out-of-plane failure mode independent of the in-plane stress state, the in-plane stresses in von Mises criterion expressed in Eq. (4-1) do not dominate and can thus be excluded from the original von Mises, resulting in

$$\sigma_e' = \sqrt{\sigma_z^2 - \sigma_y\sigma_z - \sigma_z\sigma_x + 3(\tau_{yz}^2 + \tau_{zx}^2)} \tag{4-2}$$

which is a derivative of von Mises criterion and will be used for the prediction of the interlaminar failure.

4.2.3 Results and discussions

The interlaminar normal stress σ_{zz} and shear τ_{zx} of the critical resin layer going along the line ABCD (horizontal for sections AB and CD and inclined for section BC) as shown in Figure 4-2 are determined at the region close to the drop-off. The influence of the third interlaminar stress τ_{zy} on the stress state of the laminate is negligible in the analysis. The interlaminar stresses in the resin layer are averaged and plotted with respect to the longitudinal coordinate normalized by the thickness of the ply (X/H, H denotes the ply thickness), starting at the drop step (Point B as indicated in Figure 4-2) with positive direction towards thin section and negative towards thick section. The interlaminar normal stress shown in Figure 4-4 indicates peaks near the points of B and C, where geometric and material discontinuities occur. At the drop step of point B, the stress changes from a high compressive value immediately to the left of the drop-off to a high

tensile value immediately to the right of ply drop-off. Interlaminar shear stress along the taper line is plotted in Figure 4-5. High interlaminar shear is observed at Point B. Comparing these results, it is found that the higher positive normal and shear stress magnitudes occur at the drop step (Point B). These sudden changes in the normal and shear stress distributions at Point B and Point C (taper root) are not unexpected. Since there are geometric and material discontinuities, it was suggested that stress singularities might exist at the place of discontinuity. The results suggest that stress singularities exist at the ply drop locations, as demonstrated by the steep peaks at those locations.

The von Mises stress and the stress in the derivative form of von Mises were employed to predict the strength of the laminate and substantiate the conclusion drawn above. To determine whether the calculated stress state within a given resin element is critical or not, the von Mises stress and its derivative stress must be determined first. If the calculated stress is equal to the characteristic strength of the resin layer, failure is assumed to occur.

It has been found in the analysis that the location of critical site predicted using these two criteria appears at the point B (Refer to Figure 4-2), bottom of the resin layer. This correlates well the experimental observation. Also note that comparison of the predicted and experimental far-field stresses (at the thin end) on damage onset load, which is listed Table 4-2, shows a good consistence between them. It shows that the derivative form of von Mises criterion, which captures all interlaminar stress components that dominate the delamination at the critical interface, can be a potentially useful and simple one in prediction of delamination failure.

Table 4-1 Material Properties of NCT – 301 Graphite Fiber Reinforced Epoxy

NCT 301 epoxy unidirectional tape	
Elastic moduli	E_{11} = 114 GPa, E_{22} = 7.9 GPa
Shear moduli	G_{12} = 3.1 GPa, G_{23} = 2.8 GPa
Poisson's ratio	ν_{12} = 0.28
Tensile strengths	σ_{11} = 1621 MPa, σ_{22} = 48.2 MPa
In-plane shear strength	S = 33.3 MPa
Neat Resin	
Elastic modulus	E = 3.1 GPa
Shear modulus	G = 1.2 GPa
Poisson's ratio	ν = 0.38
Tensile strength	σ = 57.2 MPa

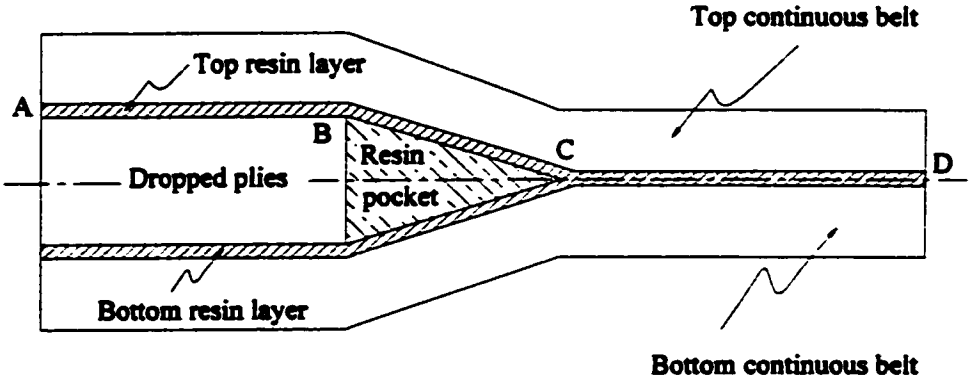

Figure 4-2 Intact tapered laminate with ply-drop at mid-plane

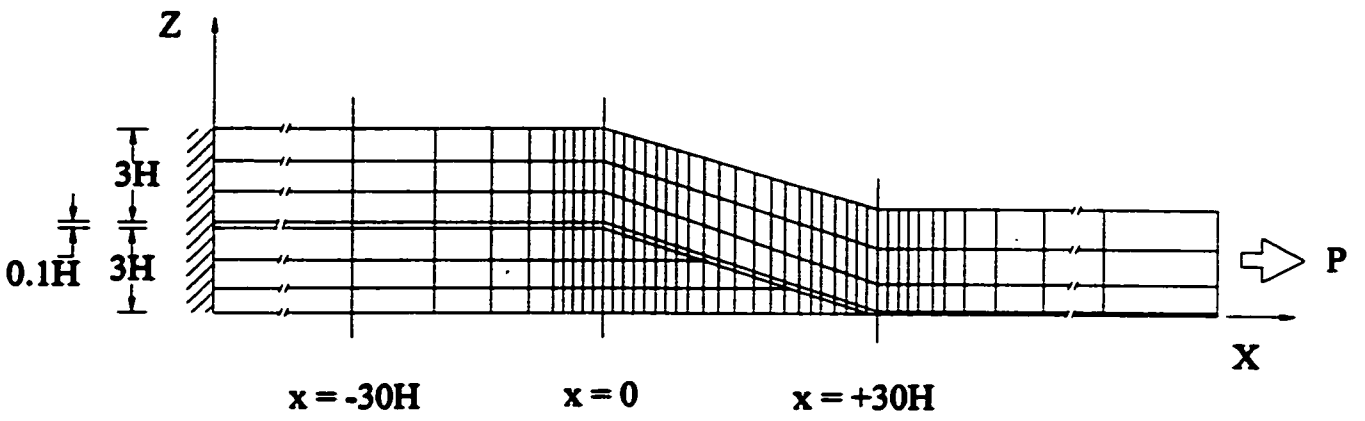

Figure 4-3 Finite element model for taper

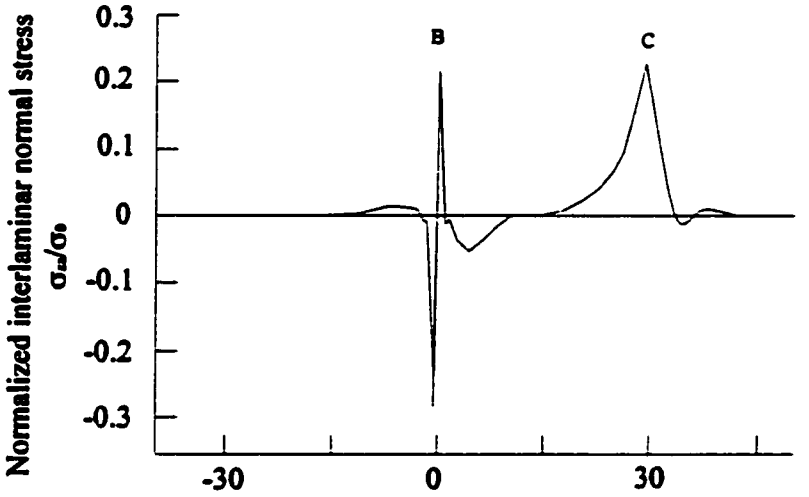

Figure 4-4 Normalized interlaminar normal stress distribution along taper line

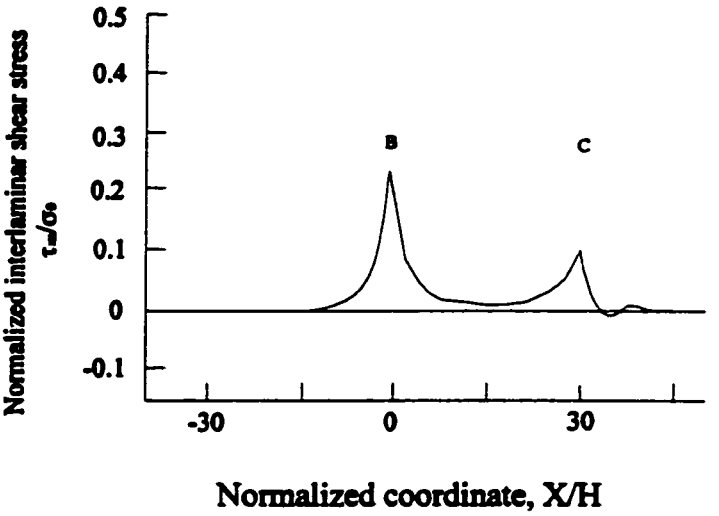

Figure 4-5 Normalized interlaminar shear stress distribution along taper line

Table 4-2 Predicted and Experimental Far-Field Stresses at Damage Onset

Predicted Stress, MPa (% error)	Max von Mises criteron	426 (14.2)
	von Mises derivative criterion	412 (10.5)
Experimental Stress, MPa		373

4.3 Damage Tolerance Behavior of Composites

The concept of damage tolerance in fiber-reinforced composites has been used primarily by the aerospace industry, and encompasses a design philosophy based on ensuring safety and integrity of a material/structural system. The basis of the damage tolerance methodology as it applies to composite systems is the assumption that the material system is not defect free and that structural design is modeled on the basis of the presence of an assumed damage level. Structural defects can arise through fabrication, processing, assembly and normal service. Some of the typical defects and damage modes encountered within the framework of these damage sources include fiber misalignment, improper cure, density variations, voids, inclusions, debonds, resin cracks, delaminations, and broken fibers.

To adequately assess structural damage tolerance, the designer must assume that initial defects exist in the structure, and that repeated service loading can cause the existing damage to propagate. The response of a component containing a defect is shown schematically in Figure 4-6 (See Ref. 72). In the fatigue environment, the effective damage size may increase, progressively reducing the residual stiffness and strength and therefore the lifetime of the components. Before laminated components can be utilized in major load bearing application, initiation and growth of damage must be studied.

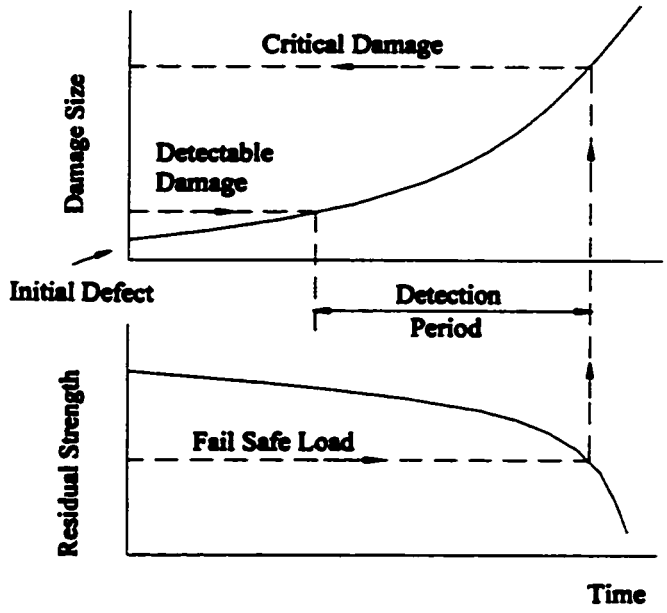

Figure 4-6 Schematic of the effect of a defect in structure

A comparison of the damage behavior of a metallic and a composite component containing a defect is shown schematically in Fig 4-6, which was given in Ref. 73. The primary mode of damage in a metal structure is self-similar cracking. Cracks propagate in a relatively well-defined manner with respect to the applied stress, and the critical crack size and rate of crack propagation can be related to specimen data through analytical fracture mechanics. The crack initiation occupies a large part of the fatigue life of a metal part. The composite damage propagation shown in Figure 4-7 is in a less regular manner and damage modes can change. It is also expected that composite materials will be more damage tolerant than metals.

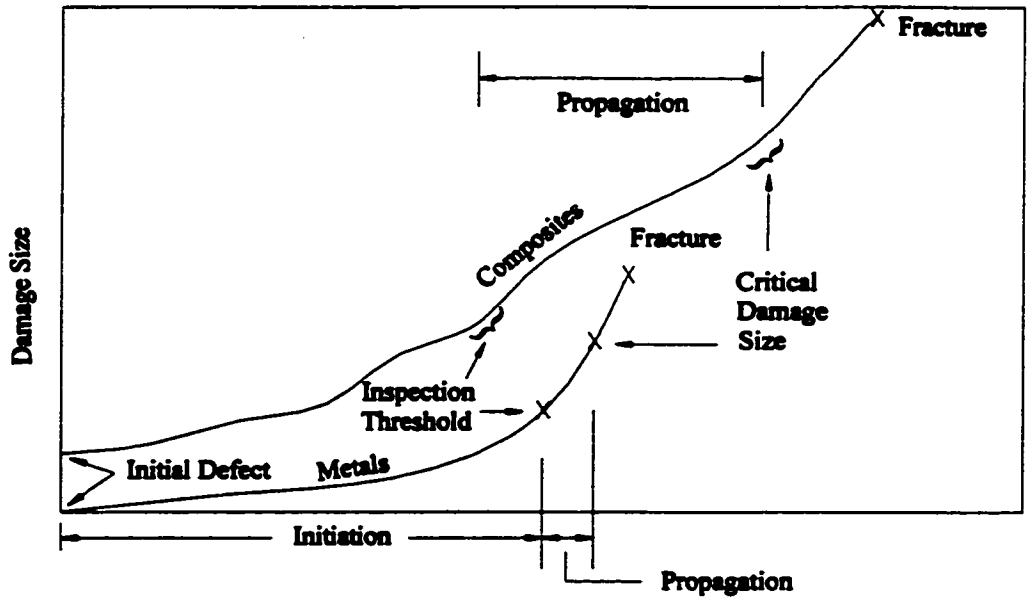

Figure 4-7 Damage development behavior of composites and metals

Damage tolerance is defined as the ability of a structure to resist failure in the presence of flaws, cracks, or other damage for a specified period of time. As shown in Figure 4-6, this technique involves determining a functional relationship between damage size and the length of time that the component has been in service. Similarly, the component residual strength must be evaluated and related to the damage size. Once these relationships have been developed, the damage tolerance approach utilizes a design load as input. This load level is generally associated with a defined degree of confidence in the component structural integrity. Through residual strength, this fail-safe load is associated with an elapsed time of service loading. In turn, the functional form describing defect accumulation relates this elapsed time to a critical in-service defect size. In effect, this procedure defines a limited service lifetime for the component.

The minimum detectable damage size is also of importance. As initial defects accumulate, the effective damage size will eventually reach a magnitude that can be detected by non-destructive evaluation techniques. The associated time in service can be viewed as the beginning of an inspection period (See Figure 4-7). The end of the inspection period is the time required for the damage to reach a critical size.

In summary, an acceptable structural component requires that damage be detected before it has developed to a dangerous size. Alternatively, damage must not reach a dangerous size within a specified lifetime. This involves periodic inspections of the component within the service life of the part. Therefore to achieve a damage tolerant structure, the components must be designed to resist damage growth. To date, this is accomplished through judicious choice of structural material. Obviously, a high residual strength and high resistance to fracture, during both static and fatigue loading, are desired. Design to minimize the magnitude of an existing stress concentrator is another valid approach.

To this point the discussion of damage tolerance has considered general damage in a load-bearing component. For laminated fiber reinforced composite structures it has been observed that delamination is a common type of defect. The susceptibility of laminated composites to delamination has been illustrated in many works. The occurrence of interlaminar stresses, combined with the inherent minimum toughness of the material, results in the minimum tolerance of the materials to existing damage. Therefore delamination is the most likely growth related failure to limit the life of a laminated composite structure.

To study the resistance of a laminated composite structure to delamination, we assume that the component of interest contains an initial debonding. The general loading of the component results in a very complicated stress state in the region of the damage. To simplify the analysis of this phenomenon, the actual loading situation can be viewed as a superposition of three pure mode loads as shown in Figure 4-8. Mode I, also known as the opening mode, results when the surface of the crack or delamination is displaced normal to the defect plane. Mode II or forward shear is characterized by delamination surface displacements in the plane of the delamination and normal to the delamination front. Finally, when the delamination surfaces are displaced in the plane of the delamination and parallel to the delamination front, the fracture process is termed as Mode III or the tearing mode.

In reality, practical structures experience combined tension, shear and torsional loading and existing defects are therefore exposed to mixed-mode fracture. In order to characterize the damage tolerance of a practical structure a mixed-mode failure criterion is required. It should be pointed out that the validity of any mixed-mode fracture criterion depends on accurate pure mode fracture toughness measurements. Producing accurate and reproducible pure mode static-fracture toughness data is a major contribution towards characterizing the damage tolerance of fiber reinforced material systems. Relating the damage size within the structure to its residual strength is also an important step in the damage tolerance approach, toward characterizing the performance of composite structures.

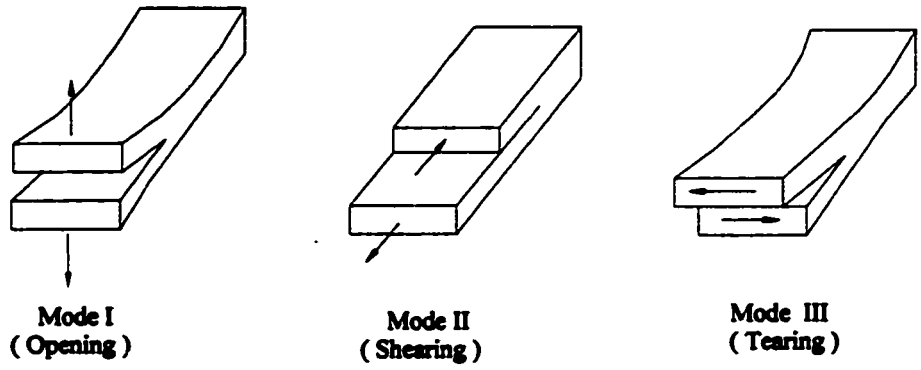

Figure 4-8 Three modes of crack extension

4.4 Strain Energy Release Rate

The strain energy release rate G is the crack-extension force characterizing delamination initiation and propagation. It is defined as the energy required to grow a crack by a unit length. A measure of the energy release rate thus provides information on the tendency of a delamination to grow. Computed as a function of the advance of the crack front, it can also be used to determine the stability of delamination growth under constant loading conditions.

In this section, the various approaches to the determination of the energy release rates are briefly reviewed. These are, respectively,

- Method of direct calculation, which is based on the determination of the potential energy using prescribed stresses and end displacements;
- The J integral;

- Evaluation of modal contributions G_I and G_{II} using crack tip stresses.

The direct method is displacement based, and is one of the popular methods used to calculate the total strain energy release rate. According to this method, delamination will occur in a laminate when the total strain energy release rate at the critical interface exceeds the total critical strain energy release rate.

Most numerically based research to date has relied on either the use of the crack closure method or the evaluation of the path independent J-integral. In both of these methods, only one analysis may be necessary to approximate the strain energy release rate. Another method to determine the total strain energy release rate is the direct calculation of the rate as the change in potential energy for two crack lengths. This method requires two analyses.

The crack closure method[136] may be used to compute the values of G_I and G_{II}, and the total strain energy release rate is obtained by additions of these terms. For instance, for an isotropic material in plane strain, Irwin's closure integral may be used to establish a relationship between the total strain energy release rate and the stress intensity factors, in the context of linear elastic fracture mechanics (LEFM), as

$$G = \frac{(1-\nu)}{E} K_I^2 + \frac{(1-\nu^2)}{E} K_{II}^2 \tag{4-3}$$

and the total energy release rates as

$$G = G_I + G_{II} \tag{4-4}$$

Also, from Sun[68] the energy release rates for a crack lying along the interface of two dissimilar elastic media, neglecting the oscillatory stress term, (again in the context of LEFM), are given as

$$G_I = G_{II} = \frac{1}{2}G \tag{4-5}$$

4.4.1 Direct method

The direct calculation of the total strain energy release rate is an effective way in obtaining the global energy change of the laminate due to delamination growth. The strain energy of the laminate, U, can be conveniently computed as $U = \frac{1}{2}\sum f_i u_i$, where f_i and u_i are the nodal forces and corresponding nodal displacements, respectively, for all nodes i on the loaded end. The strain energy release rate for successive delamination growth can be calculated as

$$G = \frac{dW - dU}{dA} \tag{4-6}$$

where dW/dA and dU/dA are the rate of change of work and strain energy, respectively, with change in delamination area. In the finite element analysis, the above equation can be computed as

$$G = (U_{a+da} - U_a)/da \tag{4-7}$$

where U_{a+da} and U_a are respectively the strain energies for delamination lengths $a+da$ and da corresponding to a same external loading condition. The value of G thus calculated is considered to be the strain energy release rate at $(a+da/2)$, which is located at the center of the interval.

4.4.2 Modified crack closure method

Irwin postulated that the energy release rate associated with a crack extension of Δa was equal to the amount of energy required to close the crack by an amount Δa. This concept leads a way to calculate the strain energy release rate. Referring to Figure 4-9, let $\Delta\vec{u}$ be a vector representing the relative normal and sliding displacements between the crack faces.

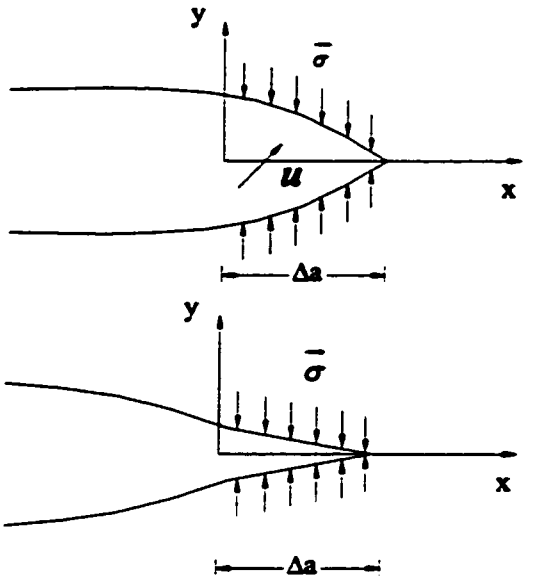

Figure 4-9 Schematic of crack closure

Let $\vec{\sigma}$ be a vector defining the normal and shear force components per unit area which are required to close the crack. Then the crack closure integral can be expressed as

$$G_T = G_I + G_{II} + G_{III} = \lim_{\Delta a \to 0} \frac{1}{2\Delta a} \int_0^{\Delta a} \vec{\sigma} \cdot \Delta \vec{u} da \tag{4-8}$$

where

$$G_I = \lim_{\Delta a \to 0} \frac{1}{2\Delta a} \int_0^{\Delta a} \sigma_I \Delta u_I da$$

$$G_{II} = \lim_{\Delta a \to 0} \frac{1}{2\Delta a} \int_0^{\Delta a} \sigma_{II} \Delta u_{II} da \tag{4-9}$$

$$G_{III} = \lim_{\Delta a \to 0} \frac{1}{2\Delta a} \int_0^{\Delta a} \sigma_{II} \Delta u_{III} da$$

The subscripts I, II and III denote stress and displacement components corresponding to pure Mode I, Mode II, and Mode III strain energy release rates, respectively.

Two general methods have been used to obtain the required forces and displacements. The strain energy release rates for delamination growth may be calculated using two separate finite element models, in which the delamination lengths differ by a small amount. This procedure is cumbersome because two separate problems need to be solved. An alternate method, based on a crack-closure method, uses the forces ahead of the crack tip and the displacements behind the crack tip to solve for the strain energy release rates. Although the forces ahead of the crack tip are only approximations of the closure forces, the method has been favored over the use of two separate models.

For finite element models, the strain energy release rate components in Mode I and Mode II, based on the local forces ahead of, and the relative displacements behind, the delamination tip can be calculated using the following equations:

$$G_I = -\frac{1}{2\Delta}[F_{ni}(v_k - v_{k'}) + F_{nj}(v_m - v_{m'})]$$
$$G_{II} = -\frac{1}{2\Delta}[F_{ti}(u_k - u_{k'}) + F_{tj}(u_m - u_{m'})] \quad (4\text{-}10)$$

where Δ is the element size, F_{ni} and F_{ti} are the normal (n) and tangential (t), forces respectively, at node i, and $(v_k - v_{k'})$ and $(u_k - u_{k'})$ are the relative opening and sliding displacements, respectively, at node k (see Figure 4-10), force at node j and relative displacements at nodes m and m' are defined similarly.

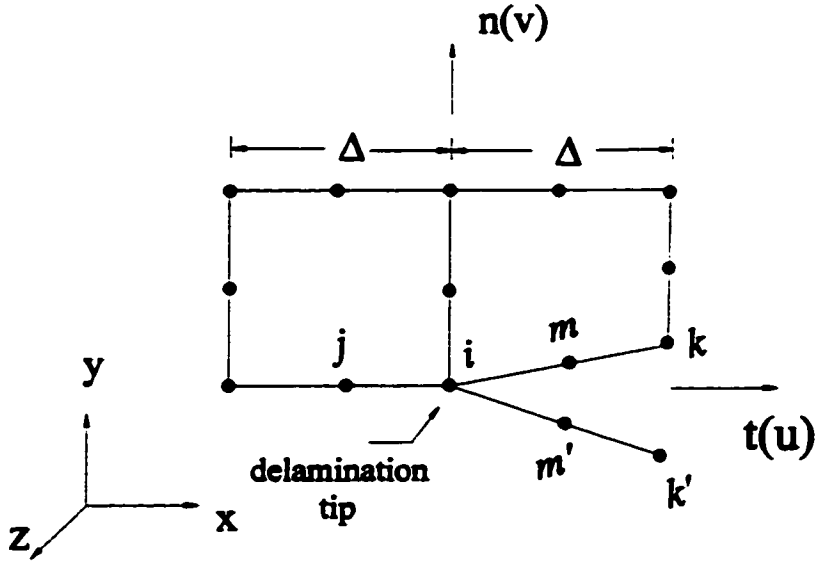

Figure 4-10Finite element idealization near the delamination tip for calculating G

4.4.3 J-integral

In the context of fracture behavior analysis for composite materials, the path-independence of J is an important property. Thus, once we calculate the value of J around any admissible path Γ, its value can be used to estimate the crack tip stress and strain fields. The fact the J can be estimated from stress and displacement quantities far away from the crack tip is very important in numerical analysis for determining J because numerical solutions are often not accurate in the immediate vicinity of the crack tip but increase in accuracy as one moves away from the crack tip. The path-independence of J implies that J can also be measured at points remote from the crack tip and therefore computing efforts are significantly reduced. These are the major initiatives in exploring the current method in calculation of fracture parameter of strain energy release rate in this research work.

Rice[70] defined the J-integral for a cracked body in two-dimensional problems as

$$J = \int_{\Gamma} (W n_1 - T_i \cdot \frac{\partial u_i}{\partial x_1}) ds \qquad (4\text{-}11)$$

where Γ is a counter clockwise contour as shown in Figure 4-11 which begins at a point on the lower crack surface and ends on any point on the upper crack surface, W is elastic strain energy density given by

$$W = \int_0^{\varepsilon_{ij}} \sigma_{ij} d\varepsilon_{ij}$$
$$\sigma_{ij} = \frac{\partial W}{\partial \varepsilon_{ij}} \tag{4-12}$$

and T is traction vector defined according to the outward normal n to the contour $T_i = \sigma_{ij} n_j$, and u is the displacement vector $u = u_1 i + u_2 j$

$$J = \int_\Gamma (W dy - T_i \cdot \frac{\partial u_i}{\partial x_1}) ds \quad \text{(in the x, y coordinate system)} \tag{4-13}$$

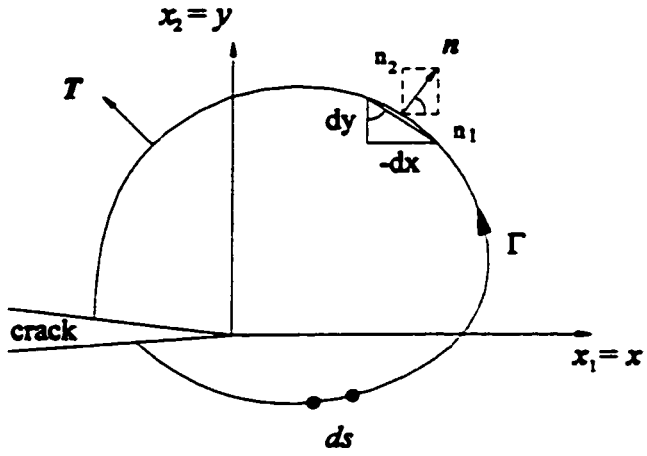

Figure 4-11 Crack body with a contour Γ

J-integral can be shown as follows to relate to the rate of change of potential energy with respect to change in crack size, for a body of thickness B

$$J = -\frac{1}{B}\frac{dU}{da} \tag{4-14}$$

Thus, the path-independent J-integral can be interpreted as being directly related to the rate of release of potential energy with respect to crack length. For linear elastic bodies, value of J-integral is equivalent to strain energy release rate G (also called the Griffith's crack extension force).

J-integral mode separation (J_I, J_{II})

As indicated in the above, evaluation of J-integral is more efficient than some other methods such as the stress based approach in determination of total strain energy release rate. J-integral, however, could not be separated for pure fracture modes. In the following, a so-called restrained J-integral mode separation[75] is introduced.

Isolation of fracture mode with the restrained J-integral involves several steps. Supposing that only Mode I and Mode II are considered. Isolation of Mode I strain energy release rate can be realized first by directly suppressing the Mode II contribution. This is done by prescribing $\Delta u = 0$ over the area of crack extension (see Figure 4-12). Similarly, isolation of Mode II can be realized by suppressing the Mode I contribution by prescribing $\Delta v = 0$ over the area of crack extension (see Figure 4-13). The resulting solution offers an alternative approach to mode separation.

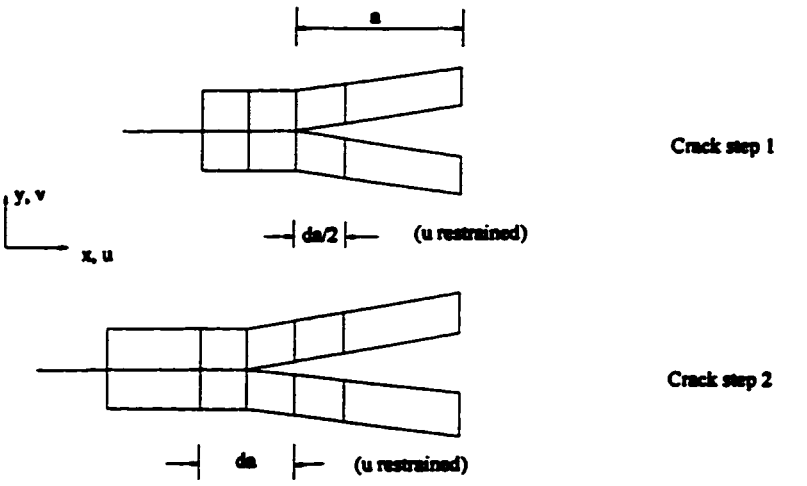

Figure 4-12 Isolation of Mode I energy release rate mode

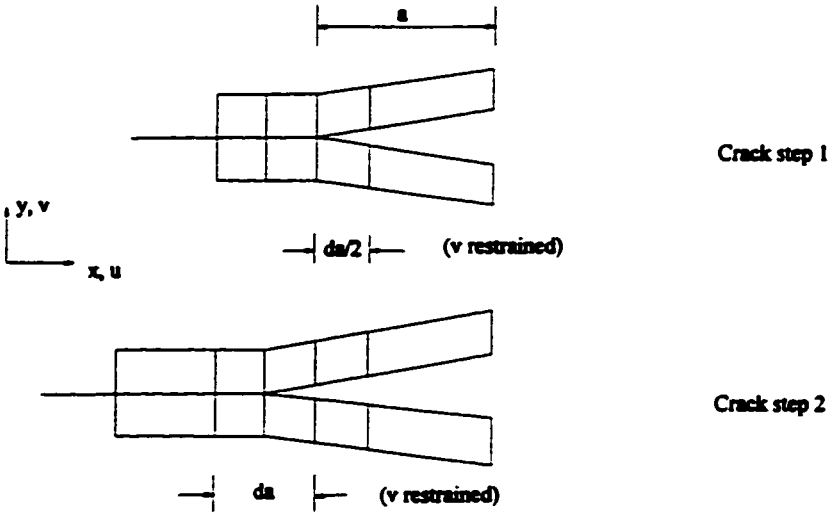

Figure 4-13 Isolation of Mode II energy release rate mode

For this analysis, the change in u (or v) over the crack extension was suppressed, for both crack step 1 and step 2, as shown in Figure 4-12 and 4-13. Under the restraints

of the two models, mode J_I (J_{II}) for the strain energy release rate can be computed with general J-integral approach.

It is of note that the path-independent property of the J-integral is, in general, not valid in heterogeneous media. When a path of integration crosses an interface, the path-independence is not always guaranteed. For instance, for a crack that is perpendicular to and terminating at the interface of a bi-material system, the J-integral is path-dependent and its physical meaning lost [154]. Thus, the use of the J-integral in heterogeneous media must be invoked with caution. In the present thesis a crack is assumed to propagate parallel to an interface of laminated composite and path independence is valid.

4.5 Numerical Calculation of Strain Energy Release Rates

4.5.1 Model description

The direct calculation (also called global method) and J-integral approaches combined with the quasi three dimensional partial hybrid elements developed in Chapter 2 were employed to compute strain energy release rates associated with the delamination at critical interfaces of tapered composite laminates. After calculation of the stresses and displacements based on the newly developed elements (quasi-three dimensional 6-node triangular and 8-node quadrilateral partial hybrid stress finite elements), the Gaussian integration quadrature is employed as the numerical integration scheme for line integrals appearing in the J-integral module. To perform this type of integration stresses, strains, and displacements must be obtained at each gauss point. It should be noted that

displacements are given at nodal points, while stresses and strains are given at gauss points. Therefore, for stresses and strains appearing in Eq. (4-11) and Eq. (4-15) the finite element results at gauss points are directly used. However, displacements at the gauss points must be calculated using the interpolation functions.

Rice's J-integral is extendable to quasi- and full-three dimensional problems. The J-integral for Q3D is of the form

$$J = \int_{\Gamma} (W n_1 - T_i \cdot \frac{\partial u_i}{\partial x_1}) ds \tag{4-15}$$

which has the same form as Eq. (4-11) for two dimensional crack materials, but with i = 1, 2, 3, rather than 1, 2. It should be pointed out that this J-integral involves the integration of 3D displacements, and stresses and strains, i.e., all three components of displacement and, further the six components of stress and strain are involved. However, only two-dimensional quantities are involved in the original J integral proposed by Rice[70]. The conservation property of the J-integral in the homogeneous and layered non-homogenous quasi three-dimensional problems is provided in Ref. [69].

A thickness tapered laminate with a matrix tension crack at drop-off location as shown in Figure 4-14 is considered for modeling and evaluating strain energy release rates associated with two crack configurations assumed in the laminate. Interply layers (resin layer or interleaf) are included in the models so as to directly predict the interlaminar response as well as to closely approximate the true stress state of the laminate. Due to symmetry, only half of the laminate is modeled. An interply layer configuration (α-crack), shown in Figure 4-15, in which the crack lies along a finite

thickness isotropic resin or adhesive layer between continuous composite plies or between continuous and dropped plies, is considered. The crack is assumed to be at the center of the resin or adhesive layer. The second crack configuration is interfacial (β-crack) in which the crack is assumed to lie along the interface between the resin or adhesive layers and drop plies, starting from the drop-off step into the thick section of the laminate.

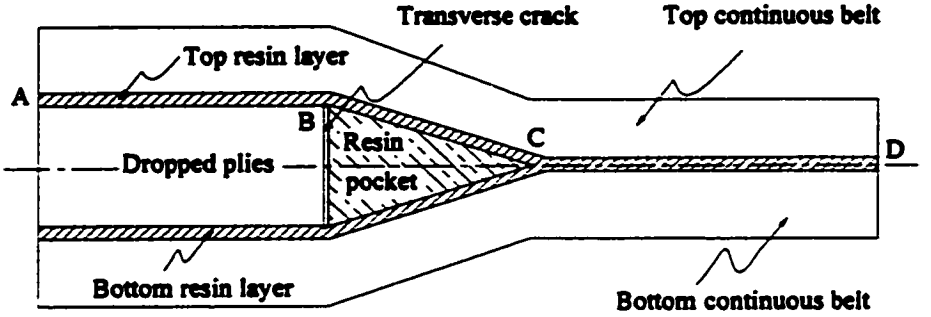

Figure 4-14 Tapered laminate with transverse matrix crack assumed at ply drop-off location

In practice, cracks propagate into thin and taper sections simultaneously, either in a stable manner or in an unstable manner, after their initiation. Therefore the crack configurations selected have to account for the influence of the double embedded cracks, with one at the thin section approaching towards the right hand side end of the laminate and the other at thick section to the left hand side end, on the structural performance of the tapered composites. The interfaces above and below the resin pocket element between Points B and C remained intact in the delaminated models. In α_1 - α_2 configuration as shown in Figure 4-15, both the cracks are embedded in the interply layers, one in the thin

section of the laminate and the other in the thick section. Taking into account the assumption that the α_1 crack is at the mid-plane of the laminate, loading condition and configuration of the lamination, it is assumed that there exists only mode I in this crack. However, at the position where α_2 is located both Modes I and II are present. In α_1-β configurations, an interfacial crack β is assumed to be located at the thick section. Both the J-integral method and direct calculation method outlined in Section 4.4 are used to obtain the strain energy release rate associated with α_1 crack since the general J-integral value is exactly equivalent to the entire energy release rate ($J = G = G_I$). It was shown that the J-integral that avoids the requirement for the accurate description of stress state at the critical region as does the stress based method, is more effective for the determination of single mode fracture parameter (mode I for tearing or mode II for shearing). Meanwhile, in the restrained J-integral (Jr) method, in which one of the displacements is suppressed, separation of pure modes can be realized. Analysis of α_2 and β cracks requires the direct calculation and Jr methods. Finite element mesh and J-integral paths for the three cracks are shown in Figure 4-16. Fine meshes that have 20 elements with a size of half of ply thickness 0.5H are used to model the vicinity close to the crack tip. The ply thickness is assumed to be 0.125 mm. The thickness of the baseline resin layers is one-tenth of the thickness of the ply. Each of the 12 plies in the thick section and 6 plies in the thin section, and the resin layer are modeled with a row of elements in the longitudinal direction and one element in normal directions. The resin is assumed to be isotropic and the plies to be orthotropic. The material properties used are listed in Table 4-1 of Section 4.2. The total number of degrees of freedom in this basic laminate is 1238. To model the failed resin pocket, the stiffness of three elements at the resin pocket

adjacent to the ply drop-off is set to zero, and stresses around the failed interface are determined.

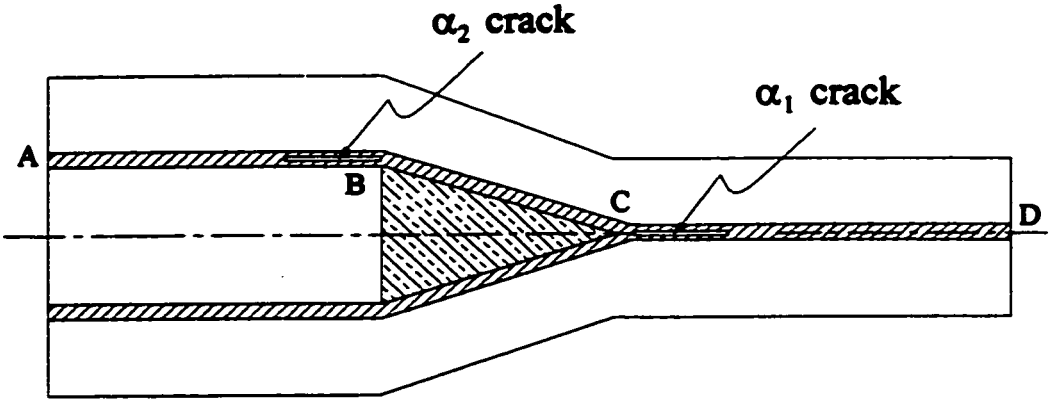

(a) $\alpha_1 - \alpha_2$ crack

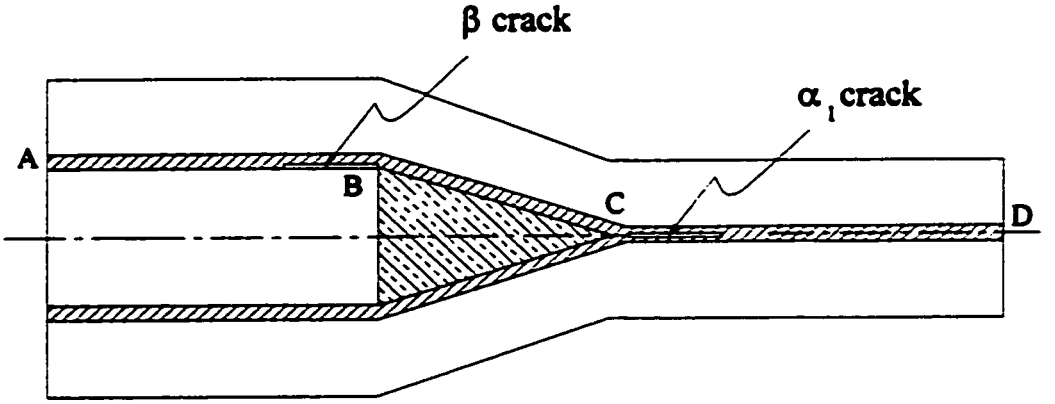

(a) $\alpha_1 - \beta$ crack

Figure 4-15 Crack configurations considered in the analysis

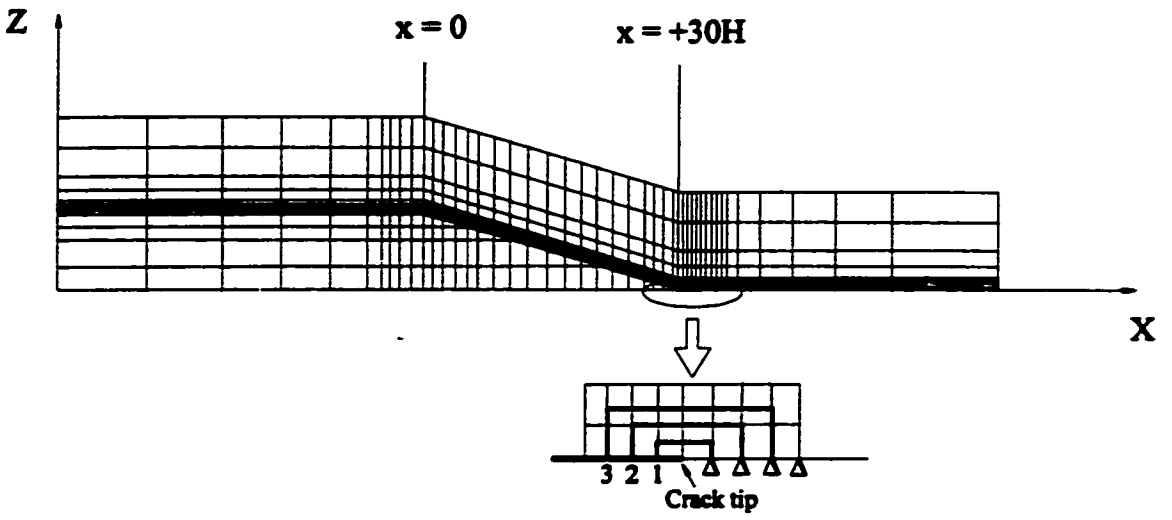

(a)

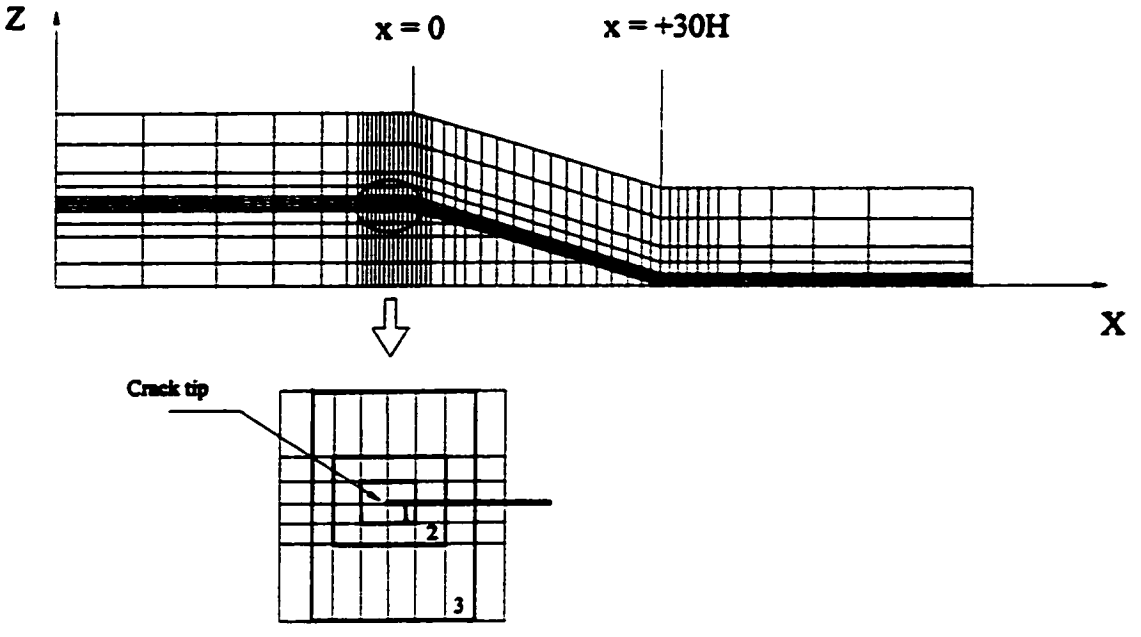

(b)

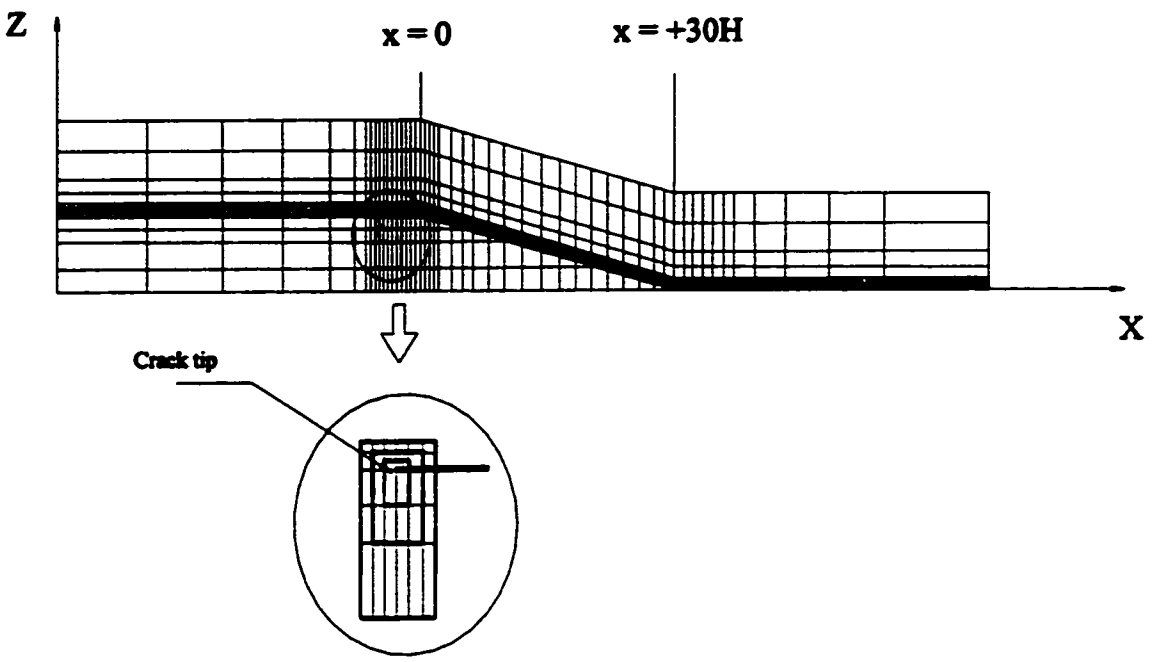

(c)

Figure 4-16 Paths for contour J-integral in the laminate with: (a) α_1 crack, (b) α_2 crack and (c) β crack

4.5.2 Results and discussion

Stress distribution around the crack tip

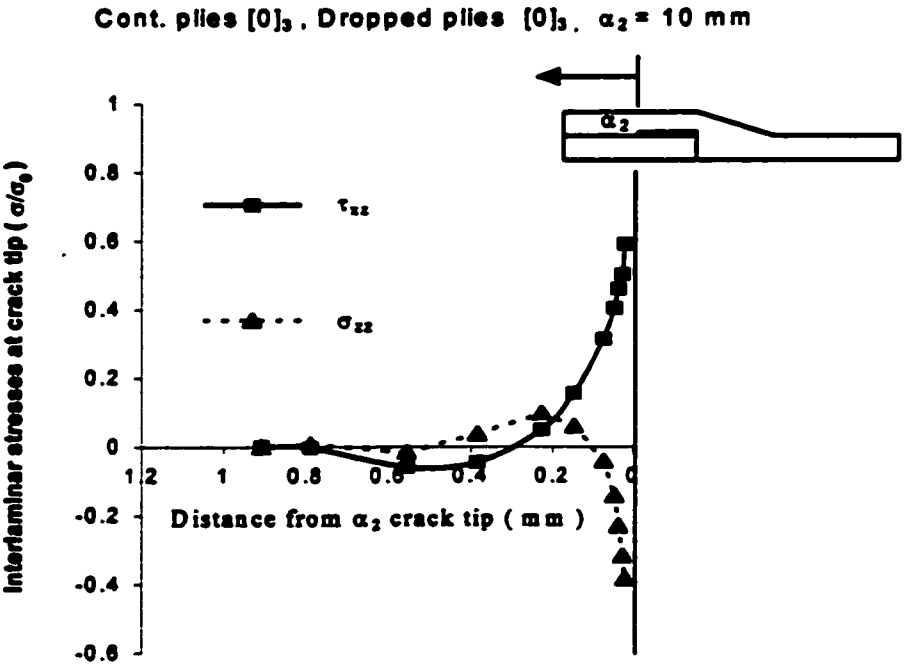

Figure 4-17 Stress distribution ahead of α_2 crack tip

Figure 4-17 illustrates the interlaminar stress distributions ahead of α_2 crack. Very near the delamination tip (α_2 =10 mm), interlaminar shear and normal stresses show steep gradients. The normal stress shows a sign reversal at about 0.1 mm from the crack tip and assumes values close to zero at about 1.2 mm away from the crack tip. Similarly, interlaminar shear stress diminishes to near zero values at a nearly same distance from the crack tip.

As discussed in the introductory section, the β crack is inherently in the mixed mode. Figure 4-18 shows the distributions of normal and shear stresses ahead of β crack with assumed crack length of 10 mm starting at the ply-drop step. The shear stress is more localized near the crack tip than the normal stress.

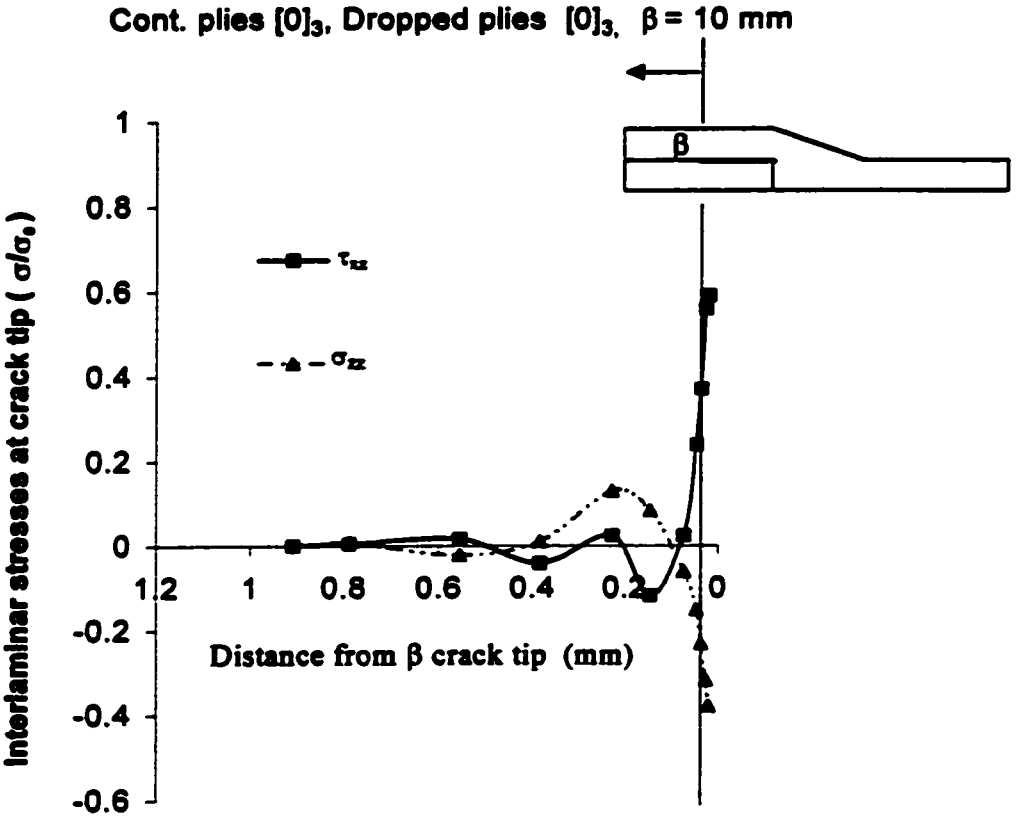

Figure 4-18 Stress distribution ahead of β crack tip

Influence of thin section debond length (length of α_1)

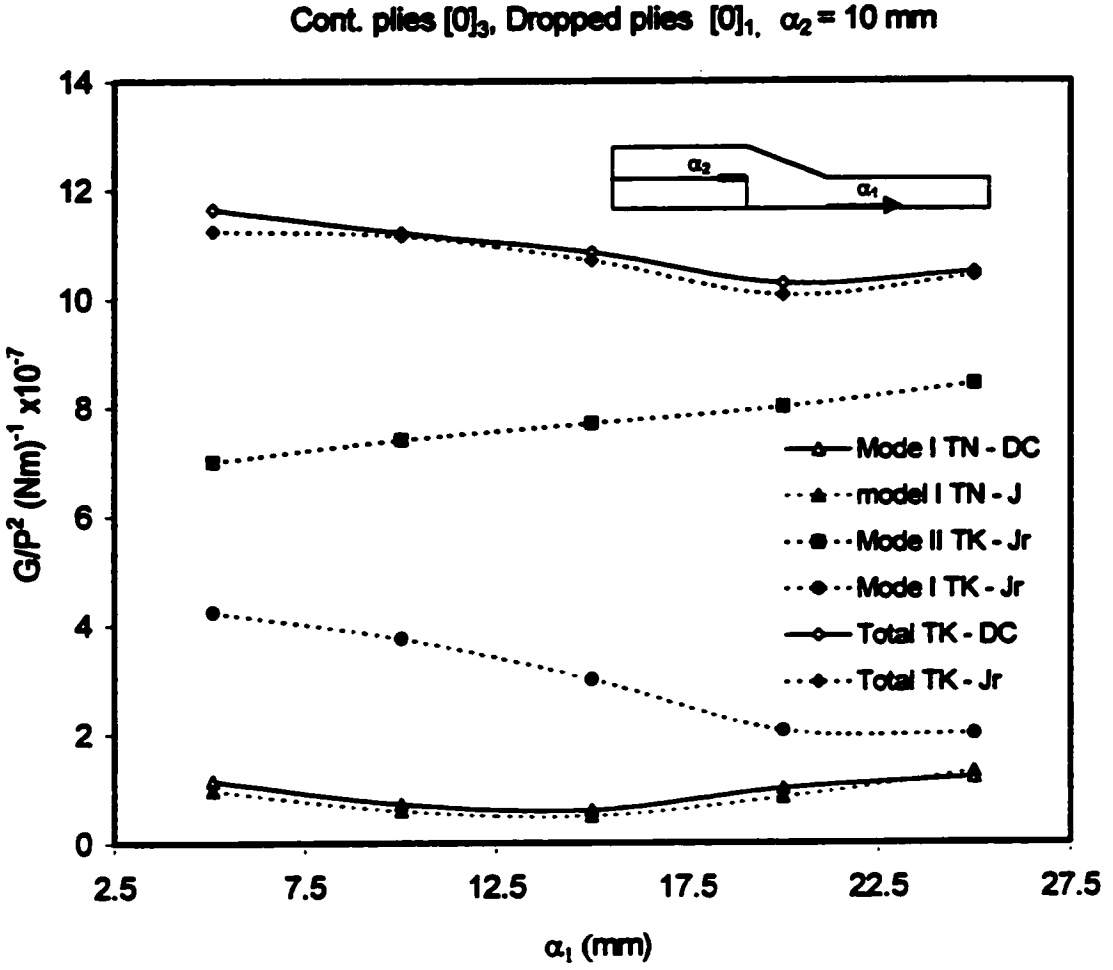

Figure 4-19 Influence of thin section cracking length (TN: thin section, TK: thick section, DC: direction calculation, J: J-integral method, and Jr: displacement restrained J-integral method)

The strain energy release rate results obtained using different methods are presented in Figure 4-19. It illustrates the variation in the strain energy release rate results for a fixed delamination length in the thick section and variable delamination length in the thin section. For the entire range of crack lengths shown, the total G calculated using the direct method and J-integral method are in good agreement for delamination both in thin and thick sections The Mode II component was always dominant, with a ratio of

G_{II}/G_I equal to 1.97, for example, for the delaminations at $\alpha_1 = \alpha_2 = 10$ mm. A pure Mode I value is assumed to exist at the thin section tip due to the symmetric configuration and the loading condition.

Influence of thick section debond length (length of α_2)

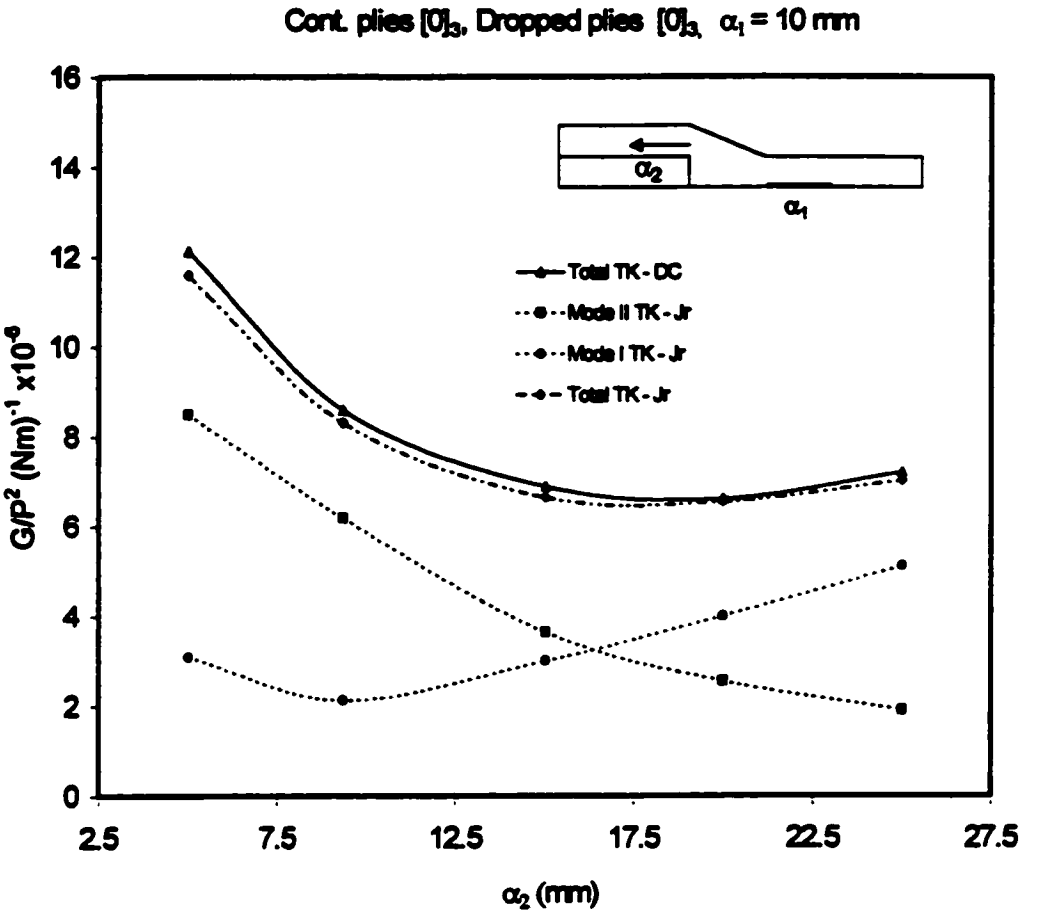

Figure 4-20 Comparison of restrained J-integral method and direct calculation method for 3 dropped plies

Figure 4-20 illustrates the comparison for a thin section delamination length of 10 mm and a variable delamination length in the thick section. The dotted lines represent the prediction of the J-integral model and the solid line corresponds to the results of the

direct calculation method. The values of total G calculated from these approaches are in good agreement for the entire range of delamination lengths shown. The small difference between the predictions is that the J-integral method underestimates the values of total G by at most 5 percent in comparison with that of the direct calculation method. This is due to the restrained condition imposed for the mode separation. Also shown in the figure are the individual mode components.

Influence of dropped ply thickness on delamination

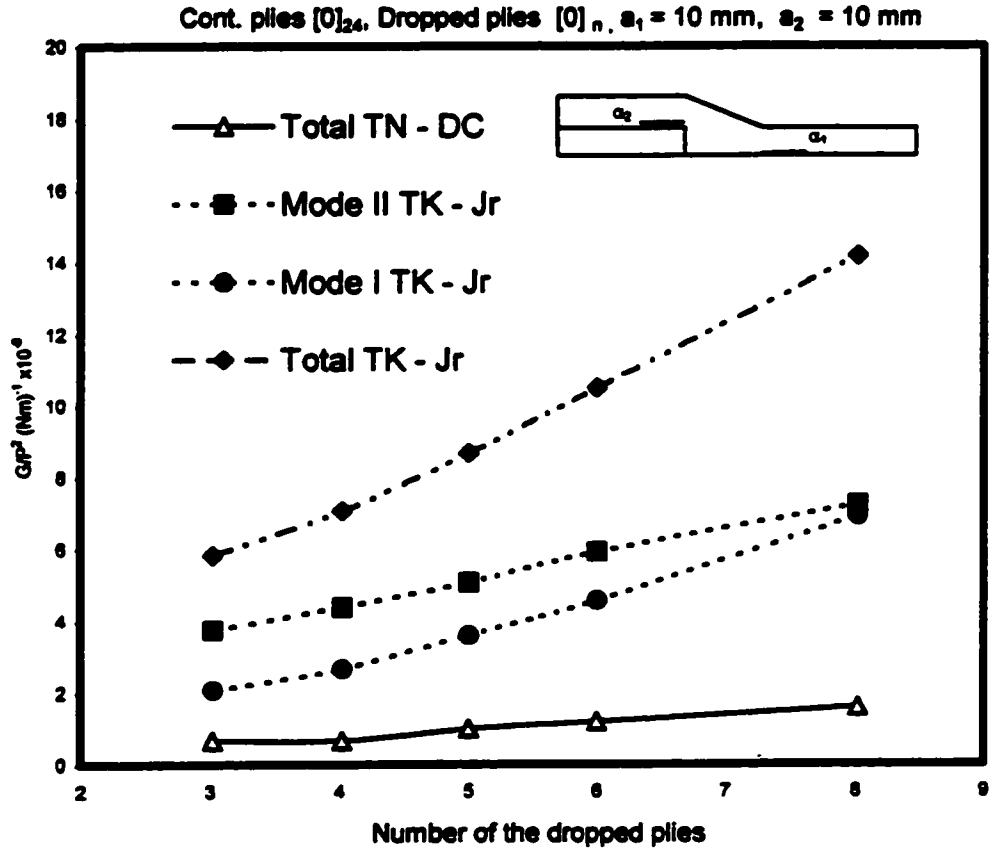

Figure 4-21 Influence of the number of dropped plies on delamination

The strain energy release rate corresponding to a given load is presented in Figure 4-21. It shows that the total strain energy release rate calculated at both the thick and thin

section delamination fronts increases quite linearly with the thickness of the dropped sublaminate. This trend is expected since the eccentricity of the load path is increasing. The total strain energy release rate at the thick section delamination front is significantly higher than the value at the delamination front in the thin section. However, the slope of the curve for the thick section delamination is much larger. This results in an increasing sensitivity to delamination at the thick section delamination front relative to that at the thin section delamination front, as the thickness of the discontinuous layer is increased. Both the Mode I and II components calculated at the thick section delamination front increase with increasing drop thickness. However, the Mode I component increases at a larger rate than the Mode II component. Therefore the model predicts a change from a Mode II dominated delamination front to mixed mode when the drop ply thickness increases to a certain value.

Influence of resin / adhesive layer thickness

The resin layer has been separated in the model to characterize the fracture behavior of laminate composites. This is because the resin layer is a definable region of matrix material existing between plies as shown in Figure 4-1, which is on the order of fiber diameter. Also considered is the fact that delamination is an interply phenomenon and is dependent upon the load-carrying capacity of the matrix phase, instead of the fiber phase. A singularity develops at the ply drop if a zero thickness interply layer is assumed (i.e., no interply resin layer), meaning that if a thinner resin layer is modeled higher stresses are produced. The minimum thickness of interply layer used in the models is one

tenth of the ply thickness. It has been shown that the interlaminar response predicted with the inclusion of interply layer reflects more realistic cases than those without it [9]. One of the objectives for the present work is to understand the influence of the thickness of interply on the structural strength. Thickness values larger than resin layer thickness are utilized to conduct the simulation. Strain energy release rates calculated are presented in Table 4-3. For the laminate with thin interply (up to 12 μm), the energy release rate is almost unaffected by the presence of the interlayer. For the laminate with thicker interply, however, G_I increases over the baseline value. Energy release rates computed by DC method are larger than the restrained J-integral values. This is expected because of displacement restraints imposed in the J-integral model. Comparison of the magnitudes of the energy release rate for interply crack and interfacial crack configurations shows that, for a given interply thickness, the interfacial crack model provides a somewhat larger energy release rate than the interply crack model, although the difference is relatively small (less than 8% in all cases).

Table 4-3 Energy release rate components computed from finite element analysis

$\alpha_1 = 10$ mm, $\alpha_2 = \beta = 10$ mm

	Resin layer thickness (μm)	Thick Section				Thin Section	
		G_I/P^2 (Jr) $(N\text{-}m)^{-1}x10^{-6}$	G_{II}/P^2 (Jr) $(N\text{-}m)^{-1}x10^{-6}$	G_T/P^2 (Jr) $(N\text{-}m)^{-1}x10^{-6}$	G_T/P^2 (DC) $(N\text{-}m)^{-1}x10^{-6}$	G_I/P^2 (J) $(N\text{-}m)^{-1}x10^{-6}$	G_T/P^2 (DC) $(N\text{-}m)^{-1}x10^{-6}$
Interply	12	37.51	74.33	111.84	121.51	5.92	5.95
Configuration	30	38.43	78.18	116.61	123.73	6.11	6.14
(α_1 - α_2)	60	39.70	82.25	121.95	135.62	6.20	6.25
	100	41.24	85.61	136.85	140.18	6.31	6.37
Interfacial	12	39.10	77.27	116.37	126.36	6.25	6.27
Configuration	30	40.13	82.47	122.60	129.88	6.40	6.48
(α_1 - β)	60	41.76	87.81	129.57	143.76	6.59	6.70
	100	43.42	89.62	133.04	145.28	6.71	6.81

Jr, DC and J stand for Restrained J-integral, Direct Calculation, and J-integral, respectively.

4.5.3 Concluding remarks

The developed quasi three-dimensional partial hybrid elements have been utilized to characterize interlaminar fracture behavior of tapered laminate embedded with two crack configurations. Quasi three-dimensional J-integral, which is of the same form as Rice's J integral for a two dimensional crack problem as well as path independent, has been used to calculate the strain energy release rates at embedded crack tips assumed in both interply crack and interfacial crack models. Magnitudes of strain energy release rate calculated using J-integral and restrained J-integral agree well with that obtained using conventional direct calculation approach. Of all the parameters studied, material and geometric properties of interply layers present significant influences on delamination. It is shown that thick and tough resin/interleaf layers will increase the fracture toughness

and subsequent structural performance of the laminate. It is therefore suggested that interleaved tapered laminates are good candidates for effectively enhancing the fracture behavior of the laminate. For the case of a thin interply layer, the strain energy release rate predicted for the interfacial crack configuration ($\alpha_1 - \beta$) is slightly higher than that for the interply crack configuration ($\alpha_1 - \alpha_2$) (less than 5%), but for the thicker interply layers the difference becomes larger. The estimation of strain energy release rate rendered by interfacial model provides conservative observation regarding the delamination in the tapered laminate.

4.6 Summary

In this chapter, both stress- and fracture mechanics based methods are studied for characterizing fracture behavior of tapered laminates. The damage onset was first investigated based on stress based criterion. The critical stress values and region were predicted with the developed hybrid elements and they correlate well with experimental observations. The analysis results proved that the von Mises derivative criterion is practical in the prediction of delamination initiation failure. Various approaches to calculate the strain energy release rate are further discussed in this Chapter. The direct method of calculation of the energy release rate has been shown to be reliable and gives its use credibility. For linear elastic analysis, J-integral is equivalent to strain energy release rate. Meanwhile, Rice's J-integral, which is originally developed for two-dimensional problems, is extendable to quasi and full-three dimensional problems. J-integral of Q3D is of the same as the original J-integral, but with a wider range of variables involved. J-integral shows promising in improving calculation efficiency due to

its path independent property. The developed quasi-three-dimensional partial hybrid elements were implemented to model the tapered laminate that has the same configuration as the one tested in the lab and has been considered to be under the generalized plane deformation. Through the example analyzed, it is seen that increase of resin thickness, by whole or partial interleaving of the tapered laminate at critical interfaces, rational selection of ratio of the number of the continuous and dropped sublaminates, and manufacturing the composite with proper taper angle would enhance fracture performance of the tapered laminate.

Chapter 5

MODIFIED SHEAR-LAG ANALYSIS

5.1 Introduction

Finite element methods, as indicated in the review part of the thesis, have been extensively used to predict interlaminar stress distributions and delamination in tapered composite structures. These methods were included in works by Kemp[1], Curry[2], Hoa[3], Fish [4], Llanos[24], Salpekar[5], etc. In contrast, there are few approaches solely independent of finite element methods that have been addressed to the tapered laminate problems. Harrison[13] developed a mixed formulation that correlates well with the finite element model of the tapered section. However, this model lacks a physical description of the load transfer mechanism.

Some simplified mechanical models were developed which include, for example, extensional and shear spring model by Armanios[7] and shear-lag model by Vizzini[14]. Throughout their efforts one objective has been to understand the load transfer mechanism and to describe it in a simple analytical form.

Armanios developed a model composed of extensional and shear springs and predicted the interlaminar stresses based on the tendency of the plies to align themselves to the applied load. Although the comparison between his model and a finite element solution is good for interlaminar shear, it fails to capture the tensile nature of the interlaminar normal stress at the ply drops.

Vizzini [14] first applied the ordinary shear model to predict the load transfer mechanism in tapered composite structures. The fundamental basis of his shear-lag model consists of three elastic layers separated by two shear layers. It was shown that this ordinary shear-lag model could capture a majority of the load transfer mechanism for the composite structures only when the Young's modulus of resin layer is lower compared with the Young's modulus of unidirectional tape. Meanwhile, this model has difficulty in addressing the matrix cracking problems that often exist in composite laminates because of the assumptions made in the model. These limitations constrain its wide applications.

In general, simplified mechanical models, as shown in the above work, for the interlaminar analysis of tapered laminates provide more physical insight than that by FEM, and reasonable results in comparison to that calculated with FEM are reachable based upon physically appropriate assumptions.

With above in mind, a new approach, named modified shear-lag model hereafter, has been developed to overcome the limitations of the model with ordinary shear-lag. The essential assumptions for the new model are that both plies and resin layers are treated to act as carriers of tensile stress and also to act as stress-transfer media. On the basis of these assumptions, more complicated mathematical forms were established as to

get a close solution to the true responses of loaded tapered composites. The reasons for selecting the shear-lag model for taper composites lie in the fact that this model is formulated based on a conceptual model with comparatively simple formulations and that it can provide more accurate stress responses for any composite material consisting of tapered laminates than the ordinary shear-lag model. Less computing efforts are involved in the current shear-lag model than in finite element methods. The model is also capable of being applied to any type of composite laminates

5.2 General Formulation

Assumptions used in the current shear-lag model are that both plies and resin layers are treated to act as tensile stress carriers and also to act as stress-transfer media. Two types of laminates are separately considered in the analysis.

5.2.1 Laminate without drop-off layers

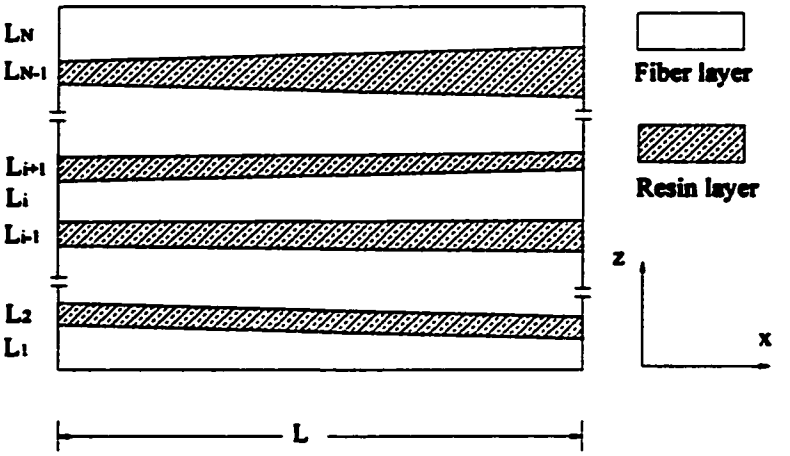

Figure 5-1 Schematic drawing of model with variable layer thicknesses

For equilibrium of the force in each layer in x direction, as indicated in Fig. 5-2, there exists:

$$\frac{dP_1}{dx} + \tau_{2/1} = 0 \qquad (Bottom \quad layer, \quad i = 1) \tag{5-1a}$$

$$\frac{dP_i}{dx} + \tau_{i+1/i} - \tau_{i/i-1} = 0 \qquad (Intermidate\ layers, i = 2, 3, \cdots N-1) \tag{5-1b}$$

$$\frac{dP_N}{dx} - \tau_{N/N-1} = 0 \qquad (Top\ layer, i = N) \tag{5-1c}$$

where, P_i, $\tau_{i/j}$ are, respectively, the axial force per unit thickness of the i-th layer and interfacial shear stress. $(2i-1)^{th}$ and $(2i)^{th}$ layers are corresponding to plies and resin layers, respectively. In the above equation, x is the global horizontal coordinate.

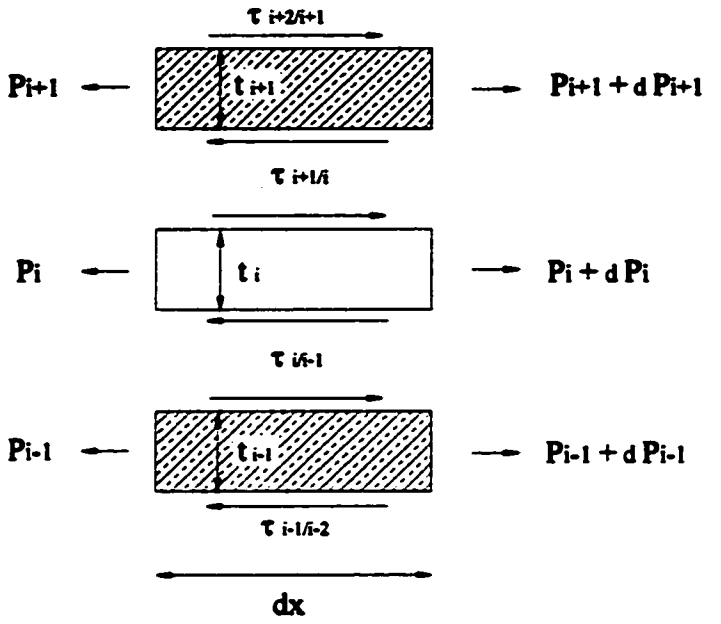

Figure 5-2 Diagram of free body

Under the conditions of linear elasticity, the following equations hold, considering the assumptions above:

$$P_i = E_i t_i \frac{du_i}{dx} \qquad (i = 1, 2, \cdots N) \tag{5-2}$$

$$\tau_{i/j} = \frac{2G_i G_j}{t_i G_j + t_j G_i}(u_i - u_j) = K_{i/j}(u_i - u_j) \tag{5-3}$$

where, E_i – Elastic modulus, E_{2i-1} for plies, and E_{2i} for resin layers;

G_i – Shear modulus, G_{2i-1} for plies, and G_{2i} for resin layers;

u_i – Displacement of the i th layer;

t_i – Thickness of layer as $t_i = a_i + b_i x/L$ (i =1, 2, 3, ... N);

$K_{i/j}$ - Interfacial modulus, derived using the definition of shear deformation as follows (Refer to Figure 5-3 for the derivation).

$$\tau_{i/j} = \frac{G_i\left(u_i - u_{i/j}\right)}{\left(t_i/2\right)} = \frac{G_j\left(u_{i/j} - u_j\right)}{\left(t_j/2\right)} \tag{5-4}$$

In the above equation, it was assumed that each layer i has a constant displacement u_i, and the equation is valid whether t_i is constant or not.

The final differential system can be obtained by the substitutions of the latter equations into Eq. (5-1).

$$E_1\left(\frac{dt_1}{dx}\frac{du_1}{dx} + t_1\frac{d^2u_1}{dx^2}\right) + K_{2/1}\left(u_2 - u_1\right) = 0 \tag{5-5a}$$

$$E_i\left(\frac{dt_i}{dx}\frac{du_i}{dx}+t_i\frac{d^2u_i}{dx^2}\right)+K_{i+1/i}(u_{i+1}-u_i)-K_{i/i-1}(u_i-u_{i-1})=0$$

$$i=2,3,4,\cdots N-1 \qquad \text{(5-5b)}$$

$$E_N\left(\frac{dt_N}{dx}\frac{du_N}{dx}+t_N\frac{d^2u_N}{dx^2}\right)-K_{N/N-1}(u_N-u_{N-1})=0 \qquad \text{(5-5c)}$$

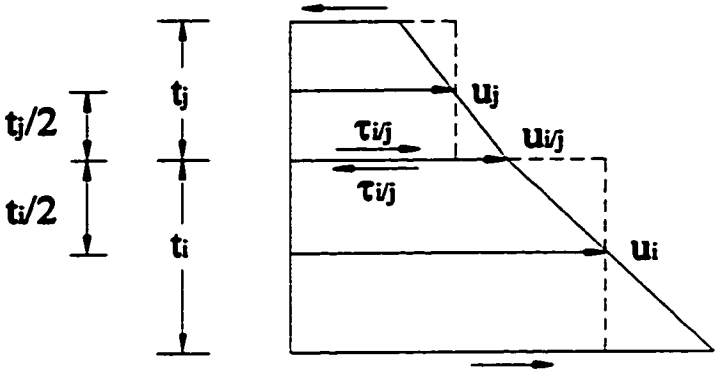

Figure 5-3 Derivation for interfacial modulus

For the differential equation system in Eq. (5-5), it is impossible to obtain a closed form solution, so we can solve it in a numerical way. Suppose that the displacements in each layer are of the following form:

$$u_i=\sum_{n=0}^{\infty}C_n^i\left(\frac{x}{L}\right)^n \qquad i=1,2,3,\cdots N \qquad \text{(5-6)}$$

Substituting Eq. (5-6) and formulation for $t_i(x)$ into Eq. (5-5) results in a series of recursive equations involving C_n for each layer. By setting the coefficients of like terms on both sides of the equations equal, a solution can be obtained with two initial values for each layer determined by boundary conditions.

More commonly applied modeling for this problem can be established with only 5 layers or 5 sublaminates, i.e. one continuous belt sublaminate, one continuous core sublaminate, one dropping sublaminate, and two resin layers between belt and dropping sublaminate, and between dropping sublaminate and core. Under this situation, Eq (5-5) becomes

$$\left.\begin{aligned} E_1\left(\frac{dt_1}{dx}\frac{du_1}{dx}+t_1\frac{d^2u_1}{dx^2}\right)+K_{2/1}(u_2-u_1)=0 \\ E_i\left(\frac{dt_i}{dx}\frac{du_i}{dx}+t_i\frac{d^2u_i}{dx^2}\right)+K_{i+1/i}(u_{i+1}-u_i)-K_{i/i-1}(u_i-u_{i-1})=0 \qquad i=2,3,4 \\ E_5\left(\frac{dt_5}{dx}\frac{du_5}{dx}+t_5\frac{d^2u_5}{dx^2}\right)-K_{5/4}(u_5-u_4)=0 \end{aligned}\right\} \quad (5\text{-}7)$$

Note that in this analysis, equilibrium along the z direction is not considered. This is due to the basic assumption of the shear lag model. It can also be the weakness of the model.

5.2.2 Laminate with drop-off layers

The simplest tapered laminate consists of a two-zone area close to the drop off location, as shown in Fig. 5-4. The first zone consists of four constant thickness plies and resin layer and one variable thickness resin layer. The top ply is inclined. In zone two, three resin layers are located between the top and bottom plies. Similarly to the derivation of equations for the regular plate without drop-off layer, the governing equilibrium equations for general laminate with total number of N layers and with drop-off layer at the top the laminate are given in the following.

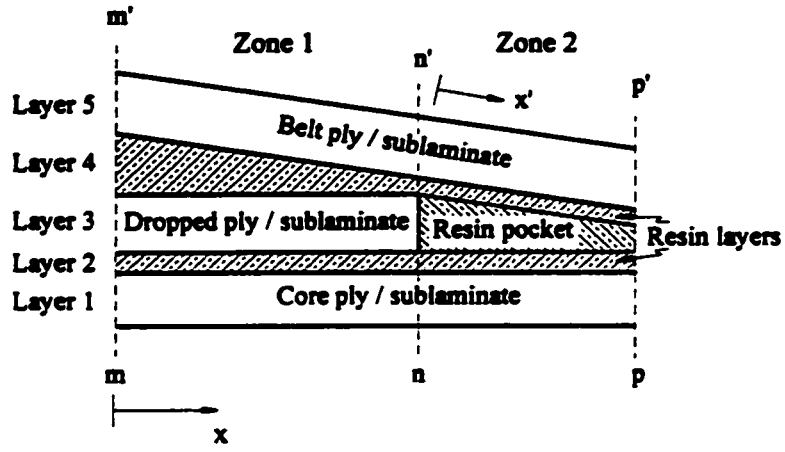

Figure 5-4 Schematic drawing of typical ply drop region

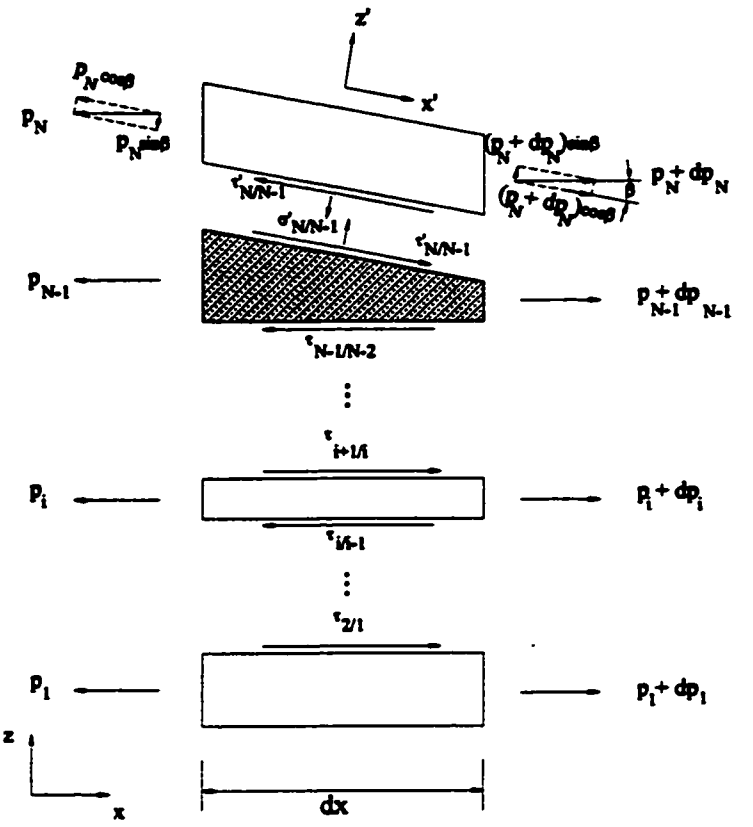

Figure 5-5 Equilibrium conditions of ply drop at zone 1

For the above equilibrium of the force in each layer in zone 1 of the typical drop off, as indicated in Fig. 5-5, there exists:

Bottom layer ($i = 1$):

$$\frac{dP_1}{dx} + \tau_{2/1} = 0 \tag{5-8}$$

Intermediate layers ($i = 2, 3, \ldots N\text{-}2$):

$$\frac{dP_i}{dx} + \tau_{i+1/i} - \tau_{i/i-1} = 0 \tag{5-9}$$

Intermediate thickness variable resin layer (i = N-1):

$$\begin{aligned} &\frac{dP_{N-1}}{dx} + \dot{\tau}_{N/N-1} + \tan\beta\dot{\sigma}_{N/N-1} - \tau_{N-1/N-2} = 0 \\ &\dot{\sigma}_{N/N-1} - \tan\beta\dot{\tau}_{N/N-1} = 0 \end{aligned} \tag{5-10}$$

or

$$\frac{dP_{N-1}}{dx} + \dot{\tau}_{N/N-1}(1+\tan^2\beta) - \tau_{N-1/N-2} = 0 \tag{5-10'}$$

Top inclined ply (i = N):

$$\begin{aligned} &\frac{dP_N}{dx}\cos^2\beta - \dot{\tau}_{N/N-1} = 0 \\ &\dot{\sigma}_{N/N-1} - \dot{\tau}_{N/N-1}\tan\beta = 0 \end{aligned} \tag{5-11}$$

The governing equilibrium equations in each layer in zone 2 as shown in Figure 5-6 below are of the forms:

Bottom layer (N = 1):

$$\frac{dP_1}{dx} + \tau_{2/1} = 0 \tag{5-12}$$

Intermediate layers (i = 2, 3, ... N-3):

$$\frac{dP_i}{dx} + \tau_{i+1/i} - \tau_{i/i-1} = 0 \tag{5-13}$$

Intermediate thickness variable resin layer (i = N-2):

$$\begin{aligned} &\frac{dP_{N-2}}{dx} + \dot{\tau}_{N-1/N-2} + \tan\beta\dot{\sigma}_{N-1/N-2} - \tau_{N-2/N-3} = 0 \\ &\dot{\sigma}_{N-1/N-2} - \tan\beta\dot{\tau}_{N-1/N-2} = 0 \end{aligned} \tag{5-14}$$

or
$$\frac{dP_{N-2}}{dx} + \dot{\tau}_{N-1/N-2}(1+\tan^2\beta) - \tau_{N-2/N-3} = 0 \qquad (5\text{-}14')$$

Top inclined resin layer ($i = N$-1):

$$\frac{dP_{N-1}}{dx} + (\dot{\tau}_{N/N-1} - \dot{\tau}_{N-1/N-2}) + \tan\beta(\dot{\sigma}_{N/N-1} - \dot{\sigma}_{N-1/N-2}) = 0$$
$$(\dot{\sigma}_{N/N-1} - \dot{\sigma}_{N-1/N-2}) - \tan\beta(\dot{\tau}_{N/N-1} - \dot{\tau}_{N-1/N-2}) = 0 \qquad (5\text{-}15)$$

or
$$\frac{dP_{N-1}}{dx}\cos^2\beta + (\dot{\tau}_{N/N-1} - \dot{\tau}_{N-1/N-2}) = 0 \qquad (5\text{-}15')$$

Top inclined ply ($i = N$):

$$\frac{dP_N}{dx}\cos^2\beta - \dot{\tau}_{N/N-1} = 0$$
$$\dot{\sigma}_{N/N-1} - \dot{\tau}_{N/N-1}\tan\beta = 0 \qquad (5\text{-}16)$$

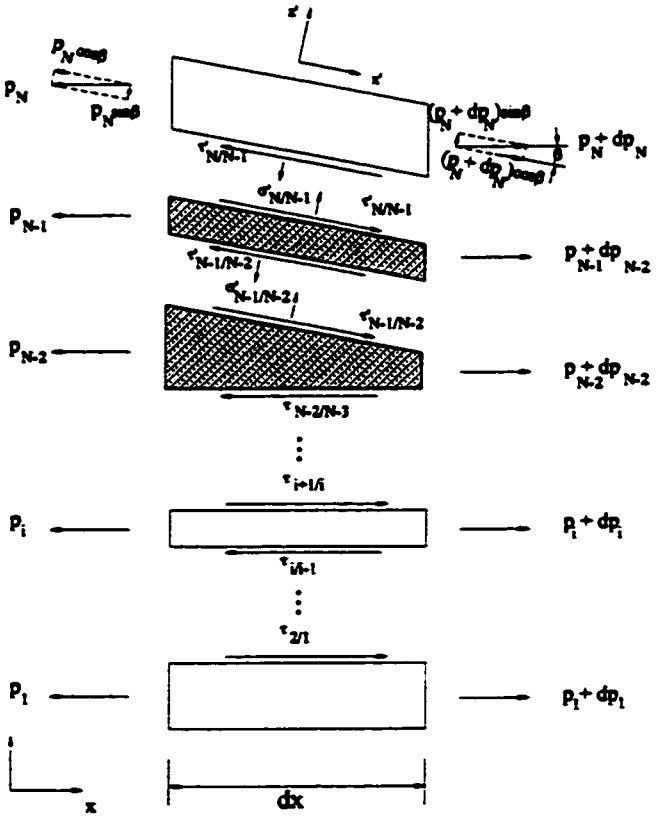

Figure 5-6 Equilibrium conditions of ply drop at zone 2

In the governing equations above, P_i is a function of (E_i, t_i, u_i) which is of the same form as in Eq. (5-2), while τ_{ij} is a function of (G_i, G_j, t_i, t_j, u_i, u_j) as in Eq. (5-3). The recursive formulation for the coefficients of polynomial is described as follows. The required coefficients are contained in a linear system. Coefficients in one layer are coupled with that in adjacent layer as well as the sequential dependence of former term coefficient on the latter in the same layer. If the boundary conditions such as C_0^l *and* C_1^l for displacements and stress/strain on one side of each layer are known, the total coefficients are defined using the above recursive formulation. The convergence of the series depends on the number of terms chosen. In this model using the modified shear-lag analysis, we can also present its difference from the model using original shear-lag method. The comparison with FEM results is performed so as to further determine the accuracy of the model.

The next step is concerned about implementation of the modeling. It consists of the consideration of boundary conditions/constraints, converting of the global system to local system (tapered coordinate system) for obtaining correlation between FEM and current method, determination of interlaminar normal stress with force equilibrium considerations, and finally comparison of the current modeling results with others available in the literature.

5.3 Derivation of the Coefficients of Polynomials

Derivation of polynomial coefficients that are used to approximate displacements and deformations of the laminate in tension is given below for a general laminate consisting of total of N layers with or without taper on the top one. A general formulation for straight laminates was first derived and a layer correction for taper was thus further made and adjusted for the corresponding layer in the straight laminate without taper in order to account for tapered influence.

5.3.1 Laminate without drop-off layers

Eq. (5-7) for the laminate without drop-off layers can be rewritten as

$$E_1\left(\frac{dt_1}{dx}\frac{du_1}{dx}+t_1\frac{d^2u_1}{dx^2}\right)+\frac{2G_1G_2}{t_1G_2+t_2G_1}(u_2-u_1)=0 \qquad (5\text{-}17a)$$

$$E_i\left(\frac{dt_i}{dx}\frac{du_i}{dx}+t_i\frac{d^2u_i}{dx^2}\right)+\frac{2G_{i+1}G_i}{t_{i+1}G_i+t_iG_{i+11}}(u_{i+1}-u_i)$$

$$-\frac{2G_iG_{i-1}}{t_iG_{i-1}+t_{i-1}G_i}(u_i-u_{i-1})=0 \quad i=2,3,4,\cdots N-1 \qquad (5\text{-}17b)$$

$$E_N\left(\frac{dt_N}{dx}\frac{du_N}{dx}+t_N\frac{d^2u_N}{dx^2}\right)-\frac{2G_NG_{N-1}}{t_NG_{N-1}+t_{N-1}G_N}(u_N-u_{N-1})=0 \qquad (5\text{-}17c)$$

If the thicknesses are constant, the above differential equations become homogeneous with constant coefficients and can be solved in closed form. However, the thickness of all layers can vary as indicated in Figure 5-1 (although, in this development, only the thickness of resin layers will vary). In particular, assume in general expressions, that:

$$\left.\begin{aligned} t_i &= a_i + b_i \frac{x}{L} \\ t_{i+1} &= a_{i+1} + b_{i+1} \frac{x}{L} \\ t_{i-1} &= a_{i-1} + b_{i-1} \frac{x}{L} \\ G_{i+1}G_i &= G_iG_{i-1} = G \end{aligned}\right\} \qquad (5\text{-}18)$$

Denoting that

$$\left.\begin{aligned} a_{i+1/i} &= a_{i+1}G_i + a_iG_{i+1} \\ a_{i/i-1} &= a_iG_{i-1} + a_{i-1}G_i \\ b_{i+1/i} &= b_{i+1}G_i + b_iG_{i+1} \\ b_{i/i-1} &= b_iG_{i-1} + b_{i-1}G_i \end{aligned}\right\} \qquad (5\text{-}19)$$

Eq (5-17) thus becomes:

$$E_1\left(\frac{dt_1}{dx}\frac{du_1}{dx}+t_1\frac{d^2u_1}{dx^2}\right)+\frac{2G}{a_{2/1}+b_{2/1}\dfrac{x}{L}}(u_2-u_1)=0 \qquad \text{(5-20a)}$$

$$E_i\left(\frac{dt_i}{dx}\frac{du_i}{dx}+t_i\frac{d^2u_i}{dx^2}\right)+\frac{2G}{a_{i+1/i}+b_{i+1/i}\dfrac{x}{L}}(u_{i+1}-u_i)$$

$$-\frac{2G}{a_{i/i-1}+b_{i/i-1}\dfrac{x}{L}}(u_i-u_{i-1})=0 \qquad i=2,3,4,\cdots N-1 \qquad \text{(5-20b)}$$

$$E_N\left(\frac{dt_N}{dx}\frac{du_N}{dx}+t_N\frac{d^2u_N}{dx^2}\right)-\frac{2G}{a_{N/N-1}+b_{N/N-1}\dfrac{x}{L}}(u_N-u_{N-1})=0 \qquad \text{(5-20c)}$$

To solve for the system of governing differential equations, u_i, assume that the displacements have the following form:

$$u_i=\sum_{n=0}^{\infty}C_n^i\left(\frac{x}{L}\right)^n \qquad (i=1,2,3\cdots N) \qquad \text{(5-21)}$$

Substitution of Eq. (5-21) into Eq (5-20), considering:

$$\left.\begin{aligned} \frac{du_i}{dx} &= \sum_{n=0}^{\infty} C_n^i \frac{n}{L}\left(\frac{x}{L}\right)^{n-1} \\ \frac{d^2u_i}{dx^2} &= \sum_{n=0}^{\infty} C_n^i \frac{n(n-1)}{L^2}\left(\frac{x}{L}\right)^{n-2} \\ \frac{dt_i}{dx} &= b_i \frac{1}{L} \end{aligned}\right\} \qquad (5\text{-}22)$$

gives a solution for each layer as discussed in the following.

Bottom layer (i = 1)

With substitution of Eq. (5-22), Eq. (5-20a) becomes:

$$E_1\left[b_1 \frac{1}{L}\sum_{n=1}^{\infty} C_n^1 \frac{n}{L}\left(\frac{x}{L}\right)^{n-1} + \left(a_1 + b_1 \frac{x}{L}\right)\sum_{n=2}^{\infty} C_n^1 \frac{n(n-1)}{L^2}\left(\frac{x}{L}\right)^{n-2}\right] + \frac{2G}{a_{2/1} + b_{2/1}\frac{x}{L}}\left[\sum_{n=0}^{\infty}\left(C_n^2 - C_n^1\left(\frac{x}{L}\right)^n\right]\right] = 0 \qquad (5\text{-}23a)$$

Re-arrangement of Eq (5-23a) yields:

$$\sum_{n=1}^{\infty}\left[q_1 C_n^1 n\left(\frac{x}{L}\right)^{n-1}+q_2 C_n^1 n\left(\frac{x}{L}\right)^{n}\right]$$

$$+\sum_{n=2}^{\infty}\left[q_3 C_n^1 n(n-1)\left(\frac{x}{L}\right)^{n-2}+q_4 C_n^1 n(n-1)\left(\frac{x}{L}\right)^{n-1}+q_5 C_n^1 n(n-1)\left(\frac{x}{L}\right)^{n}\right] \qquad \text{(5-23b)}$$

$$+\sum_{n=0}^{\infty}\left[q_6 (C_n^2 - C_n^1)\left(\frac{x}{L}\right)^{n}\right]=0$$

where:

$$\left.\begin{aligned} q_1 &= E_1 a_{2/1} b_1 \frac{1}{L^2} \\ q_2 &= E_1 b_{2/1} b_1 \frac{1}{L^2} \\ q_3 &= E_1 a_{2/1} a_1 \frac{1}{L^2} \\ q_4 &= E_1 (a_{2/1} b_1 + a_1 b_{2/1}) \frac{1}{L^2} \\ q_5 &= E_1 b_{2/1} b_1 \frac{1}{L^2} \\ q_6 &= 2G \end{aligned}\right\} \qquad \text{(5-24)}$$

For the six series in Eq. (5-23), the lowest common power of (x/L) is 2, so the terms with power 0 or 1 can be separated out first. Letting each of the summations of the coefficient

$f(x/L)$ power be equal to zero leads to the eternal validity of the equation. So Eq. (5-23) becomes:

$$q_1C_1^1+2q_1C_2^1\left(\frac{x}{L}\right)+\sum_{n=3}^{\infty}\left[q_1C_n^1n\left(\frac{x}{L}\right)^{n-1}\right]$$

$$+q_2C_1^1\left(\frac{x}{L}\right)+\sum_{n=2}^{\infty}\left[q_2C_n^1n\left(\frac{x}{L}\right)^{n}\right]$$

$$+2q_3C_2^1+6q_3C_3^1\left(\frac{x}{L}\right)+\sum_{n=4}^{\infty}\left[q_3C_n^1n(n-1)\left(\frac{x}{L}\right)^{n-2}\right]$$

$$+2q_4C_2^1\left(\frac{x}{L}\right)+\sum_{n=3}^{\infty}\left[q_4C_n^1n(n-1)\left(\frac{x}{L}\right)^{n-1}\right]+\sum_{n=2}^{\infty}\left[q_5C_n^1n(n-1)\left(\frac{x}{L}\right)^{n}\right]$$

$$+q_6(C_0^2-C_0^1)+q_6(C_1^2-C_1^1)\left(\frac{x}{L}\right)+\sum_{n=2}^{\infty}\left[q_6(C_n^2-C_n^1)\left(\frac{x}{L}\right)^{n}\right]=0 \qquad (5\text{-}25)$$

Also with:

$$\sum_{n=3}^{\infty}\left[q_1 C_n^1 n\left(\frac{x}{L}\right)^{n-1}\right]=\sum_{k=2}^{\infty}\left[q_1 C_{k+1}^1 (k+1)\left(\frac{x}{L}\right)^{k}\right]$$

$$\sum_{n=2}^{\infty}\left[q_2 C_n^1 n\left(\frac{x}{L}\right)^{n}\right]=\sum_{k=2}^{\infty}\left[q_2 C_k^1 k\left(\frac{x}{L}\right)^{k}\right]$$

$$\sum_{n=4}^{\infty}\left[q_3 C_n^1 n(n-1)\left(\frac{x}{L}\right)^{n-2}\right]=\sum_{k=2}^{\infty}\left[q_3 C_{k+2}^1 (k+2)(k+1)\left(\frac{x}{L}\right)^{k}\right]$$

$$\sum_{n=3}^{\infty}\left[q_4 C_n^1 n(n-1)\left(\frac{x}{L}\right)^{n-1}\right]=\sum_{k=2}^{\infty}\left[q_4 C_{k+1}^1 (k+1)k\left(\frac{x}{L}\right)^{k}\right]$$

$$\sum_{n=2}^{\infty}\left[q_5 C_n^1 n(n-1)\left(\frac{x}{L}\right)^{n}\right]=\sum_{k=2}^{\infty}\left[q_5 C_k^1 k(k-1)\left(\frac{x}{L}\right)^{k}\right]$$

$$\sum_{n=2}^{\infty}\left[q_6 (C_n^2 - C_n^1)\left(\frac{x}{L}\right)^{n}\right]=\sum_{k=2}^{\infty}\left[q_6 (C_k^2 - C_k^1)\left(\frac{x}{L}\right)^{k}\right] \qquad (5\text{-}26)$$

Eq. (5-25) becomes:

$$q_1 C_1^1 + 2q_3 C_2^1 - q_6 C_0^1 + q_6 C_0^2 = 0 \qquad (5\text{-}27a)$$

$$(q_2 - q_6)C_1^1 + 2q_4 C_2^1 + 6q_3 C_3^1 + q_6 C_1^2 + 2q_1 C_2^1 = 0 \qquad (5\text{-}27b)$$

$$\begin{aligned}&[q_2 k + q_5 k(k-1) - q_6]C_k^1 + [q_1(k+1) + q_4(k+1)k]C_{k+1}^1 \\ &+ q_3(k+2)(k+1)C_{k+2}^1 + q_6 C_k^2 = 0 \quad k = 2,3,4\cdots\infty\end{aligned} \qquad (5\text{-}27c)$$

Top layer (i = N)

Similarly as in the calculation of coefficients related to the bottom layer, substitution of Eq. (5-22) into Eq (5-20c) yields

$$E_N\left[b_N\frac{1}{L}\sum_{n=1}^{\infty}C_n^N\frac{n}{L}\left(\frac{x}{L}\right)^{n-1}+\left(a_N+b_N\frac{x}{L}\right)\sum_{n=2}^{\infty}C_n^N\frac{n(n-1)}{L^2}\left(\frac{x}{L}\right)^{n-2}\right]$$

$$-\frac{2G}{a_{N/N-1}+b_{N/N-1}\dfrac{x}{L}}\left[\sum_{n=0}^{\infty}\left(C_n^N-C_n^{N-1}\right)\left(\frac{x}{L}\right)^n\right]=0 \qquad (5\text{-}28)$$

Re-arrangement of Eq (5-28) leads to:

$$\sum_{n=1}^{\infty}\left[s_1C_n^Nn\left(\frac{x}{L}\right)^{n-1}+s_2C_n^Nn\left(\frac{x}{L}\right)^n\right]$$

$$+\sum_{n=2}^{\infty}\left[s_3C_n^Nn(n-1)\left(\frac{x}{L}\right)^{n-2}+s_4C_n^Nn(n-1)\left(\frac{x}{L}\right)^{n-1}+s_5C_n^Nn(n-1)\left(\frac{x}{L}\right)^n\right] \qquad (5\text{-}29)$$

$$-\sum_{n=0}^{\infty}\left[s_6(C_n^N-C_n^{N-1})\left(\frac{x}{L}\right)^n\right]=0$$

where:

$$
\left.
\begin{aligned}
s_1 &= E_N a_{N/N-1} b_N \frac{1}{L^2} \\
s_2 &= E_N b_{N/N-1} b_N \frac{1}{L^2} \\
s_3 &= E_N a_{N/N-1} a_N \frac{1}{L^2} \\
s_4 &= E_N (a_{N/N-1} b_N + a_N b_{N/N-1}) \frac{1}{L^2} \\
s_5 &= E_N b_{N/N-1} b_N \frac{1}{L^2} \\
s_6 &= 2G
\end{aligned}
\right\} \qquad (5\text{-}30)
$$

For the six series in Eq. (5-29), the lowest common power of (x/L) is 2, so the terms with power 0 or 1 can be separated out first. Letting each of the summations of the coefficient $f(x/L)$ power be equal to zero leads to the eternal validity of the equation. So Eq. (5-29) becomes:

$$s_1 C_1^N + 2s_1 C_2^N \left(\frac{x}{L}\right) + \sum_{n=3}^{\infty}\left[s_1 C_n^N n\left(\frac{x}{L}\right)^{n-1}\right]$$

$$+ s_2 C_1^N \left(\frac{x}{L}\right) + \sum_{n=2}^{\infty}\left[s_2 C_n^N n\left(\frac{x}{L}\right)^{n}\right]$$

$$+ 2s_3 C_2^N + 6s_3 C_3^N \left(\frac{x}{L}\right) + \sum_{n=4}^{\infty}\left[s_3 C_n^N n(n-1)\left(\frac{x}{L}\right)^{n-2}\right]$$

$$+ 2s_4 C_2^N \left(\frac{x}{L}\right) + \sum_{n=3}^{\infty}\left[s_4 C_n^N n(n-1)\left(\frac{x}{L}\right)^{n-1}\right] + \sum_{n=2}^{\infty}\left[s_5 C_n^N n(n-1)\left(\frac{x}{L}\right)^{n}\right]$$

$$- s_6(C_0^N - C_0^{N-1}) - s_6(C_1^N - C_1^{N-1})\left(\frac{x}{L}\right) + \sum_{n=2}^{\infty}\left[s_6(C_n^N - C_n^{N-1})\left(\frac{x}{L}\right)^{n}\right] = 0 \qquad (5\text{-}31)$$

Also with:

$$\sum_{n=3}^{\infty}\left[s_1 C_n^N n\left(\frac{x}{L}\right)^{n-1}\right]=\sum_{k=2}^{\infty}\left[s_1 C_{k+1}^N (k+1)\left(\frac{x}{L}\right)^k\right]$$

$$\sum_{n=2}^{\infty}\left[s_2 C_n^N n\left(\frac{x}{L}\right)^n\right]=\sum_{k=2}^{\infty}\left[s_2 C_k^N k\left(\frac{x}{L}\right)^k\right]$$

$$\sum_{n=4}^{\infty}\left[s_3 C_n^N n(n-1)\left(\frac{x}{L}\right)^{n-2}\right]=\sum_{k=2}^{\infty}\left[s_3 C_{k+2}^N (k+2)(k+1)\left(\frac{x}{L}\right)^k\right]$$

$$\sum_{n=3}^{\infty}\left[s_4 C_n^N n(n-1)\left(\frac{x}{L}\right)^{n-1}\right]=\sum_{k=2}^{\infty}\left[s_4 C_{k+1}^N (k+1)k\left(\frac{x}{L}\right)^k\right]$$

$$\sum_{n=2}^{\infty}\left[s_5 C_n^N n(n-1)\left(\frac{x}{L}\right)^n\right]=\sum_{k=2}^{\infty}\left[s_5 C_k^N k(k-1)\left(\frac{x}{L}\right)^k\right]$$

$$\sum_{n=2}^{\infty}\left[s_6 (C_n^N - C_n^N)\left(\frac{x}{L}\right)^n\right]=\sum_{k=2}^{\infty}\left[s_6 (C_k^N - C_k^{N-1})\left(\frac{x}{L}\right)^k\right] \qquad (5\text{-}32)$$

Eq. (5-31) thus becomes:

$$s_1 c_1^N + 2s_3 c_2^N - s_6 c_0^N + s_6 c_0^{N-1} = 0 \qquad (5\text{-}33a)$$

$$(s_2 - s_6)c_1^N + 2(s_4 + s_1)c_2^N + 6s_3 c_3^N + s_6 c_1^{N-1} = 0 \qquad (5\text{-}33b)$$

$$\begin{aligned}&[s_2 k + s_5 k(k-1) + s_6]c_k^N + [s_1(k+1) + s_4(k+1)k]c_{k+1}^N \\ &+ s_3(k+2)(k+1)c_{k+2}^N - s_6 c_k^{N-1} = 0 \qquad k = 2,3\cdots\infty\end{aligned} \qquad (5\text{-}33c)$$

Intermediate layers (i = 2, 3, ... N-1)

Substitution of Eq. (5-22) into Eq. (5-20b) leads to:

$$E_i\left[b_i\frac{1}{L}\sum_{n=0}^{\infty}c_n^i\frac{n}{L}(\frac{x}{L})^{n-1}+(a_i+b_i\frac{x}{L})\sum_{n=0}^{\infty}c_n^i\frac{n(n-1)}{L^2}(\frac{x}{L})^{n-2}\right]$$

$$+2G\left[\frac{\sum_{n=0}^{\infty}c_n^{i+1}(\frac{x}{L})^n-\sum_{n=0}^{\infty}c_n^i(\frac{x}{L})^n}{a_{i+1/i}+b_{i+1/i}\frac{x}{L}}-\frac{\sum_{n=0}^{\infty}c_n^i(\frac{x}{L})^n-\sum_{n=0}^{\infty}c_n^{i-1}(\frac{x}{L})^n}{a_{i/i-1}+b_{i/i-1}\frac{x}{L}}\right]=0 \tag{5-34}$$

Re-arrangement of Eq. (5-34) leads to

$$\sum_{n=2}^{\infty}c_n^ir_4^in(n-1)(\frac{x}{L})^{n-2}$$

$$+\sum_{n=1}^{\infty}c_n^ir_1^in(\frac{x}{L})^{n-1}+\sum_{n=2}^{\infty}c_n^i(r_5^i+r_7^i)n(n-1)(\frac{x}{L})^{n-1}$$

$$+\sum_{n=1}^{\infty}c_n^ir_2^in(\frac{x}{L})^{n}+\sum_{n=2}^{\infty}c_n^i(r_6^i+r_8^i)n(n-1)(\frac{x}{L})^{n}$$

$$+\sum_{n=0}^{\infty}\left[(c_n^{i+1}-c_n^i)r_{10}^i+(c_n^i-c_n^{i-1})r_{12}^i\right](\frac{x}{L})^n$$

$$+\sum_{n=1}^{\infty}c_n^ir_3^in(\frac{x}{L})^{n+1}+\sum_{n=2}^{\infty}c_n^ir_9^in(n-1)(\frac{x}{L})^{n+1}$$

$$+\sum_{n=0}^{\infty}[(c_n^{i+1}-c_n^i)r_{11}^i+(c_n^i-c_n^{i-1})r_{13}^i](\frac{x}{L})^{n+1}=0 \tag{5-35}$$

The lowest common term of $(\frac{x}{L})$ power for the series in Eq. (5-35) above is $(\frac{x}{L})^3$. By the same way as used in obtaining top and bottom layer coefficients before, we can obtain:

$\left(\frac{x}{L}\right)^{n-2}$:

$$2c_2^i r_4^i + 6c_3^i r_4^i(\frac{x}{L}) + 12c_4^i r_4^i(\frac{x}{L})^2 + \sum_{n=5}^{\infty} c_n^i r_4^i n(n-1)(\frac{x}{L})^{n-2} \qquad (5\text{-}36a)$$

$\left(\frac{x}{L}\right)^{n-1}$:

$$c_1^i r_1^i + 2c_2^i r_1^i(\frac{x}{L}) + 3c_3^i r_1^i(\frac{x}{L})^2 + 2c_2^i(r_5^i + r_7^i)(\frac{x}{L}) + 6c_3^i(r_5^i + r_7^i)(\frac{x}{L})^2$$
$$+ \sum_{n=4}^{\infty} c_n^i r_1^i n(\frac{x}{L})^{n-1} + \sum_{n=4}^{\infty} c_n^i(r_5^i + r_7^i)(n-1)n(\frac{x}{L})^{n-1} \qquad (5\text{-}36b)$$

$\left(\frac{x}{L}\right)^{n}$:

$$c_1^l r_2^l(\frac{x}{L}) + 2c_2^l r_2^l(\frac{x}{L})^2 + 2c_2^l(r_6^l + r_8^l)(\frac{x}{L})^2 + (c_0^{l+1} - c_0^l)r_{10}^l + (c_0^l - c_0^{l-1})r_{12}^l$$

$$+[(c_1^{l+1} - c_1^l)r_{10}^l + (c_1^l - c_1^{l-1})r_{12}^l](\frac{x}{L})$$

$$+[(c_2^{l+1} - c_2^l)r_{10}^l + (c_2^l - c_2^{l-1})r_{12}^l](\frac{x}{L})^2 \qquad \text{(5-36c)}$$

$$+\sum_{n=3}^{\infty} c_n^l r_2^l n(\frac{x}{L})^n + \sum_{n=3}^{\infty} c_n^l(r_6^l + r_8^l)n(n-1)(\frac{x}{L})^n$$

$$+\sum_{n=3}^{\infty} [(c_n^{l+1} - c_n^l)r_{10}^l + (c_n^l - c_n^{l-1})r_{12}^l](\frac{x}{L})^n$$

$\left(\frac{x}{L}\right)^{n+1}$:

$$c_1^l r_3^l(\frac{x}{L})^2 + [(c_0^{l+1} - c_0^l)r_{11}^l + (c_0^l - c_0^{l-1})r_{13}^l](\frac{x}{L})$$

$$+[(c_1^{l+1} - c_1^l)r_{11}^l + (c_1^l - c_1^{l-1})r_{13}^l](\frac{x}{L})^2 \qquad \text{(5-36d)}$$

$$+\sum_{n=2}^{\infty} c_n^l r_3^l n(\frac{x}{L})^{n+1} + \sum_{n=2}^{\infty} c_n^l r_9^l n(n-1)(\frac{x}{L})^{n+1}$$

$$+\sum_{n=2}^{\infty} \{(c_n^{l+1} - c_n^l)r_{11}^l + (c_n^l - c_n^{l-1})r_{13}^l\}(\frac{x}{L})^{n+1}$$

Letting the sum of the coefficients for each like of power $(\frac{x}{L})$ be equal to zero leads to:

$$2c_2^l r_4^l + c_1^l r_1^l + (c_0^{l+1} - c_0^l)r_{10}^l + (c_0^l - c_0^{l-1})r_{12}^l = 0 \qquad \text{(5-37a)}$$

$$6c_3^i r_4^i + 2c_2^i r_1^i + 2c_2^i (r_5^i - r_7^i) + c_1^i r_2^i + (c_1^{i+1} - c_1^i) r_{10}^i + (c_1^i - c_1^{i-1}) r_{12}^i + (c_0^{i+1} - c_0^i) r_{11}^i + (c_0^i - c_0^{i-1}) r_{13}^i = 0 \quad \text{(5-37b)}$$

$$12c_4^i r_4^i + 3c_3^i r_1^i + 6c_3^i (r_5^i + r_7^i) + 2c_2^i r_2^i + 2c_2^i (r_6^i + r_8^i) + (c_2^{i+1} - c_2^i) r_{10}^i + (c_2^i - c_2^{i-1}) r_{12}^i + c_1^i r_3^i + (c_1^{i+1} - c_1^i) r_{11}^i + (c_1^i - c_1^{i-1}) r_{13}^i = 0 \quad \text{(5-37c)}$$

$$c_{k+2}^i r_4^i (k+2)(k+1) + c_{k+1}^i r_1^i (k+1) + c_{k+1}^i (r_5^i + r_7^i)(k+1)k + c_k^i r_2^i k + c_k^i (r_6^i + r_8^i) k(k-1) + \left[(c_k^{i+1} - c_k^i) r_{10}^i + (c_k^i - c_k^{i-1}) r_{12}^i \right] + c_{k-1}^i r_3^i (k-1) + c_{k-1}^i r_9^i (k-1)(k-2) + (c_{k-1}^{i+1} - c_{k-1}^i) r_{11}^i + (c_{k-1}^i - c_k^{i-1}) r_{13}^i = 0 \quad \text{(5-37d)}$$

$$(k = 3,4,.....),\ (i = 2,3,.....,N-1)$$

where

$$
\left.
\begin{aligned}
r_1^i &= E_i b_i a_{i+1/i} a_{i/i-1} / L^2 \\
r_2^i &= r_8^i = E_i b_i (b_{i+1/i} a_{i/i-1} + a_{i+1/i} b_{i/i-1}) / L^2 \\
r_3^i &= r_9^i = E_i b_{i+1/i} b_{i/i-1} b_i / L^2 \\
r_4^i &= E_i a_i a_{i+1/i} a_{i/i-1} / L^2 \\
r_5^i &= E_i a_i b_{i+1/i} a_{i/i-1} / L^2 \\
r_6^i &= E_i b_{i+1/i} b_{i/i-1} a_i / L^2 \\
r_7^i &= E_i a_i a_{i+1/i} b_{i/i-1} / L^2 \\
r_{10}^i &= 2G a_{i/i-1} \\
r_{11}^i &= 2G b_{i/i-1} \\
r_{12}^i &= -2G a_{i+1/i} \\
r_{13}^i &= -2G b_{i+1/i}
\end{aligned}
\right\} \qquad (5\text{-}38)
$$

Eqs. (5-27), (5-33) and (5-37) can be applied to derive all the coefficients required, if boundary conditions used to determine the initial values of each layer are given.

5.4 Model Implementation and Validation

The model developed was applied to examine the local stress distribution of the tapered laminate. The actual problem of interest to be solved involves partitioning the region about the drop-off into two zones as shown in Figure 5-4. The 2-zone model has 10 boundary conditions, related to five deflections at each end of the model. The additional constraints on the system are the continuity requirements at the boundary between zone 1 and 2, where displacement and force must be continuous. To solve the 2-zone problem, a set of 20 equations is set up and the initial coefficients in each zone can be determined. Based on these initial coefficients, all of the coefficients can be determined. Thus, the displacements, strains, and stresses can be determined. All of the constraints can be reduced by the definitions of the assumed displacements. For example in layer 5

$$u_5(x) = \sum_{n=0}^{\infty} C_n^5 \left(\frac{x}{L}\right)^n \tag{5-40}$$

Thus the displacements at the boundary for any layer i are given by

$$\begin{aligned} u_i(0) &= C_0^i \\ u_i(L) &= \sum_{n=0}^{\infty} C_n^i \end{aligned} \tag{5-41}$$

where i = 1, 2, ... 5, designating 0^0 as zero. The origin of x-coordinate for zone 1 is located 10H away from the foremost ply drop off (at the left side of Point C in Figure 5-7), and the origin of x-coordinate for zone 2 is just located at the ply drop off (Point C).

The force, in each layer, can be determined by

$$\begin{aligned} F_i(x) &= \sigma(x)t(x) \\ &= E_i\varepsilon(x)t(x) \\ &= E_i u_i'(x)t(x) \\ &= E_i t(x)\sum_{n=1}^{\infty}\frac{C_n^i n}{L}\left(\frac{x}{L}\right)^{n-1} \end{aligned} \tag{5-42}$$

Thus the forces per unit width at the boundaries in each layer are given by

$$\begin{aligned} F_i(0) &= E_i t_i(0)\frac{C_1^i}{L} \\ F_i(L) &= E_i t_i(L)\sum_{n=1}^{\infty}\frac{nC_n^i}{L} \end{aligned} \tag{5-43}$$

For a 2-zone problem as shown in Figure 5-4, total of 20 constraints must be applied. Each zone generates ten unknowns (C_0^i and C_1^i, i = 1, 2, ... 5). The 20 constraints can be broken into constraints on displacements at the boundaries, continuity of displacements between zones, and continuity of forces between zones. For this problem, the 20 constraints are:

- Boundary Conditions (10)

1. Left boundary condition on each ply and resin layer (total 5)
2. Right boundary condition on each ply and resin layer (total 5)

- Displacement continuity conditions (5)

3. Displacement continuity between zone 1 and 2 in each ply and resin layer

- Force continuity conditions (5)

4. Force continuity between zone 1 and 2 in each ply and resin layer

To demonstrate the capability of the shear-lag model developed, an application of the model to predict interlaminar stresses about the ply drop region in the uniaxially loaded tapered laminate was made. All plies in the model as shown in Figure 5-7 are 0° unidirectional glass/epoxy with material properties given in Table 5-1, which, for convenience of comparison and evaluation, are quoted from Ref.14. Also, thin (0.1-t_{ply} thick) resin layers are included in the model to allow for the direct calculation of interlaminar stresses. In this problem, an eight-ply laminate is tapered to four plies in a symmetric fashion. The laminate is 50.8 mm (2 in) long in the thick section, 50.8 mm (2 in) long in the thin section, 25.4 mm (1in) wide and has a taper ratio of 10:1 (The

distance between the ply drop-off steps is 10 times ply thickness). Uniaxial tension is applied by fixing thicker end of the laminate and applying an axial displacement of 0.0254 mm (0.001in) at the other end. Convergence of the shear-lag model is controlled by the term at which the infinite series in Eq. (5-21) are terminated. Figure 5-8 indicates the peak values of interlaminar shear stress in the top resin layer using 5, 10, 15 and 20 terms in the series. For this analysis the series will be truncated at 20 terms.

Table 5-1 Material Properties

Glass/Epoxy Unidirectional Tape			Resin
Extensional Moduli, msi			Young's Modulus, msi
$E_L = 6.4$	$E_T = 1.8$	$E_N = 1.8$	$E = 0.57$ msi
Shear Moduli, msi			Shear Moduli, msi
$G_{LT} = 0.65$	$G_{TN} = 0.65$	$G_{NL} = 0.60$	$G = 0.21$
Poisson's Ratios			Poisson's Ratio
$\nu_{LT} = 0.29$	$\nu_{LN} = 0.29$	$\nu_{TN} = 0.50$	$\nu = 0.37$
			Tensile Strength
			$\sigma_0 = 9$ ksi

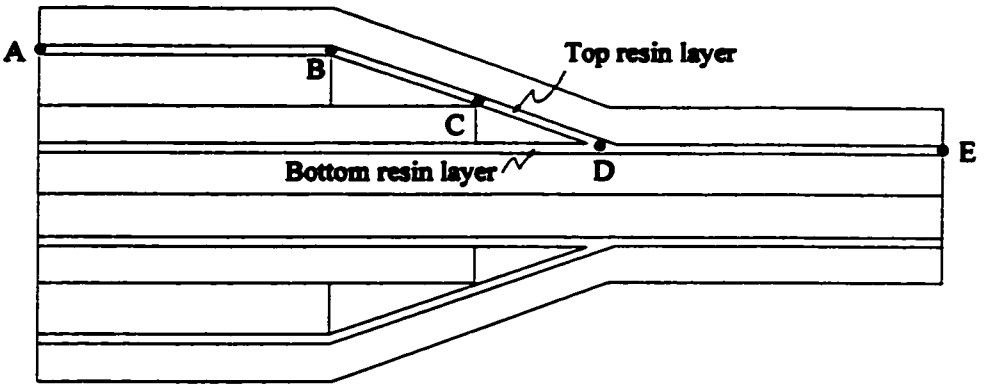

Figure 5-7 Schematic drawing of tapered laminate

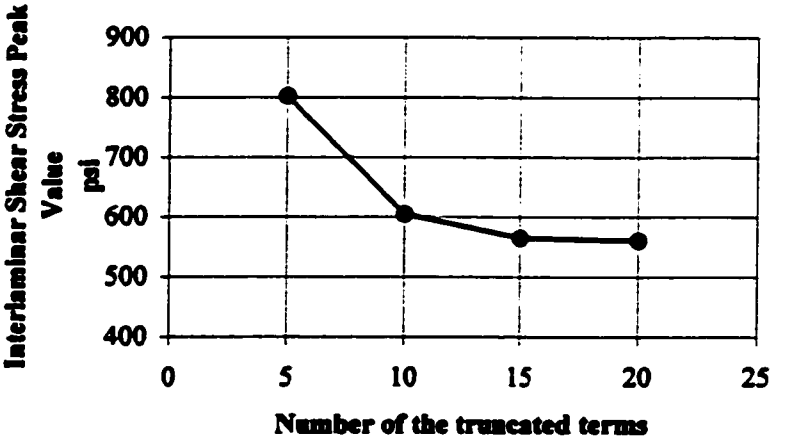

Figure 5-8 Convergence for the shear-lag model

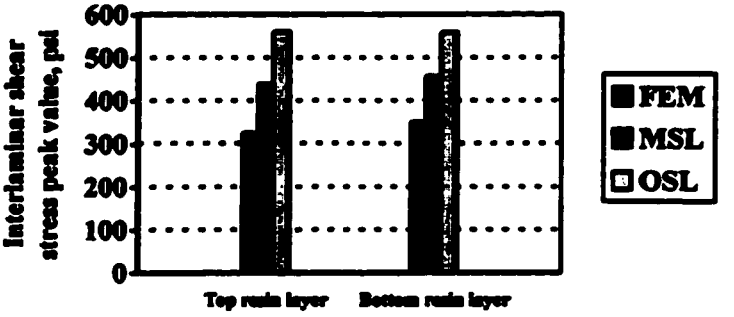

Figure 5-9 Comparison of different models for interlaminar shear peak values in the top resin layer (left) and bottom resin layer (right). FEM: Partial Hybrid Finite Element Method; MSL: Modified Shear-Lag model; and OSL: Ordinary Shear-Lag model

Figure 5-9 illustrates interlaminar shear peak values about the foremost ply drop region (Point C), where a critical load transferring occurs and, it further induces delamination failure at the interfaces (ABCDE) between dropped plies and continuous plies. Improvement of MSL model over OSL model is observed with direct comparison of estimations of stresses components against the partial hybrid finite element solution, which has proved to be effective in analysis of laminated composites as indicated in the former chapters of the thesis. Predictions by both shear-lag models agree well with finite element solution, with results obtained from MSL being closer to the stress state rendered by FEM. Over the range of dropped ply region as shown in Figures 5-10 and 5-11, it is indicated that about 26 to 43 percent of improvement in the magnitudes of interlaminar stress components is found with the present model.

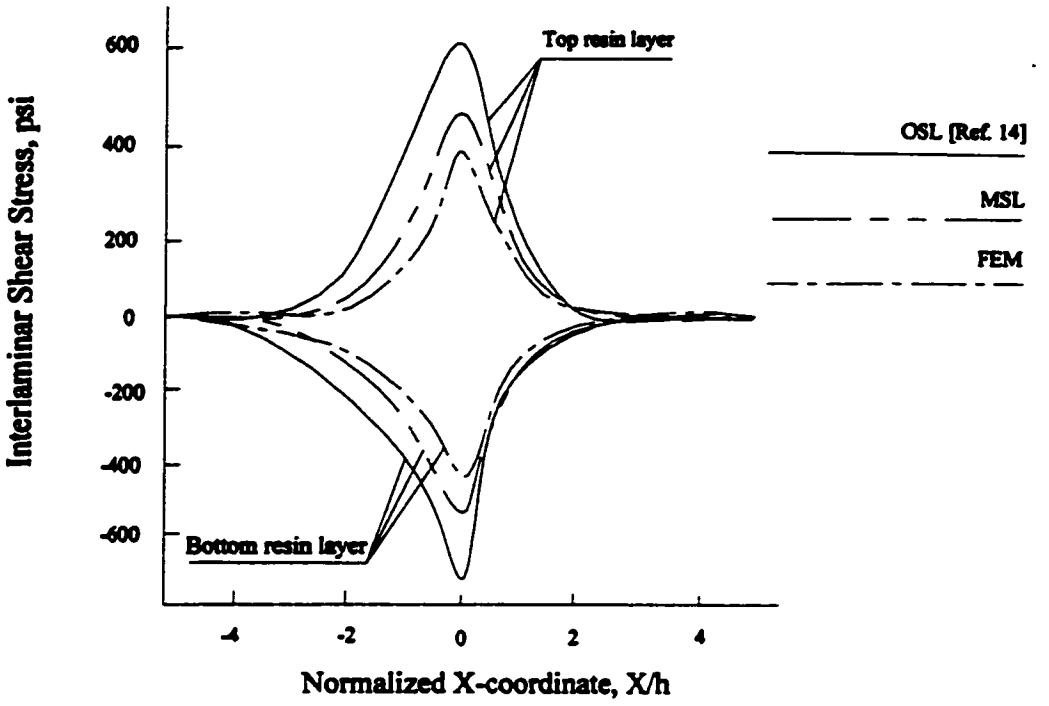

Figure 5-10 Interlaminar shear stress distributions

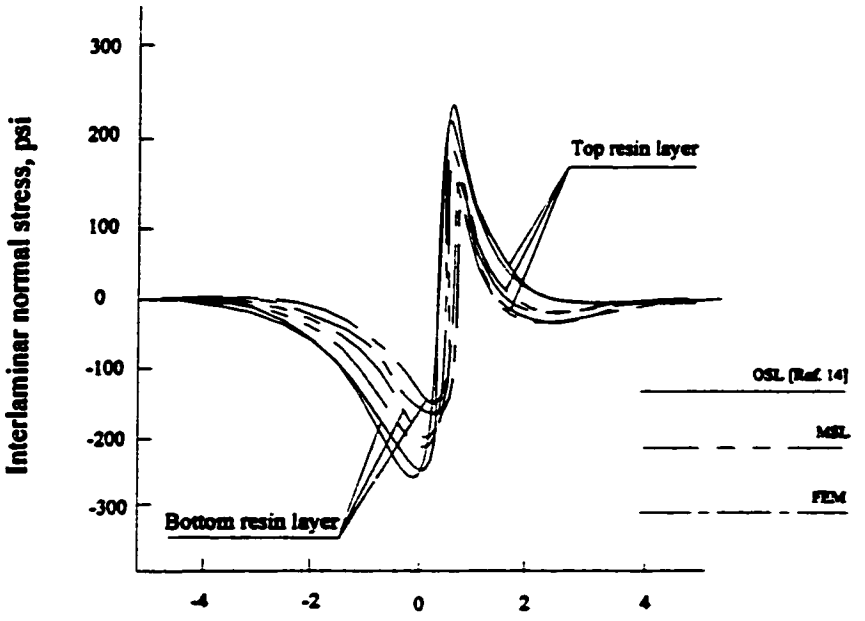

Figure 5-11 Interlaminar normal stress distributions

5.5 Summary

The modified shear-lag model developed demonstrates through the example studied its significant advantages over conventional shear-lag theory, both in computational accuracy and in application capability. Implementation of the model to analysis of interlaminar stresses at the critical location in the tapered laminate provides a closer solution to the true one rendered with finite element method. Majority of the stress values were captured by the current model. With the confidence in applying this model to prediction of a stress state in the tapered laminate, the model, based upon its essential assumptions, can also be further extended to conduct delamination initiation and propagation analysis of the tapered laminate.

It is of note that although the new model is capable of providing a more realistic prediction than the ordinary model, irrespective of the stiffness value of the ply and the resin layer, some limitations are inherent in the model. Since the assumptions allow both plies and resin layers to sustain tension and shearing only, the model is unable to address problems with transverse loading.

In the local analysis of tapered laminate, a two-zone problem was considered. The finite element model provided the boundary conditions at the two ends of the local model, but only the deflections along x-direction were imposed on each layer of the local shear-lag model to approximate solutions.

The convergence for the shear-lag model is also dependent of the numbers of the truncated terms applied. A good approximation can be made by at least 15 terms for the serials in the model.

Chapter 6

CONCLUSIONS AND RECOMMENDATIONS

Combined numerical and experimental analyses have been conducted to investigate stress distributions and delamination behavior of the tapered composite laminate having internal drop plies at certain locations of the laminate. Delamination initiation and propagation of the laminate are in general characterized by an interlaminar stress state at the critical interfaces and a strain energy release rate. On the basis of the critical and comprehensive review on the tapered composite, the partial hybrid stress finite elements offering a high capability in analysis of composite laminates, together with the modified shear-lag model, were developed as tools for examining the interlaminar stress state created by the internal ply drops. The interply resin was simulated at the critical ply interfaces in all the models considered. Interlaminar fracture behavior of the tapered laminate was studied based on modeling the laminate as a generalized plane deformation problem. The formulated quasi three-dimensional partial hybrid elements were accordingly applied in order to reduce computing efforts involved in calculating the strain energy release rate of delamination. *J*-integral, which is equal to G in the context of linear elastic fracture mechanics (LEFM), was introduced to evaluate strain energy release rates associated with delamination initiation and propagation in the tapered laminate. An experimental investigation was carried out to validate the analytical models.

The following conclusions were drawn based on the results of the models analyzed:

1. Proposed partial hybrid stress finite elements have been demonstrated to be advantageous over the counterpart elements through their usage in analysis of tapered laminated composites, which has been validated numerically and experimentally.
2. A simple and innovative shear-lag model shows a significant improvement over the conventional shear-lag theory, both in computational accuracy and in application capability. The true interlaminar stress magnitudes in the laminate of interest have been better approximated by the current model than the existing shear-lag model.
3. Identity of resin layer(s) for modeling and analysis of the tapered laminate composite, which was validated both in the shear-lag model and finite element model, exhibits significant influences on stress and delamination results.
4. Failure in the tapered laminates with negligible free-edge effects is caused by the interlaminar shear stress, τ_{xz}, and initiates at the bottom of the foremost ply drop step.
5. In simulation of interlaminar fracture behavior a transverse matrix crack occurring at ply drop locations must be taken into account in order to validate the model properly with experimental observations.
6. Delamination analysis using interfacial model presents a conservative result for the characterization of delamination initiation and propagation.
7. Structural performance of tapered laminates is affected by many parameters, but, of them, material and geometric properties of the resin layer proved to be significant factors; in this regard, increase of resin layer toughness, increase of the thickness

value of resin layer, full or partial interleaving along the critical interface are prominent means of improving the fracture resistant performance.

8. Von Mises derivative criterion proved to be suitable as an effective means for determining delamination strength in the tapered laminated composite.

The contributions made in the thesis are summarized below:

1. The first of its kind review article on thickness tapered laminated composites, which was published on *Composites Science and Technology*, Vol. 60 (2000), pp. 2643-2657, elaborates advances achieved in the past two decades and tendency on analysis and design of tapered laminated composites. It is certainly beneficial to those who are of interest in study of this kind of structures.
2. As a significant contribution to the realm of partial hybrid elements, 5 novel and highly efficient elements, i.e. 3-D 6- & 15- node triangular prism elements, 3-D 6-node wedge element, and quasi 3-D 6-node triangular & 8- node quadrilateral elements, have been developed as to implement structural analysis of composite laminated plates.
3. Energy based *J*-integral approaches was proposed for the first time to account for interlaminar fracture behavior of the tapered laminate, which have proved to be an effective and competitive means of evaluating the strain energy release rate associated with such a crack tip as embedded in the tapered laminate.
4. A simple modified shear-lag model based upon its essential assumption has been developed, implemented and validated in examination of the interlaminar behavior of the composite laminate.

The following recommendations for the future study can be considered:

1. Formulation of crack tip elements based on partial hybrid stress method.
2. Nonlinear analysis of fracture behavior in the composite tapered laminate.
3. Accounting for manufacturing induced loads such as residual stresses due to thermal history for improved prediction of stress and fracture response.
4. Inclusions of contact and friction effects in calculation of strain energy release rate.
5. Idealization of analysis model for delamination from two-dimensional crack tip to three-dimensional crack plane.
6. Experimental program for whole and partial interleaving of tapered laminate at the critical interfaces so as to further validate predicted results shown in the model.

APPENDICES

A.1 Transformation of Stress and Strain From Material Coordinate to Global Coordinate System

Figure A-1 shows a sketch of the material coordinate (1, 2 and 3) and the global coordinate (x, y and z), respectively in the different regions. The stress and strain transformation from the global coordinate to the material coordinate can be written as

$$\begin{aligned} \{\sigma\} &= [T_\sigma]\{\bar{\sigma}\} \\ \{\varepsilon\} &= [T_\varepsilon]\{\bar{\varepsilon}\} \end{aligned} \tag{A-1}$$

where

$$\{\sigma\} = \begin{Bmatrix} \sigma_1 \\ \sigma_2 \\ \sigma_3 \\ \sigma_4 \\ \sigma_5 \\ \sigma_6 \end{Bmatrix} \quad \text{and} \quad \{\bar{\sigma}\} = \begin{Bmatrix} \sigma_{xx} \\ \sigma_{yy} \\ \sigma_{zz} \\ \sigma_{yz} \\ \sigma_{xz} \\ \sigma_{xy} \end{Bmatrix} \tag{A-2}$$

$$\{\varepsilon\}=\begin{Bmatrix}\varepsilon_1\\ \varepsilon_2\\ \varepsilon_3\\ \varepsilon_4\\ \varepsilon_5\\ \varepsilon_6\end{Bmatrix} \quad \text{and} \quad \{\bar{\varepsilon}\}=\begin{Bmatrix}\varepsilon_{xx}\\ \varepsilon_{yy}\\ \varepsilon_{zz}\\ \gamma_{yz}\\ \gamma_{xz}\\ \gamma_{xy}\end{Bmatrix} \tag{A-3}$$

and $[T_\sigma]$ and $[T_\varepsilon]$ are 6x6 transformation matrix dependent on the rotation angle.

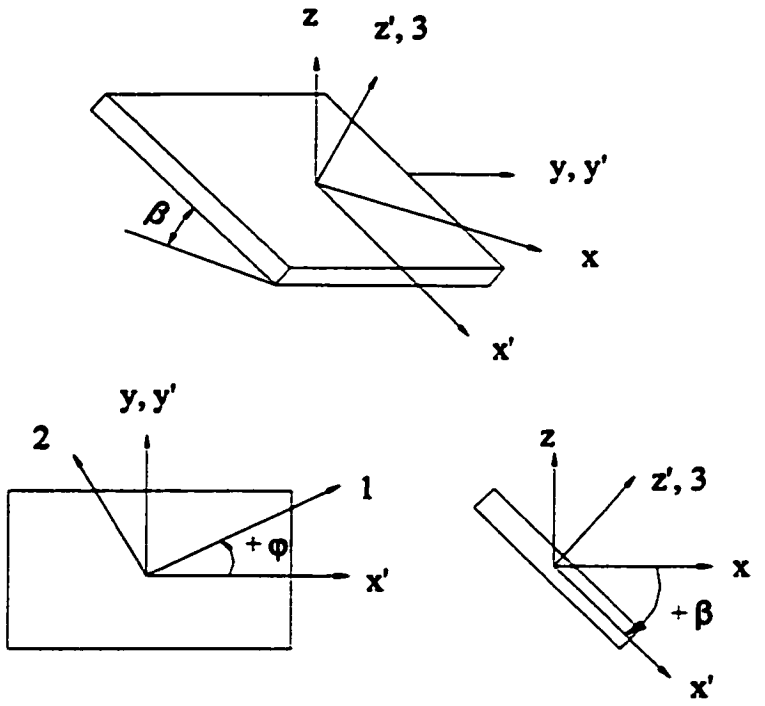

Figure A-1 Sketch of coordinate systems in the taper region - 1, 2, 3: Material coordinate system; x, y, z: Global coordinate system; φ: Ply orientation about 3-axis; β: Taper angle oriented about y-axis.

Explicit form of the matrices will be given in section A.3

Rewriting Equation (A-1), we have

$$\{\bar{\sigma}\} = [T_\sigma]^{-1}\{\sigma\}$$
$$\{\bar{\varepsilon}\} = [T_\varepsilon]^{-1}\{\varepsilon\} \tag{A-4}$$

Now let us consider stress and strain matrix transforming from the material coordinate to the global coordinate by rotating a negative angle. Then Equation (A-1) can be also rewritten as

$$\{\bar{\sigma}\} = [T_\sigma(-\theta)]\ \{\sigma\}$$
$$\{\bar{\varepsilon}\} = [T_\varepsilon(\theta)]\ \{\varepsilon\} \tag{A-5}$$

The relation of $[T_\sigma]$ and $[T_\varepsilon]$ can be written as

$$[T_\varepsilon(\theta)] = [T_\sigma(-\theta)]^T \tag{A-6}$$

A.2 Transformation of Stiffness Matrix From Material to Global Coordinate System

The stress and strain relationship in the global and material coordinates are expressed as

$$\{\bar{\sigma}\} = [\bar{Q}]\{\bar{\varepsilon}\}$$
$$\{\sigma\} = [Q]\{\varepsilon\} \tag{A-7}$$

where $[\bar{Q}]$ and $[Q]$ are the reduced stiffness matrices referring to global and material coordinates, respectively. Next, a relationship between $[\bar{Q}]$ and $[Q]$ can be established as follows:

$$\{\sigma\} = [Q]\{\varepsilon\}$$
$$\{\bar{\sigma}\} = [T_\sigma(-\theta)]\{\sigma\} = [T_\sigma(-\theta)][Q]\{\varepsilon\} \tag{A-8}$$
$$= [T_\sigma(-\theta)][Q][T_\sigma(-\theta)]^T\{\bar{\varepsilon}\}$$

Comparing equation (A-6) and (A-8), we have

$$[\bar{Q}] = [T_\sigma(\theta)][Q][T_\sigma(-\theta)]^T \tag{A-9}$$

A.3 Stiffness Matrix in the Tapered Region

Referring to Figure A-1, transformation matrix in the tapered region rotated a taper angle β about the y-axis can be written as

$$[T_\sigma]_y = \begin{bmatrix} c_y^2 & 0 & s_y^2 & 0 & -2s_yc_y & 0 \\ 0 & 1 & 0 & 0 & 0 & 0 \\ s_y^2 & 0 & c_y^2 & 0 & 2s_yc_y & 0 \\ 0 & 0 & 0 & c_y & 0 & s_y \\ s_yc_y & 0 & -s_yc_y & 0 & c_y^2 - s_y^2 & 0 \\ 0 & 0 & 0 & -s_y & 0 & c_y \end{bmatrix} \quad \text{(A-10)}$$

where $s_y = \sin\beta$ and $c_y = \cos\beta$

The stiffness matrix of 0°ply, [Q] is given as

$$[Q] = \begin{bmatrix} Q_{11} & Q_{12} & Q_{13} & 0 & 0 & 0 \\ Q_{12} & Q_{22} & Q_{23} & 0 & 0 & 0 \\ Q_{13} & Q_{23} & Q_{33} & 0 & 0 & 0 \\ 0 & 0 & 0 & Q_{44} & 0 & 0 \\ 0 & 0 & 0 & 0 & Q_{55} & 0 \\ 0 & 0 & 0 & 0 & 0 & Q_{66} \end{bmatrix} \quad \text{(A-11)}$$

where

$$Q_{11} = \frac{1 - \nu_{23}\nu_{32}}{E_2 E_3 \Delta}$$

$$Q_{12} = \frac{\nu_{12} + \nu_{32}\nu_{13}}{E_1 E_3 \Delta}$$

$$Q_{13} = \frac{\nu_{13} + \nu_{12}\nu_{23}}{E_1 E_2 \Delta}$$

$$Q_{22} = \frac{1 - \nu_{13}\nu_{31}}{E_1 E_3 \Delta}$$

$$Q_{23} = \frac{\nu_{23} + \nu_{21}\nu_{13}}{E_1 E_2 \Delta}$$

$$Q_{33} = \frac{1 - \nu_{12}\nu_{21}}{E_1 E_2 \Delta} \qquad \text{(A-12)}$$

$$Q_{44} = G_{23}, \quad Q_{55} = G_{31}, \quad Q_{66} = G_{12}$$

and

$$\Delta = \frac{1 - \nu_{12}\nu_{21} - \nu_{23}\nu_{32} - \nu_{31}\nu_{13} - 2\nu_{21}\nu_{32}\nu_{13}}{E_1 E_2 E_3} \qquad \text{(A-13)}$$

E_1, E_2 and E_3 are Young's moduli in the 1-, 2- and 3-directions; G_{12}, G_{23} and G_{31} are shear moduli in 1-2, 2-3 and 3-1 planes, respectively. The Poisson's ratio ν_{ij} is

$$\nu_{ij} = -\frac{\varepsilon_i}{\varepsilon_j} \qquad \text{(A-14)}$$

The corresponding stiffness matrix $[\overline{Q}]$ is given by Equation (A-9) as

$$[\overline{Q}] = [T_\sigma(-\beta)]_y [Q][T_\sigma(-\beta)]_y^T \tag{A-15}$$

where

$$\begin{aligned}
\overline{Q}_{11} &= Q_{11}c_y^4 + 2(Q_{13} + 2Q_{55})s_y^2 c_y^2 + Q_{33}s_y^4 \\
\overline{Q}_{12} &= Q_{12}c_y^2 + Q_{23}s_y^2 \\
\overline{Q}_{13} &= (Q_{11} + Q_{33} - 4Q_{55})s_y^2 c_y^2 + Q_{13}(s_y^4 + c_y^4) \\
\overline{Q}_{14} &= 0 \\
\overline{Q}_{15} &= -[Q_{11}c_y^2 - Q_{33}s_y^2 - (Q_{13} + 2Q_{55})(c_y^2 - s_y^2)]s_y c_y \\
\overline{Q}_{16} &= 0 \\
\overline{Q}_{22} &= Q_{22} \\
\overline{Q}_{23} &= Q_{12}s_y^2 + Q_{23}c_y^2 \\
\overline{Q}_{24} &= 0 \\
\overline{Q}_{25} &= -(Q_{12} - Q_{23})s_y c_y \\
\overline{Q}_{26} &= 0 \\
\overline{Q}_{33} &= Q_{11}s_y^4 + 2(Q_{13} + 2Q_{55})s_y^2 c_y^2 + Q_{33}c_y^4 \\
\overline{Q}_{34} &= 0 \\
\overline{Q}_{35} &= -[Q_{11}s_y^2 - Q_{33}c_y^2 + (Q_{13} + 2Q_{55})(c_y^2 - s_y^2)]s_y c_y \\
\overline{Q}_{36} &= 0 \\
\overline{Q}_{44} &= Q_{44}c_y^2 + Q_{66}s_y^2 \\
\overline{Q}_{45} &= 0 \\
\overline{Q}_{46} &= -(Q_{66} - Q_{44})s_y c_y \\
\overline{Q}_{55} &= (Q_{11} + Q_{33} - 2Q_{13})s_y^2 c_y^2 + Q_{55}(c_y^2 - s_y^2)^2
\end{aligned} \tag{A-16}$$

$$\overline{Q}_{36} = 0$$
$$\overline{Q}_{66} = Q_{66}c_y^2 + Q_{44}s_y^2$$

References

1. Kemp, B.L., and Johnson, E.R., "Response and failure analysis of graphite-epoxy laminate containing terminating internal plies", Proceedings of the AIAA/ASME/ASCE/AHS 26th Structures, Structural Dynamics, and Materials Conference, Pt. 1, AIAA, New York, April 1985, pp.13-24; AIAA Paper 85-0608.

2. Curry, J.M., Johnson, E.R., and Starnes Jr, J.H., "Effect of dropped plies on the strength of graphite-epoxy laminates", AIAA Journal, Vol 30, No. 2, February 1992, 449-456.

3. Hoa, S.V., Du, B.L., and Vu-Khanh, T., "Interlaminar stresses in tapered laminates", Polymer Composites, October 1988, Vol.9, No. 5, 337-344.

4. Fish, J.C. and Lee, S.W., "Delamination of tapered composite structures", Engineering Fracture Mechanics Vol. 34, No. 1, pp43-54, 1989.

5. Salpekar, S.I., Raju, I.S., and O'Brien, T.K., "Strain-energy-release rate analysis of delamination in a tapered laminate subjected to tension load", J. of Composite Materials, Vol. 25, Febrary 1991, pp 118-141.

6. Murri, G.B., O'Brien, T.K., and Salpekar, S.A., "Tension fatigue of glass/epoxy and graphite/epoxy tapered laminates", American Helicopter Society Journal, Vol. 38, No. 1, 1993, pp. 29-37.

7. Armanios, E.A. and Parnas, L., "Delamination analysis of tapered laminated composites under tensile loading", Composite Materials: Fatigue and Fracture (Third Volume). ASTM STP 1110. T.K. O'Brien, Ed., American Society for Testing and Materials, Philadephia, 1991, pp340-358.

8. Murri, G.B., Salpekar, S.A., and O'Brien, T.K., "Fatigue delamination onset prediction in unidirectioal tapered laminates", Composite Materials: Fatigue and Fracture (Third Volume). ASTM STP 1110. T.K. O'Brien, Ed., American Society for Testing and Materials, Philadelphia, 1991, pp312-339.

9. Vizzini, A.J. and Lee, S.W., "Damage analysis of composite tapered beams", Journal of The American Helicopter Society, Vol. 40, No. 2, April 1995, pp. 43-49.

10. Wisnom, M.R., Jones, M.I., Cui, W., "Failure of tapered composites under static and fatigue tension loading", AIAA Journal 33, No. 5, May 1995, p 911-918.

11. Wisnom, M.R., Dixon, R., and Hill, G., "Delamination in asymmetrically tapered composites loaded in tension", Composite Structures 35 (1996) 309-322.

12. Wisnom, M.R., Jones, M.I. and Cui, W.,"Delamination in composite with terminating internal plies under tension fatigue loading", Composite Materials: Fatigue and Fracture-Fifth Volume, ASTM STP 1230, R.H. Martin, Ed., American Society for Testing and materials, Philadelphia, 1995, pp.486-508.

13. Harrison, P.N. and Johnson, E.R., "A mixed variational formulation for interlaminar stresses in thickness-tapered composite laminates", Int. J. Solids Structures Vol. 35, No. 16, pp.2377-2399, 1996.

14. Vizzini, A.J., "Shear-lag analysis about an internally-dropped ply", Journal of Reinforced Plastics and Composites, Vol. 16, No. 1/1997.

15. Varughese, B., and Mukherjee, A., "Analysis of Tapered laminated composites with non-symmetric lay-up", Journal of Reinforced Plastics and Composites, Vol. 16, No. 7/1997.

16. Murri, G.B., O'Brien, T.K., and Rousseau, C.Q., "Fatigue life methodology for tapered composite flexbeam laminates", Journal of the American Helicopter Society, Vol. 43, No. 2, April 1998, pp. 146-155.

17. Rhim J. and Vizzini, A.J., "Analysis of interlaminar stresses in an internally-dropped ply region", Proceedings of the 11th International Conference on Composite Materials, Queensland, Australia, July 1997.

18. Mortensen F. and O.T. Thomsen, " A Simple approach for the analysis of embedded ply drops in composite and sandwich laminates", Composite Science and Technology, Vol. 59, 1999, pp. 1213-1226.

19. Wu, C.M.L. and Webber, J.P.H., "Analysis of tapered (in steps) laminated plates under uniform in-plane load", Composite Structures 5 (1986) 87-100.

20. Wu, C.M.L., "Non-linear analysis of tapered (in steps) laminated plate under uniform in-plane load", Composite Structures 7 (1987) 205-223.

21. Miravete, A., "Strain and stress analysis in tapered laminated composite structures", Composite Structures 16 (1990) 64-84.

22. Mukherjee, A. and Varughese, B., "A ply drop-off element for inclusion of drop-off in the global analysis of layered composite structures", Computers & Structures Vol. 54, No. 5, pp. 865-870, 1995.

23. Daoust, J. and Hoa, S.V., "Parameters affecting interlaminar stresses in tapered laminates under static loading conditions", Polymer Composites, October 1989, Vol. 10, No. 5, 374-383.

24. Llanos, A.S. and Vizzini, A.J., "The effect of film adhesive on the delamination strength of tapered composites ", Journal of Composite Materials, Vol. 26, No. 13, 1992, pp. 1968-1983.

25. Thomas, D.M, Webber, P.H., "A design study into the delamination behavior of tapered composites", Composite Structures 27 (1994) 379-388.

26. Cui, W., Wisnom, M.R., and Jones, M., "Effect of step spacing on delamination of tapered laminates", Composite Science and Technology 52 (1994) 39-46.

27. Vizzini, A.J., "Influence of realistic ply-drop geometries on interlaminar stresses in tapered laminates", Composite Materials: Fatigue and Fracture-Fifth Volume, ASTM STP 1230, R.H. Martin, Ed., American Society for Testing and Materials, Philadelphia, 1995, pp.467-485.

28. Botting, A.D, Vizzini, A.J., Lee, S.W., "Effect of ply-drop configuration on delamination strength of tapered composite structures", AIAA J., Vol. 34, No. 8, August 1996, pp. 1650-1656.

29. Manne, P.M. and Tsai, S.W., "Plydrops for tapered design optimization of composite plates", Proceedings of the 11th International Conference on Composite Materials, Queensland, Australia, July 1997.

30. Cairns, D.S., Mandell, J.F., Scott, M.E., and Maccagnano, J.Z., "Design considerations for ply drops in composite structures", Proceedings of the 11th International Conference on Composite Materials, Queensland, Australia, July 1997.

31. Hofman, B.B. and Ochoa, O.O., "Shear deformable user finite element for MARC to model composite with taper", Proceedings of the 12th American Society for Composites, Dearborn, Michigan, 1997.

32. Vizzini, A.J., "Strength of laminated composites with internal discontinuities parallel to the applied load, AIAA Journal, Vol.30, No. 6, June 1992.

33. Pian, T.H.H. and Tong, P., "Basis of finite element methods for solid continua", International Journal for Numerical Methods in Engineering, Vol. 1, 3-28 (1969).

34. Pian, T.H.H., "Derivation of element stiffness matrices by assumed stress distributions", AIAA J. 2, p.1333-1336, 1964.

35. Poon, C.Y., Ruiz, C., and Allen, C.B., "Finite element analysis of a tapered composite", Composite Science and Technology 51 (1994) 429-440.

36. Hoa, S.V. and Feng, W., "Hybrid finite element method for stress analysis of laminated composites", Kluwer Academic Publishers, 1998.

37. Lekhnitskii, S.G., "Theory of elasticity of an anisotropic elastic body", Holden-Day, Inc. San Francisco, 1963.

38. Reddy, J.N., Murty, A.V.K., "Composite structures", Springer-Verlag, Narosa Publishing House, 1992.

39. Fish, J.C. and Vizzini, A.J., "Delamination of ply-drop configurations", Composite Materials: Testing and Design (Eleven Volume), ASTM STP 1206. E.T. Camponeschi, Jr., Ed., American Society for Testing and Materials, Philadelphia, 1993, pp. 323-332.

40. Fish, J.C. and Vizzini, A.J., "Tailoring concepts for improved structural performance of rotorcraft flexbeams", Composites Engineering, Vol. 2, No. 5-7, pp. 303-312, 1992.

41. Thomsen, O.T., Rits, W., Eaton, D.C.G. and Brown, S."Ply drop-off effects in CFRP/honeycomb sandwich panels- theory", Composite Science and Technology, Vol. 56, 1996, 407-422.

42. Thomsen, O.T., Rits, W., Eaton, D.C.G., Dupont, O. and Queekers, P. "Ply drop-off effects in CFRP/honeycomb sandwich panels- experimental results", Composite Science and Technology, Vol. 56, 1996, 423-437.

43. Thomsen, O.T., Mortensen, F. and Frostig, F., " Interface failure at ply drops in CFRP/honeycomb sandwich panels", Journal of Composite Materials, Vol. 34, No. 02/2000, pp. 135-157.

44. Pogue, W. R. and Vizzini, A.J., "Structural tailoring techniques to prevent delamination in composite laminates", Journal of the American Helicopter Society, Vol. 35, No. 4, 1990.

45. Ochoa, O.O. and Chan, W.S., " Tapered laminates: A study on delamination characterization", Proceedings of the American Society for Composites Third Technical Conference, Technomic, Lancaster, PA, September 1988, pp. 633-641.

46. Trethewey, R.B, Gillespie, J.W., and Wilkins, D.J., "Interlaminar performance of tapered composite laminates", Proceedings of the American Society for Composites Fifth Technical Conference, Technomic, Lancaster, PA, June 1990, pp. 361-372.

47. Adams, D. F., Ramkumar, R.L., and Walrath, D.E., "Analysis of porous laminates in the presence of ply drop-offs and fastener holes", Northrop Technical Report NOR 84-113, Northrop Corporation, Hawthorne, CA 90250, and the University of Wyoming, laramie, Wyoming 820271, May 1984.

48. ESDU Data Item 91003, "Delamination of tapered composites", ESDU international Plc., London, November 1991.

49. Davila, C.G. and Johnson, E.R., "Analysis of delamination initiation in post-buckled dropped-ply laminates", AIAA Journal, Vol. 31 (4), 1993, pp. 721-727.

50. Pian, T.H.H. & Chen, D.P. "On the suppression of zero energy deformation modes", *Int. J. Num. Meth. Eng.*, **19**, pp.1741-1752, 1983.

51. Feng, W., Hoa, S.V. & Huang, Q. "Classification of stress modes in assumed stress fields of hybrid finite element", *Int. J. Num. Meth. Eng.*, **40**, pp. 4313- 4339, 1997.

52. Reddy, C.T., "Improved three point integration schemes for triangular finite elements", *Int. J. Num. Meth. Eng.*, **12**, pp. 1890-1896 (1978).

53. Raju, I.S. & Crews, J. H., Jr., "Three-dimensional analysis of [0/90]$_s$ laminates with a central circular hole", *Composites Technol. Rev.* 1982, No. 4, (4), pp. 116-24.

54. Spilker, R. L., "High order three-dimensional hybrid-stress elements for thick-plate analysis", Int. J. Num. Meth. Enggr., Vol. 17, 53-69, 1981.

55. Jing, H. and Liao, M., "Partial hybrid stress element for the analysis of thick laminated composite plates", International J. for Numerical Methods in Engineering, Vol. 28, 2813-2827, 1989.

56. Pagano, N J., "Exact solutions for composite laminates in cylindrical bending", J. Compos. Mater., 3, 398-411, 1969.

57. Pagano, N.J. and Hatfield, S.J., "Elastic behavior of multiplayered bi-directional composites", AIAA J., 10, 931-933, 1972.

58. Reddy, J. N., "Energy and variational methods in applied mechanics", John Wiley and Sons, New York, 1984.

59. Amijima, S. and Adachi, T., "Nonlinear stress-strain response of laminated composites", J. Composite Materials, Vol. 13, 1979, p.206.

60. Hahn, H.T. and Tsai, S.W., " Nonlinear elastic behavior of unidirectional composite laminae" J. Comp. Mat. , Vol. 7, 1973, p. 102.

61. Hahn, H.T, "Nonlinear behavior of laminated composites", J. Comp. Mat., Vol. 7, 1973, p.257.

62. Ditcher, A.K., Rhodes, F.E. and Webber, J.P.H., " Nonlinear stress-strain behavior of carbon fibre reinforced plastic laminates", J. Strain Analysis, Vol. 16, No 1, 1981.

63. Xie, M. and Adams, D.F. " A nonlinear finite element analysis for composite materials", Finite Elements in Analysis and Design, 22 (1996) 211-223.

64. Chang, F. and Scott, R.A., " Failure Strength of nonlinearly elastic composites containing a pin loaded hole", J. Comp. Mat., Vol. 18, 1984.

65. Shokrieh, M.M. and Lessard, L. B., " Effects of material nonlinearity on the three-dimensional stress state of pin-loaded composite laminates", J. Comp. Mat., Vol. 30, No. 7, 1996.

67. Zienkiewicz, O.C., " The finite element method", Mcgraw-Hill Book Company (UK) Limited, 1983.

68. Sun, C.T. and Jih, C.J., "On strain energy release rates for interfacial cracks in bi-material media", Engineering Fracture Mechanics, Vol. 28, No.1, pp. 13-20, 1987.

69. Yan, X., Du, S. and Wang, D., "J-integral criterion of delamination onset in toughened matrix composite laminates", Engineering Fracture Mechanics, Vol. 40, No. 1, pp. 67-74, 1992.

70. Rice, J.R., "A path independent integral and the approximate analysis of strain concentrations by notches and cracks", J. Appl. Mech., Vol. 35, pp. 397-386, 1968.

71. Ozdil, F. and Carlsson, L.A., "Finite element analysis of interleaved DCB specimen, Engineering Fracture Mechanics", Vol. 41, No. 4, pp. 475-485, 1992.

72. Albert H. Cardon, "Durability analysis of structural Composite systems", AIB-Vincotte 1995.

73. Horst, B., "Advanced aerospace materials", Berlin ; New York : Springer-Verlag, c1992

74. Han, J. and Hoa, S.V., "A three-dimensional multiplayer composite finite element for stress analysis of composite laminates", International Journal for Numerical methods in engineering, Vol. 36, pp. 3903-3914, 1993.

75. Johnson, M.J. and Sridharan, S., "Evaluation of strain energy release rates in delaminated laminates under compression", AIAA, Vol. 37, No. 8,954-963, 1999.

76. Pian, T.H.H. "Nonlinear creep analysis by assumed stress finite element methods", AIAA Journal, Vol. 12, No. 12, 1974, pp.1756.

77. Mau, S.T. P., Tong, and Pian, T.H.H., " Finite element solution for laminated thick plates", J. Composite Materials, Vol.6, April 1972, p.304.

78. T. H.H. Pian, D.P Chen, and D. Kang, " A new formulation of hybrid/mixed finite element, Computers & Structures, Vol. 16. No. 1-4. Pp.81-87, 1983.

79. T. H. H. Pian, " Finite elements based on consistently assumed stresses and displacements", Finite Elements in analysis and Design, Vol. 1, 1985, pp. 131-140.

80. P. Tong and T.H.H. Pian, "A variational principle and the convergence of a finite-element method based on assumed stress distribution", Int. J. Solids Structures, 1969, Vol. 5, pp. 463-472.

81. T.H.H. Pian, "Reflections and remarks on hybrid and mixed finite element methods", Hybrid and Mixed Finite Element Methods, Edited by S.N. Atluri, R.H. Gallaher, and O.C. Zienkiewicz, 1983, John Wiley & Sons, Ltd.

82. W.J. Liou and C.T. Shun, "A three-dimensional hybrid stress isoparametric element for the analysis of laminated composite plates", Computers & Structures, Vol. 25, No.2, pp 241-249, 1987.

83. R.L. Spilker, "Hybrid-stress eight-node elements for thin and thick multilayer laminated plates", International Journal for Numerical Methods in Engineering, Vol. 18, 801-828 (1982).

84. T.H.H. Pian, " State-of-the-art development of hybrid/mixed finite element method", Finite Elements in Analysis and Design, 21 (1995) 5-20.

85. Y. Yamada, S. Nakagiri, and K. Takatsuka, " Elastic-plastic analysis of saint-venant torsion problem by a hybrid stress model", International Journal for Numerical Methods in Engineering, Vol. 5, 193-207 (1972).

86. E. Reissner. "On mixed variational theorem and on shear deformable plate theory", International Journal for Numerical Methods in Engineering, Vol. 23, 193-198 (1986).

87. E. Reissner. "On certain mixed variational theorem and a proposed application", Short communications, 1984, John Wiley & Sons, Let.

88. C. Liao and J.S. Tsai, "Partial mixed 3-D element for the analysis of thick laminated composite structures", International Journal for Numerical Methods in Engineering, Vol. 35, 1521-1539 (1992).

89. Y. Yong and Y. Cho, " Higher-order, partial hybrid stress, finite element formulation for laminated plate and shell analyses", Computers & Structures, Vol. 57, N. 5, pp.817-827, 1995.

90. R.L. Spilker and T.H.H. Pian, " Hybrid-stress model for elastic-plastic analysis by the initial-stress approach", International Journal for Numerical Methods in Engineering, Vol. 14, 359-378 (1979).

91. H. Murakawa and S.N. Atluri, "Finite element solutions using hybrid finite elements based on a complementary energy principle", Journal of Applied Mechanics, Vol. 45, 1978, pp.539.

92. L. Carlsson and A. Aksoy, "Analysis of interleaved end-notched flexure specimens for measuring mode II fracture toughness", International Journal of Fracture 52:67-77, 1991.

93. C.S. Desai and J.F. Abel, " Introduction to the finite element method", Van Nostrand Reinhold Company, 1972.

94. Q. Huang, "Three dimensional composite finite element for stress analysis of anisotropic laminate structures", Ph.D. Dissertation, Concordia University, Montreal, Canada (1989).

95. J. Han, "Three dimensional multiplayer composite finite element for stress analysis of composite laminates", Ph.D. Dissertation, Concordia University, Montreal, Canada (1993).

96. W. Feng, "Development of partial hybrid finite elements for 3-D global/local analysis of laminated composite structures", 1998.

97. T.H.H. Pian, "Nonlinear analysis by assumed stress hybrid models", Theoretical and Applied Mechanics, Vol. 24, Proceedings of the 24th Japan National Congress for Applied Mechanics, 1974.

98. H. Owen, "Finite elements in plasticity, theory and practice", Pineridge Press Limited, Swansea, U.K., 1982.

99. K. Washizu, "Variational methods in elasticity and plasticity", Pergamon Press, 1968.

100. M.Kleiber, "Incremental finite element modelling in nonlinear solid mechanics", Ellis Horwood Limited, 1989.

101. A. Tabiei, Y. Jiang, "Woven fabric composite material model with material nonlinearity for nonlinear finite element simulation", Int. J. Solids and Structures, 36 (1999) 2757-2771.

102. W. Jordan, W. Bradley, and R. Moulton, " Relating resin mechanical properties to composite delamination fracture toughness", J. Comp. Mat., Vol. 23, 1989, pp.923.

103. M. Hojo, S. Ochiai, C. Gustafson, K. Tanaka, " Effect of matrix resin on delamination fatigue crack growth in CFRP laminates", Engineering Fracture Mechanics, Vol. 49, No.1, pp.35-47, 1994.

104. M. Oriunno, A. Frediani, and A. Lazzeri, "Influence of the constitutive characteristics of reins on the composite materials delamination", Engineering Fracture Mechanics, Vol. 55, No. 6, pp. 1001-1012, 1996.

105. S.C. Pradhan and T.E. Tay, "Three-dimensional finite element modelling of delamination growth in notched composite laminates under compression loading", Engineering Fracture Mechanics, Vol. 60, No. 2, pp. 157-171, 1998.

106. D.J. Chen, W.S. Chan, and B.P. Wang, "An efficient method to simulate one and two-dimensional delamination growth in composite laminates", J. Reinforced plastics and Composites, Vol. 15, 1996.

107. S. Kyung, S Han, and K. James, " The interlaminar fracture energy of glass fiber reinforced polyester composites", J. Comp. Mat., Vol. 15, 1981, p. 371.

108. T. Y. H. Yang and C.C. He, " Three-dimensional finite element analysis of free edge stresses and delamination of composite laminates", J. Comp. Mat., Vol. 28, No. 15, 1994.

109. E.D. Reedy, Jr., E.J. Mello and T.R. Guess, "Modelling the initiation and growth of delaminations in composite structures", J. Comp. Mat., Vol. 31, No. 8, 1997.

110. S.S. Wang, "Failure modes of interlaminar crack in quasi-isotropic fiber-reinforced composites containing a surface notch", Failure modes in Composites IV, Ed. By J.A Cornie, F.W. Crossman, The Metallurgical Society of AIME, 1977.

111. J. H. Crews, Jr., K.N. Shivakumar, and I.S. Raju, " Factors influencing elastic stresses in double cantilever beam specimens", Adhesivly bonded joints: testing, analysis, and design, ASTM STP 981, W.S. Johnson, Ed., American society for Testing and Materials, Philadelphia, 1988, pp. 119-132.

112. C. Hwu, C.J. Kao, and L.E. Chang, "Delamination fracture criteria for composite laminates", J. Comp. Mat., Vol. 29, No.5, 1995, pp. 1962.

113. D. Hitchings, P. Robinson and F. Javidrad, "A finite element model for delamination propagation in composites", Computers & Structures, Vol. 60, pp. 1093-1104, 1996.

114. P.E. Keary, L.B. Ilcewicz, C. Shaar, J. Trostle, "Mode I interlaminar fracture toughness of composites using slender double cantilevered beam specimens", J. Comp. Mat., Vol. 19, 1985, pp. 154.

115. R. J. Bankert, N. D. Lanbropoulos, M.S. Shephard, and S.S. Sternstein, " Thermoplastic matrix composites: Finite-element analysis of Mode I and Mode II failure specimens", Advances in thermoplastic matrix composite materials, ASTM STP 1044, G.M. Newaz, Ed., American Society for testing and Materials, Philadephia, 1989, pp. 73-90.

116. J. A Hinkley, N. J. Johnston, and T.K. O'brien, " Interlaminar Fracture toughness of thermoplastic composites", Advances in thermoplastic matrix composite materials, ASTM STP 1044, G.M. Newaz, Ed., American Society for testing and Materials, Philadephia, 1989, pp. 251-263.

117. M. Chiang and H. Chai, "Finite element analysis of interfacial crack propagation based on local shear, part I – near tip deformation", Int. J. Solids Structures Vol. 35, No. 9-10, pp. 799-813, 1998.

118. P. Tong, T.H.H. Pian, and S.J. Lasry, "A hybrid-element approach to crack problems in plane elasticity", Int. J. numerical method Engger. Vol. 7. 297-308, 1973.

119. I Jeon, B.W. Cha and S. IM, " Edge delamination in a laminated composite strip under generalized plane deformations", Int. J. Fracture, 77:95-110, 1996.

120. W. Chen and S. Yang, "Multilayer hybrid-stress finite element analysis of composite laminates with delamination cracks originating from transverse cracking", Engineering Fracture Mechanics", Vol. 54, No. 5, pp. 713-729, 1996.

121. F. Ozdil and L. Carlsson, "Plastic zone estimates in mode I interlaminar fracture of interleaved composites", Engineering Fracture Mechanics, Vol. 41, No.5, pp. 645-658, 1992.

122. B. P. Naganarayana, S.N. Atluri, "Energy-release-rate evaluation for delamination growth prediction in multi-plate mode of a laminate composite", Computational Mechanics 15 (1995) 443-459.

123. I. Sheinman and G. A Kardomateas, "Energy release rate and stress intensity factors for delaminated composite laminates", Int. J. Solids Structures, Vol. 34, No. 4, pp. 451-459, 1997.

124. E.F. Rybicki, D.W. Schmueser, and J. Fox, "An energy release rate approach for stable crack growth in the free-edge delamination problem", J. Comp. Mat. Vol. 11, 1977, p. 470.

125. N. Sela, O. Ishai and L. Sills, "The effect of adhesive thickness on interlaminar fracture toughness of interleaved CFRP specimens, Composites", Vol. 20, 1989, pp. 257-264.

126. B. Budiansky and J.R. Rice, "Conservation laws and energy-release rates", J. Applied Mechanics, 1973, pp.201.

127. B. Cotterell and A.G. Atkins, "A review of the J and I integrals and their implications for crack growth resistance and toughness in ductile fracture", Int. J. Fracture 81:357-372, 1996.

128. C.T. Sun and X.X. Wu, "On the J-integral in periodically layered composites", Int. J. Fracture 78:89-100, 1996.

129. M. Lu and F. Erdogan, "Stress intensity factors in two bonded elastic layers containing cracks perpendicular to and on the interface – I analysis", Engineering Fracture Mechanics, Vol. 18. No. 1, pp. 491-506, 1983.

130. M. He and J. Jutchinson, "Crack deflection at an interface between dissimilar elastic materials", Int. J. Solids Structures, Vol. 25, No. 9, pp. 1053-1067, 1989.

131. X. Han and T. Wang, "Interacting multiple cracks with complicated crack surface conditions", Int. J. Fracture, 82: R53-R57, 1996.

132. R.E. Smelser and M. E. Gurtin, "On the J-integral for bi-material bodies", Int. J. Fracture 13:1997.

133. M. D. Caprice and M. Oriunno and C. Vermeeren, "Evaluation of residual strength of Glare by experimental measurement of the J-integral", Engineering Fracture Mechanics, Vol. 49, No. 5, pp. 727-740.

134. S.J. Chu and C.S. Hong, " Application of the J_k integral to mixed mode crack problems for anisotropic composite laminates", Engineering Fracture Mechanics, Vol. 35, No. 6, pp. 1093-1103, 1990.

135. R. Mao and G. Sun, "A study of the interface between matrix crack and matrix-fiber interface", Engineering Fracture Mechanics, Vol. 51, No. 3, pp. 469-477, 1995.

136. T.K. Hellen, " On the method of virtual crack extensions", Int. J. Numerical Meth. Engr., Vol. 9, 187-207, 1975.

137. O. Ishai and H. Rosenthal, "Effect of selective adhesive interleaving on interlaminar fracture toughness of graphite/epoxy composite laminates", Composites, Vol. 19, 1988, pp. 49-54.

138. I.S. Raju and K.N. Shivakumar, " An equivalent domain integral method in the two-dimensional analysis of mixed mode crack problems', Engineering Fracture Mechanics, Vol.37, No. 4, pp. 707-725, 1990.

139. G.P. Nikishkov and S.N. Atluri, "An equivalent domain integral method for computing crack-tip integral parameters in non-elastic, thermo-mechanical fracture", Engineering Fracture Mechanics, Vol. 26, No. 6. Pp. 851-867, 1987.

140. S.J. Chu and C.T. Sun, "Energy release rate for a dynamically growing crack at the interface of dissimilar isotropic materials", Engineering Fracture Mechanics, Vol. 50. No. 3, pp. 369-375, 1995.

141. J. P. Hickerson, Jr., "Experimental confirmation of the J integral as a thin section fracture criterion", Engineering Fracture Mechanics, Vol. 9, pp. 75-85, 1977.

142. K. B. Broberg, "Critical review of some methods in nonlinear fracture mechanics", Engineering Fracture Mechanics, Vol. 50, No. 2, pp. 157-164, 1995.

143. G. Fernlund and J.K. Spelt, " Analytical method for calculating adhesive joint fracture parameters", Engineering Fracture Mechanics, Vol. 40, No. 1, pp. 119-132, 1991.

144. A. Saxena, " Nonlinear fracture mechanics for engineers", CRC Press LLC, 1998

145. K. Friedrich, "Application of fracture mechanics to composite materials", Composite materials series 6, Elsevier, 1989.

146. A. N. Atluri, "Computational methods in the mechanics of fracture", Elsevier Science Publishers, V.V., 1986.

147. K.H. Schwalbe, "The crack tip opening displacement in elastic-plastic fracture mechanics", Springer-Verlag Berlin, Heidelberg 1986.

148. N.J. Papano, " Interlaminar response of composite materials", Composite material series 5, Elsevier Science Publishers V. V., 1989.

149. J. N. Reddy and A. V. K. Murty, " Composite Structures, Testing, analysis and design", Narosa Publishing House, 1992.

150. N. J. Johnston, (Editor), "Toughened Composites", Symposium on toughened composites 1985, STP 937.

151. M.F. Kannien and C.H. Popelar, "Advanced fracture mechanics", Oxford Engineering Science Series 15, Oxford University Press 1985.

152. G. Zboinsk, "Application of the three-dimensional triangular-prism *hpq* adaptive finite element to plate and shell analysis", Computer & Structures, Vol. 65, No. 4, pp. 497-514, 1997.

153. J. No. Reddy, "An evaluation of equivalent-single-layer and layer-wise theories of composite laminates", Composite Structures 25 (1993) 21-35.

154. W.H. Chen and C.W. Wu, "On the J-integral for a pressurized crack in bonded materials", International Journal of Fracture 16 (1980) R47-51.

155. E. Carrera, "C^0 Reissner-Mindlin multiple-layered plate elements including zig-zag and interlaminar stress continuity", International Journal for Numerical Methods in Engineering, Vol. 39, 1797-1820 (1996).

156. T. Hughes and J. Akin, "Techniques for developing 'special' finite element shape functions with particular reference to singularities", International Journal for Numerical Methods in Engineering, Vol. 15, 733-751 (1980).

157. P. Gaudenzi, A. Mannini and R. Carbonaro, "Multi-layer higher-order finite element for the analysis of free-edge stresses in composite laminates", International Journal for Numerical Methods in Engineering, Vol. 41, 851-873 (1998).

158. X. Lu and D. Liu, "An interlaminar shear stress continuity theory for both thin and thick composite laminates, Journal of Applied Mechanics", Vol. 59, pp. 502-509.

159. H. Yu, "A higher-order finite element for analysis of composite laminated structures", Composite Structures 28 (1994) 375-383.

160. P. Gaudenzi, "A general formulation of higher-order theories for the analysis of laminated plate", Composite Structures 20 (1992) 103-112.

161. E. Rybicki and D. Schmueser, "Effect of stacking sequence and lay-up angle on free edge stresses around a hole in a laminated plate under tension", Journal of Composite Materials, Vol. 12 (1978) pp. 300-313.

162. L. Lee and D. Tu, "J-integral for delaminated composite laminates", Composites Sciences and Technology 47 (1993) 185-192.

163. V. ukadgaonker and D. Rao, "Stress distribution around triangular holes in anisotropic plates", Composite Structures 45 (1999) 171-183.

164. R. Barboni, R. Carbonaro and P. Gaudenzi, "On the use of a multiplayer higher-order theory for the stress analysis around a circular hole of laminates under tension" , Composite Structures 32(1995) 649-658.

165. I. S. Raju and J. Crews, "Interlaminar stress singularities at a straight free edge in composite laminates", Computers & Structures, Vol. 14, No. 1-2, pp. 21-28, 1981.

166. Z. Petrossian and M. Wisnom, "Parametric study of delamination in composites with discontinuous plies using an analytical solution based on fracture mechanics", Composites Part A 29A 403-413, 1997.

167. F. Hu, C. Soutis and E. Edge, "Interlaminar stress in composite laminates with a circular hole", Composite Structures 37 (1997) 223-232.

168. A. Khan and S. Yuan, "A three-dimensional finite element program for prediction of crack initiation and growth", Computers & Structures, Vol. 31, No.3, pp.439-444, 1989.

169. M. Savoia and J. Reddy, "A variational approach to three-dimensional elasticity solutions of laminated composite plates", Journal of Applied Mechanics, Vol. 59, S166-S175.

170. D. Liu, L. Xu and X. Lu, "Stress analysis of imperfect composite laminates with an interlaminar bonding theory", International Journal for Numerical Methods in Engineering, Vol. 37, 2819-2839 (1994).

171. W. Yin, "Interlaminar stress analysis of composite laminates using a sublaminate/layer model", Int. J. Solids Structures Vol. 31, No. 11, pp. 1549-1564, 1994.

172. C. Ko and C. Lin, "Method for calculating the interlaminar stresses in symmetric laminates containing a circular hole", AIAA Journal Vol. 30, pp. 197-204, 1992.

173. P. Caudenzi, R. Barboni and A. Mannini, "A finite element evaluation of single-layer and multi-layer theories for the analysis of laminated plates", Composite Structures 30 (1995) 427-440.

174. M. Liao, H.Jing and M. Hwang, "Improvements on the higher order plate element with partial hybrid stress model", Computers & Structures, Vol. 42, No. 1, pp. 45-51, 1992.

175. J. Ohgi and K. Hatanaka, "Assessment of J-integral for three-dimensional surface crack at notch root", JSME International Journal, Series A, Vol. 40, No. 3., 1997, pp. 290-297.

176. N. Pagano, "Stress fields in composite laminates", Int. J. Solids Structures Vol. 14, pp. 385-400, 1978.

177. R. Spilker, "A hybrid-stress finite-element formulation for thick multiplayer laminates", Computers & Structures, Vol. 11, pp. 507-514, 1980.

178. N. Pagano, "On the calculation of interlaminar normal stress in composite laminate", Journal of Composite Materials, Vol. 8 (1974) pp. 65-81.

179. T. Nishioka and S. Atlur, "Stress analysis of holes in angle-ply laminates: an efficient assumed stress 'Special-hole-element' approach and a simple estimation method", Computers & Structures, Vol. 15, No. 2, pp. 135-147, 1982.

180. J. Hutchinso, M. Mear and J. Rice, "Crack paralleling an interface between dissimilar materials", Journal of Applied Mechanics, Vol. 54, pp. 828-832, 1987.

181. Y. Shi and H. Chen, "A mixed finite element for interlaminar stress computation", Composite Structures 20 (1992) 127-136.

182. N. Ahmed and P. Basu, "Higher-order finite element modeling of laminated composite plates", International Journal for Numerical Methods in Engineering, Vol. 37, 123-139 (1994).

183. C. Lee and J Chen, "Interlaminar shear stress analysis of composite laminate with layer reduction technique", International Journal for Numerical Methods in Engineering, Vol. 39, 847-865 (1996).

184. G. Schoeppener and N. Pagano, "Stress fields and energy release rates in cross-ply laminates", Int. J. Solids Structures Vol. 35, No. 11, pp. 1025-1055, 1998.

185. O. Polit and M. Touratier, "A new laminated triangular finite element assuring interface continuity for displacements and stresses", Composite Structures 38, No. 1-4, pp.37-44, 1997.

186. N. Pagano and S. Soni, "Global-local laminate variational model", Int. J. Solids Structures Vol. 19, No. 3, pp. 207-228, 1983.

187. I. Paris and A. Poursartip, "Delamination crack tip behavior at failure in composite laminates under Mode I loading", Journal of Thermoplastic Composite Materials, Vol. 11- January 1998.

188. C. Wu, "Nonlinear thermal and mechanical analysis of step-tapered laminated plate under uniform in-plane load", Composite Structures 22 (1992) 33-45.

189. L. Zhao and Y. Chen, "The J-integral analysis of an interface main crack interfacing with near tip surinterface microcracks", International Journal of Fracture 80: R25-R30, 1996.

190. A. Aksoy and L. Carlsson, "Interlaminar shear fracture of interleaved graphite/epoxy composites", Composites Sciences and Technology 43 (1992) 55-69.

191. Y. Lin and J. Sung, "Stress singularities at the apex of a dissimilar anisotropic wedge", Journal of Applied Mechanics, Vol. 65, pp. 454-463.

192. I. Jeon, Y. Kim and S. Im, "Enriched finite element analysis for a delamination crack in a laminated composite strip", Computational Mechanics 17 (1996) 262-269.

193. A. Haddi and D. Weichert, "On the computation of the J-integral for three-dimensional geometries in inhomogeneous materials", Computational Materials Science, 5 (1996) 143-150.

194. W. Chow and S. Atluri, "Stress intensity factors as the fracture parameters for delamination crack growth in composite laminates", Composites Part B 28B (1997) 375-384.

195. J. Polana, B. Davidson, R. Hudson and A. Pieracci, "Effects of Mode ratio, ply orientation and precracking on the delamination toughness of laminated composite", Journal of Reinforced Plastics and Composites, Vol. 15, pp. 144-173, 1996.

196. M. Wisnom and M. Jones, "Delamination due to interaction between curvature induced interlaminar tension and stresses at terminating plies", Composite Structures 32 (1995) 615-620.

197. S. Swanson and Y. Qian, "Material characterization of T800/3900-2 carbon/epoxy composites", Composites Sciences and Technology 43 (1992) 197-203.

198. M. Pachajoa, M. Frances and J. Lee, "Stress and failure analysis of composite structures", Engineering Fracture Mechanics, Vol. 50, No. 5/6, pp. 883-902, 1995.

199. M. Stten and J. Valles, "Determination of in-situ fiber, matrix and interface properties in a composite using tensile tests and an extended shear-lag model", Materials Science & Engineering A250 (1998) 217-221.

200. D. Polyzois, I. Raftoyiannis and S. Ibrahim, "Finite element method for the dynamic analysis of tapered composite poles", Composite Structures 43 (1998) 25-34.

201. B. Agarwal and K. Gajpai, "Fracture toughness of glass/epoxy laminates through the J-integral approach", Composite Structures 9 (1988) 37-51.

202. H. Fukuda and T. Chou, "An advanced shear-lag model applicable to discontinuous fiber composites", Journal of Composite Materials, Vol. 15 (1981) pp. 79-91.

203. I. Beyerlein and L. Phoenix, "Comparison of shear-lag theory and continuum fracture mechanics for modeling fiber and matrix stresses in an elastic cracked composite lamina", Int. J. Solids Structures Vol. 33, No. 18, pp. 2543-2574, 1996.

204. P. Zhao and S. Ji, "Refinements of shear-lag model and its applications", Tectonophysics 279 (1997) 37-53.

205. C. Landis, R. Mcmeeking, "A shear-lag model for a broken fiber embedded in a composite with a ductile matrix", Composites Sciences and Technology 59 (1999) 447-457.

206. I Beyerlein and C. Lanids, "Shear-lag model for failure simulation of unidirectional fiber composites including matrix stiffness", Mechanics of Materials 31 (1999) 331-350.

207. S. Ochiai, M. Hojo, K. Schulte and B. Fiedler, "A shear-lag approach to the early stage of interfacial failure in the fiber direction in notched two-dimensional unidirectional composites", Composites Sciences and Technology 57 (1997) 775-785.

208. J. Nairn, "On the use of shear-lag methods for analysis of stress transfer in unidirectional composites", Mechanics of Materials 26 (1997) 63-80.

209. S. Ochiai, K. Schulte and P. Peters, "Strain concentration factors for fibers and matrix in unidirectional composites", Composites Sciences and Technology 41 (1991) 237-256.

210. K. He, S. V. Hoa, and R. Ganesan, "The study of tapered laminated composite structures: a review", Composites Science and Technology, Vol. 60, pp. 2643-2657, 2000.

211. K. He, and S. V. Hoa & R. Ganesan, "Partial hybrid stress element modeling and analysis of composite laminate plates", the Thirteenth International Conference on Composite Materials (13th ICCM), Beijing, China, June 2001.

212. K. He, R. Ganesan & S.V. Hoa, "Interlaminar fracture behavior of internally-tapered composite laminates", the Third Canadian International Composites Conference (CADCOM 2001), Montreal, Canada, August 2001.

213. K. He, R. Ganesan and S. V. Hoa, "Local analysis of tapered composite laminates using modified shear-lag model", Prepared for submission to publication on journal.

214. K. He, S. V. Hoa and R. Ganesan, "Partial hybrid-stress finite element modeling and analysis of tapered laminated composites", Prepared for submission to publication on journal.

215. K. He, R. Ganesan and S.V. Hoa, "Interlaminar fracture analysis of tapered composite laminates", Prepared for submission to publication on journal.